frontiers | Research Topics

Smart grid opportunities and challenges in integrating renewable energies

Edited by
Muhammad Faizan Tahir, Salah Kamel, Jose Luis Domínguez-García, Khalid Mehmood Cheema and Kashif Mehmood

Published in
Frontiers in Energy Research

ISSN 1664-8714
ISBN 978-2-8325-2654-5
DOI 10.3389/978-2-8325-2654-5

About Frontiers

Frontiers is more than just an open access publisher of scholarly articles: it is a pioneering approach to the world of academia, radically improving the way scholarly research is managed. The grand vision of Frontiers is a world where all people have an equal opportunity to seek, share and generate knowledge. Frontiers provides immediate and permanent online open access to all its publications, but this alone is not enough to realize our grand goals.

Frontiers journal series

The Frontiers journal series is a multi-tier and interdisciplinary set of open-access, online journals, promising a paradigm shift from the current review, selection and dissemination processes in academic publishing. All Frontiers journals are driven by researchers for researchers; therefore, they constitute a service to the scholarly community. At the same time, the *Frontiers journal series* operates on a revolutionary invention, the tiered publishing system, initially addressing specific communities of scholars, and gradually climbing up to broader public understanding, thus serving the interests of the lay society, too.

Dedication to quality

Each Frontiers article is a landmark of the highest quality, thanks to genuinely collaborative interactions between authors and review editors, who include some of the world's best academicians. Research must be certified by peers before entering a stream of knowledge that may eventually reach the public - and shape society; therefore, Frontiers only applies the most rigorous and unbiased reviews. Frontiers revolutionizes research publishing by freely delivering the most outstanding research, evaluated with no bias from both the academic and social point of view. By applying the most advanced information technologies, Frontiers is catapulting scholarly publishing into a new generation.

What are Frontiers Research Topics?

Frontiers Research Topics are very popular trademarks of the *Frontiers journals series*: they are collections of at least ten articles, all centered on a particular subject. With their unique mix of varied contributions from Original Research to Review Articles, Frontiers Research Topics unify the most influential researchers, the latest key findings and historical advances in a hot research area.

Find out more on how to host your own Frontiers Research Topic or contribute to one as an author by contacting the Frontiers editorial office: frontiersin.org/about/contact

Smart grid opportunities and challenges in integrating renewable energies

Topic editors

Muhammad Faizan Tahir — South China University of Technology, China
Salah Kamel — Aswan University, Egypt
Jose Luis Domínguez-García — Energy Research Institute of Catalonia, Spain
Khalid Mehmood Cheema — Fatima Jinnah Women University, Pakistan
Kashif Mehmood — Southeast University, China

Citation

Tahir, M. F., Kamel, S., Domínguez-García, J. L., Cheema, K. M., Mehmood, K., eds. (2023). *Smart grid opportunities and challenges in integrating renewable energies*. Lausanne: Frontiers Media SA. doi: 10.3389/978-2-8325-2654-5

Table of contents

frontiers | Frontiers in Energy Research

TYPE Original Research
PUBLISHED 25 August 2022
DOI 10.3389/fenrg.2022.971384

OPEN ACCESS

EDITED BY
Sudhakar Babu Thanikanti,
Chaitanya Bharathi Institute of Technology, India

REVIEWED BY
Daniel Tudor Cotfas,
Transilvania University of Brașov, Romania
Karthik Balasubramanian,
McMaster University, Canada
R.P. Saini,
Indian Institute of Technology Roorkee, India

*CORRESPONDENCE
Elmazeg Elgamli,
ELGAMLIES@CARDIFF.AC.UK

SPECIALTY SECTION
This article was submitted to Smart Grids,
a section of the journal
Frontiers in Energy Research

RECEIVED 17 June 2022
ACCEPTED 28 July 2022
PUBLISHED 25 August 2022

CITATION
Yahiaoui F, Chabour F, Guenounou O, Zaouche F, Belkhier Y, Bajaj M, Shouran M, Elgamli E and Kamel S (2022), Experimental validation and intelligent control of a stand-alone solar energy conversion system using dSPACE platform.
Front. Energy Res. 10:971384.
doi: 10.3389/fenrg.2022.971384

Experimental validation and intelligent control of a stand-alone solar energy conversion system using dSPACE platform

Fatah Yahiaoui[1], Ferhat Chabour[2], Ouahib Guenounou[1], Faika Zaouche[1], Youcef Belkhier[3], Mohit Bajaj[4], Mokhtar Shouran[5], Elmazeg Elgamli[5]* and Salah Kamel[6]

[1]Laboratoire de Technologie Industrielle et de l'Information (LTII), Faculté de Technologie, Universite de Bejaia, Bejaia, Algeria, [2]GREAH Laboratory, University of Le Havre, Lebon, France, [3]Centre for Ocean Energy Research, Maynooth University, Maynooth, Kildare, Ireland, [4]Department of Electrical Engineering, Graphic Era (Deemed to be University), Dehradun, India, [5]Wolfson Centre for Magnetics, School of Engineering, Cardiff University, Cardiff, United Kingdom, [6]Electrical Engineering Department, Faculty of Engineering, Aswan University, Aswan, Egypt

This paper presents the performances of an artificial intelligent fuzzy logic controller (FLC) based maximum power point tracking (MPPT) and a conventional perturb and observe (P&O) based MPPT controller is presented for a stand-alone PV system and tested in an emulated test bench experimentation. The studied system is composed of a DC power supply emulating the PV panel, a DC/DC boost converter, a variable resistive load and a real-time MPPT controller implemented in the dSPACE DS1104 controller. To verify the performance of the FLC proposed, several simulations have been performed in Matlab/Simulink environment. The proposed method outperforms the P&O method in terms of global search capability and dynamic performance, according to the comparison with the P&O method. To verify the practical implementation of the proposed method, the control of the emulated PV source and the MPPT algorithms are designed using the simulink/Matlab environment and implemented on dSPACE DS1104 controller. Experimental results confirm the efficiency of the proposed method and its high accuracy to handle the resistance varying.

KEYWORDS

experimental validation, fuzzy logic control, intelligent control, stand-alone solar energy system, DSPACE platform

1 Introduction

Photovoltaic (PV) systems are a clean energy technology that employs solar energy, the planet's most abundant and broadly distributed renewable energy source. PV power generation systems have outperformed even the most optimistic predictions. The grid linked PV system, the stand-alone PV system, and the hybrid system are the three main

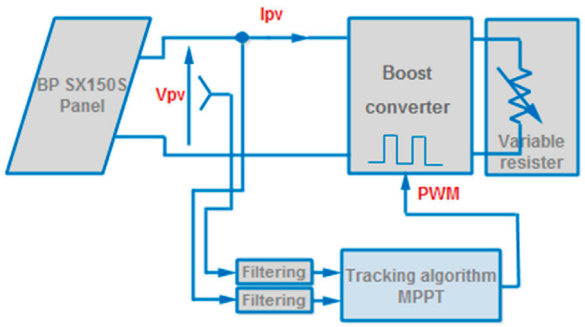

FIGURE 1
Diagram block of stand-alone photovoltaic energy conversion system.

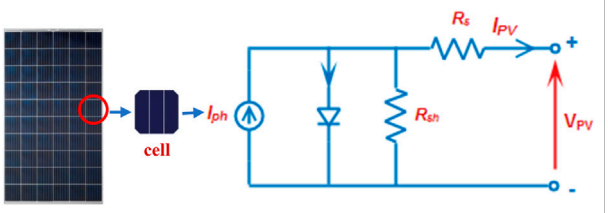

FIGURE 2
Modeling of a solar cell by the one-diode model.

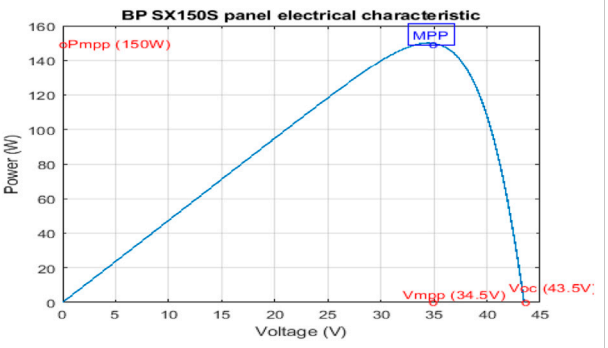

FIGURE 3
BP SX150S panel electrical characteristic.

TABLE 1 Electrical specifications of BP SX150S panel at STC.

Electrical specifications	
STC rated output (P_{MPP})	150 W
Output power tolerance	± 5%
Rated voltage (V_{MPP}) at STC	34.5 V
Rated current (I_{MPP}) at STC	4.35 A
Open circuit voltage (V_{oc}) at STC	43.5 V
Short circuit current (I_{sc}) at STC	4.75 A
Temperature coefficient of Voc	(160 ± 20)mV/°C
Temperature coefficient of Isc	(0.065 ± 0.015)%/°C
Temperature coefficient of power	(0.5 ± 0.05)%/°C
No. of cells	72

types of PV systems now being used in different parts of the world (Mao et al., 2020). Stand-alone PV systems are utilized in distant and specialized locations including an energy storage system, usually installed as a battery system, although alternative options, such as fuel cells, are available. To fulfill the increased demand for alternative sources of energy, grid-connected PV systems are being used. Wind, tidal, and thermal energy may be used in conjunction with solar photovoltaic systems to create hybrid power systems (Mohapatra et al., 2017). However, Power fluctuations produced by atmospheric factors affect PV systems, i.e., solar irradiation and ambient temperature. Maximum power point tracking (MPPT) algorithms are used to harvest maximum power from a PV panel under specific operating conditions, allowing the generated power to be controlled (Mohapatra et al., 2017), (Zaouche et al., 2017).

Several publications have been published to help solar power plants extract the most power possible. In PV systems, a suitable MPPT controller tracks the maximum power point in all environmental conditions. In recent years, a number of MPPT controllers have been proposed, including P&O (Mohammadinodoushan et al., 2021; Mousa et al., 2021; İnci, 2021), incremental conductance (INC) (Nadeem and Hussain, 2021), and fuzzy logic controller (FLC) (Yang et al., 2020). A little variance in the step size causes the control parameter to be perturbed in the P&O approach. Due to the measurement of PV system output power, the orientation of the step size determined by the P&O technique is altered somewhat. When a PV system's output power is lowered or raised, problems might arise (Sarvi and Azadian, 2021).

The P&O algorithm is the most commonly used MPPT algorithm in renewable energy conversion system because it is relatively simple to implement at low cost (Motahhir et al., 2020). The system control commands are determined using this method based on the difference in power output between the current and prior system states. However, this method has given rise to oscillations around the point of operation of MPP leading to significant energy losses (Zaouche et al., 2017), (Vicente et al., 2020). Furthermore, in rapidly changing atmospheric conditions, P&O does not adapt correctly. Because it is established on the equivalence of increment and conductance, the INC technique enables for the search for the greatest power to be achieved (Yilmaz et al., 2018). The P&O and INC controllers are among the most widely used MPPT controllers, owing to their ease of

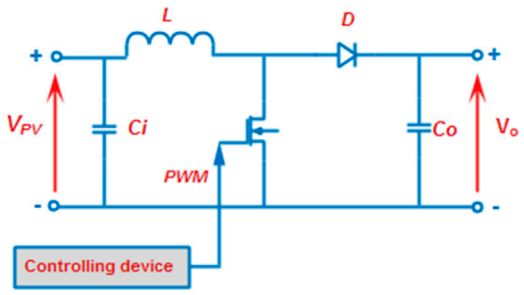

FIGURE 4
Structure of the Boost converter.

installation and straightforward design. Nonetheless, rapid changes in weather conditions have an impact on the controllers' ability to function properly. Furthermore, even in constant climatic conditions, oscillations around the MPP have been seen using such methods. To put it another way, a decrease in Sun irradiation can have an impact on the operation of these controllers (Sarvi and Azadian, 2021). Recently MPPT methods based on artificial intelligence techniques such as artificial neural networks (ANN) and fuzzy logic controllers (FLC) have emerged (Yang et al., 2020). The FLC is another well-known MPPT controller that has significant advantages over traditional INC and P&O control strategies (Youssef et al., 2018). The outputs/inputs of these controller are fully dependent on system model information. In (Harrag and Messalti, 2019), it is suggested that an enhanced MPPT technique based on the SMC be used. The suggested controller's key advantages are its fast dynamic response, high stability, and simplicity. A sliding mode MPPT based improved krill herd algorithm for variable step size P&O strategy is proposed in (Latifi et al., 2021), adaptive MPPT based sliding mode and fuzzy controls (Miqoi et al., 2019), optimized MPPT algorithm based on fuzzy logic control (Farajdadian and Hosseini, 2019). Recent studies (Dorji et al., 2020; Pandey et al., 2022) have compared between perturb and observe (P&O) and fuzzy logic based on PV-MPPT algorithms. Simulation results confirm the effectiveness of the FLC method.

When using a standard P&O strategy based on a predetermined step size perturbation, output power variations in solar systems are cancelled at the MPP, but this is not possible. It is possible to repair a quicker dynamic response by using greater step sizes, but this leads to huge changes with in output of photovoltaic panels around their maximum point and increased power loss. Small step sizes, on the other hand, lower PV array output power fluctuation, but they might lead to a delayed dynamic response when solar irradiation is quickly altered.

In this paper, performances of an artificial intelligent FLC and a conventional perturb and observe (P&O) controller are presented of a stand-alone PV system and tested in a real test bench experimentation using dSPACE DS1104 controller card.

TABLE 2 Electrical specifications of Boost converter.

Electrical specifications	
Inductor (L)	0.6 mH
Input capacitor (C_i)	500 μF
Output capacitor (C_o)	2,200 μF
Switching frequency (f_s)	10 kHz
IGBT SKM50GB12T4	

The studied system is composed by a DC power supply emulating the PV panel, a DC/DC boost converter, a resistive load and a real-time maximum power point tracking controller implemented in the dSPACE card. Under the above test conditions, a comparative analysis is performed for the proposed artificial intelligent FLC and conventional P&O control algorithm. Traditionally, the control algorithms of power converters in real time are designed with microcontrollers (Yang et al., 2020). But microcontrollers suffer from a limited performance when used in control applications requiring high operating speeds. Furthermore, comprehending the microcontroller capabilities is difficult in the event of complicated control structures, and programming them becomes a time-consuming operation, resulting in poor performance. A recent study (Altwallbah et al., 2022) presented a hardware implementation of a P&O algorithm under the partial shading condition on a digital signal processing controller (TMS320F28335). The digital processing boards (DSP) with rapid computational capacity, increased flexibility, and ease of programming have emerged, they may now serve as an alternative for numerical implementation of more complicated control algorithms. In this paper the dSPACE DS1104 controller is used to test the proposed control algorithms.

The main originality and contribution of the present work over the related papers in the literature are summarized as given below:

- An artificial intelligent fuzzy logic based MPPT controller and a conventional perturb and observe controller are presented for a stand-alone PV system, investigated and compared to demonstrate the superiority of the FLC over the conventional P&O.
- Extensive numerical investigations are made to demonstrate the robustness of the proposed FLC approach against parameter changes, external disturbances, and the conventional P&O.
- Extensive experimental validation is performed with a real test bench experimentation using dSPACE DS1104 controller.

The present form organizes the present paper: in Section 2, the system description is established. Section 3 deals with the

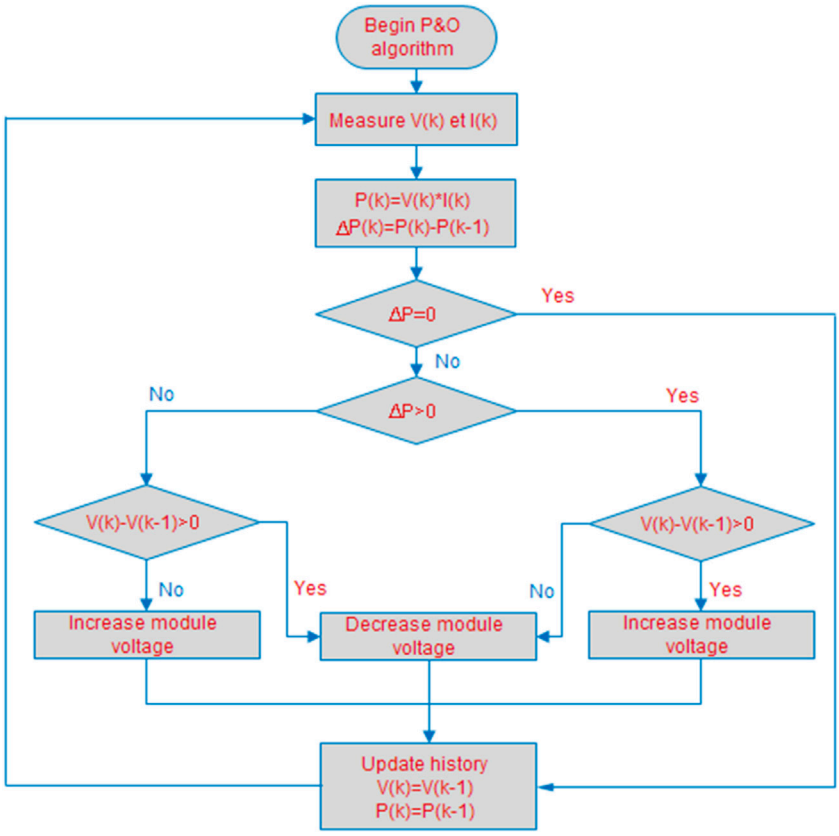

FIGURE 5
Flowchart of the P&O algorithm.

TABLE 3 MPP search rules.

Case	ΔP	ΔV	Research direction	Duty ratio
1	+	+	Right direction	$D(k) = D(k-1) - \alpha$
2	+	−	Right direction	$D(k) = D(k-1) + \alpha$
3	−	−	Wrong direction	$D(k) = D(k-1) - \alpha$
4	−	+	Wrong direction	$D(k) = D(k-1) + \alpha$

proposed strategy design procedure. Section 4, described in detail the extensive numerical investigation of the proposed candidate strategy and the extensive experimental investigation. Finally, Section 5 deals with the main conclusion of the present paper.

2 PV system description

Figure 1 shows the diagram block of the stand-alone photovoltaic energy conversion system. It mainly contains a BP SX150S panel and a variable resistive load that are interconnected via a boost converter controlled by the MPPT controller:

2.1 BP SX150S panel modeling

The fundamental composition element of a PV panel is the solar cell. A cell can be assimilated to a photocell in generator convention. The BP SX150S PV panel is composed of 72 multi-crystalline silicon PV cells connected in series (N_s). To comprehend and investigate the features of a solar cell, mathematical models have been created. There are a few different sorts of models, such as single-diode and two-diode models (Bennett et al., 2012), (Dhaundiyal and Atsu, 2019). The two diode model takes into consideration an additional diode in the equivalent circuit of a single diode, this diode connected in parallel with the first diode. The one-diode model contains few parameters and easier to model compared to a two-diode model. According to the article (Dhaundiyal and Atsu, 2019), the simulation results and the experimental results of the electrical characteristics P(V) and I(V) of the solar panel clearly show that the results are similar. In this paper, the

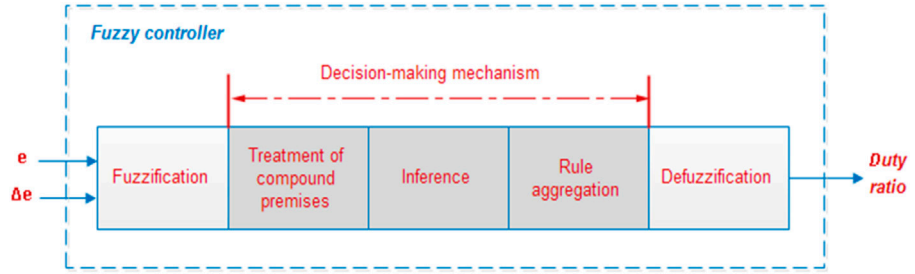

FIGURE 6
Fuzzy controller structure.

TABLE 4 Rule base table for fuzzy MPPT controller.

e	Δ*e*				
	NB	**NS**	**ZE**	**PS**	**PB**
NB	Rule 1 ZE	Rule 2 ZE	Rule 3 PB	Rule 4 PB	Rule 5 PB
NS	Rule 6 ZE	Rule 7 ZE	Rule 8 PS	Rule 9 PS	Rule 10 PS
ZE	Rule 11 PS	Rule 12 ZE	Rule 13 ZE	Rule 14 ZE	Rule 15 NS
PS	Rule 16 NS	Rule 17 NS	Rule 18 NS	Rule 19 ZE	Rule 20 ZE
PB	Rule 21 NB	Rule 22 NB	Rule 23 NB	Rule 24 ZE	Rule 25 ZE

one-diode model is chosen to model the solar cell (Dhaundiyal and Atsu, 2019).

The electrical circuit equivalent to a one-diode model is presented in Figure 2. The chosen model is efficient, less complex to model and reproduces the electrical characteristic of the BP SX150S panel, as shown in Figure 3. The mathematical equation of the PV panel model is given by the current I_{pv} versus the voltage V_{pv} in Eq. 1:

$$I_{pv} = I_{Ph} - I_s\left(\exp\left(\frac{V_{pv} + I_{pv}R_s}{N_s V_T}\right) - 1\right) - \left(\frac{V_{pv} + I_{pv}R_s}{R_{sh}}\right) \quad (1)$$

where V_T (equal to $(a.k.T/q)$) is the diode thermal voltage, k is the Boltzmann constant, q is the electron charge, a is the diode ideality factor and T is the temperature in Kelvin. I_{Ph} is the light generated current, I_s is the diode saturation current, R_s and R_{sh} are the series and parallel equivalent resistances.

Table 1 lists the electrical parameters of the BP SX150S panel used in this study, which are reported at Standard Test Condition (STC ie. 1000 W/m^2 and 25°C).

2.2 Boost converter modeling

Figure 4 shows the boost converter's construction, which is used to boost the PV output voltage (Vo) for a resistive load. It controls the input source to load power transmission through a Pulse Width Modulation (PWM) technology provided by a high frequency regulating device called an Insulated Gate Bipolar Transistor (IGBT). A 10 kHz PWM signal is injected into the converter's switch S by a controlling device.

The PWM signal's duty cycle D may be changed in real-time to follow the PV panel's highest available power and extract as much of it as possible. The parameter values of the designed boost converter are listed in Table 2. The equations characterizing these parameters are given as follows (Weng et al., 2019):

$$\begin{cases} V_o = \dfrac{1}{1-D} V_{pv} \\ L = \dfrac{V_{pv} \times \left(V_o - V_{pv}\right)}{\Delta I_{ripple} \times f_s \times V_o} \\ C_o = \dfrac{I_o \times D}{f_s \times \Delta V_{ripple}} \end{cases} \quad (2)$$

where ΔI_{ripple} is the inductor ripple current and ΔV_{ripple} is the output voltage ripple.

3 MPPT algorithms

3.1 Conventional perturb and observe algorithm

The P&O algorithm uses current and voltage sensors to measure the solar array's output power. Because of its simplicity, the conventional P&O algorithm has been widely used. The algorithm mechanism has been depicted in Figure 5. After a prolonged process of data collection of perturbation and observation, the operating point converges to the MPP. The algorithm forecasts the time to approach MPP by comparing the power and voltages of time (k) with the sample at a time $(k-1)$. If the power change is positive, a little voltage fluctuation affects the power of the solar panel, and the voltage perturbation

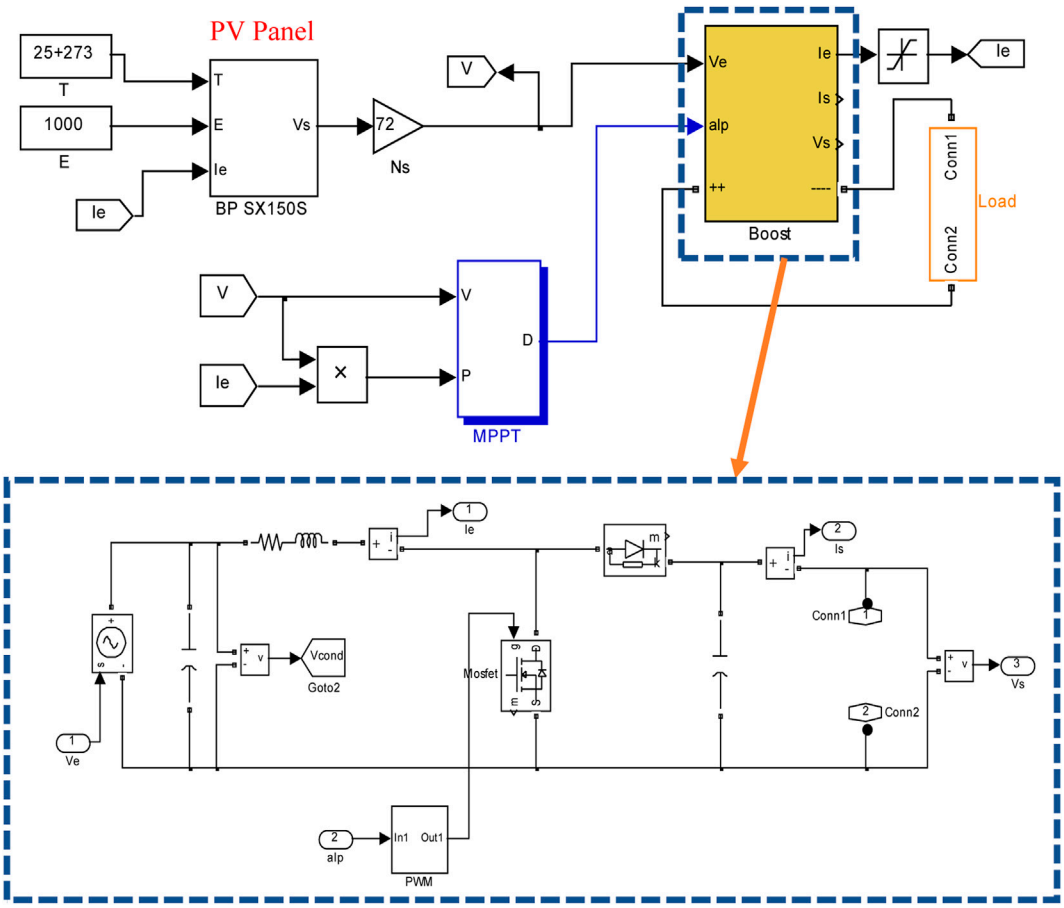

FIGURE 7
The PV system under MATLAB/Simulink.

continues in the same direction. However, if delta power is negative, the MPP is far away, and the perturbation must be reduced to approach it (Yanarates et al., 2021). The P&O algorithm is summarized in Table 3. As a result, the entire PV curve is examined by minor perturbations to discover the MPP, which increases the algorithm's response time. When the perturbation size is increased, steady state oscillations around the MPP result. To alleviate the response time problem and steady state oscillations, many researchers have proposed other algorithms.

3.2 The proposed fuzzy controller based MPPT algorithm

The MPPT algorithm based on a fuzzy logic controller (FLC) is an intelligent way of tracking the maximum power point in a PV system. It makes use of fuzzy set theory rather than a rigorous mathematical model. It is made up of a step-by-step adaptive search that achieves rapid convergence. Fuzzification, inference engine and defuzzification are functional blocks of the fuzzy controller. Figure 6 shows the main components of the Mamdani type fuzzy controller (Shiau et al., 2015).

MFs are used to convert actual input values back to linguistic values during the fuzzification process. The "if-then" rules that make up the heuristic engine link the input and output. The defuzzification step is used to return the output linguistic variable to its original state of the clear output. The slope of the power-voltage curve ($P_{pv} - V_{pv}$) is the most common input to the fuzzy controller in PV systems (Guenounou et al., 2021), (Zaouche et al., 2016).

In this case, triangular and trapezoidal MFs are used as input and output because they are simple to implement and reduce computational complexity. These functions are simple to implement. For the linguistic variables depicted in Figure 10, P denotes positive and N denotes negative. Furthermore, the letters B, S, and ZE stand for Big, Small, and Zero. In Figure 9, each input variable, $e(k)$ and $\Delta e(k)$, is assigned to one of five

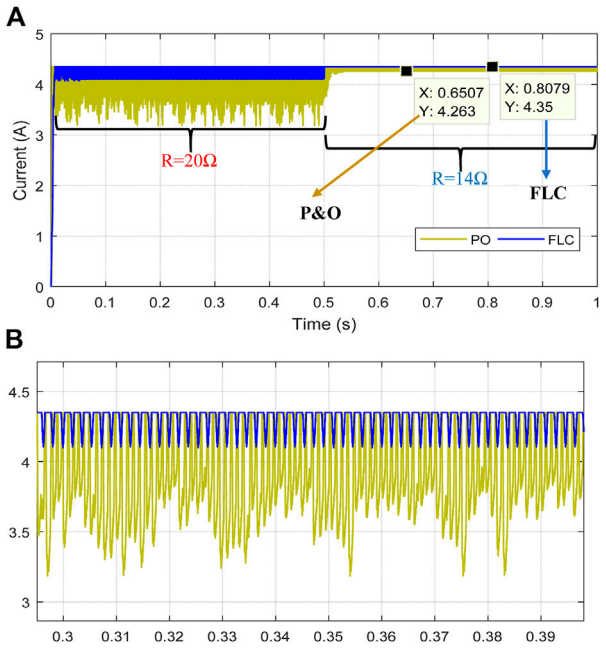

FIGURE 8
Generated PV currents for FLC and P&O controls. **(A)** current response. **(B)** Zoom on the current response.

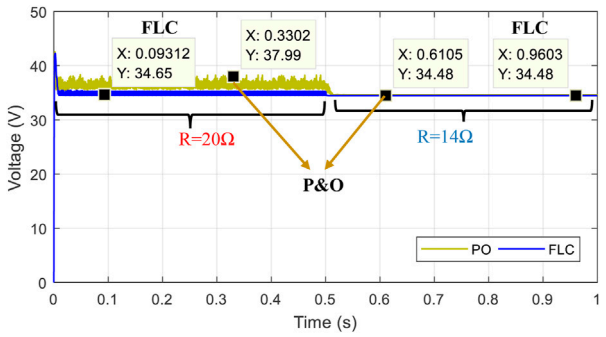

FIGURE 9
Generated PV voltages for FLC and P&O controls.

different linguistic variables. As a result, the proposed fuzzy rules set contains 25 distinct fuzzy rules. Table 4 contains the entire set of fuzzy rules.

The error and error variation are the two inputs variables that are described at a sampling instant k by following:

$$e(k) = \frac{P_{pv}(k) - P_{pv}(k-1)}{V_{pv}(k) - V_{pv}(k-1)} \tag{3}$$

$$\Delta e(k) = e(k) - e(k-1) \tag{4}$$

The FLC determines the next operating point based on these two inputs, using MFs and a rule table. Depending on whether E is negative or positive, the operating point will be on the right or left side of the MPP. The MPP is reached that E is equal to zero. The Δe input determines whether or not the operating point moves along the MPP direction.

A fuzzy-based PI controller is considered in this work, with a duty ratio D computed as given below:

$$D(k) = G_D \times \Delta D_N(k) + D(k-1) \tag{5}$$

where, G_D represents the factor's scaling output and ΔD_N is the normalized incremental change of the duty cycle.

4 Results and discussion

4.1 Simulation section

The simulation tests of the PV system depicted in Figure 1 have been performed under MATLAB/Simulink environment. The panel's maximum output power is 150W. The output capacitance and the series input inductance of the boost converter are C_o = 1100 µF and L = 0.6mH, respectively. A variable resistive load is connected to the boost's output. The Simulink diagram of the studied system is shown in Figure 7, where the DC-DC boost converter is implemented using the MathWorks Simscape library.

The FLC output variable (D) and input variables (e and Δe) are both computed by five membership functions. The variation's ranges are [−50,50] for Δe [−35,5] for e, and [−1.5,1] for the output. In order to determine these intervals, the maximum values permitted are used for our PV system in the testing environment for each variable.

The factor's scaling output is set to 0.04. The increment step of the P&O method is set at 0.02.

The standard test conditions (STC) are adopted for the simulations, which are STC: S = 1000W/m^2 and T = 25°C. Due to the lack of place, the impact of the variation of atmospheric conditions will be studied in future work.

The system is simulated in a 1s total time with a 50 µs fixed step size. At time 0.5 s, a variation of the load from R = 20 Ω to R = 14 Ω was performed to test the MPPT's performance.

4.1.1 Simulation results discussion

Figure 8 shows the results of the generated PV currents for each the proposed FLC and the P&O method (Motahhir et al., 2020). In the presented results during the transient load step of R = 20 Ω between 0 and 0.5 s, it can be seen that the proposed FLC generates a current which is around the rated value 4.35 A with a tracking error of 4% and with extremely reduced oscillations (the minimal generated current is 4.2 A as shown in the zoom on the current given in Figure 8B). Contrary to the conventional P&O method, which generates a current around the rated value with an important tracking error of 27% and it presents a high oscillation (a minimal current value of 3.2 A is

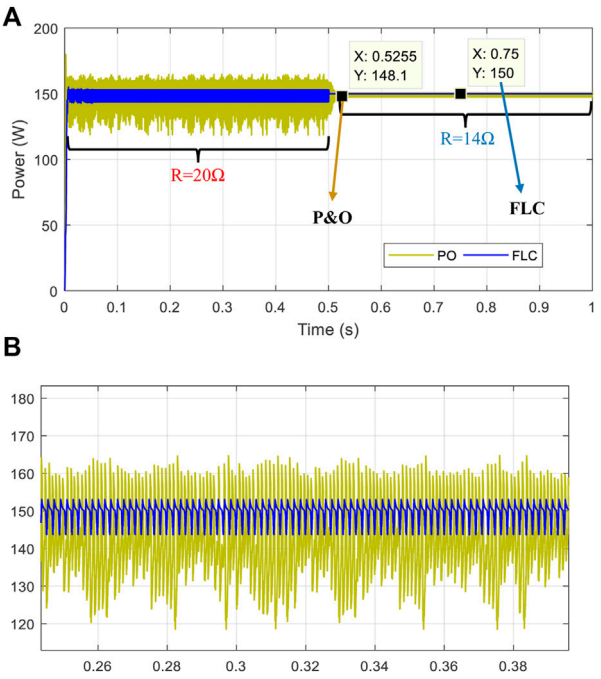

FIGURE 10
Generated PV powers for both FLC and P&O controls. **(A)** Power response. **(B)** Zoom on power response.

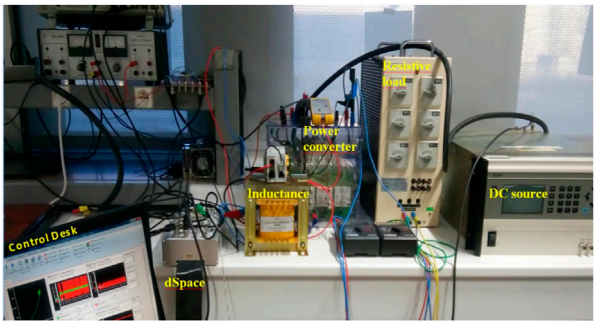

FIGURE 11
Laboratory experimental setup of the emulated PV system.

observed). In the second transient load step of R = 14 Ω between 0.5 and 1s, it is clearly observed that the proposed FLC shows the better current generation, which much perfectly the rated value 4.35 A as depicted in Figure 8. Contrary to the conventional P&O, which shows the lowest oscillations compared to the first step but a tracking error of 2% is observed (minimal current value of 4.26 A).

Figure 9 shows the results of the generated PV voltages for each the proposed FLC and the conventional P&O. In the presented results during the transient load step of R = 20 Ω between 0 and 0.5 s; it can be seen that the P&O generates a voltage which is around the value 37 V which diverge from the maximum power point (MPP) voltage of 34.5 V as given in Table 1. Contrary to the proposed FLC method, which generates a voltage around the rated MPP voltage value. In the second transient load step of R = 14 Ω between 0.5 and 1s, it is clearly observed that both proposed FLC and P&O generate a voltage which much perfectly the MPP voltage value 34.5 V as depicted in Figure 9.

Figure 10 shows the results of the generated PV powers for each the proposed FLC and the conventional P&O. In the presented results during the transient load step of R = 20 Ω between 0 and 0.5 s; it is observed that the proposed FLC generates a power which is around the rated value 150 W with a tracking error of 6 W under the rated value and 1 W after the rated value which represents an error of 4.66% with extremely reduced oscillations. Contrary to the conventional P&O method, which generates power with an important tracking power error of 28.66% and it presents a high oscillation. In the second transient load step of R = 14 Ω between 0.5 and 1 s, it is clearly observed that the proposed FLC shows better power generation, which much perfectly the rated value 150 W as depicted in Figure 10. Contrary to the conventional P&O, which shows the lowest oscillations compared to the first step but a power loss of 1.26% is observed.

4.2 Experimental section

Figure 11 shows the experimental test bench of the emulated PV system. The hardware implementation has been developed in the GREAH laboratory - France. Different components of experimental test bench of the emulated PV system have been discussed in this section by giving a list of components and their specifications.

The suggested MPPT controller is implemented on a dSPACE DS1104 platform, which allows real-time testing. An Emulated PV Source (EPVS) was linked to a variable DC load using a boost converter which specifications are listed in Table 2. To generate the necessary PWM signal, a DS1104SL-DSP-PWM block is used. This later is depicted in Figure 12B. For the measurement of both the current and the voltage of the EPVS, two sensors have been used: Cleqee A622 for the current and TA057 for the voltage. The measured voltage and current are subsequently transformed to digital signals using a DSP Analog Digital Converter (ADC) interface that operates over a voltage range of −10 V to +10 V and filtered with implemented digital filters. By multiplying the instant current and voltage, the instantaneous power is computed. A gain scale of 10 and a gain scale of 20 are respectively programmed to rescale the measured current and voltage signals. Figure 12A shows the used Digital Analog Converter (DAC) blocks providing calculated

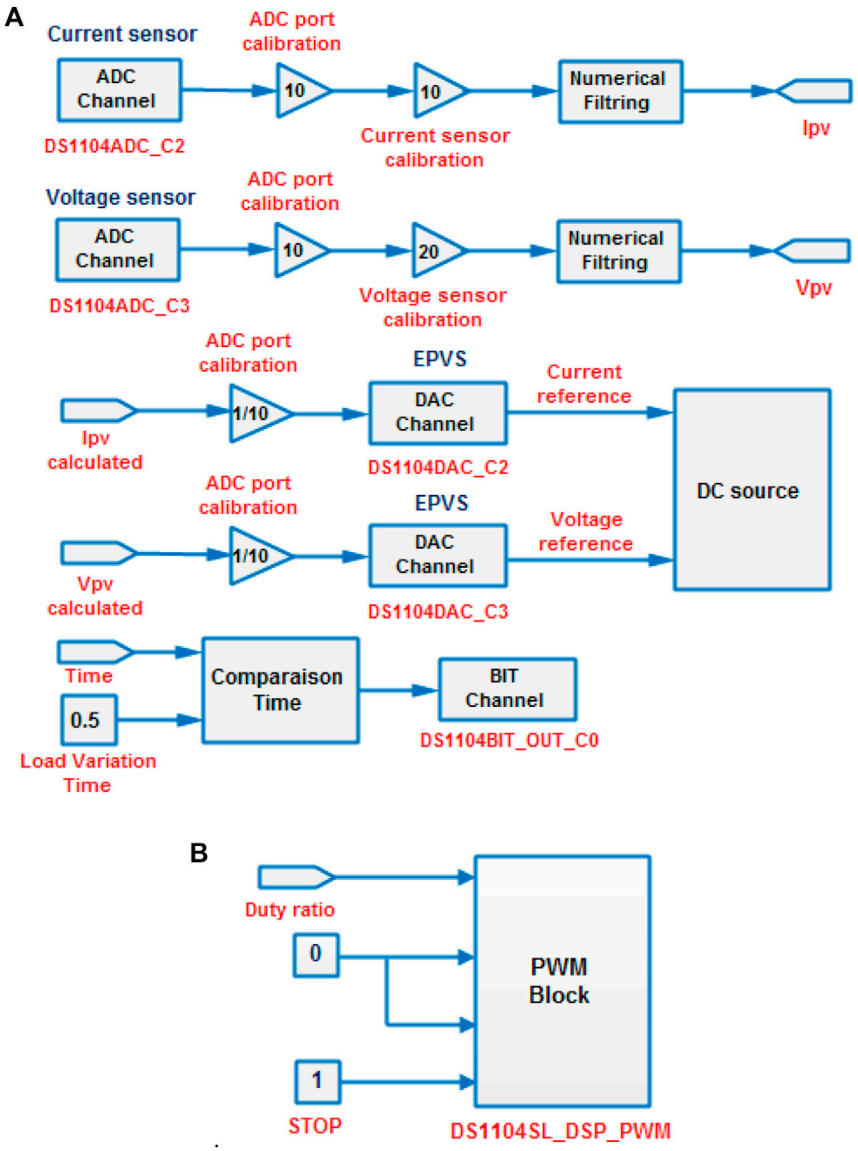

FIGURE 12
(A) ADC and DAC conversion blocks of the EPVS current and voltage, **(B)** PWM generation block.

EPVS's current and voltage references that will be injected into the programmable DC source. In this study, the sampling step time is programmed equal to 50 μs

4.2.1 Emulated PV source

A DC power supply Elgar 5,500 which is programmable is used to generate the output characteristics of a BP SX150S PV panel (Weng et al., 2019). This emulation makes it possible to compensate for the lack of the PV panel and facilitates the emulation of weather changes. The used Simulink model of the PV panel is implemented in a dSPACE DS1104 controller using a 50 μs sampling time. This last generates the PWM signals controlling the boost converter with a 10 kHz switching frequency. The analog signal (0–10 V range) required to control the DC power supply is generated from a DAC output. Figure 13 shows the practical characteristics of the EPVS obtained by varying the output current of the power DC supply.

4.2.2 Experimental results discussion

In the experimental steps, the system is also tested in a 1s total time with a 50 μs fixed step size. At time 0.5s, a variation

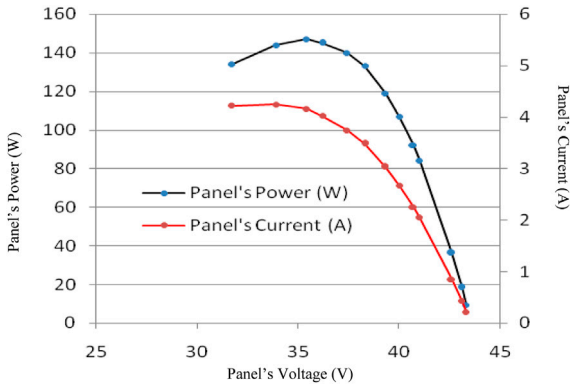

FIGURE 13
Electrical characteristics of the PV panel BP SX150S.

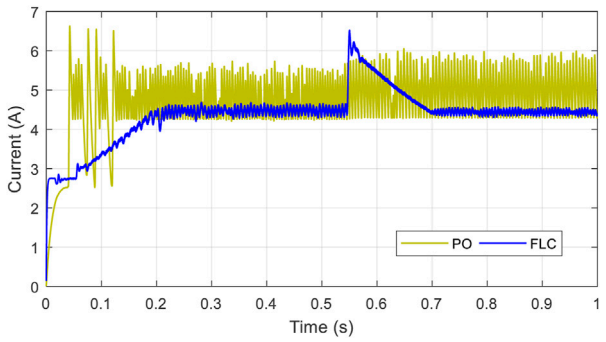

FIGURE 14
Experimental currents for both FLC and P&O controls.

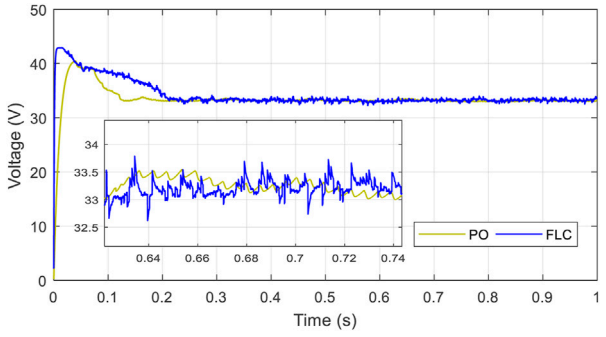

FIGURE 15
Experimental voltages for both FLC and P&O controls.

of the load from R = 20 Ω to R = 14 Ω was performed to test the MPPT's performance is also applied in this testing part. Figure 14 shows the experimental current generated by the

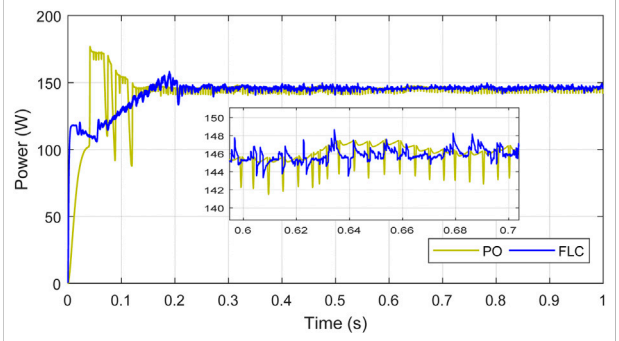

FIGURE 16
Experimental power for both FLC and P&O controls.

emulated PV system due to the proposed FLC and the conventional P&O. It is observed that the proposed FLC offers the best results as it shows extremely lowest oscillations compared to the P&O at the transient load step R = 20Ω and more important the current is maintained close to the rated value with the FLC than the second one at the transient load step R = 14Ω.

Figure 15 presents the experimental generated voltage by both the FLC and P&O. Here also it is clearly shown that the first control maintains the generated voltage very close to the rated value with the fastest convergence than the P&O. Figure 16 shows the experimental generated power by the test bench. It is is clearly observed that the FLC offers the highest power generation and performance than the conventional control. In fact, the power generated by the FLC converges progressively to the MPP with a fast criterion, as can be seen at 0s where the conventional control shows oscillations between 0 and 0.2 s which is not good for the dynamic of the test bench.

The comparative analysis of the proposed FLC and the conventional P&O shows that the FLC ensures fast convergence, high stability, and lowest tracking errors in comparaison to the conventional P&O. In a general way, the proposed method outperforms the P&O method in terms of global search capability. Thus, from the previous simulation and experimental results, the proposed method validates the objective mentioned in the introduction part which is to shows that the FLC based MPPT guarantee efficient, secure, and reliable power to the load side than the conventional MPPT methods.

5 Conclusion

This paper presents a simulation and experimental validation of a stand-alone photovoltaic system. A DC

power supply imitating a solar panel, a DC/DC boost converter, a resistive load, and a real-time maximum power point tracking controller built-in a dSPACE DS1104 controller make up the investigated system. In the details of the work, performances of an intelligent FLC and a P&O controller are presented. Both simulated and experimental results are given to demonstrate the obtained performances. The main highlights of the present work are summarized as follows:

- The comparative analysis shows that the FLC proposed ensures fast convergence, high stability, and the lowest tracking errors in comparison to P&O method.
- The FLC proposed reacts quickly to load variations and keeps power at its highest level.
- The proposed FLC shows the lowest transitional state response time, and the steady state variations are significantly minimized over the P&O algorithm, which shows an overtaking.

The practical results obtained in the different tests show the effectiveness of the proposed method. The proposed method is a solution for solving the problem of MPP tracking and the study carried out in this paper answers the questions studied. This work can be used to implement different practical applications of solar energy conversion systems.

Data availability statement

The original contributions presented in the study are included in the article/Supplementary Material, further inquiries can be directed to the corresponding author.

Author contributions

All authors listed have made a substantial, direct, and intellectual contribution to the work and approved it for publication.

Conflict of interest

The authors declare that the research was conducted in the absence of any commercial or financial relationships that could be construed as a potential conflict of interest.

Publisher's note

All claims expressed in this article are solely those of the authors and do not necessarily represent those of their affiliated organizations, or those of the publisher, the editors and the reviewers. Any product that may be evaluated in this article, or claim that may be made by its manufacturer, is not guaranteed or endorsed by the publisher.

References

Altwallbah, N. M. M., Radzi, M. A. M., Azis, N., Shafie, S., and Zainuri, M. A. A. M. (2022). New perturb and observe algorithm based on trapezoidal rule: Uniform and partial shaing conditions. *Energy Convers. Manag.* 264, 115738. doi:10.1016/j.enconman.2022.115738

Bennett, T., Zilouchian, A., and Messenger, R. (2012). Photovoltaic model and converter topology considerations for MPPT purposes. *Sol. Energy* 86 (7), 2029–2040. doi:10.1016/j.solener.2012.04.005

Dhaundiyal, A., and Atsu, D. (2019). Modeling of photovoltaic module using the MATLAB. *JNRD-Journal Nat. Resour. Dev.* 9, 59–69. doi:10.5027/jnrd.v9i0.06

Dorji, S., Wangchuk, D., Choden, T., and Tshewang, T. (2020). Maximum power point tracking of solar photovoltaic cell using perturb & observe and fuzzy logic controller algorithm for boost converter and quadratic boost converter. *Mater. Today Proc.* 27, 1224–1229. doi:10.1016/j.matpr.2020.02.144

Farajdadian, S., and Hosseini, S. H. (2019). Optimization of fuzzy-based MPPT controller via metaheuristic techniques for stand-alone PV systems. *Int. J. Hydrogen Energy* 44 (47), 25457–25472. doi:10.1016/j.ijhydene.2019.08.037

Guenounou, O., Belkaid, A., Colak, I., Dahhou, B., and Chabour, F. (2021). "Optimization of fuzzy logic controller based maximum power point tracking using hierarchical genetic algorithms," in *2021 9th international conf*erence on Smart grid (icSmartGrid) (New Jersey, United States: IEEE), 207–211.

Harrag, A., and Messalti, S. (2019). PSO-based SMC variable step size P&O MPPT controller for PV systems under fast changing atmospheric conditions. *Int. J. Numer. Model.* 32, e2603. doi:10.1002/jnm.2603

İnci, M. (2021). A flexible perturb & observe MPPT method to prevent surplus energy for grid-failure conditions of fuel cells. *Int. J. Hydrogen Energy* 46 (79), 39483–39498. doi:10.1016/j.ijhydene.2021.09.185

Kurokawa, K., Inui, T., Lin, L., and Fukui, M. (2016). "Development and evaluation of a photovoltaic emulation system," in IEEE International Conference on Consumer Electronics (ICCE), Las, vegas,NV, USA, 07-11 junary, 2016.

Latifi, M., Abbassi, R., Jerbi, H., Ohshima, K., and khaksar, M. (2021). Improved krill herd algorithm based sliding mode MPPT controller for variable step size P&O method in PV system under simultaneous change of irradiance and temperature. *J. Frankl. Inst.* 358 (7), 3491–3511. doi:10.1016/j.jfranklin.2021.02.021

Mao, M., Cui, L., Zhang, Q., Guo, K., Zhou, L., and Huang, H. (2020). Classification and summarization of solar photovoltaic MPPT techniques: A review based on traditional and intelligent control strategies. *Energy Rep.* 6, 1312–1327. doi:10.1016/j.egyr.2020.05.013

Miqoi, S., El Ougli, A., and Tidhaf, B. (2019). Adaptive fuzzy sliding mode based MPPT controller for a photovoltaic water pumping system. *Int. J. Power Electron. Drive Syst.* 10 (1), 414. doi:10.11591/ijpeds.v10.i1.pp414-422

Mohammadinodoushan, M., Abbassi, R., Jerbi, H., Ahmed, F. W., and Rezvani, A. (2021). A new MPPT design using variable step size perturb and observe method for PV system under partially shaded conditions by modified shuffled frog leaping algorithm-SMC controller. *Sustain. Energy Technol. Assessments* 45, 101056. doi:10.1016/j.seta.2021.101056

Mohapatra, A., Nayak, B., Das, P., and Mohanty, K. B. (2017). A review on MPPT techniques of PV system under partial shading condition. *Renew. Sustain. Energy Rev.* 80, 854–867. doi:10.1016/j.rser.2017.05.083

Motahhir, S., El Hammoumi, A., and El Ghzizal, A. (2020). The most used MPPT algorithms: Review and the suitable low-cost embedded board for each algorithm. *J. Clean. Prod.* 246, 118983. doi:10.1016/j.jclepro.2019.118983

Mousa, H. H., Youssef, A. R., and Mohamed, E. E. (2021). State of the art perturb and observe MPPT algorithms based wind energy conversion systems: A technology review. *Int. J. Electr. Power & Energy Syst.* 126, 106598. doi:10.1016/j.ijepes.2020.106598

Nadeem, A., and Hussain, A. (2021). A comprehensive review of global maximum power point tracking algorithms for photovoltaic systems.. *Energy Syst.*, 1–42. doi:10.1007/s12667-021-00476-2

Pandey, A. K., Singh, V., and Jain, S. (2022). "Study and comparative analysis of perturb and observe (P&O) and fuzzy logic based PV-MPPT algorithms," in *Applications of AI and IOT in renewable energy* (Massachusetts, United States: Academic Press), 193–209.

Sarvi, M., and Azadian, A. (2021). A comprehensive review and classified comparison of MPPT algorithms in PV systems. *Energy Syst.* 13, 281–320. doi:10.1007/s12667-021-00427-x

Shiau, J. K., Wei, Y. C., and Chen, B. C. (2015). A study on the Fuzzy-logic based solar power MPPT algorithms using different fuzzy input variables. *Algorithms* 8 (2), 100–127. doi:10.3390/a8020100

Vicente, E. M., dos Santos Vicente, P., Moreno, R. L., and Ribeiro, E. R. (2020). High-efficiency MPPT method based on irradiance and temperature measurements. *IET Renew. Power Gener.* 14, 986–995. doi:10.1049/iet-rpg.2019.0849

Weng, X., Xiao, X., He, W., Zhou, Y., Shen, Y., Zhao, W., et al. (2019). Comprehensive comparison and analysis of non-inverting buck boost and conventional buck boost converters. *J. Eng. (Stevenage).* 2019 (16), 3030–3034. doi:10.1049/joe.2018.8373

Yanarates, C., Wang, Y., and Zhou, Z. (2021). Unity proportional gain resonant and gain scheduled proportional (PR-P) controller based variable perturbation size real-time adaptive perturb and observe (P&O) MPPT algorithm for PV systems. *IEEE Access* 9, 138468–138482. doi:10.1109/ACCESS.2021.3119042

Yang, B., Zhu, T., Wang, J., Shu, H., Yu, T., Zhang, X., et al. (2020). Comprehensive overview of maximum power point tracking algorithms of PV systems under partial shading condition. *J. Clean. Prod.* 268, 121983. doi:10.1016/j.jclepro.2020.121983

Yilmaz, U., Kircay, A., and Borekci, S. (2018). PV system fuzzy logic MPPT method and PI control as a charge controller. *Renew. Sustain. Energy Rev.* 81, 994–1001. doi:10.1016/j.rser.2017.08.048

Youssef, A., El Telbany, M., and Zekry, A. (2018). Reconfigurable generic FPGA implementation of fuzzy logic controller for MPPT of PV systems. *Renew. Sustain. Energy Rev.* 82, 1313–1319. doi:10.1016/j.rser.2017.09.093

Zaouche, F., Rekioua, D., Gaubert, J-P., and Mokrani, Z. (2017). Supervision and control strategy for photovoltaic generators with battery storage. *Int. J. Hydrogen Energy* 42 (30), 19536–19555. doi:10.1016/j.ijhydene.2017.06.107

Zaouche, F., Mokrani, Z., and Rekioua, D. (2016). "Control and energy management of photovoltaic pumping system with battery storage," in 2016 International Renewable and Sustainable Energy Conference (IRSEC)IEEE), 917–922. doi:10.1109/IRSEC.2016.7983890

frontiers | Frontiers in Energy Research

TYPE Original Research
PUBLISHED 20 September 2022
DOI 10.3389/fenrg.2022.1008989

OPEN ACCESS

EDITED BY
Ningyi Dai,
University of Macau, China

REVIEWED BY
Mamdouh El Haj Assad,
University of Sharjah, United Arab Emirates
K Sudhakar,
Universiti Malaysia Pahang, Malaysia

*CORRESPONDENCE
Han Guangze,
phgzhan@scut.edu.cn

SPECIALTY SECTION
This article was submitted to Smart Grids,
a section of the journal
Frontiers in Energy Research

RECEIVED 01 August 2022
ACCEPTED 22 August 2022
PUBLISHED 20 September 2022

CITATION
Tahir MF, Haoyong C, Guangze H and Mehmood K (2022), Energy and exergy analysis of wind power plant: A case study of Gharo, Pakistan.
Front. Energy Res. 10:1008989.
doi: 10.3389/fenrg.2022.1008989

Energy and exergy analysis of wind power plant: A case study of Gharo, Pakistan

Muhammad Faizan Tahir[1], Chen Haoyong[1], Han Guangze[2]* and Kashif Mehmood[3]

[1]School of Electric Power, South China University of Technology, Guangzhou, China, [2]School of Physics and Optoelectronics, South China University of Technology, Guangzhou, China, [3]Department of Electrical Engineering, The University of Lahore, Lahore, Pakistan

Sustainable, inexhaustible, economical, and clean energy has become a vital prerequisite to replace fossil fuel sources for power production. In such a context, countries like Pakistan, which are heavily skewed towards fossil fuel-fired plants, are diverting attention to install more and more indigenous renewable energy sources projects such as solar-photovoltaic and wind turbine power plants. In order to harness the maximum energy of wind turbines, it is crucial to factually and precisely assess system performance, which is traditionally inferred by energy analysis (first law analysis). Nevertheless, this analysis only computes the nominal power generation output and ignores the effect of meteorological variables that can lead to some serious errors during the energy planning phase. Consequently, this case study presents both the energy and exergy analysis of a wind farm located in Gharo town of Thatta District along the coastline of the Indus Delta. Energy analysis is carried out to quantify energy efficiency, while exergy analysis computes exergy efficiency by taking into account the effect of pressure, temperature, and wind speed. Comparisons of both efficiencies are provided, and the result substantiates that exergy efficiency turns out to be lower than energy efficiency. However, exergy is a more viable index due to the inclusion of exergy destruction, and in comparison to the energy indicator, it presents the actual performance of a thermodynamic system. The monthly energy and exergy efficiency of the general electric wind turbines are maximum in July having values of 0.5 and 0.41, respectively.

KEYWORDS

energy analysis and exergy analysis, renewable energy, wind energy, Pakistan, efficiency

1 Introduction

The tremendous increase in energy demands due to extensive population growth, technological development, and industrialization is primarily met by prevalent fossil fuel sources (Rapier, 2020; Tahir and Haoyong, 2020). Recently, the atmosphere is witnessing worse global warming because of over-reliance on these finite and polluted fossil fuel sources (Tahir et al., 2020; Welsby et al., 2021). In order to meet energy demands with

minimal detrimental environmental impact, researchers are heading toward renewable energy source integration into the power grid (Alves et al., 2020; Tahir et al., 2021a). Amongst various renewable energy sources such as water, solar, and geothermal, wind energy utilization has increased manifolds due to its ease of availability, abundance, cost-competitiveness, and environmentally benign features (Wagner and Mathur, 2018; Tahir et al., 2019a).

Pakistan, being a third world country and the fifth most populated country in the world, is facing a demand-supply gap that led to several blackouts during the last decade (Tahir and Saqib, 2016). Similar to the rest of the world, Pakistan's energy mix is heavily dependent on costlier thermal power plants, fired by imported fuel. Fuel import not only declines the foreign exchange reserves but also worsens climate issues. For that reason, the Pakistan government has established the Alternative Energy Development Board (AEDB) to improve the integration of renewable energy sources in a grid for reducing dependency on polluted finite fossil fuel sources. According to the renewable energy leap-forward development policy, AEDB issued letters of intent to various private and government companies to install renewable energy projects in the country. Two of the provinces (Sindh and Balochistan) are more suitable for wind turbine installation as these are closer to the coastline. At present, the Government entails painstaking attention to Sindh province as it is the second most populated province of the country and has plenty of vacant space available for wind farm projects. Furthermore, this province has suffered prolonged power outages and blackouts due to various reasons in the present electric grid infrastructure.

Most of the research activities regarding wind energy are about harnessing maximum energy (Minaeian et al., 2017; Abdolkhalig et al., 2018), overcoming stochastic nature (Yuan et al., 2014; Jabir et al., 2017), and cost and size optimization (Fetanat and Khorasaninejad, 2015; Johnston et al., 2015; Tahir et al., 2019b; Sun et al., 2020). Conversely, these studies do not present the accurate behavior of wind power generation because conventionally wind power systems use energy analysis. The energy analysis computes energy efficiency by nominal power generation, the ratio of energy generation to wind potential or in other words how much kinetic energy is converted to electricity. On the contrary, it ignores the prominent feature that wind speed/energy is dependent on many meteorological variables (such as temperature, pressure, air density, and humidity), and changes in wind speed due to these meteorological variables will result in different energy production. Hence, exergy analysis (also known as second law analysis) takes into account the effect of the above variables, wherein internal irreversibilities and external losses are included while assessing wind energy generation. Exergy is defined as the maximum work potential of a system when it comes to equilibrium with respect to the reference environment (Gaggioli, 1998; Tahir et al., 2021b; Tahir et al., 2022). Recently, exergy analysis has also been employed on other renewable energy technologies such as solar photovoltaic plants (Shukla et al., 2016a; Shukla et al., 2016b; Kumar et al., 2017) and biomass (Mehrpooya et al., 2018; Yang et al., 2020); however, wind energy power plants are gaining more attention due to its widespread usage and large capacity. A few of the most pertinent studies pertaining to second law analysis for wind energy systems are briefly elaborated below.

Horizontal and vertical axis wind turbine energy and exergy efficiency are evaluated by (Pope et al., 2010) for four different wind turbines such as NACA 63 (2)-215 Airfoil, FX 63-137 Airfoil, Savnious VAWT, and Zephyr VAWT. Subsequently, four different definitions of outlet velocity (V_2) are outlined while efficiencies (energy and exergy) are computed by varying inlet velocity (V_1) against four different V_2. Ozgener et al. (Ozgener and Ozgener, 2007; Ozgener et al., 2009) concluded that exergy efficiency varies between 0 and 48.7% depending on wind speed while Jia et al. (Guang-Zheng et al., 2004) analyzed that exergy efficiency fluctuates between 35 and 45% when wind speeds are between 5 and 9 m/s.

In addition, meteorological variable effects on the exergy efficiency of wind turbines are contemplated in (Baskut et al., 2010). Baskut et al., (2011) employed exergy analysis on a wind farm in Turkey, wherein they pointed out that a decrease in the reference temperature results in considerable energetic and exegetic losses. However, for computing exergy efficiency, only the pressure differences between the inlet and outlet of wind turbines are taken into account while temperature and humidity differences are ignored. Exergy analysis of wind turbines for the location of Tehran is performed by Mehdi et al. (Ehyaei and Assad, 2021), which is given in the 13th chapter of book "Design and Performance Optimization of Renewable Energy Systems", while Adel Mohammed Redha et al. (Redha et al., 2011) employed thermodynamic analysis (exergy analysis) for computing Sharjah-based VESTAS V52 wind turbine exergy efficiency for 3 months (January–March). Unlike Omer et al., it exploited the temperature differences but ignored the pressure and humidity differences when employing exergy analysis. Furthermore, Diyoke, (2020). investigated the exergy performance of wind turbines at four different sites in Nigeria, while Koroneos et al., (2003) investigated the exergy analysis of renewable energy sources including wind turbines, but wind speeds greater than 9 m/s are assumed as zero, which is not true in a practical world.

In a nutshell, most of the preliminary studies did not conduct a long term energy and exergy analysis as conducted by Baskut et al., (2011), which utilized 11-months data, while most of the aforementioned studies either used temperature differences or pressure differences when evaluating exergy efficiency. Herein, to fill this substantial and core pivotal gap, this study takes into account both the temperature and pressure differences for performing exergy analysis of the whole year. Afterward, pressure and temperature differences against the wind speed are exploited by observing the last 10 years (2009–2019) weather pattern. To the best of our best knowledge, this is the first time when energy and exergy analysis are carried out for any Pakistan

FIGURE 1
Wind farm location map.

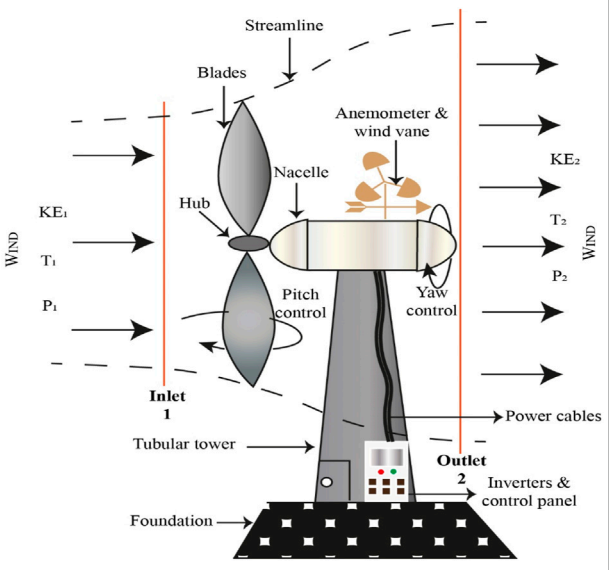

FIGURE 2
Side view of the horizontal axis three-blade wind turbine.

location. This case study provides the technical characteristics of the wind farm installed in Gharo town, Sindh province (taken from the National Electric Power Regulatory Authority (NEPRA) (National Electric Power Regulatory Authority, 2021)) and observes meteorological variables (Online, 2021) to compute the wind speed of the year 2020. This study furthermore computes energy and exergy efficiency of wind turbine for a whole year, demonstrates the in-depth comparison of both

TABLE 1 Wind farm micrositting layout for 13.8 MW (6*2.3).

Turbine number	Easting [m]	Northing [m]
1	379067	2735698
2	379099	2736089
3	379493	2735343
4	379689	2735823
5	379646	2736214
6	379589	2736558

efficiency, and finally, investigates the variation in exergy efficiency by varying temperature and pressure in an attempt to accurately assess the performance of the wind power plant at a given site. The limitations and assumptions used throughout this study are listed as follows.

i) Wind flow is assumed to be uni-dimensional, steady, and incompressible
ii) Temperature and pressure differences at the inlet and outlet of a wind turbine are taken into account
iii) Heat transfer or phase changes are not considered
iv) The effect of humidity is ignored

The rest of the article is structured as follows. Section 2 elaborates on the case study, and Section 3 provides an energy and exergy analysis investigation on the given case study. Section 4 demonstrates results and discussion, while significant findings summary and future work scope are given in Section 5.

TABLE 2 Technical specifications of the Gharo wind farm.

Wind farm capacity, configuration, and location	
Wind farm location	Gharo, District Thatta, Sindh province, Pakistan
Land	25 acres
Wind turbine type, make, and model	General Electric GE 2.3–116
Installed capacity	13.8 MW
Generation capacity	5.6 MW
Number of wind turbine units/ size of each unit	06*2.3
Installation	Onshore
Life expectancy	25 years
Rotor	
Number of blades	3
Swept area	10568 m^2
Rotor diameter	116 m
Rated power at	12.5 m/s air density of 1.225 kg/m^3
Power regulation	Combination of blade pitch angle adjustments and generator/convertor torque control
Rotor speed	8–15.7 rpm
Cut-in speed	3 m/s
Cut-out speed	22 m/s
Survival speed	52 m/s
Pitch regulation	Electric motor drives a ring gear mounted to the inner race of the blade pitch bearing
Blades	
Type description	Pitching blade
Blade length	56.9 m
Material	Glass fiber reinforced polyester, PVC, and balsa foam
Weight	11,000 kg (per piece)
Gear box	
Type	Planetary/Helical
Gear ratio	1:104
Main shaft	Cast iron GGG 700/400
Oil quantity	440 L
Main shaft bearing	Roller bearing mounted in a pillow block housing arrangement
Generator	
Power	2385 kW
Type	Doubly fed induction
Speed	Rated speed 1820 rpm, range 1000–1820 rpm, and synchronous speed 1500
Enclosure class	IP 54
Voltage	690 V
Coupling	Flexible coupling
Efficiency	>97
Weight	8450 kg
Power factor	+/-0.95
Tower	
Hub height	94 m
Type	Tubular steel tower
Shape	Conical
Control system	
Type	Automatic or manually controlled
Grid connection	Via back-to-back AC–DC–AC power electronics converter connected to rotor winding
Scope of monitoring	Remote monitoring of temperature sensors, pitch parameters, speed, generator torque, wind speed, and direction
Recording	Production data, event list, long- and short-term trends
Brake	
Design	Electromechanical pitch control for each blade (3 self-contained systems)
Operational brake	Aerodynamic brake achieved by feathering blades
Secondary brake	Hydraulic parking brake
Yaw system	
Type description	Active electrical motor power through geared ground with bolt bearings and hydraulic breaks
Yaw bearing	Roller bearing
Brake	Planetary yaw drives
Yaw driving device	4 planetary yaw drives
Speed	0.5°/s
Miscellaneous	
Annual full load hours	3600
Average wind turbine generator availability	97%
Total gross generation	62.7
Array and miscellaneous losses (GWh)	8.67
Net capacity factor	41.1%

2 Case study

The present case study of a 14 MW wind farm in the Gharo wind corridor, District Thatta, and province Sindh, is being installed by Burj Wind Energy Limited, a UAE-based company. Sindh province has a 290 km long coastline that makes it apt for wind power generation. Gharo (Latitude 24.7409° or 24° 44′ 27.2″ north, Longitude 67.581° or 67° 34′ 51.6″ east), a small town close to the coastline and not so far from the two biggest cities of Sindh province (Karachi and Hyderabad), is an ideal place for wind power plant generation. Wind farm location map and micrositting layout are shown in Figure 1 and Table 1 respectively.

The nacelle contains the main shaft (low-speed shaft), gearbox, high-speed shaft, bearing, and generator. Usually, wind turbines start to turn at a very low speed, but these low-speed rotations are not enough to generate electricity. Thus, speed is increased with the help of a gearbox in the nacelle, and a

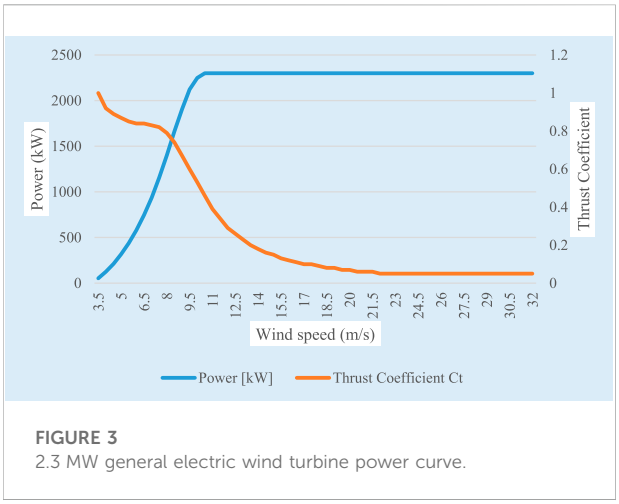

FIGURE 3
2.3 MW general electric wind turbine power curve.

high-speed shaft is connected to a generator for imperative rpms (which are usually 1000–1800 rpms) to produce power.

Wind speed is not distributed uniformly; therefore, yaw control makes sure to rotate the nacelle about the vertical axis of the tower to always align with the wind. On the other hand, there is also a chance of excessive wind speed that can damage the turbine, in such context, rotation of turbine blades about their axis can be used to control wind speed, which is known as pitch control. Based on these two control mechanisms, two types of breaks exist.

i) Pitch (rotor) brake: prevents the rotor blades from spinning too fast during high wind speed. It can be deployed during emergency operations and for maintenance purposes.
ii) Yaw brake: is used to move the nacelle away from the excessive wind that might cause torsional oscillation in a tower.

An anemometer and wind wane mounted on top of the nacelle determine wind speed and direction, respectively. For large wind turbines, a steel tubular tower is preferred over lattice towers, and it shapes like a conical as shown in Figure 1. This figure depicts the major components of the horizontal wind axis turbine under study. Horizontal axis turbines (shown in Figure 2) are superior to vertical axis because of its ability to cover a larger swept area.

The speed at which wind turbines start generating power, attaining maximum power, and before shutting down is known as cut-in (6–9 mph), rated (25–35 mph), and cut-out speeds (45–55 mph), respectively.

The International Electrochemical Commission (IEC) institution sets four different classes of wind turbines depending on the wind speed, gusts, and turbulence. In addition, wind pressure in a wind turbine installation place is also important to consider, which is covered by the wind zone section. Other than the wind zone and class, the height of the tower is also a prominent factor to infer wind speed. The taller the towers, the higher the wind velocity changes, but it suffers the transportation issues and greater costs.

General Electric (GE) company was chosen for a wind turbine that is considered one of the top manufacturers in the wind industry. After the feasibility study, the optimized size of the proposed wind farm was found out to be 13.8 MW, with six turbines of 2.30 MW each. Over the last 15 years, the wind turbine generators (WTGs) have seen a lot of improvement in their design. Though wind energy is considered to be clean, but it causes soil, water, and noise pollution during construction and operation. In particular, noise pollution (after project completion) makes it difficult for communities to live nearby any wind farm. In this regard, turbine blades by airfoil design help to attain maximum energy production at an economical expedient level with minimum noise, but still a lot of work needs to be done to eradicate such pollution. All of these technical specifications are enlisted in Table 2, and the wind turbine power curve is depicted in Figure 3.

Thrust coefficient, as shown in Figure 3, is generally used to describe the wakes of wind turbines because the wind exiting the turbine has lower energy content in comparison to the wind entering the turbine. Consequently, wind turbines create a wind shade in the form of turbulent and slowed-down wind trail in the downwind direction, which is known as the wake of a turbine. Such effect is characterized by the power/thrust coefficient which is a nondimensional quantity; it is the axial force applied to the flow by the turbine in comparison to the flow's incoming momentum, and it can be computed by using thefollowing equation (Martínez-Tossas et al., 2022):

$$C_T = \frac{F}{\frac{1}{2}\rho A v_\infty^2}, \tag{1}$$

where F, ρ, A, and v are the thrust force, fluid density, rotor swept area, and upstream velocity, respectively. Higher thrust coefficient due to the initial change in wind velocity (in the range of 3.5 m/s to 8 m/s velocity) indicates higher wake turbulence near the rotor, and in such cases, more recovery and effective control are needed. It can be seen that the lower the wake turbulence or lower the thrust coefficient between cut-in and cut-out velocity, the higher the power production.

3 Energy and exergy analysis formulation

3.1 Energy analysis

General energy balance for a control volume can be represented as

$$E_{in} = E_{out} \rightarrow \frac{dE_{CV}}{dt} = Q_{cv} - W_{cv} + \sum_i m_i \left(h + \frac{v^2}{2} + gz\right)_i - \sum_o m_o \left(h + \frac{v^2}{2} + gz\right)_o, \tag{2}$$

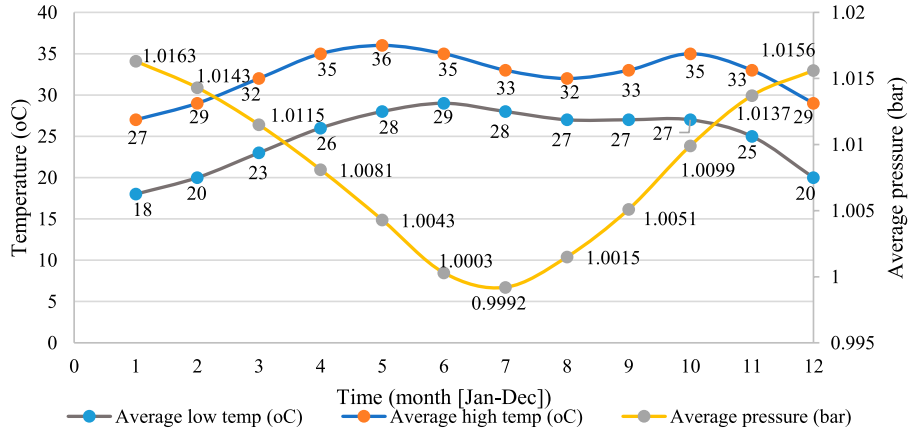

FIGURE 4
Average temperature and pressure of the Gharo site.

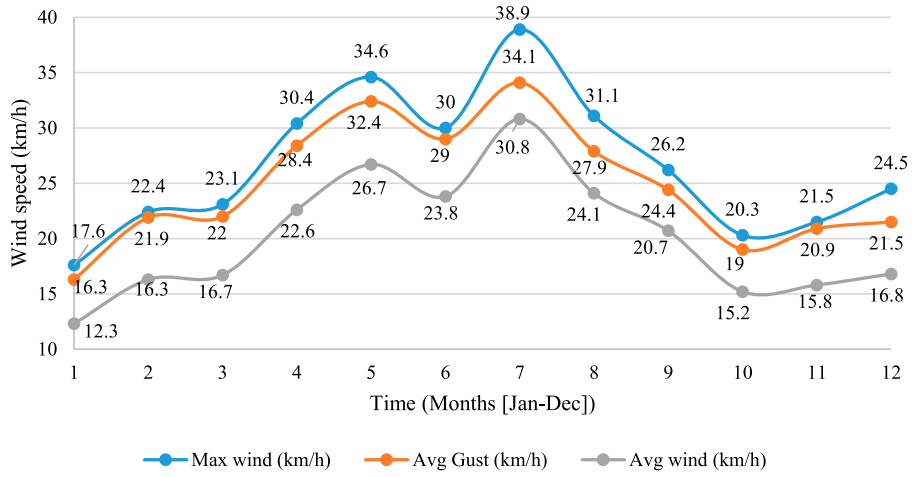

FIGURE 5
Wind variation for the Gharo site.

where $\frac{dE_{CV}}{dt}$ is the time rate of change of energy under control volume, and W_{cv} is work effects like generating power in terms of mechanical energy by rotating shaft or electrical energy with the help of a synchronous generator. h, v , and z represents enthalpy, velocity, and elevation, respectively. In the case of a wind energy system under steady-state conditions, the above equation reduces to the below expression.

Under steady-state conditions, $\frac{dE_{CV}}{dt} = 0$.

Work is measured only in terms of generated power, and heat transfer is ignored. $Q_{cv} = 0$, $W_{cv} = P_e$.

There is no height difference between the inlet and outlet of a wind turbine ($z = 0$). Now, the equation reduces to the following expression:

$$m_1 h_1 + m_1 \frac{v^2}{2} = m_2 h_2 + m_2 \frac{v^2}{2}. \tag{3}$$

The air is assumed to be incompressible for a wind turbine system that makes the inlet and outlet air mass flow rates equal. ($m_i = m_o$). As a result, power generation in the case of wind turbine systems is only related to converting mechanical power (kinetic energy) to electrical energy as shown below. The energy balance between the inlet and outlet of a wind turbine can be expressed as

$$KE_1 = KE_2 + Pow_e, \tag{4}$$

$$E_{in} = E_{KE} = \Delta KE = KE_1 - KE_2, \tag{5}$$

$$E_{out} = Pow_e. \tag{6}$$

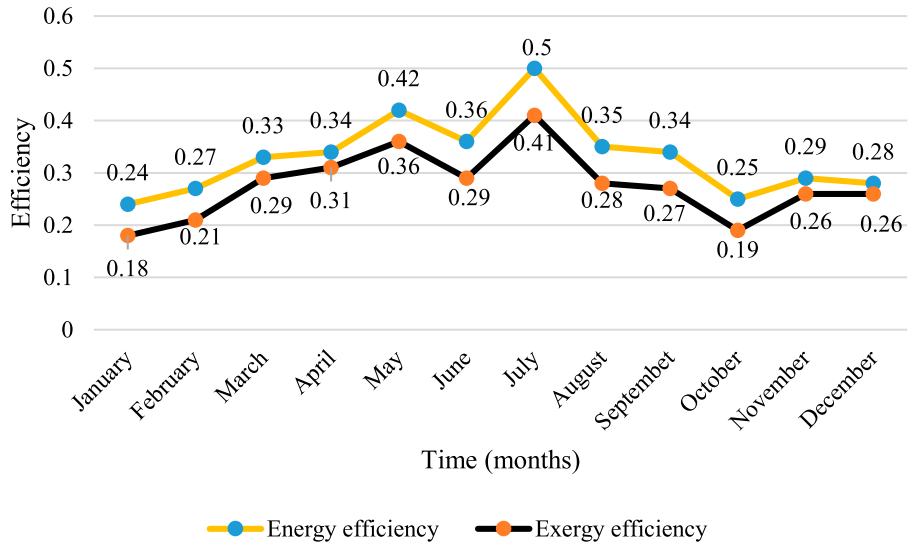

FIGURE 6
Monthly energy and exergy efficiency quantification of GE-wind turbine.

Kinetic energy is generally evaluated as

$$KE = \frac{1}{2}mv^2. \tag{7}$$

It is cumbersome to compute the mass of wind; therefore, it can be computed in terms of density of air shown as follows:

$$\rho = \frac{m}{V}, \tag{8}$$

$$m = \rho \times V, \tag{9}$$

where $V = A \times L$, and $L = vt$. By putting these values in (9), the following equation is generated:

$$m = \rho Avt. \tag{10}$$

Now, putting values of m in Equation 7 results in

$$KE = \frac{1}{2}\rho Atv^3, \tag{11}$$

$$\eta = \frac{E_{out}}{E_{in}}. \tag{12}$$

3.2 Exergy analysis

Exergy has four types: potential, kinetic, physical, and chemical exergy. In case of the wind turbine system, chemical and potential exergy are ignored due to no chemical affinity involvement and non-significant height difference between the inlet and outlet of the turbine, respectively. Additionally, kinetic energy and exergy share the same value as this is considered high quality energy. Though kinetic energy in energy balance covers the wind velocity, but it ignores the paramount parameters which effect or vary wind velocity such as temperature difference (chilling effect), pressure difference (velocity effect), and humidity. Usually, the air is assumed to be dry and the role of humidity is ignored, but temperature and pressure differences play a decisive role in evaluating the true performance of the wind energy system, which is provided by exergy analysis.

$$Ex_{out} = Ex_{in} + Ex_{dest}. \tag{13}$$

Ex_{dest} represents exergy destruction.

The wind pressure effect is determined by Bernoulli's equation, while the wind-chill effect leads to temperature differences, which are attributed to enthalpy and entropy components.

$$Ex_{in} = Ex_{KE} + Ex_{phy}, \tag{14}$$

$$Ex_{KE} = E_{in}, \tag{15}$$

$$Ex_{phy} = (H - H_o) + T_o(S - S_o), \tag{16}$$

$$\Delta H = mC_p(T_2 - T_1), \tag{17}$$

$$\Delta S = mT_o\left(C\ln\left(\frac{T_2}{T_1}\right) - R\ln\left(\frac{P_2}{P_1}\right) - \frac{Q_{loss}}{T_o}\right). \tag{18}$$

T_1, and T_2 are the wind chill temperatures at the outlet of turbine. P_1, and P_2 are the pressure differences at the inlet and outlet of the wind turbine, respectively. C and Q_{loss} represents heat capacity the wind turbine heat losses, respectively. $(\therefore Q_{loss} = mC(T_o - T_{avg}))$

The total input wind exergy is represented as

$$Ex_{in}^{w} = Ex_{e}^{w} + mC(T_2 - T_1) + \underbrace{mT_o\left(C_p\ln\left(\frac{T_2}{T_1}\right) - R\ln\left(\frac{P_2}{P_1}\right) - \frac{Q_{loss}}{T_o}\right)}_{Exergy\ destruction/Irreversibilities}, \tag{19}$$

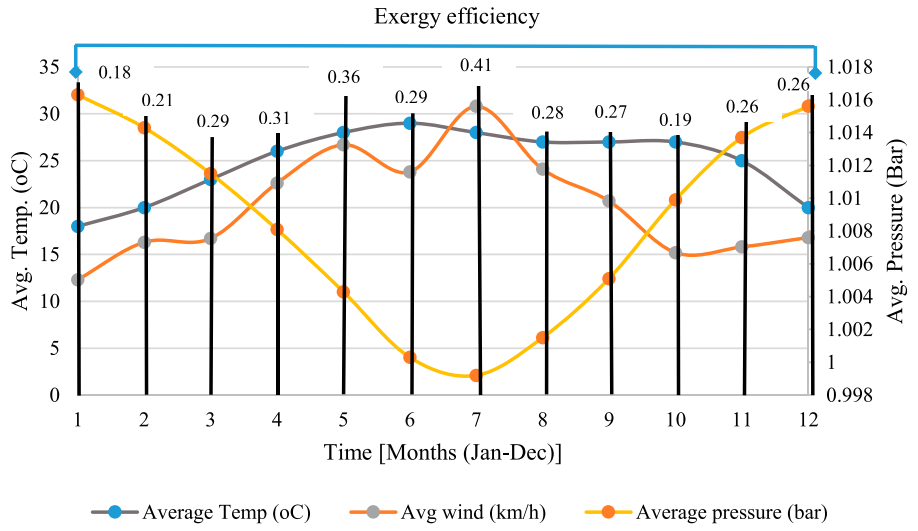

FIGURE 7
Exergy efficiency variation with changing temperature, pressure, and wind speed.

$$\psi = \frac{Ex_{out}}{Ex_{in}}. \tag{20}$$

The variations of meteorological variables that encompass average low temperature, average high temperature, and average pressure are represented in Figure 4. Furthermore, maximum wind, average wind, and average gust speeds in km/h are demonstrated in Figure 5.

4 Results and discussion

The Gharo wind farm comprises six wind turbines of 2.3 MW each, generating electricity at a capacity of around 5.6 MW. GE wind turbine models with 10568 m^2 rotor swept area, 116 m rotor diameter, and 56.8 blade length are installed around 25 acres of land on a given site. The understudy (GE 2.3–116 MW) wind turbine swept area is 27% more than GE 1.7 MW, which helps to generate 26% more energy annually. In addition, a wind turbine having 56.7 m blade length with state of the art airfoil design guarantees higher energy production with a reduced noise level at a lower cost for Class II/III sites.

The energy and exergy analysis of wind turbines is conducted to compute energy and exergy efficiency by using (10) and 18. These analyses are intended to evaluate the effectiveness of wind turbines by observing how much wind KE is converted into power generation. Air density, reference temperature, and pressure are assumed as 1.225 kg/m3, 27°C (300.15 K), and 1 bar (100 kPa), respectively. The average monthly energy and exergy efficiency of the GE-wind turbine according to the weather data of the Gharo site is plotted in Figure 6.

Though energy and exergy efficiency follows the same trend throughout the year but exergy efficiency tends to be lower than energy efficiency as energy efficiency is overestimated. Energy efficiency cannot provide the precise performance of a system, which often leads to inaccurate results and misguide us from the factual assessment. This is due to the fact that energy efficiency only takes into account the effect of nominal power generation depending on the conversion of kinetic energy to electrical energy. Contrarily, it ignores the foremost fact that kinetic energy conversion is influenced by wind speed, and this wind speed is dependent on meteorological variables such as temperature and pressure.

Accordingly, variation in exergy efficiency can be understood by the three most predominant parameters: 1) change in speed/velocity; 2) change in temperature; and 3) change in pressure.

Wind velocity is categorized into three types: cut-in, rated, and cut-out velocity. No power is generated below cut-in speed (3 m/s) and after cut-out speed (22 m/s), controllers are designed to shut down turbines to protect wind turbines. For that reason, it does not make sense to talk about efficiency when there is no power generation below cut-in and after cut-out, whereas fluctuating efficiency trends are being observed that usually following the linear trend with a velocity between the cut-in and cut-out range. In this regard, the higher the wind velocity, the more exergetically efficient a wind turbine is. Nonetheless, the change in velocity is influenced by the change in temperature and pressure. The increase in exergy efficiency is associated with a rise in temperature that increases wind velocity (follow the direct relation).

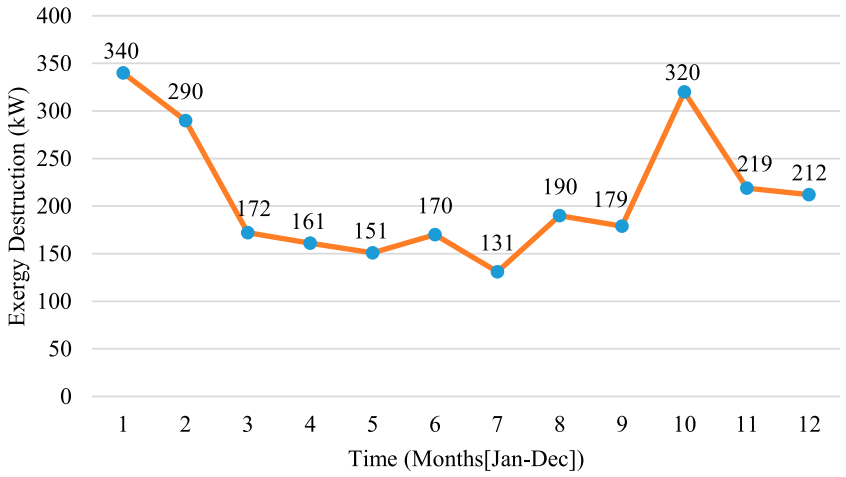

FIGURE 8
Monthly exergy destruction variation.

Exergy efficiency is maximum during the month of July because the wind is blowing at maximum speed during this month. Furthermore, the temperature is also higher during this month though not maximum. This can be understood by taking into account the effect of pressure as high pressure differences result in low exergy efficiency (follow the inverse relation). In particular, the difference between temperature and pressure is greatest in July due to high wind velocity that ultimately results in the least exergy destruction and higher exergy efficiency. The thermodynamic assessment of GE 2.3–116 MW is better comprehended by the illustration of change in wind speed, temperature, and pressure effect on exergy efficiency as presented in Figure 7.

In short, energy analysis ignores environmental conditions, internal irreversibilities, enthalpy, and entropy contributions that result in the overestimation of energy efficiency. To this end, exergy efficiency computation becomes increasingly critical in order to determine the actual performance by taking into account the effect of meteorological variables such as temperature, pressure, and wind speed. In comparison to temperature and pressure, variation of wind speed plays an indispensable role in exergy efficiency since wind energy fluctuation is proportional to the cube of wind velocity (see Eq. 9). Exergy analysis identifies that only 40% of wind energy can be converted to useful work that is producing power while the rest of 60% is destroyed (termed as anergy), which is accounted as exergy destruction. Though exergy efficiency turns out to be lower than energy efficiency but it depicts the true thermodynamic assessment of the proposed system by addressing the Frontier issue of meteorological variables and exergy losses effect on efficiency quantification. Therefore, higher exergy destruction means lower exergy efficiency and vice versa, as it is corroborated in Figure 8, wherein depicts that exergy destruction is lowest during the month of July, resulting in the highest exergy efficiency during this month.

5 Conclusion

Being a third world country, Pakistan is giving priority to indigenous renewable energy sources such as wind turbines to diversify the country's energy portfolio. It enhances the energy security of the country, thereby reducing the dependence on imported furnace oil and carbon emissions by generating clean electricity. This study investigates one of the wind power plant projects in a small town, Gharo (along the coastline of Sindh province, Pakistan) by employing energy and exergy analysis. Energy analysis computes the energy efficiency by just evaluating the conversion of kinetic energy to electrical energy, but exergy analysis also takes into account the effect of pressure, temperature, and wind speed to compute exergy efficiency. The results substantiate that both efficiencies (energy and exergy) are maximum during the month of July, while exergy efficiency varying between 18 and 41% turns out to be lower than energy efficiency that lies within 24–50%. Maximum exergy efficiency during the month of July is corroborated by maximum exergy destruction during this month. According to the local weather data, a comparative performance assessment reveals that the exergy analysis results are inferior to energy analysis, but it demonstrates factual assessment and performance of wind turbines that can help engineers and government administrators to formulate policies accordingly in order to foster the actual performance of wind energy plants.

This study can be further extended to envisage advanced exergy analysis, with a focus to include avoidable and unavoidable losses. There is also a scope of presenting insightful results by evaluating hidden exergy destruction costs and the environmental impact of wind turbines with the aid of exergoeconomic and exergoenvironment assessment.

Data availability statement

The original contributions presented in the study are included in the article/Supplementary Material; further inquiries can be directed to the corresponding author.

Author contributions

Conception and design of the study was carried out by CH and HG. Problem formulation, acquisition of data, and result simulation were carried out by MT. Drafting and writing of the manuscript were carried out by all authors collaboratively.

Funding

This work was supported by the National Natural Science Foundation of China under Grant 51937005.

Conflict of interest

The authors declare that the research was conducted in the absence of any commercial or financial relationships that could be construed as a potential conflict of interest.

Publisher's note

All claims expressed in this article are solely those of the authors and do not necessarily represent those of their affiliated organizations, or those of the publisher, the editors, and the reviewers. Any product that may be evaluated in this article, or claim that may be made by its manufacturer, is not guaranteed or endorsed by the publisher.

References

Abdolkhalig, A., Fang, Q., and Mohamed, A. (2018). Effective harness of wind energy turbines. *J. Electr. Electron. Syst.* 7, 2332–0796. doi:10.4172/2332-0796.1000256

Alves, M., Segurado, R., and Costa, M. (2020). On the road to 100% renewable energy systems in isolated islands. *Energy* 198, 117321. doi:10.1016/j.energy.2020.117321

Baskut, O., Ozgener, O., and Ozgener, L. (2010). Effects of meteorological variables on exergetic efficiency of wind turbine power plants. *Renew. Sustain. Energy Rev.* 14, 3237–3241. doi:10.1016/j.rser.2010.06.002

Baskut, O., Ozgener, O., and Ozgener, L. (2011). Second law analysis of wind turbine power plants: Cesme, Izmir example. *Energy* 36, 2535–2542. doi:10.1016/j.energy.2011.01.047

Diyoke, C. (2020) Comparative thermo-economic and advanced exergy performance assessment of wind energy for distributed generation in four sites in Nigeria. *Int. J. Renew. Energy Dev.* 9, 339–351. doi:10.14710/ijred.9.3.339-351

Ehyaei, M. A., and Assad, M. E. H. (2021). "Energy and exergy analyses of wind turbines," in *Design and performance optimization of renewable energy systems* (Amsterdam, Netherlands: Elsevier), 195–203.

Fetanat, A., and Khorasaninejad, E. (2015). Size optimization for hybrid photovoltaic–wind energy system using ant colony optimization for continuous domains based integer programming. *Appl. Soft Comput.* 31, 196–209. doi:10.1016/j.asoc.2015.02.047

Gaggioli, R. (1998). Available energy and exergy. *Int. J. Thermodynamics* 1, 1.

Guang-Zheng, J., Xuan-yin, W., and Gen-mao, W., (2004). "Investigation on wind energy-compressed air power system. *J. Zhejiang University-Science A* 5, 290–295. doi:10.1007/BF02841013

Jabir, M., Azil Illias, H., Raza, S., and Mokhlis, H. (2017). Intermittent smoothing approaches for wind power output: A review. *Energies* 10, 1572. doi:10.3390/en10101572

Johnston, L., Díaz-González, F., Gomis-Bellmunt, O., Corchero-García, C., and Cruz-Zambrano, M. (2015). Methodology for the economic optimisation of energy storage systems for frequency support in wind power plants. *Appl. Energy* 137, 660–669. doi:10.1016/j.apenergy.2014.09.031

Koroneos, C., Spachos, T., and Moussiopoulos, N. (2003). Exergy analysis of renewable energy sources. *Renew. energy* 28, 295–310. doi:10.1016/s0960-1481(01)00125-2

Kumar, P., Shukla, A. K., Sudhakar, K., and Mamat, R. (2017). Experimental exergy analysis of water-cooled PV module. *Int. J. Exergy* 23, 197–209. doi:10.1504/ijex.2017.085768

Martínez-Tossas, L. A., Branlard, E., Shaler, K., Vijayakumar, G., Ananthan, S., Sakievich, P., and et al. (2022). Numerical investigation of wind turbine wakes under high thrust coefficient. *Wind Energy* 25, 605–617. doi:10.1002/we.2688

Mehrpooya, M., Khalili, M., and Sharifzadeh, M. M. M. (2018). Model development and energy and exergy analysis of the biomass gasification process (Based on the various biomass sources). *Renew. Sustain. Energy Rev.* 91, 869–887. doi:10.1016/j.rser.2018.04.076

Minaeian, A., Sedaghat, A., Mostafaeipour, A., and Alemrajabi, A. A. (2017). Exploring economy of small communities and households by investing on harnessing wind energy in the province of Sistan-Baluchestan in Iran. *Renew. Sustain. Energy Rev.* 74, 835–847. doi:10.1016/j.rser.2017.02.065

National Electric Power Regulatory Authority. (2021). Tariff IPPs wind. Available at: https://nepra.org.pk/tariff/Generation%20IPPs%20Wind.php November 2021

Online, W. W. (2021). *Gharo climate weather averages*. PK: Sindh.

Ozgener, O., and Ozgener, L. (2007). Exergy and reliability analysis of wind turbine systems: A case study. *Renew. Sustain. Energy Rev.* 11, 1811–1826. doi:10.1016/j.rser.2006.03.004

Ozgener, O., Ozgener, L., and Dincer, I. (2009). Analysis of some exergoeconomic parameters of small wind turbine system. *Int. J. Green Energy* 6, 42–56. doi:10.1080/15435070802701777

Pope, K., Dincer, I., and Naterer, G. (2010). Energy and exergy efficiency comparison of horizontal and vertical axis wind turbines. *Renew. energy* 35, 2102–2113. doi:10.1016/j.renene.2010.02.013

Rapier, R. (2020). *Fossil fuels still supply 84 percent of world energy—and other eye openers from BP's annual review*. Canada: EnergyNow Media.

Redha, A. M., Dincer, I., and Gadalla, M. (2011). Thermodynamic performance assessment of wind energy systems: An application. *Energy* 36, 4002–4010. doi:10.1016/j.energy.2011.05.001

Shukla, K., Rangnekar, S., and Sudhakar, K. (2016). Mathematical modelling of solar radiation incident on tilted surface for photovoltaic application at Bhopal, MP, India. *Int. J. Ambient Energy* 37, 579–588. doi:10.1080/01430750.2015.1023834

Shukla, A. K., Sudhakar, K., and Baredar, P. (2016). Exergetic analysis of building integrated semitransparent photovoltaic module in clear sky condition at Bhopal India. *Case Stud. Therm. Eng.* 8, 142–151. doi:10.1016/j.csite.2016.06.009

Sun, H., Qiu, C., Lu, L., Gao, X., Chen, J., and Yang, H. (2020). Wind turbine power modelling and optimization using artificial neural network with wind field experimental data. *Appl. Energy* 280, 115880. doi:10.1016/j.apenergy.2020.115880

Tahir, M. F., and Haoyong, C. (2020). Socioeconomic analysis of integrated energy system of China for 2020. *IEEE Syst. J.* 15, 1979–1988. doi:10.1109/JSYST.2020.2977657

Tahir, M. F., and Saqib, M. A. (2016). Optimal scheduling of electrical power in energy-deficient scenarios using artificial neural network and Bootstrap aggregating. *Int. J. Electr. Power. Energy Syst.* 83, 49–57. doi:10.1016/j.ijepes.2016.03.046

Tahir, M. F., Haoyong, C., Mehmood, K., Ali, N., and Bhutto, J. A. (2019). Integrated energy system modeling of China for 2020 by incorporating demand response, heat pump and thermal storage. *Ieee Access* 7, 40095–40108. doi:10.1109/access.2019.2905684

Tahir, M. F., Haoyong, C., Khan, A., Javed, M. S., Laraik, N. A., and Mehmood, K. (2019). Optimizing size of variable renewable energy sources by incorporating energy storage and demand response. *IEEE Access* 7, 103115–103126. doi:10.1109/access.2019.2929297

Tahir, M. F., Chen, H., Khan, A., Javed, M. S., Cheema, K. M., and Laraik, N. A. (2020). Significance of demand response in light of current pilot projects in China and devising a problem solution for future advancements. *Technol. Soc.* 63, 101374. doi:10.1016/j.techsoc.2020.101374

Tahir, M. F., Haoyong, C., and Guangze, H. (2021). Exergy hub based modelling and performance evaluation of integrated energy system. *J. Energy Storage* 41, 102912. doi:10.1016/j.est.2021.102912

Tahir, M. F., Haoyong, C., and Guangze, H. (2021). A comprehensive review of 4E analysis of thermal power plants, intermittent renewable energy and integrated energy systems. *Energy Rep.* 7, 3517–3534. doi:10.1016/j.egyr.2021.06.006

Tahir, M. F., Haoyong, C., and Guangze, H. (2022). Evaluating individual heating alternatives in integrated energy system by employing energy and exergy analysis. *Energy* 249, 123753. doi:10.1016/j.energy.2022.123753

Wagner, H.-J., and Mathur, J. (2018). "Wind energy today," in *Introduction to wind energy systems* (Heidelberg Germany: Springer), 1

Welsby, D., Price, J., Pye, S., and Ekins, P. (2021). Unextractable fossil fuels in a 1.5 C world. *Nature* 597, 230–234. doi:10.1038/s41586-021-03821-8

Yang, Q., Xu, S., Yang, Q., Zhang, D., Li, Z., Zhou, H., et al. (2020). Optimal design and exergy analysis of biomass-to-ethylene glycol process. *Bioresour. Technol.* 316, 123972. doi:10.1016/j.biortech.2020.123972

Yuan, B., Zhou, M., Li, G., and Zhang, X.-P. (2014). Stochastic small-signal stability of power systems with wind power generation. *IEEE Trans. Power Syst.* 30, 1680–1689. doi:10.1109/tpwrs.2014.2353014

Nomenclature

Abbreviations

AEDB Alternative Energy Development Board

GE General Electric

IES International Electrochemical Commission

NEPRA National Electric Power Regulatory

WTG Wind turbine generator

Symbols

Subscripts

o Ambient

avg Average

cv Control volume

dest Destruction

e Electricity

i or 1 Inlet of wind turbine

KE Kinetic energy/exergyKinetic energy/exergy [J/kg]

loss Losses

o or 2 Outlet of wind turbine

phy Physical

Superscripts

w Wind

Constants and variables

E Energy [kJ]

Ex Exergy [kJ]

T Temperature [K]

P Pressure [kPa]

Q Heat transfer

W Work done [kJ]

C Heat capacity [kJ/kg]

KE Kinetic energy/exergyKinetic energy/exergy [J/kg]

η Wind turbine energy efficiency

ψ Wind turbine exergy efficiency

C_T Thrust coefficient

H Enthalpy [kJ]

S Entropy [kJ/K]

v Velocity [m/s]

g Gravitational force [m/s^2]

z Elevation [m]

ς Exergy factor

m Mass flow [kg]

Pow Power generation [kW]

F Thrust force [N]

T_o Absolute temperature [K]

ρ Air density [kg/m^3],L ,V swept area [m^2], length [m], and volume [m^3]

frontiers | Frontiers in Energy Research

TYPE Original Research
PUBLISHED 23 September 2022
DOI 10.3389/fenrg.2022.1008099

OPEN ACCESS

EDITED BY
Muhammad Faizan Tahir,
South China University of Technology, China

REVIEWED BY
Srikanth Goud B,
Anurag Group of Institutions, India
Youcef Belkhier,
Maynooth University, Ireland

*CORRESPONDENCE
Mohammed Alharbi,
mohalharbi@ksu.edu.sa

SPECIALTY SECTION
This article was submitted to Smart Grids, a section of the journal Frontiers in Energy Research

RECEIVED 31 July 2022
ACCEPTED 17 August 2022
PUBLISHED 23 September 2022

CITATION
Khan SA, Ansari JA, Chandio RH, Munir HM, Alharbi M and Alkuhayli A (2022), AI based controller optimization for VSC-MTDC grids.
Front. Energy Res. 10:1008099.
doi: 10.3389/fenrg.2022.1008099

AI based controller optimization for VSC-MTDC grids

Shahid Aziz Khan[1], Jamshed Ahmed Ansari[2], Rashid Hussain Chandio[2], Hafiz Mudassir Munir[2], Mohammed Alharbi[3]* and Abdulaziz Alkuhayli[3]

[1]Department of Electrical and Computer Engineering, University of Michigan, Dearborn, MI, United States, [2]Department of Electrical Engineering, Sukkur IBA University, Sukkur, Pakistan, [3]Department of Electrical Engineering, College of Engineering, King Saud University, Riyadh, Saudi Arabia

Electric power industry is continually adopting new techniques to improve the reliability and efficiency of the energy system and to cope with the increasing energy demand and the associated technical challenges. In recent years, the maturation of Artificial Intelligence (AI) led researchers to solve various problems in the power system by using AI techniques. Voltage Source Converter is the result of advancements in the field of power electronics and semiconductors technology, which holds a promising future for the realization of smart grid, renewable energy integration, and HVDC transmission system. Usually hit and trial method or the design engineer's experience is used for the manual tuning of the PI controllers, which cannot yield superior performance. The process becomes more complicated when multiple grids are involved, such as in VSC-based MTDC grids. This research article use a deep learning optimization technique for the tuning of the VSC controllers, which resulted in quick settling time, better slew rate, less undershoot and low overshoot. The deep learning neural network is trained through the Particle Swarm Optimization (PSO) algorithm to produce the best possible tuned or optimally tuned parameters for the controllers. The optimal tuning of the controller will result in an overall better performance of the converter and the grid. A four-layered deep learning neural network and a three-terminal MTDC grid were designed and simulated in MATLAB/SIMULINK environment.

KEYWORDS

optimization, artificial intelligence, deep learning, smart grid, voltage source converter, particle swarm optimization (PSO), smartgrid

1 Introduction

The power system is undergoing revolutionary changes due to technological advancement, high computational resources, increasing demand, and focus on green energy. Many countries such as China, E. U. members, Australia, etc., are working to shift a significant proportion of their energy consumption from conventional to renewable sources. As a result, there is an increased influx of renewable energy into the system. However, the system cannot readily absorb and distribute this incoming energy. Unlike

conventional sources, renewable energy sources cannot be scheduled and are sometimes connected directly to the distributed system instead of the transmission system (Freris and Infield, 2008). The integration of such time variables and distributed sources into the electrical network requires special consideration.

Multi-terminal direct current (MTDC) grids are overlaying their counterparts due to the advantages and flexibility in terms of large-scale integration of remotely located renewable energy resources into the existing AC grids (RODRIGUEZ and ROUZBEHI, 2017). Energy conversion is done through converters such as the matured line commutated converters, the recent voltage source converter, the advanced modular multilevel converter, etc., VSC is a developing technology because of its benefits, such as independent power control, low power loss, dynamic response, etc., (Reed et al., 2003). Inside the VSC converter, PI controllers are used to control the operation of the converter. PI controller is very famous in industrial systems due to its ease of implementation and robustness. The PI controller helps drive the system variables to their target values through the variation of l gain and time constant (O'Dwyer, 2009). The performance of the converter depends on how accurately the controller is tuned. Typically, no specialized or intelligent technique is adopted for the tuning process; instead, the hit and trial method or the engineer's experience is used to tune the PI controller manually. However, the situation becomes complex when multiple grids are interconnected, such as in MTDC grids. So, with the advancement in grid interconnection, an intelligent technique must be adopted to tune the PI controllers, which can lead to better response and performance. In this research article, a deep learning technique is applied for the tuning of the controllers to yield the best responses in terms of slew rate, settling time, undershoot and overshoot. Although the transformation rate of power generation, transmission, and distribution technology is relatively slow, the power industry researchers are trying to apply AI to every possible section of the power system. For instance, AI has proven to be of great help in power system planning, scheduling, and control (Madan and Bollinger, 1997; Yousaf et al., 2021; Sharma et al., 2022).

2 Literature review

The majority of the industrial processes use PI controllers due to their robustness and reliable performance. The recent industrial advancement leads to the development of systems with multipThele and complex closed-loop systems. The performance of these systems greatly depends on how small is the error. So, the tuning of the PI controller is important and directly impacts the overall performance. The control loops for which random tuning may not be sufficient are subjected to various tuning and optimization techniques. A model predictive-based tuning technique was presented in (O'Dwyer, 2003) which was primarily designed to produce quarter decay responses. The Direct Synthesis method (Seborg et al., 2004) is becoming popular amongst engineers due to its ability to tune through a single tuning parameter which has a significant effect on the performance of the closed-loop. The AMIGO tuning rule is based on the 63% step response experiment (Åström et al., 2006) The objective of this method is to minimize error and disturbances. The SIMC optimization or tuning method was obtained through the reduction of the higher models using the half rule approach (Skogestad, 2003).

In (He et al., 2000) an optimal tuning technique based on LQR (Linear Quadratic Regulator) approach is presented. This method is useful for the process that involves time delay and is of low order. The proposed LQr criteria lead to the desired natural frequency and damping ratio. In (Kookos et al., 1999) an online PI controller tuning method for dead time processes is explained, specifically suitable for various chemical processes. This model is an approximation of various complex models such as the first-order plus dead time model having large time constants. A fractional-order proportional and derivative (FOPD) was explained in (Li et al., 2010). This method is specifically beneficial for the application of fractional-order controllers having complicated closed loop. For closed loops systems a droop control optimization (Khan and Ahmed, 2020) technique is also widely used but it doesn't involve optimization on the controller level.

Moreover, Literature depicts multiple classical and modern optimization or tuning techniques for the PI controller. Due to the widespread industrial applications of the PI or PID controller, it is a well-searched area. More than ninety percent of the industrial system still uses PI or PID controllers due to its ease of implementation and robustness.

Classical techniques are based on assumptions about the plant and output. These assumptions help the controller to reach the optimal setting (Liu and Ansari, 2020). However, classical optimization techniques seem simple and robust, but the desired response may not be obtained due to the assumptions involved.

Ziegler Nichols and Cohen Coons methods are among the classical introductory techniques discovered. The Nichols technique was based on the assumption (Izci, 2021), (Araki and Unbehauen, 2020), while the Coons method involved the FOLPD model (Ziegler and B Nichols, 1942), (Salunkhe et al., 2018). Coons method was built on a better model, but there is no significant difference between the performance of both methods. Specifically, the Nichols method cannot evaluate system parameters in an environment with noisy conditions. The drawback associated with the Coons method under abnormal conditions is the fact that it pushes the system towards instability. It is evident from the literature that complex, intelligent techniques were built from simple logic, such as the Immune algorithm was inspired by the vertebrate immune system. It is a system that protects the internal system from foreign objects. The

optimum response is generated based on Learning about the antigen to generate an optimized response (Sebtahmadi et al., 2017).

Ant Colony Optimization technique was inspired by an ant colony and is based on a meta-heuristic approach. This algorithm works like insects looking out for food by following the optimal path (Al-Mogren, 2008), (Dai et al., 2017). Genetic Algorithm (G.A.) navigates the search, similar to the pattern of evolution in nature. It utilizes cost functions and probabilistic rules (Gonçalves et al., 2018). The name genetic comes from the fact that the solution is represented in binary format which is similar to genetic representation (Oshaba et al., 2017). The Differential Evolution (D.E.) technique is used for problems that require numerical optimization. This problem gradient is not known in detail to complete this procedure. The need for a gradient is eliminated because it works in a way that doesn't require the need for a gradient and results in quality (Geweda et al., 2017).

Another global optimization technique is Evolutionary Programming (E.P.) which involves the steps of initialization, mutation, competition, and reproduction. A quasi-random sequence (QRS) is applied to generate the initial sequence (Liang et al., 2020). Annealing (Badar et al., 2022), Vector Support Machine (SVM) (Kumar et al., 2008) and Surface Method response (Reynoso-Meza et al., 2016) are among the other methods which are not too popular because these are very specifically used for a narrow category of applications.

In one of the popular methods called Particle Swarm Optimization, in search for the optima, a particle population moves through the solution, while keeping track best solution (local and global) (Najeeb et al., 2017). PSO leads to better responses than G.A. The drawback of PSO is its property falls into a local optimum. In this research, the PSO algorithm is used to train the deep learning neural network. The normal way to train the neural network is through the data sets, but in this particular application due to the unavailability of the data set and due to the nature of the problem PSO algorithm is used to train the neural network (Zhao et al., 2015).

Inspired by the biological neural network, in Artificial Neural Network (ANN) there are artificial neurons that can be multilayered. To process the data, a connectionist approach is applied (Ilten and Demirtaş, 2016). AI technology is based fundamentally on ANN, extending to the concepts of deep learning and machine learning. ANN is applied to solve complex nonlinear problems. This research adopted a deep learning technique due to its self-learning capability. The successful implementation of deep learning networks depends upon two key parameters, i.e., hidden layers and neurons in each hidden layer. The performance of the deep learning network depends upon the setting of these two key parameters. However, setting them manually or through the grid search method is time-consuming. PSO algorithm has a great potential to optimize parameter settings (Behera et al., 2016). Apart from industrial processes the applications relating to power system can be found in the literature this research is focused on the power system application and optimization (Ehsan et al., 2021; Shehzad et al., 2021; Chi et al., 2021; Autonomous, 2021; Guasti Junior and Santos, 2021; Lau and Lim, 2018; Fan et al., 2019; Hu and Eberhart, 2002; Dashtdar et al., 2022; Soliman et al., 2021).

The novelty of this research lies in the selection of optimization techniques, i.e., deep learning. The deep neural network is trained through a particle swarm optimization (PSO) algorithm. Previously deep Learning has been applied for image processing, signal processing, computer vision, power system planning, etc., But it has never been applied to the optimization of a VSC controller in a power system setting. This research focuses on the application of deep Learning for power system optimization in a VSC-MTDC grid system.

This work can also be considered an improved version of our previous work, in which fuzzy logic was applied to optimize such systems (Qolomany and Maabreh, 2017). The results of this deep learning optimization are much better than the fuzzy logic technique, so it forms the foundation for applying the artificial intelligence techniques for power system optimization and control. The key contributions of this paper include:

1) An AI-based optimization technique has been exploited for the optimization of power converters Controller (PI tuning).
2) Optimization of the weights and biases of the neural network has been undergone using the Particle Swarm Optimization technique.
3) A step forward towards the application of AI on power systems.
4) Improved performance of the converter in terms of overall stability, overshoot, undershoot, settling time, and slew rate.
5) Increased reliability of the system by combining the benefits of AI-based optimization with the robustness of PI controller.

The paper is structured as follows:

The introduction section focuses on the background and the need for an intelligent and self-learning optimization method for power converters. The second section which is a literature review covers all the significant work already done in this domain. It includes all the optimization techniques that are reported and can be applied to power system problems. It also mentions the drawback of every technique and that is why need to improve the existing techniques. In the third section of the methodology, we covered the steps involved to realize our proposed solution. It focuses on the construction of the deep learning network, mathematical modeling, and how the PSO algorithm is applied to optimize the weights and biases of the neural network itself.

The result and analysis section compares and analyzes the obtained simulated results. From the graphs and table, the superior performance of the proposed solution is proved as compared to other traditional techniques.

The conclusion concludes the contribution of the proposed strategy and it also mentions the future potential research areas

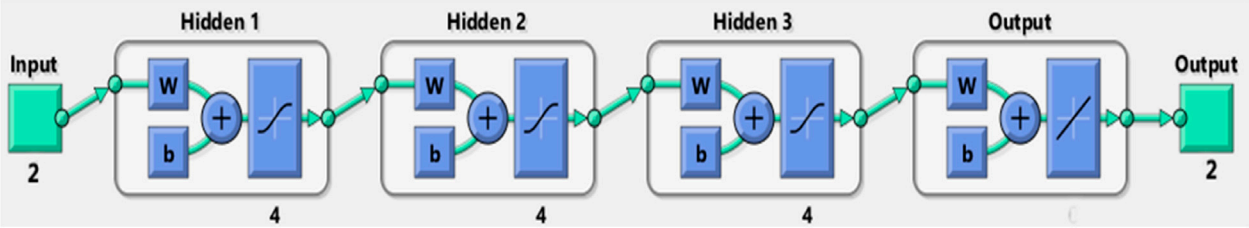

FIGURE 1
Designed deep learning neural network.

in this domain to extend this optimization approach to other converters.

3 Methodology

The deep Learning-based optimization process involves the following steps and methodology.

3.1 Constructing a deep learning algorithm

Deep Learning algorithms process the data through various layers of neural network algorithms. In simple words, deep learning refers to the training of the neural network. The neural network consists of several neurons. A neuron can be understood as a building block of a neural network. A network comprises three layers, i.e., input layer, hidden layer, and output layer. The two key hyperparameters that control the network topology include the number of layers and the number of nodes inside each hidden layer.

The input layer is responsible for passing on the initial information to the network. The hidden layer is located between the input and output layer, where all the computations are performed. The outer layer is responsible for producing the results based on the inputs and computations. In the research problem investigated in this article, we have two inputs [error (e) and the derivative of error (de)]. We have three hidden layers, and each hidden layer contains four neurons. The outputs are the optimized parameters for the PI controller, i.e., "Kp" and "Ki." Figure 1 shows the architecture of the constructed network.

The target value of the error is set at 1×10^{-4}. It implies that the network will keep searching for the PI controller's optimized parameters until the error value reaches the target value.

3.2 Mathematical modeling

A feed-forward network architecture was chosen while constructing the neural network (Babaie et al., 2019), (Shehzad et al., 2021). In a feed-forward neural network, the node connections don't form a cycle. In this case, multiple layers of computational units are connected in a feed-forward manner. Figure 2 shows the interconnections of a feed-forward network with two inputs ($x1 = error$, $x2 = derivative\,of\,error$), three hidden layers (4 neurons in each layer) and two outputs ($y1 = kp\,and\,y2 = ki$). "a" represents the pre-activation function which is a weighted sum of inputs plus the bias. "h" represents the activation function of a neuron which is a sigmoid function.

A mathematical representation can help to understand the whole interconnected network and the interaction of these neurons with each other easily. Going forward, the format used to indicate the weights and biases associated with a neuron is as follows

$$W\,(layer\,number)\,(neuron\,number)\,(Input\,number)$$
$$b\,(layer\,number)\,(Bias\,number\;for\,that\,input)$$

Here, we have two inputs and four neurons in each hidden layer. So, the corresponding weighted matrixes can be written as (Chi et al., 2021),

$$W1 = \begin{bmatrix} w_{111} & w_{112} \\ w_{121} & w_{122} \\ w_{131} & w_{132} \\ w_{141} & w_{142} \end{bmatrix} \quad (1)$$

$$W2 = \begin{bmatrix} w_{211} & w_{212} \\ w_{221} & w_{222} \\ w_{231} & w_{232} \\ w_{241} & w_{242} \end{bmatrix} \quad (2)$$

$$W3 = \begin{bmatrix} w_{311} & w_{312} \\ w_{321} & w_{322} \\ w_{331} & w_{332} \\ w_{341} & w_{342} \end{bmatrix} \quad (3)$$

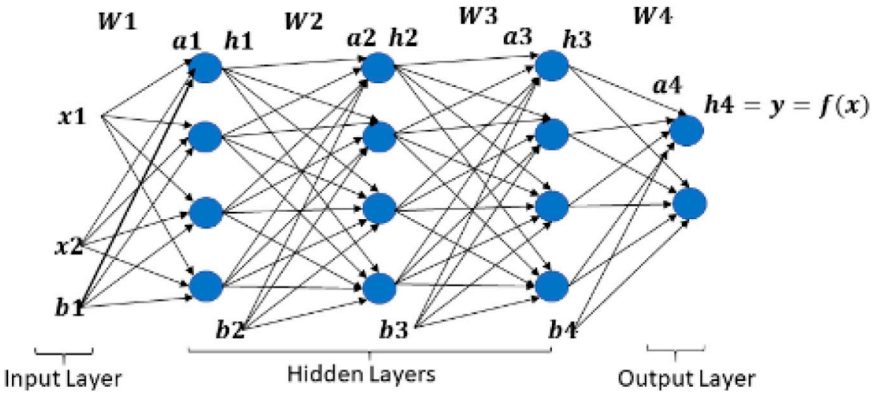

FIGURE 2
Interconnections of the designed network.

W1, *W2 and W3* represent the weighted matrixes of the three hidden layers, respectively. The input matrix "X" is shown in Eq. 4.

$$X = \begin{bmatrix} x_1 \\ x_2 \end{bmatrix} \tag{4}$$

To compute the pre-activation functions for each neuron of each hidden layer, consider the generic expression of the pre-activation function shown in Eq. 5.

$$a_i(x) = W_i h_{i-1}(x) + b_i \tag{5}$$

The activation at each layer is equivalent to applying a sigmoid function to the pre-activation of that respected layer. The expression for activation at each layer is depicted in Eq. 6.

$$h_i(x) = g(a_i(x)) \tag{6}$$

Where "g" is called the activation function.

We can compute the pre-activation for each neuron of each layer in the following manner (Autonomous, 2021).

$$a_{11} = w_{111}x_1 + w_{112}x_2 + b_{11} \tag{7}$$
$$a_{12} = w_{121}x_1 + w_{122}x_2 + b_{12} \tag{8}$$
$$a_{13} = w_{131}x_1 + w_{132}x_2 + b_{13} \tag{9}$$
$$a_{14} = w_{141}x_1 + w_{142}x_2 + b_{14} \tag{10}$$

Eqs 7, 8, 9, 10 represent the pre-activation for the four neurons in the first hidden layer.

In short, the pre-activation of the first layer is given by (Guasti Junior and Santos, 2021)

$$a_1 = W1^*x + b1 \tag{11}$$

W1 is the matrix containing individual weights, and *b1* is the vector containing the individual bias associated with sigmoid neurons. The activation for the first layer is

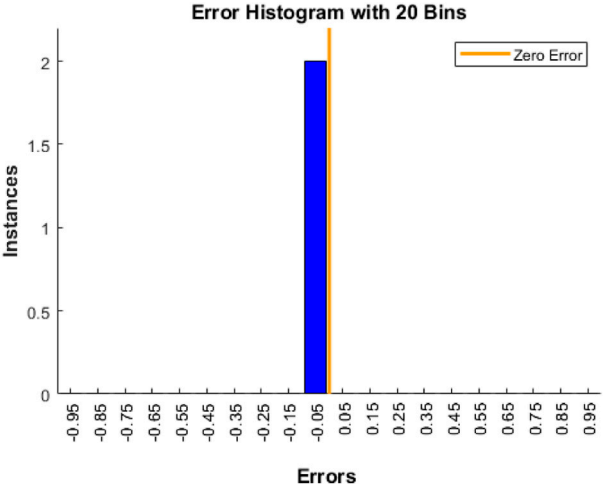

FIGURE 3
Error histogram.

$$h_1 = g(a_1) \tag{12}$$

Similarly, the pre-activation and activation functions for the remaining layers can be computed following the above topology.

The normalized mean square error (NMSE) approach is used to optimize the error values. The pseudo-code showing the input arguments to the NMSE handle and the error calculation is given by (Qolomany and Maabreh, 2017).

```
h = @ (x) NMSE (x, net, inputs, targets);
NMSE = mean (error.^2)/mean [var (target',1)];
```

Figure 3 represents the error histogram generated after the training of a controller.

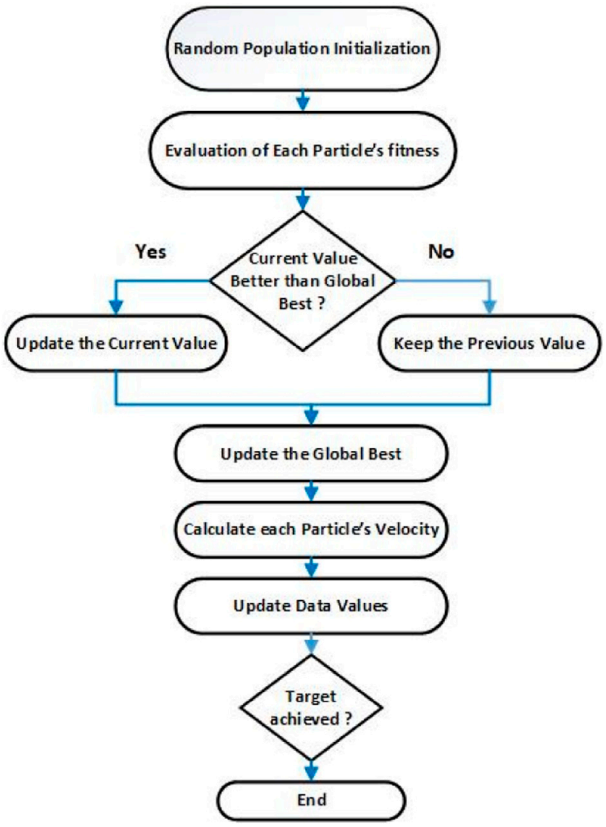

FIGURE 4
PSO algorithm.

TABLE 1 Shows a comparison of an AI-based optimized PI controller and a PI controller. It is verified from the values of the performance parameters that the responses of the optimized controller are better regarding the mentioned parameters in Table 1.

Parameter	Value
Rated Aparent Power	200 MVA
Nominal Voltage	230 KV
Nominal Frequency	50 Hz
Carrier Frequency	1350 Hz
Number of Levels	3 level NPC converter
Length of Transmission Cable	100 Km
DC Cable Resistance	0.0195 Ω/Km
DC Cable Inductance	19 mH/Km
DC Cable Capacitance	220 nF/Km

3.3 Particle swarm optimization

Considering the nature of the research problem, which involves MTDC grids, many variables keep on varying. To improve the accuracy of the deep learning algorithm, a PSO algorithm is used to find the optimum values for the weights and biases of the neural network. It also optimizes the computational time and the fitting regression, along with minimizing the mean square error. PSO was inspired form the swarm movement, which depends upon the individual and neighboring experience. PSO algorithm can be understood via four steps approach. The first step is the initiation and selection of a random population and particle, respectively. In the second step, the fitness of the previous (P_{pi}) and the next (P_{ni}) value is compared to the search for the optimized solution in the space. The third step is the selection of a local best and a global best (G_{bi}). The positions are recorded for the next step. Mathematically (Najeeb et al., 2017), it can be expressed through Eqs 13, 14.

$$V_i^{k+1} = w * V_i^k + r1c1\left(P_{ni} - X_i^k\right) + r2c2\left(G_{bi} - X_i^k\right) \quad (13)$$

$$X_i^{k+1} = X_i^k + V_i^k \quad (14)$$

Where X_i is the current position, V_i Is the speed of the particle, i is the optimization vector, and k refers to the number of iterations.w is the inertia weight factor. $c1$ is the cognitive coefficient, $c2$ is the social coefficient. $r1$ *and* $r2$ are the random velocity values in the search space. In the last step, the best particle is evaluated and saved; this process continues until the end of the iteration. Eq. 15 presents the objective function of the controller.

$$O_f(X) = \sum_{i=1}^{n} m_i f_i(X) \quad (15)$$

f_i is the performance index for the i^{th}, m_i is the weighting factor applied to the i^{th} sub-objective. Figure 4 represents the pseudo-code of the PSO algorithm. The number of iterations are directly related to the accuracy of the optimized rersults. The optimized weight and biases are the result of the PSO.

4 Result and analysis

A three-terminal VSC MTDC system with radial topology has been built in SIMULINK to test the proposed optimization strategy. The whole test system comprises of three AC grids synchronized and connected with each other. The goal of the system is do generate a stable DC output for a HVDC system to ensure the reliable performance. The layout is shown in Figure 5.

The system consists of three AC grids. The apparent power is 200 MVA, 230 kV, and the frequency is 50 Hz.

This section verifies the superior performance of the deep Learning-based optimized PI controller by comparing it with a randomly tuned PI controller. The performance parameters for the designed system include DC voltage, active power, and reactive power. We will compare the parameters like overshoot, undershoot, settling time, etc., to verify the optimal performance.

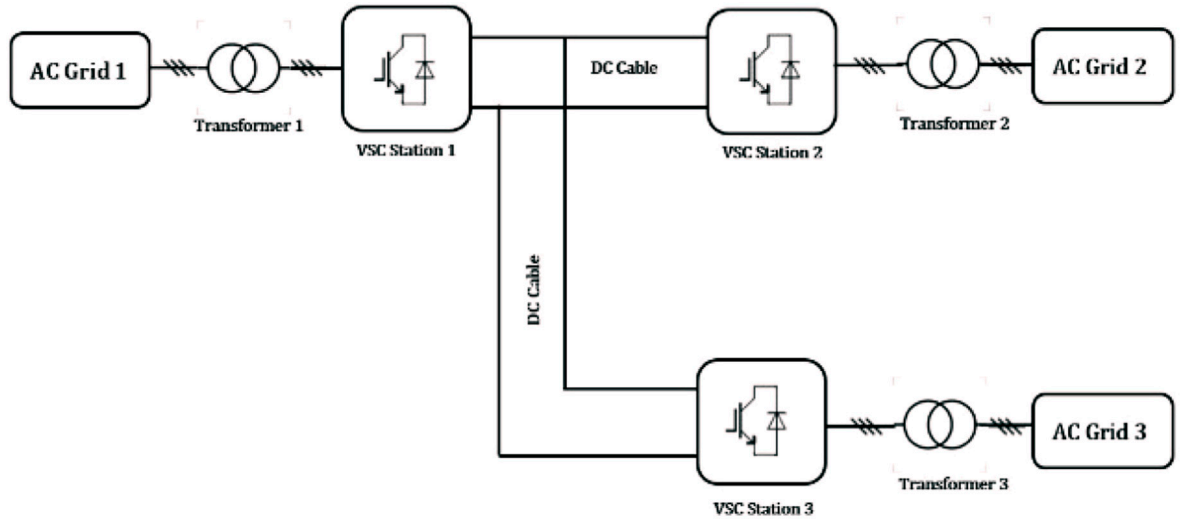

FIGURE 5
Three terminal VSC-MTDC system.

4.1 DC voltage

A smooth output DC voltage ensures the stable operation of the HVDC system and good power quality. To test our designed system for the worst-case scenario, faults were created. Figure 6 shows the response of the DC voltage for a randomly tuned PI controller. While Figure 7 shows the curve

TABLE 2 Comparison of voltage.

Quantity	Optimized PI	Simple PI
Max overshoot	34.40%	35.07%
Settling time	0.159 s	0.278 s
Undershoot	1.958%	3.48%
Rise time	4.493 ms	1.921 m s
Slew rate	17.522 V/μs	16.809 μs

TABLE 3 Comparison of active power.

Quantity	Optimized PI	Simple PI
Max overshoot	8.107%	11.446%
Settling time	0.22 s	0.24 s
Undershoot	34.4%	7.93%
Rise time	218.567 ms	514.37 ms
Slew rate	16.846 V/s	1.393 V/s

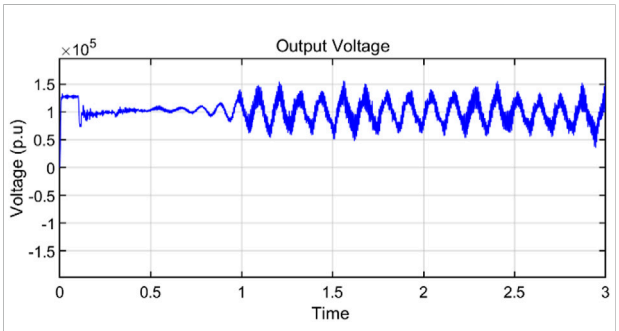

FIGURE 6
Voltage Curve for a simple PI controller.

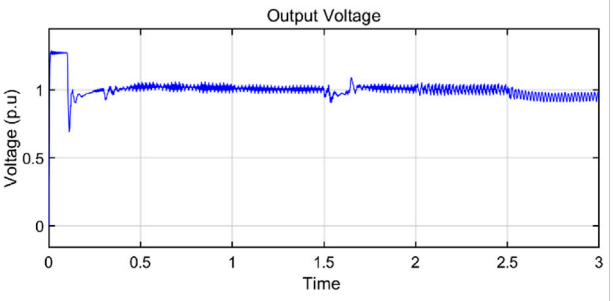

FIGURE 7
Voltage curve for the proposed controller.

TABLE 4 Compares the performance parameters of the two reactive power curves. It is evident that the optimized controller yields a better response regarding the mentioned parameters in Table 3.

Quantity	Optimized PI	Simple PI
Max overshoot	3.719%	1.326%
Settling time	0.323 s	0.499 s
Undershoot	1.68 %	2.87 %
Rise time	13.048 ms	12.18 ms
Slew rate	12.536 V/s	11.7 V/s

TABLE 5 Comparison of reactive power.

Quantity	Optimized PI	Simple PI
Max overshoot	3.719%	1.326%
Settling time	0.323 s	0.499 s
Undershoot	1.68%	2.87%
Rise time	13.048 ms	12.18 ms
Slew rate	12.536 V/s	11.7 V/s

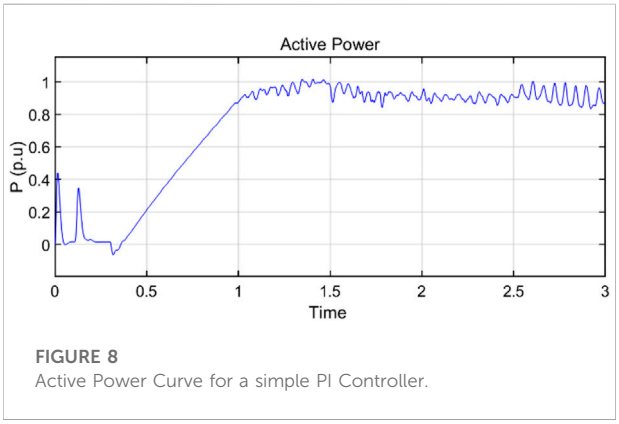

FIGURE 8
Active Power Curve for a simple PI Controller.

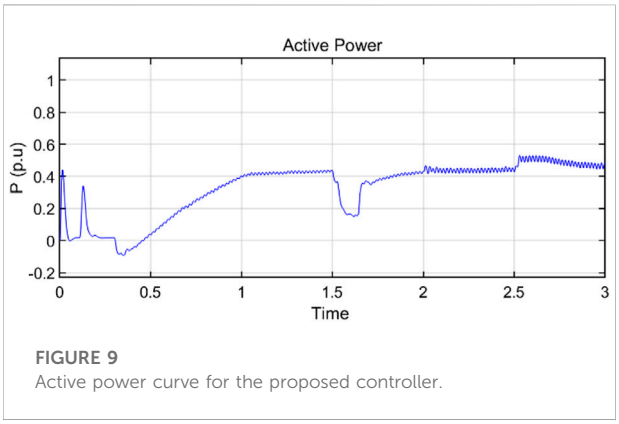

FIGURE 9
Active power curve for the proposed controller.

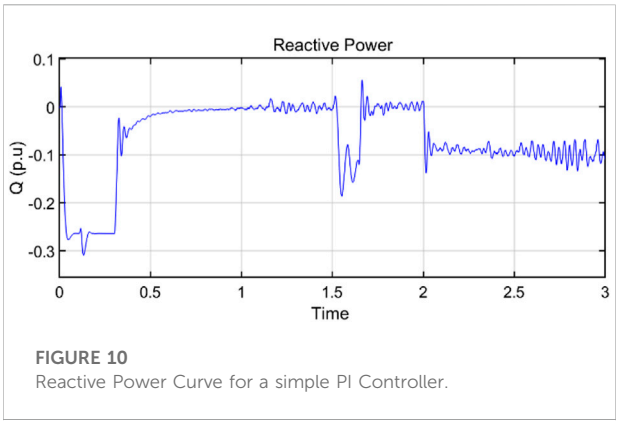

FIGURE 10
Reactive Power Curve for a simple PI Controller.

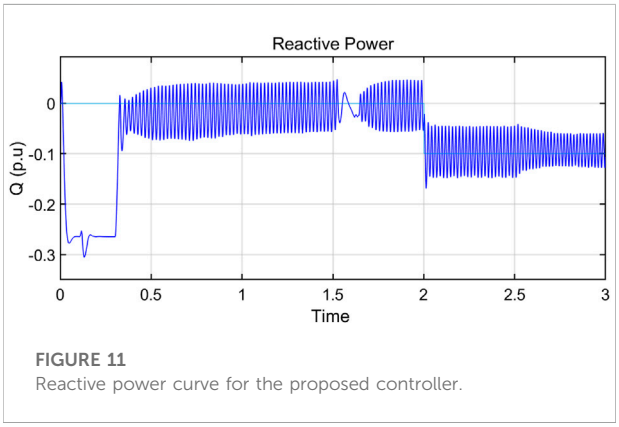

FIGURE 11
Reactive power curve for the proposed controller.

obtained after optimizing the PI controller using the proposed deep learning strategy. It is evident that the performance of deep learning optimization is superior in terms of various parameters, as shown in Table 1.

Considering the time axis at t = 1.5 s, a −0.1p. u step is introduced to the ref, DC voltage. At 2.5 s, a 3-phase to ground fault is created. The proposed deep Learning-based optimized system recovers in 0.083 s, whereas the simple controller recovers in 0.205 s, confirming the superiority of the deep learning optimization PI. Both these graphs show that for a randomly tuned PI controller, the response is not smooth and is oscillating, which can also lead to severe system damage. But after applying the proposed strategy, the graph becomes stable and smooth, even after the fault, ensuring a reliable and stable system.

It should be noted that the simple PI in this paper refers to the classic PI controller which is tuned by hit and trial method or according to the experience of the design engineer. The comparison is between the randomly tuned and the one tuned with the proposed strategy. Other PI tuning techniques are discussed in Section 1 of this paper along with their advantages and disadvantages. Applying all those techniques to pour specific converter problem and then comparing it

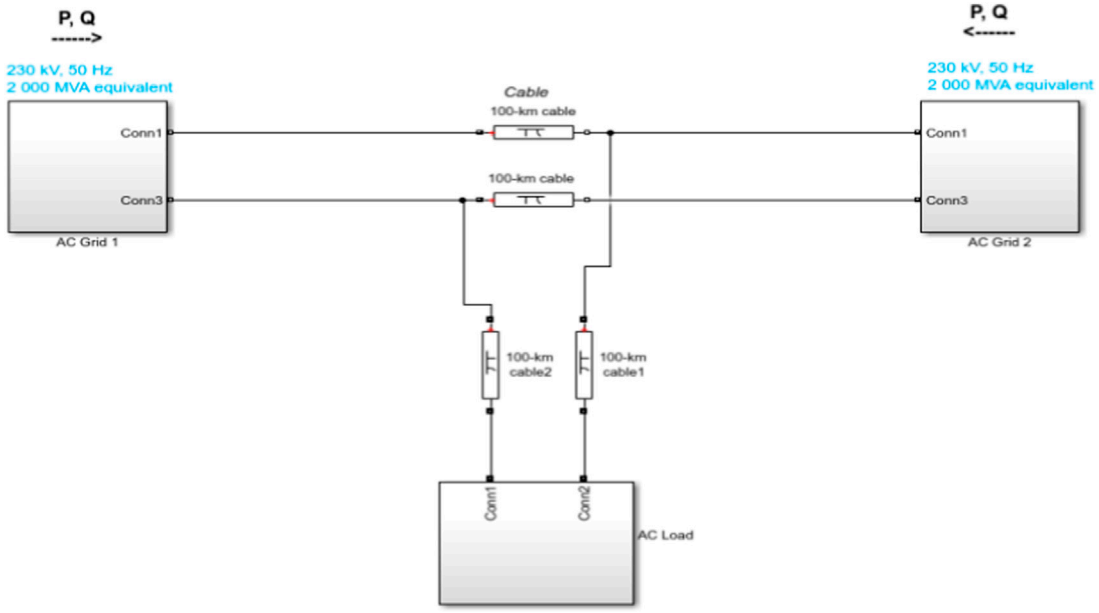

FIGURE 12
Three terminal MTDC network.

would result in complexity, so the shortcomings of those methods are highlighted.

4.2 Active and reactive power

The active and reactive power curves are crucial in determining the power quality, reliability, and system stability. The system is tested under transient conditions to verify the reliability of the proposed controller. Figures 8, 9 show the active power responses for a typical PI controller and deep learning-based optimized PI controller, respectively.

It is evident from Table 2 that the performance parameters of deep Learning-based optimized PI controllers are much better than a randomly tuned PI controller. The smooth and constant supply of active and reactive power is crucial for the loads. In the randomly tuned case, the graph shows very unsettling behavior, which is not good for the load and the overall system. By implementing our proposed strategy, In Table 3 we saw that the graph is now better and more stable than the previous version, thus ensuring a more reliable, efficient, and stable system.

Figures 10, 11 depict the reactive power responses for an AI-based optimized and a normal PI controller, respectively. it can be observed that in Table 4 and Table 5 the response of the AI-based optimized controller is smooth and contains less distortion, which helps to maintain the power stability of the system.

Figure 12 shows the real simulated system configuration.

5 Conclusion

A deep learning optimization technique for the VSC-MTDC was proposed and tested in this article. The proposed technique combines the benefits of artificial intelligence with the PI controller to achieve the best possible system response. A 200 MVA system was tested and the PI controllers were tuned using the deep learning algorithm. Performances with the classical tuning methods were compared and it was confirmed that the proposed strategy yields the best results in terms of overshoot, undershoot etc. To test the reliability of the proposed controllers, the system was tested under normal and transient operating conditions. Results and analysis of the performance parameters confirm the superior performance of the optimized PI controller using deep Learning. As a future trend in the development of a super grid or flexible distribution network, deep learning or AI can be applied to various other aspects of the power systems. This research is limited to two-level VSC topology and cannot be readily applied to MMC or any other converter without proper research and exploration. As a future goal, the optimization of MMC needs further research and exploration.

Data availability statement

The raw data supporting the conclusion of this article will be made available by the authors, without undue reservation.

Author contributions

SK and JA did all the software modeling and mathematical calculations. HM and RC helped to analyze the results and compare it with traditional methods. MA and AA helped in writing the paper and reviewing the overall project.

Acknowledgments

This work was supported by the Researchers Supporting Project number (RSP2022R467), King Saud University, Riyadh, Saudi Arabia.

Conflict of interest

The authors declare that the research was conducted in the absence of any commercial or financial relationships that could be construed as a potential conflict of interest.

Publisher's note

All claims expressed in this article are solely those of the authors and do not necessarily represent those of their affiliated organizations, or those of the publisher, the editors and the reviewers. Any product that may be evaluated in this article, or claim that may be made by its manufacturer, is not guaranteed or endorsed by the publisher.

References

Al-Mogren, A. S. (2008). Energy adaptive approach in a multi-channel dissemination-based network. *New Technol. Mobil. Secur.* 2008, 1–6. doi:10.1109/NTMS.2008.ECP.44

Aidan O'Dwyer (Editor) (2009). *Handbook of P.I.* (London: PID Controller Tuning Rules).

Araki, M. (2020). "PID control in control systems, robotics and automation, vol II," in *Encyclopedia of life Support systems (EOLSS), developed under the auspices of the UNESCO*. Editor Heinz Unbehauen (Oxford, UK: Eolss Publishers). Available from https://www.researchgate.net/publication/316990192_PID_Controller_Tuning_Techniques_A_Review.

Åström, K. J., Hägglund, T., and Astrom, K. J. (2006). *Advanced PID control*, 461. Research Triangle Park, NC: ISA-The Instrumentation, Systems, and Automation Society.

Autonomous, Author (2021). Depth-explanation-of-feedforward-in-neural-network-mathematically. Available at https://medium.com/analytics-vidhya/in-depth-explanation-of-feedforward-in-neural-network-mathematically-448092216b63. (Accessed 11 November 2021).

Babaie, M., Sharifzadeh, M., and Al-Haddad, K. (2019). "Adaptive ANN based single PI controller for nine-level PUC inverter," in 2019 IEEE Electrical Power and Energy Conference (EPEC), 1–6.

Badar, J., Hussain, R., Ahmed Ansari, J., and Munir, H. M. (2022). A detailed review of MMC circuit topologies and modelling issues. *Int. Trans. Electr. Energy Syst.*, 1–17. doi:10.1155/2022/8734010

Behera, S., Subudhi, B., and Pati, B. B. (2016). Design of PI controller in pitch control of wind turbine: A comparison of PSO and PS algorithm. *Int. J. Renew. Energy Res. (IJRER)* 6 (1), 271–281.

Chi, H. R., Domingues, M. d. F., Kostromitin, K. I., Almogren, A., and Radwan, A. (2021). Spatiotemporal D2D small cell allocation and on-demand deployment for microgrids. *IEEE Access* 9, 116830–116844. doi:10.1109/ACCESS.2021.3105750

Dai, A., Zhou, X., and Liu, X. (2017). Design and simulation of a genetically optimized fuzzy immune PID controller for a novel grain dryer. *IEEE Access* 5, 14981–14990. doi:10.1109/access.2017.2733760

Dashtdar, M., Sarada, K., Hosseinimoghadam, S. M. S., Kalyan, C. H. N. S., Venkateswarlu, A. N., Goud, B. S., et al. (2022). Faulted section identification and fault location in power network based on histogram analysis of three-phase current and voltage modulated. *J. Electr. Eng. Technol.* doi:10.1007/s42835-022-01079-2

Ehsan, Umer, Jawad, Muhammad, Javed, Umar, Zaidi, K. S., Rehman, A. U., Rassõlkin, Anton, et al. (2021). A detailed testing procedure of numerical differential protection relay for EHV auto transformer. *Energies (Basel).* 14 (24), 8447. doi:10.3390/en14248447

Fan, G. F., Guo, Y. H., Zheng, J. M., and Hong, W. C. (2019). Application of the weighted k-nearest neighbor algorithm for short-term load forecasting. *Energies* 12 (5), 916. doi:10.3390/en12050916

Freris, L., and Infield, D. (2008). *Renewable energy in power systems*. Wiley Press.

Geweda, A. E., El-Gohary, M. A., El-Nabawy, A. M., and Awad, T. (2017). Improvement of vehicle ride comfort using genetic algorithm optimization and PI controller. *Alexandria Eng. J.* 56 (4), 405–414. doi:10.1016/j.aej.2017.05.014

Gonçalves, L. C., Santos, M. F., da Silva, J. L., and Rezende, H. B. (2018). "Development of a PI controller through an ant colony optimization algorithm applied to a SMAR® didactic level plant," in 2018 19th International Carpathian Control Conference (ICCC), 150–155.

Guasti Junior, W., and Santos, I. P. (2021). "Solving differential equations using feedforward neural networks," in *Computational science and its applications – iccsa 2021. Iccsa 2021. Lecture notes in computer science.* (Cham: Springer), 12952. doi:10.1007/978-3-030-86973-1_27

Gupta, T. K., and Raza, K. (2020). Optimizing deep feed-forward neural network architecture: A tabu search based approach. *Neural process. Lett.* 51 (3), 2855–2870. doi:10.1007/s11063-020-10234-7

He, Jian-Bo, Wang, Qing-Guo, and Lee, Tong-Heng (2000). PI/PID controller tuning via LQR approach. *Chem. Eng. Sci.* 55, 2429–2439. doi:10.1016/S0009-2509(99)00512-6

Hu, X., and Eberhart, R. (2002). "Multiobjective optimization using dynamic neighborhood particle swarm optimization," in Proceedings of the 2002 Congress on Evolutionary Computation, 1677–1681.2

Ilten, E., and Demirtaş, M. (2016). *Off-line tuning of fractional order PI lambda controller by using response surface method for induction motor speed control.*

Izci, D. (2021). Design and application of an optimally tuned PID controller for DC motor speed regulation via a novel hybrid Lévy flight distribution and Nelder–Mead algorithm. *Trans. Inst. Meas. Control* 43 (14), 3195–3211. doi:10.1177/01423312211019633

Khalid, M. U., Javaid, Nadeem, Ahmad, Almogren, Ahmed, Abrar, Gulfam, Sardar Muhammad, and Radwan, Ayman (2022). Cooperative energy transactions in micro and utility grids integrating energy storage systems. *J. Parallel Distributed Comput.* 161, 48–62. doi:10.1016/j.jpdc.2021.11.006

Khan, L., and Ahmed, J. (2020). "Unified voltage droop control strategy for VSC-MTDC in HVDC system," in The 16th IET International Conference on AC and DC Power Transmission (ACDC 2020), 846–851. doi:10.1049/icp.2020.0184

Kookos, I. K., Lygeros, A. I., and Arvanitis, K. G. (1999). On-line PI controller tuning for integrator/dead time processes. *Eur. J. control* 5 (1), 19–31. doi:10.1016/s0947-3580(99)70134-2

Kumar, S. M. G., Jain, R., and Anantharaman, N. (2008). Genetic algorithm based PID controller tuning for a model bioreactor. *Indian Chem. Eng.* 50 (3), 214–226.

Lau, M. M., and Lim, K. H. (2018). "Review of adaptive activation function in deep neural network," in 2018 IEEE-EMBS Conference on Biomedical Engineering and Sciences (IECBES), 686–690.

Li, H., Luo, Y., and Chen, Y. (2010). A fractional order proportional and derivative (FOPD) motion controller: Tuning rule and experiments. *IEEE Trans. Control Syst. Technol.* 18 (2), 516–520. doi:10.1109/TCST.2009.2019120

Liang, H., Zou, J., Zuo, K., and Khan, M. J. (2020). *An improved genetic algorithm optimization fuzzy controller applied to the wellhead.*

Liu, S. A. C., and Ansari, J. A. (2020). Centralized fuzzy logic based optimization of PI controllers for VSC control in MTDC network. *J. Electr. Eng. Technol.* 15, 2577–2585. doi:10.1007/s42835-020-00556-w

Madan, S., and Bollinger, K. E. (1997). Applications of artificial intelligence in power systems. *Electr. Power Syst. Res.* 41, 117–131. doi:10.1016/S0378-7796(96)01188-1

Najeeb, M., Razali, R., Daniyal, H., Mahmood, A., and Mansor, M. (2017). *An intelligent voltage controller for a PV inverter system using simulated annealing algorithm-based PI tuning approach*.

O'Dwyer, A. (2003). *Handbook of PI and PID tuning rules*. London: Imperial College Press.

Oshaba, A. S., Ali, E. S., and Abd Elazim, S. M. (2017). Speed control of SRM supplied by photovoltaic system via ant colony optimization algorithm. *Neural comput. Appl.* 28 (2), 365–374. doi:10.1007/s00521-015-2068-8

Qolomany, B., and Maabreh, M. (2017). "Parameters optimization of deep learning models using particle swarm optimization," in The 13th International Wireless Communications and Mobile Computing Conference IWCMC.

Reed, G., Pape, R., and Takeda, M. (2003). Advantages of voltage sourced converter (VSC) based design concepts for FACTS and HVDC-link applications in 2003 IEEE Power Engineering Society General Meeting, Toronto, Ont., 1816–1821. doi:10.1109/PES.2003.1267437

Reynoso-Meza, G., Sanchis, J., Blasco, X., and Freire, R. Z. (2016). Evolutionary multi-objective optimisation with preferences for multivariable PI controller tuning. *Expert Syst. Appl.* 51, 120–133. doi:10.1016/j.eswa.2015.11.028

Rodriguez, P., and Rouzbehi, K. (2017). Multi-terminal DC grids: Challenges and prospects. *J. Mod. Power Syst. Clean. Energy* 5, 515–523. doi:10.1007/s40565-017-0305-0

Salunkhe, S., Phadke, G., Jadhav, S., and Pandeya, A. (2018). "Design and implementation of modified guo tao's algorithm for optimized PI controller for a level control system," in 2018 4th International Conference for Convergence in Technology (I2CT), 1–4.

Seborg, D. E., Edgar, T. F., and Mellichamp, D. A. (2004). *Process dynamics and control*. 2nd ed. New York: Wiley.

Sebtahmadi, S. S., Azad, H. B., Kaboli, S. H. A., Islam, M. D., and Mekhilef, S. (2017). A PSO-DQ current control scheme for performance enhancement of Z-source matrix converter to drive IM fed by abnormal voltage. *IEEE Trans. Power Electron.* 33 (2), 1666–1681. doi:10.1109/tpel.2017.2679118

Sharma, H., Mishra, S., Dhillon, J., Sharma, N. K., Bajaj, M., Tariq, R., et al. (2022). Feasibility of solar grid-based industrial virtual power plant for optimal energy scheduling: A case of Indian power sector. *Energies* 15, 752. doi:10.3390/en15030752

Shehzad, F., Javaid, N., Almogren, A., Ahmed, A., Gulfam, S. M., and Radwan, A. (2021). A robust hybrid deep learning model for detection of non-technical losses to secure smart grids. *IEEE Access* 9, 128663–128678. doi:10.1109/ACCESS.2021.3113592

Skogestad, Sigurd (2003). Simple analytic rules for model reduction and PID controller tuning. *J. Process Control* 13 (4), 291–309. doi:10.1016/s0959-1524(02)00062-8

Soliman, M. S., Belkhier, Y., Ullah, Nasim, Achour, Abdelyazid, Alharbi, Yasser M., Ahmad, Aziz Al, et al. (2021). Supervisory energy management of a hybrid battery/PV/tidal/wind sources integrated in DC-microgrid energy storage system. *Energy Rep.* 7, 7728–7740. doi:10.1016/j.egyr.2021.11.056

Xu, C., Gordan, B., Koopialipoor, M., Armaghani, D. J., Tahir, M. M., and Zhang, X. (2019). Improving performance of retaining walls under dynamic conditions developing an optimized ANN based on ant colony optimization technique. *IEEE Access* 7, 94692–94700. doi:10.1109/access.2019.2927632

Yousaf, A., Asif, R. M., Shakir, M., Rehman, A. U., Alassery, F., Hamam, H., et al. (2021). A novel machine learning-based price forecasting for energy management systems. *Sustainability* 13, 12693. doi:10.3390/su132212693

Zhao, J., Lin, M., Xu, D., Hao, L., and Zhang, W. (2015). Vector control of a hybrid axial field flux-switching permanent magnet machine based on particle swarm optimization. *IEEE Trans. Magn.* 51 (11), 1–4. doi:10.1109/tmag.2015.2435156

Ziegler, J. G., and B Nichols, N. (1942). Optimum settings for automatic controller. *Transaction ASME* 64, 759–768.

frontiers | Frontiers in Energy Research

TYPE Original Research
PUBLISHED 23 September 2022
DOI 10.3389/fenrg.2022.996206

OPEN ACCESS

EDITED BY
Dongran Song,
Central South University, China

REVIEWED BY
Feihhang Zhou,
Xi'an University of Posts and Telecommunications, China
Jian Yang,
Central South University, China

*CORRESPONDENCE
Kamel Ouari,
kamel.ouari@univ-bejaia.dz
Salah Kamel,
skamel@aswu.edu.eg

†These authors have contributed equally to this work

SPECIALTY SECTION
This article was submitted to Smart Grids,
a section of the journal
Frontiers in Energy Research

RECEIVED 17 July 2022
ACCEPTED 01 August 2022
PUBLISHED 23 September 2022

CITATION
Ouari K, Belkhier Y, Djouadi H, Kasri A, Bajaj M, Alsharef M, Elattar EE and Kamel S (2022), Improved nonlinear generalized model predictive control for robustness and power enhancement of a DFIG-based wind energy converter. *Front. Energy Res.* 10:996206. doi: 10.3389/fenrg.2022.996206

Improved nonlinear generalized model predictive control for robustness and power enhancement of a DFIG-based wind energy converter

Kamel Ouari[1*†], Youcef Belkhier[2†], Hafidh Djouadi[1†], Amel Kasri[1†], Mohit Bajaj[3,4†], Mohammad Alsharef[5†], Ehab E. Elattar[5†] and Salah Kamel[6*†]

[1]Laboratory of Industrial and Information Technology (LTII), Faculty of Technology, University of Bejaia, Bejaia, Algeria, [2]Centre for Ocean Energy Research, Maynooth University, Maynooth, Kildare, Ireland, [3]Department of Electrical and Electronics Engineering, National Institute of Technology, Delhi, India, [4]Department of Electrical Engineering, Graphic Era (Deemed to be University), Dehradun, India, [5]Department of Electrical Engineering, College of Engineering, Taif University, Taif, Saudi Arabia, [6]Electrical Engineering Department, Faculty of Engineering, Aswan University, Aswan, Egypt

Many studies have been made on the double-fed induction generator wind turbine system (DFIG-WTS) in recent decades due to its power management capability, speed control operation, low converter cost, and minimized energy losses. In contrast, induction machine control is a more complex task because of its multivariable and nonlinear nature. In this work, a new robust nonlinear generalized predictive control (RNGPC) is developed to maximize the extracted energy from the wind without the use of aerodynamic torque measurements or an observer. The aim of the predictive control is to produce an anticipated impact by employing explicit knowledge of the present condition. By revisiting the cost function of the conventional nonlinear generalized predictive control (NGPC), which is based on Taylor series expansion, in that way, the resilience of the system is improved. An integral action is included in the nonlinear predictive controller. As a result, if the closed loop system is stable, the suggested controller totally eliminates the steady state error, even if unknown perturbations and mismatched parameters are present. The output locating error's convergence to the source is utilized to show the locked system's stability. Simulation results demonstrate and verify the efficiency, the good performance, and robustness of this proposed control technique.

KEYWORDS

DFIG wind turbine systems, robust generalized predictive control, doubly fed induction generator, wind, controller

Introduction

Due to its multiple advantages over other types of wind turbines, the doubly fed induction generator (DFIG) is becoming more common in wind generation. In general, the system is designed to operate in a 33% slip range. In this situation, the power requirement of the rotor converter is 25% of the maximum power of the wind turbine (Malik et al., 2021). The supply of the rotor by a converter, with variable frequency, makes it possible to separate the mechanical speed of the rotor from the frequency of the electrical grid. The control system for an induction machine is more complicated because it is a multivariable, nonlinear, and highly linked system. Techniques like voltage-field-oriented control and power-torque direct control, which use a linear conventional controller like the proportional-integral-predictive (PID) controller, have not always achieved flawless results (Tamalouzt et al., 2021).

An important number of nonlinear controls have appeared in the literature to ensure better performances control of a DFIG-based wind turbine. In Gupta and Shukla, 2022, an algorithm is proposed for the improvement of the DFIG by sharing between the converters (machine-side and grid-side) an optimal reactive power. An active disturbance rejection control with important robustness properties to design the current control law is developed in Beltran-Pulido et al., 2018 to enhance the ride-through low voltage. A coordinated super-twisting sliding mode control is investigated in Xiong et al., 2019 for grid synchronization and power optimization of the conversion system. A new exponential reaching law-based sliding mode control is proposed in Liu et al., 2018 for hastening the approaching process and lowering the system chattering phenomena. A multi-objective particle swarm optimization algorithm in studied in Aguilar et al., 2020, improving dynamic stability under electrical disturbances and thereby assisting the ride-through low voltage.

However, to ensure higher performances of the DFIG-based wind energy converter, it requires the utilization of advanced nonlinear controllers. Indeed, model predictive control (MPC) emerged in the late 70s (Mahmoud and Oyedeji, 2019), and since then, it has evolved into a variety of forms such as model algorithmic control, predictive functional control (Nosratabadi et al., 2019), generalized predictive control (Wang and Li, 2022), extended horizon adaptive control (Younesi et al., 2022), and robust model predictive control (Pradhan et al., 2022).

The MPC is a plant model-based feedback control approach that forecasts future plant outputs over a specific time horizon. These predictions are then utilized to choose the optimum control by solving an optimization problem while adhering to a set of constraints (Schwenzer et al., 2021). To deal with the features and control needs of specific types of variable-speed wind turbines, a revisiting variant of a recent adaptive second-order sliding algorithm is presented in Evangelista et al., 2016. Robust adaptive MPC constructed through linear matrix inequality and obtained estimation with a nonlinear observer is designed in Zhang et al., 2019a for the optimal, effective, and robust operation of the conversion system. Based on an analysis of the effectiveness of nonlinear MPC with a fixed weight coefficient under various wind conditions, a fuzzy regulator is created to update the weight coefficient of the cost function, and an improved multi-objective marine predator algorithm is proposed in Song et al., 2022b for optimization on energy capture and generator torque fluctuation. A DFIG wind system based on balanced and unbalanced network conditions is proposed using a universal and low-complexity model predictive direct power control (Zhang et al., 2019b). To handle high-voltage ride through, a P-Q coordination-based MPC is developed in Zhou et al., 2021. On the basis of intelligent scenario generation (ISG), a stochastic model predictive yaw control (SMPYC) technique is suggested in Song et al., 2022a. Here, the ISG approach is suggested to develop scenarios that define the uncertainty of wind direction prediction. Then, the yaw action is improved using the suggested scenario-based SMPYC to increase the energy capture effectiveness of WTs.

For mechanical sensorless control technology of induction machines, several solutions have been developed. A direct torque control associated with an artificial neural network was applied to a dual power induction motor (Tamalouzt et al., 2022). This strategy is carried out without a mechanical sensor using the extended Kalman filter as an observer. In order to ensure the estimation of the five-phase induction motor rotor speed, the authors, in Tamalouzt et al., 2022, performed two approaches: the first is based on the adaptive flux and speed observer, the second, on the other hand, is based on a model reference adaptive system estimator. A disturbance observer is constructed to estimate the aerodynamic torque in Ouari et al., 2014a, and a nonlinear generalized predictive control for wind energy conversion systems is proposed to achieve the controller's robustness. For induction motor drives, a load torque observer based on a second-order sliding mode technique is suggested (El Daoudi et al., 2021).

The present study is aimed to design a robust controller in order to maximize the amount of energy taken from the wind without the use of an observer or aerodynamic torque measurements. The system's robustness is increased by revising the cost function of the traditional nonlinear generalized predictive control (NGPC), which is based on Taylor series expansion. The nonlinear predictive controller includes an integral action. As a result, assuming that the closed loop system is stable, the proposed controller completely eliminates the steady state error, even in the presence of unknown disturbances and mismatched parameters. The convergence of the output locating error to the source is used to demonstrate the stability of the locked system. The validation of the trajectory following and perturbation rejection of the applied control using simulation

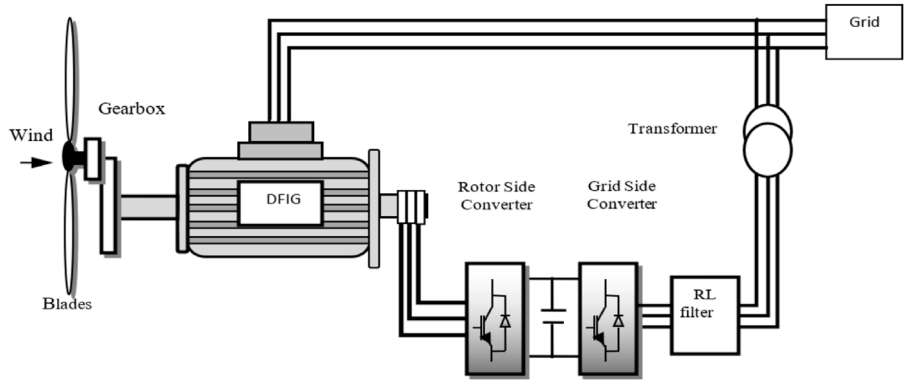

FIGURE 1
DFIG-based wind energy converter.

results of the dynamic behavior of the researched system was performed under Matlab/Simulink.

The paper is organized as follows: in the *Introduction* section, the DFIG wind turbine system is described, and in the *DFIG wind turbine system description and energy conversion* section, the DFIG modeling is examined. The *Proposed robust nonlinear generalized predictive control* section develops the proposed structure controller. Finally, in the *Simulation results* Section, the simulation results are presented.

DFIG wind turbine system description and energy conversion

The DFIG wind turbine system is depicted schematically in Figure 1. The stator is directly linked to the three-phase power grid, while the rotor is fed at a variable frequency through the AC-DC-AC converter (Tamalouzt et al., 2021).

Modeling of the wind turbine

Only a small portion of the acquired wind energy can be converted by a wind turbine; thus, the wind's mechanical power is calculated as follows (Soliman et al., 2021; Belkhier et al., 2022):

$$P_t = \frac{1}{2}\rho_a \pi R^2 C_p(\lambda,\beta) v^3 \tag{1}$$

where P_t is the wind energy extracted (power), ρ_a is the air density (kg/m^3), R is the blade radius (m), v is the wind speed (m/s), and $C_p(\lambda,\beta)$ is the turbine power coefficient as a function of speed ratio λ and blade pitch angle β given as

$$C_p(\beta,\lambda) = (0.3 - 0.0167\beta)\ \sin\left(\frac{\pi(\lambda+0.1)}{10-0.3\beta}\right) - 0.00184(\lambda-3)\beta \tag{2}$$

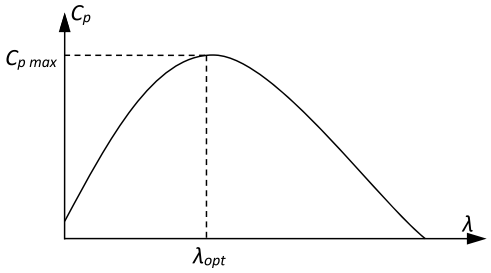

FIGURE 2
Power coefficient C_p (λ, β).

The blade's tip-speed ratio λ is defined as follows:

$$\lambda = \frac{\Omega_t R}{v} \tag{3}$$

It is preferable for the generator to have a power characteristic that follows the maximum C_{p-max} line (Figure 2) in order to convert the maximum amount of wind power. For a speed ratio $\lambda_{opt} = 8$, the power coefficient C_p achieves a maximum of 0.5506 for a blade pitch angle of $\beta = 0°$.

The control block's rotor speed and active power references were provided by maximum power point tracking (MPPT), while the reactive power was set to zero to obtain a unity power factor (Belkhier et al., 2022).

$$\begin{cases} P_{grid-\mathbf{ref}} = \frac{1}{2}\rho_a \pi R^2 C_{p-max} v^3 \\ \Omega_{r-ref} = \frac{\lambda_{opt}}{R} v \end{cases} \tag{4}$$

where $P_{grid-refis}$ the electrical grid's active power reference, Ω_{r-ref} is the rotor speed reference, λ_{opt} is the optimal speed ratio, and C_{p-max} is the maximal power coefficient.

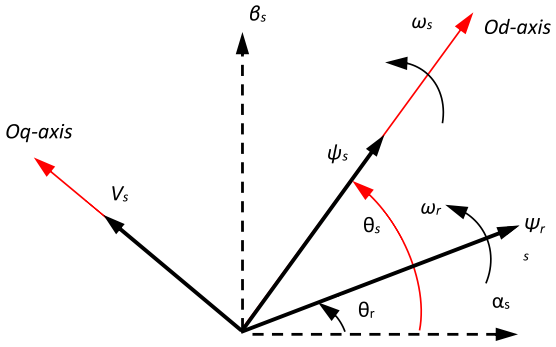

FIGURE 3
Voltage and flux vectors settings.

Model of the DFIG

The DFIG model is commonly characterized by the following state equations in the synchronous orientation frame when the d-axis is aligned with the stator flow vector (Figure 3) and by disregarding the stator resistance (Pradhan et al., 2022):

$$\begin{cases} \dfrac{di_{dr}}{dt} = -\dfrac{R_r}{\sigma L_r} i_{dr} + s\omega_s i_{qr} + \dfrac{1}{\sigma L_r} V_{dr} \\ \dfrac{di_{qr}}{dt} = -\dfrac{R_r}{\sigma L_r} i_{qr} - s\omega_s i_{dr} + s\dfrac{MV_s}{\sigma L_r L_s} + \dfrac{1}{\sigma L_r} V_{qr} \end{cases} \tag{5}$$

where $\sigma = 1 - \frac{M^2}{L_r L_s}$, $s = \frac{\omega_s - \omega_r}{\omega_s}$, V_{dr}, V_{qr}, i_{dr} and i_{qr} are the dq rotor voltage and current components, respectively. Rr is the resistance of the rotor winding, and L_r is the rotor winding inductance. ω_s *and* ω_r are, respectively, the stator and the rotor angular velocities. s and σ are, respectively, the *g*enerator *s*lip and dispersion ratio.

In the Park transformation of the rotor quantities, the relative angle between the rotor and the Park reference (dq-axis) is used, which is determined as $\theta = \theta_s - \theta_r$, where $\omega_r = P\Omega_r$, $\omega_s = 2\pi f_s$, $\theta_r = \int \omega_r dt$, $\theta_s = \int \omega_s dt$, Ω_r is the mechanical rotor s*p*eed, ω_r is the angular rotor s*p*eed, P is the *p*ole number, and f_s is the grid frequency.

The generator torque can then be expressed by

$$T_{em} = P\frac{MV_s}{\omega_s L} i_{qr} \tag{6}$$

The following formulas give active and reactive stator powers:

$$\begin{cases} P_s = -\dfrac{M}{L_s} V_s I_{qr} \\ Q_s = \dfrac{V_s^2}{\omega_s L_s} - \dfrac{M}{L_s} V_s I_{dr} \end{cases} \tag{7}$$

The mechanical equation is

$$J\frac{d\Omega_r}{dt} = T_{em} - T_r - f_r\Omega_r \tag{8}$$

where f_r is the turbine total external dam*p*ing, J is the turbine total inertia, T_{em} is the electromagnetic torque, and T_r is the aerodynamic torque after the gearbox.

Proposed robust nonlinear generalized predictive control

The predictive control idea is to create an anticipatory effect using the explicit knowledge of the current state (Ouari et al., 2014b; Tamalouzt et al., 2022). The classical cost function is given as

$$\mathfrak{J}(x,u) = \int_0^t [y_r(t+\delta) - y(t+\delta)]^T [y_r(t+\delta) - y(t+\delta)] d\delta \tag{9}$$

In this study, a robust nonlinear generalized predictive control (RNGPC) is suggested to solve the robust control problem by revising the classical cost function (9). Consider the nonlinear multivariable system:

$$\begin{cases} \dot{x}(t) = f(x) + B(x)u(t) \\ y_i(t) = h_i(x) i = 1, \ldots, m \end{cases} \tag{10}$$

where x and $u \in \mathcal{R}^n$ are the state vector and control, respectively. The function $f(x)$ and $h(x)$are assumed to be continuously differentiable a sufficient number of times, and $B(x)$is a continuous function of x. The predictive command will be optimal if the novel cost function $I(x,u)$ is minimized.

$$\mathfrak{J}(x,u) = \frac{1}{2}\Gamma(t+\tau)^T \Gamma(t+\tau) \tag{11}$$

$$\Gamma(t) = \int_0^t [\, y_r(\delta) - y(\delta)] d\delta \tag{12}$$

with $\begin{cases} \Gamma(\delta) = (\Gamma_1(t)\Gamma_2(t)\Gamma_m(t))^T \\ y(t) = (\, y_1(t)\, y_2(t) y_m(t))^T \\ y_r(t) = (\, y_{r1}(t)\, y_{r2}(t) y_{rm}(t))^T \end{cases}$

To solve the nonlinear optimization problem (11), the predicted term $\Gamma_i(t+\tau)\Gamma(t+T)$ is ex*p*anded into a $(\rho_i + 1)^{\text{th}}$ order Taylor series expansion.

$$\Gamma_i(t+\tau) = \Gamma_i(t) + \sum_{k=1}^{\rho_i+1} \frac{\tau^k}{k!} \Gamma_i^{(k)}(t) \tag{13}$$

Replacing (12) in (13)

$$\Gamma_i(t+\tau) = \Gamma_i(t) + \sum_{k=1}^{\rho_i+1} \frac{\tau^k}{k!} \int_0^t \left[\, y_{ri}^{(k)}(\delta) - y_i^{(k)}(\delta)\right] d\delta \tag{14}$$

Since ρ_i stands for the out*p*ut's relative degree for $y_i(t)$, it follows that

$$\begin{cases} y_i(t) = h_i(x) \\ y_i^{(k)}(t) = L_f^k h_i(x) \\ y_i^{(r_i)}(t) = L_f^{r_i} h_i(x) + L_B L_f^{(\rho_i - 1)} h_i(x) u(t) \end{cases} \tag{15}$$

The Lie derivation of function h(x) along a vector field f(x) is indicated by

$$\begin{cases} L_f h_i(x) = \dfrac{\partial h_i}{\partial x} f(x) \\ L_f^k h_i(x) = L_f\left(L_f^{k-1} h_i(x)\right) \\ L_B L_f h_i(x) = \dfrac{\partial L_f h_i}{\partial x} B_u(x) \end{cases} \tag{16}$$

Invoking (15) and (16) with (14) yields

$$\Gamma_i(t+\tau) = \Gamma_i(t) + \sum_{k=1}^{\rho_i+1} \frac{\tau^k}{k!} e_i^{(k-1)}(t) + \frac{\tau^{(\rho_i+1)}}{(r_i+1)!} L_B L_f^{(\rho_i-1)} h_i(x)\, u(t) \tag{17}$$

with $e_i^{(k)}(t) = y_{ri}^{(k)}(t) - L_f^k h_i(x)$

It is possible to write (17) in the following format:

$$\Gamma_i(t+\tau) = \left(1\ \tau\ .\ \ \frac{\tau^k}{k!}\ .\ \ \frac{\tau^{(\rho_i+1)}}{(r_i+1)!}\right)\left[\begin{pmatrix} \Gamma_i \\ e_i \\ . \\ e_i^{(k-1)} \\ . \\ e_i^{(\rho_i)} \end{pmatrix} - \begin{pmatrix} 0_{1*n} \\ 0_{1*n} \\ . \\ 0_{1*n} \\ . \\ G_i(x) \end{pmatrix} u\right] \tag{18}$$

where $G_i(x)_{1*n} = L_B L_f^{(\rho_i-1)} h_i(x)$

If all output systems have the same relative degree r,

$$\Gamma(t+\tau) = \bar{T}(\tau)\left[\bar{E}(t) - \bar{M}(u)\right] \tag{19}$$

where $\begin{cases} \bar{T}(\tau) = [\bar{T}_1(\tau)\bar{T}_2(\tau)\bar{T}_3(\tau)\ldots..\bar{T}_{\rho_i+1}(\tau)] \\ \bar{E}(t) = \left[\int_0^t e(t)dt \quad e(t)e^{(1)}(t)\ldots.e^{(\rho_i)}(t)\right]^T \text{ and} \\ \bar{M}(u) = [\bar{0}_{m*n}\bar{0}_{m*n}\bar{0}_{m*n}\ldots.G_u(x)]\, u(t) \end{cases}$

$\begin{cases} \bar{T}_k(\tau) = \dfrac{\tau^{(k)}}{(k)!}\bar{I}_d \\ G_u(x) = [G_1(x)G_2(x)\ldots G_m(x)]^T \end{cases}$, $\bar{I}_d$ is the diagonal of the matrix identity.

Replacing (19) in (11), the expression of the novel cost function will be

$$\mathfrak{J}(x,u) = \frac{1}{2}\left[\bar{E}(t) - \bar{M}(u)\right]^T \bar{\Psi}(\tau)\left[\bar{E}(t) - \bar{M}(u)\right] \tag{20}$$

where $\bar{\Psi}(\tau) = \bar{T}(\tau)^T \bar{T}(\tau)$

The condition that must be met in order to achieve optimal control is given by

$$\frac{\partial \mathfrak{J}(x,u)}{\partial u} = 0 \tag{21}$$

According to (20) and (21), the optimal control is calculated as follows:

$$u(t) = -\left(\bar{M}^T \bar{\Psi}(\tau)\bar{M}(x)\right)^{-1} \bar{M}^T \Psi(\tau)\bar{E}(t) \tag{22}$$

If $n = m$, then the optimal control can be indicated as follows:

$$u(t) = -G_u(x)^{-1} \Psi(\tau)\bar{E}(t) \tag{23}$$

where

$$\Psi(\tau) = \left(\frac{(\rho_i+1)!}{\tau^{(\rho_i+1)}}\bar{I}_d \frac{(\rho_i+1)!}{\tau^{\rho_i}}\bar{I}_d\ldots\frac{(\rho_i+1)!}{(k)!\tau^{(\rho_i+1-k)}}\bar{I}_d..\bar{I}_d\right) k = 0..\rho_i$$

An integral action is included in the nonlinear predictive controller (23). As a result, the suggested controller completely eliminates the steady state error even in the presence of unknown perturbations.

The control system's proposed topology consists of two loops: an inner loop that controls torque and direct current and an outside loop that controls DFIG speed (Figure 4). The rotor speed reference is specified in (4). To reduce the control effort, the reference speed signal is passed via a second-order linear filter, which is provided by

$$F(s) = \frac{w_n^2}{s^2 + 2\zeta\,\omega_n + w_n^2} \tag{24}$$

where $w_n = 5$ and $\zeta = 0.7$.

Predictive control of electromagnetic torque and current (inner loop)

The electromagnetic torque reference is calculated from the speed controller (outer loop), and to keep the DFIG reactive power at zero, the d-axis rotor current reference is determined. From (5), the electrical equations are written in the matrix form as follows:

$$\begin{cases} \dot{x}(t) = f(x) + g_u(x)u(t) \\ y = h(x) \end{cases} \tag{25}$$

with $x = (i_{dr} i_{qr})^T$, $u = (V_{dr-ref} V_{qr-ref})^T$, and $u = (T_{em}\, i_{dr})^T$

$$f(x) = \begin{pmatrix} -\dfrac{R_r}{\sigma L_r} i_{dr} + s\omega_s i_{qr} \\ -\dfrac{R_r}{\sigma L_r} i_{qr} - s\omega_s i_{dr} + s\dfrac{V_s}{\sigma L_r L_s} \end{pmatrix} and\ g_u(x) = \begin{pmatrix} \dfrac{1}{\sigma L_r} & 0 \\ 0 & \dfrac{1}{\sigma L_r} \end{pmatrix}$$

The following are the outputs that will be regulated in the inner loop:

$$\begin{cases} y_1 = h_1(x) = T_{em} = P\dfrac{MV_s}{\omega_s L_s} i_{qr} \\ y_2 = h_2(x) = i_{dr} \end{cases} \tag{26}$$

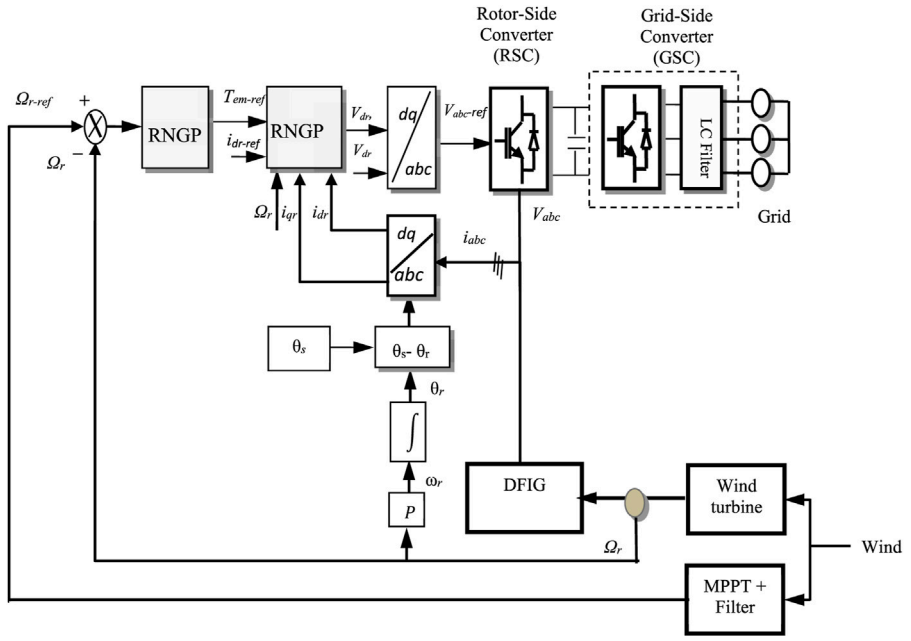

FIGURE 4
Block Diagram of the proposed RNGPC applied to the RSC.

The relative degrees ρ_1 and ρ_2 of the outputs y_1 and y_2 are equal to 1; it follows that

$$\dot{y}(t) = L_f h(x) + G_{u1}(x)u(t) \tag{27}$$

with $G_{u1} = \begin{pmatrix} L_{gu}L_f h_1(x) & 0 \\ 0 & L_{gu}L_f h_2(x) \end{pmatrix}$, $h(x) = \begin{pmatrix} h_1(x) \\ h_2(x) \end{pmatrix} = \begin{pmatrix} T_{em} \\ I_{dr} \end{pmatrix}$ and $y_r = \begin{pmatrix} y_{r1} \\ y_{r2} \end{pmatrix} = \begin{pmatrix} T_{em-ref} \\ i_{dr-ref} \end{pmatrix}$

Thus, as follows, the predicted term is expanded into a second-order Taylor series expansion:

$$\Gamma(t+\tau) = \bar{\Psi}\left[\bar{E}(t) - \bar{M}\,u(t)\right] \tag{28}$$

where

$$\begin{cases} \bar{\Psi} = \left[\dfrac{2}{T_{p1}^2} \quad \dfrac{2}{T_{p1}} \quad 1\right]\bar{I}_d \\ \bar{E}(t) = \left[\displaystyle\int_0^t \mathbf{e}(\delta)d\delta \quad \mathbf{e}(t) \quad \dot{\mathbf{e}}(t)\right]^T \\ \bar{M}(u) = [\bar{O}_{2*2}\bar{O}_{2*2} \quad G_{u1}(x)]^T u(t) \end{cases}$$

$$e^{(k)}(t) = \begin{pmatrix} e_1^{(k)}(t) \\ e_2^{(k)}(t) \end{pmatrix}\begin{pmatrix} y_{r1}^{(k)}(t) - L_f^k h_1(x) \\ y_{r2}^{(k)}(t) - L_f^k h_2(x) \end{pmatrix}$$

where k = 0, 1 and $\bar{I}_d\bar{I}_d$ is the diagonal of the matrix identity (2*2). Replacing (28) in (23), the optimal nonlinear control law is determined as

$$u(t) = -G_{u1}(x)^{-1}\left[k_{i1}\int_0^t e(\delta)d\delta \quad k_{p1}e(t) \quad K_{d1}\dot{e}(t)\right] \tag{29}$$

where $K_{i1} = \frac{2}{T_{p1}^2}$, $K_{p1} = \frac{2}{T_{p1}}$, $K_{d1} = 1$.

Predictive control of the speed (outer loop)

The DFIG's mechanical dynamics are given by the equation below:

$$\begin{cases} \dot{x}(t) = f(x) + g_u(x)u(t) \\ y = h(x) \end{cases} \tag{30}$$

where $x(t) = \Omega_r$, $u(t) = T_{em}$, $y(t) = \Omega_r$, $y_r(t) = \Omega_{r-ref}$, $f(x) = -\frac{f_r}{J}\Omega_r$, and $g_u(x) = \frac{1}{J}$.

We do not consider the aerodynamic torque in the mechanical Equation 8. The relative degree of the outputs $y(t)$ is equal to 1, and it follows that

$$\dot{y}(t) = L_f h(x) + G_{u2}(x)u(t) \tag{31}$$

where $G_{u2}(x) = L_{gu}L_f h(x)$.

A second-order Taylor series expansion is used to expand the expected term $\Gamma(t+\tau)$:

$$\Gamma(t+T) = \bar{\Psi}\left[\bar{E}(t) - \bar{M}u(t)\right]\bar{E}(t) \tag{32}$$

where

$$\begin{cases} \psi(\tau) = \left[\dfrac{2}{T_{p2}^2} \quad \dfrac{2}{T_{p2}} \quad 1\right] \\ \bar{E}(t) = \left[\int_0^t e(\delta)d\delta \quad e(t) \quad \dot{e}(t)\right]^T \\ \bar{M} \end{cases} \quad (u) =$$

$$[\overline{00} \quad G_{u2}(x)]^T u(t)^{(k)}(t) = y_r^{(k)}(t) - L_f^k h(x), k = 0, 1$$

TABLE 1 Parameter values.

Parameter	Value
Generator rated power	1.5 Mw
Nominal voltage	690v
Nominal frequency	50 hz
Poles	2
Rotor resistance	0.021 Ω
Stator resistance	0.012 Ω
Rotor inductance	0.0137 H
Stator inductance	0.0137 H
Mutual inductance	0.0135 H
Coefficient of friction	0.0071
Moment of inertia	50 kg m^2
Turbine diameter	60 m
number of blades	3
hub height	85 m
Rayon	36.5 m
Gearbox	90
Filter resistance	1Ω
Filter inductance	30 mH
Capacitance	500 μF
Nominal voltage	500v

Replacing (32) in (23), the optimal control is calculated as

$$u(t) = -G_{u2}(x)^{-1}\left[K_{i2}\int_0^t \mathrm{e}(\delta)d\delta \;\; K_{p2}\mathrm{e}(t) \;\; K_{d2}\dot{\mathrm{e}}(t)\right] \quad (33)$$

where $K_{i2} = \frac{2}{T_{p2}^2}, K_{p2} = \frac{2}{T_{p2}}, K_{d2} = 1$

Closed-loop system stability

The convergence of the output tracking error to the origin can be used to demonstrate the closed-loop system's stability. Substituting control law (33) into Equation 31 yields

$$K_{i2}\int_0^t e(\delta)d\delta + K_{p2}e(t) + K_{d2}\dot{e}(t) = 0 \quad (34)$$

where K_p is the proportional gain, K_i is the integral gain, and K_d is the derivative gain.

As a result of (34), the closed loop system's characteristic polynomial equation is given as

$$K_{d2}s^2 + K_{p2}s + K_{i2} = 0 \quad (35)$$

Computing the solutions of Equation 35 may be used to determine the stability condition that is given as follows:

$$s_{1,2} = \frac{-1 \pm j}{T} \quad (36)$$

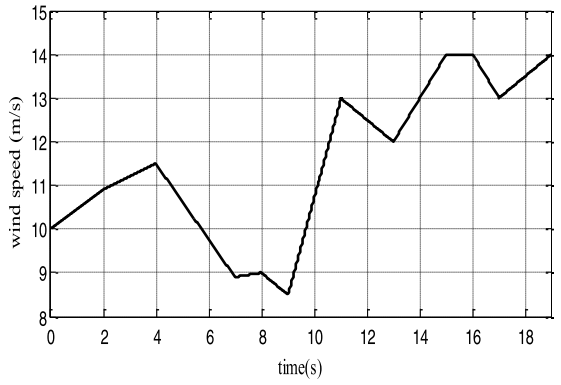

FIGURE 5
Wind speed profile.

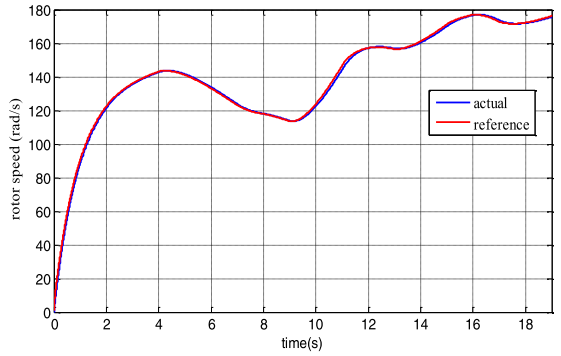

FIGURE 6
Rotor speed response.

The true parts of the roots (36) are positive because the predicted time T is positive can be proven to be negative.

Simulation results

The operation performance of the DFIG wind system and control scheme has been investigated using Matlab/Simulink software. Table 1 lists the system's parameters. The prediction horizon is set to T_{p1} = 0.5 ms (inner loop) and T_{p2} = 5 ms (outer loop). Figure 5 depicts the wind speed profile utilized in the simulation.

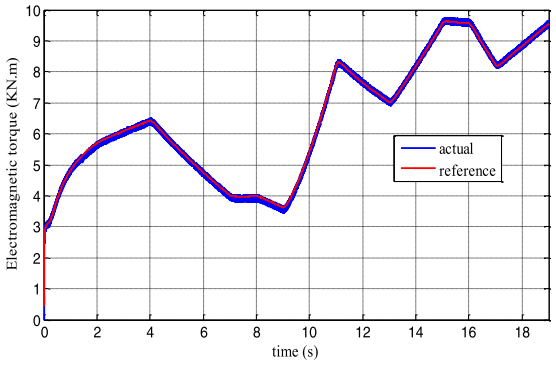

FIGURE 7
Electromagnetic torque.

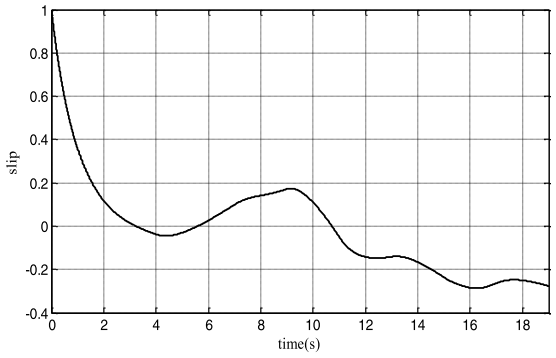

FIGURE 8
DFIG slip.

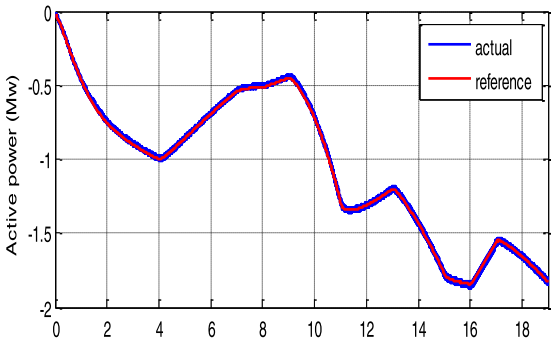

FIGURE 9
DFIG active power.

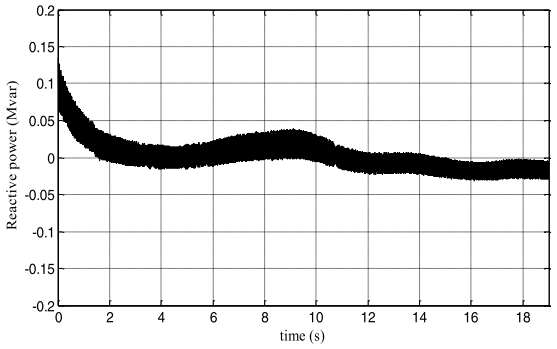

FIGURE 10
DFIG reactive power.

Reference tracking test performance

Figures 6, 7 show that the rotor speed and electromagnetic torque follow their references correctly and with good performance. Figure 8 depicts the DFIG slip's'. As a consequence, in Figure 9, the DFIG active power flawlessly tracks its reference to enhance the conversion efficiency. From Figure 10, it can be noticed that the DFIG reactive power is kept at zero, which helps to adjust for the grid power factor. The rotor voltage-current at sub-synchronous ($s > 0$), synchronous ($s = 0$), and hyper-synchronous modes ($s < 0$) is plotted in Figure 11. These results clearly show that the proposed RNGPC algorithm provides great performance in both steady state and dynamic modes.

Robustness under DFIG's parameter and prediction horizon variations

The values for the parameter variations included in the DFIG model are as follows: 10% in the coefficient of friction at t = 7s and 25% in the rotor resistance at t = 10s. This test is also used to assess the controller's performance when the prediction horizon is changed. Only the outer loop Tp_2 prediction horizon is lowered from 15 ms to 1.5 ms. These variations are not taken into account in the controller.

Figures 12, 13 show that despite the DFIG's parameter fluctuation, the system response converges to the reference values. Indeed, the speed and the electromagnetic torque track perfectly their references. From Figures 14, 15, the control effort is limited by the speed filter; thus, a smaller prediction horizon results in faster disturbance rejection.

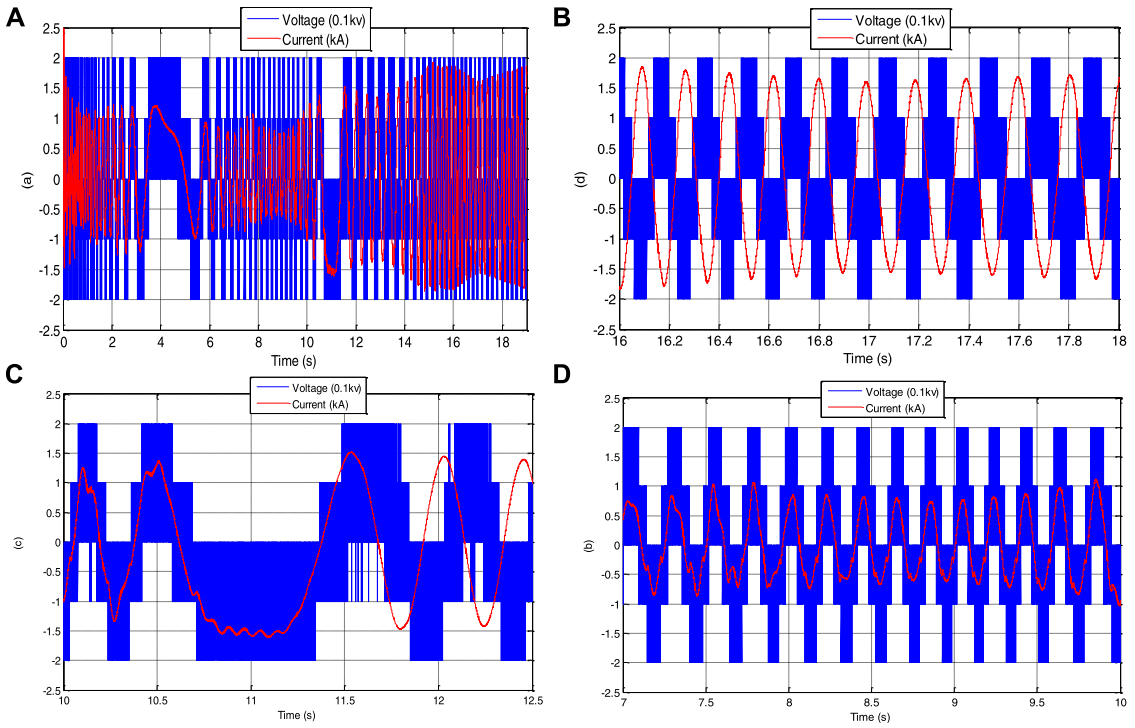

FIGURE 11
(A) Rotor voltage and current, **(B)** sub-synchronous mode, **(C)** synchronous mode, and **(D)** super-synchronous mode.

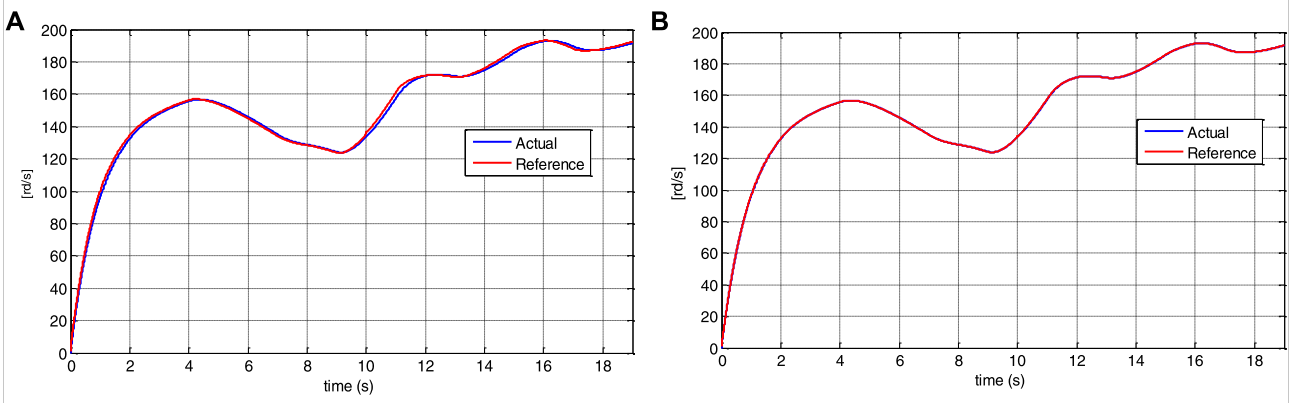

FIGURE 12
Speed tracking underprediction horizon change: **(A)** for T_{p2} = 15 ms and **(B)** for T_{p2} = 1.5 ms.

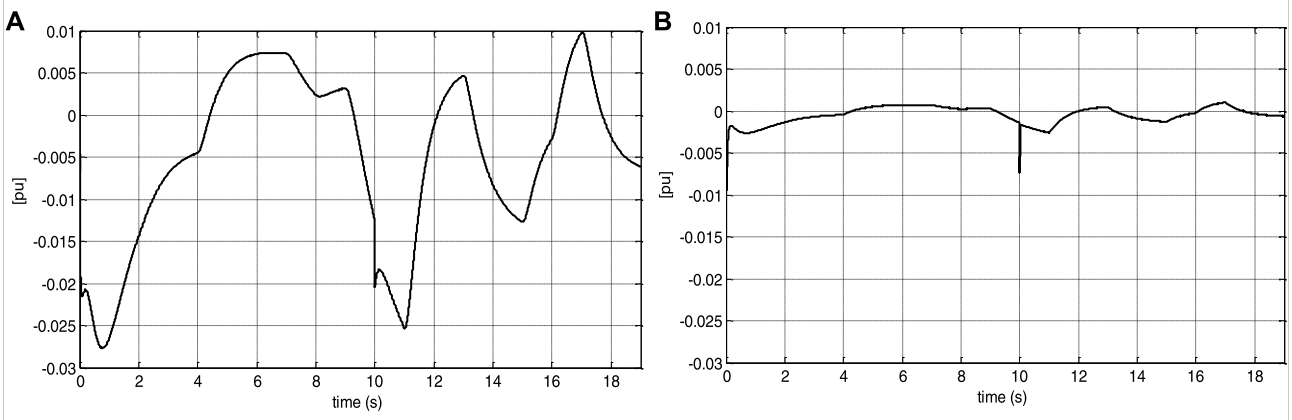

FIGURE 13
Speed tracking error under prediction horizon change: **(A)** for T_{p2} = 15 ms and **(B)** for T_{p2} = 1 ms.

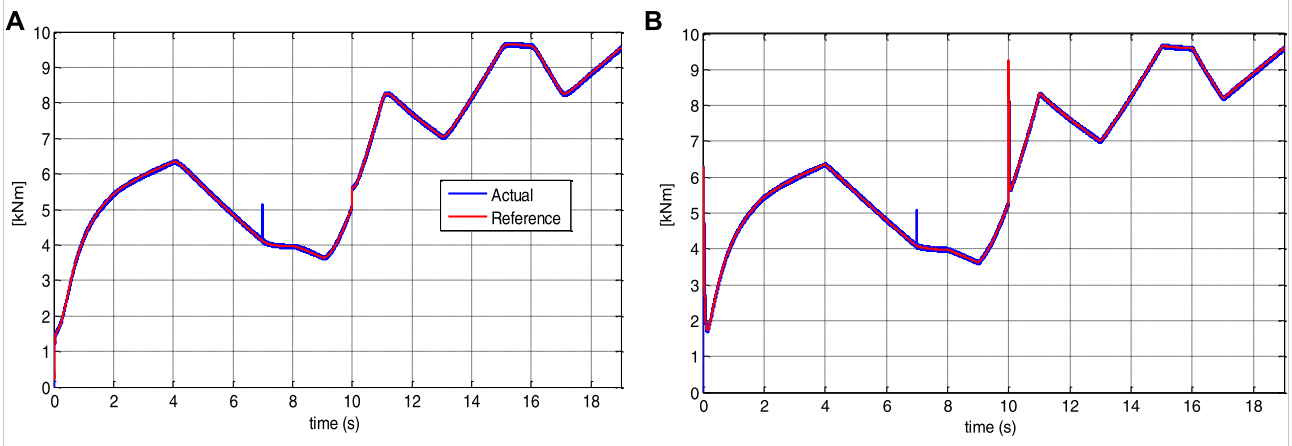

FIGURE 14
Electromagnetic torque tracking underprediction horizon change: **(A)** for T_{p2} = 15 ms and **(B)** for T_{p2} = 1.5 ms.

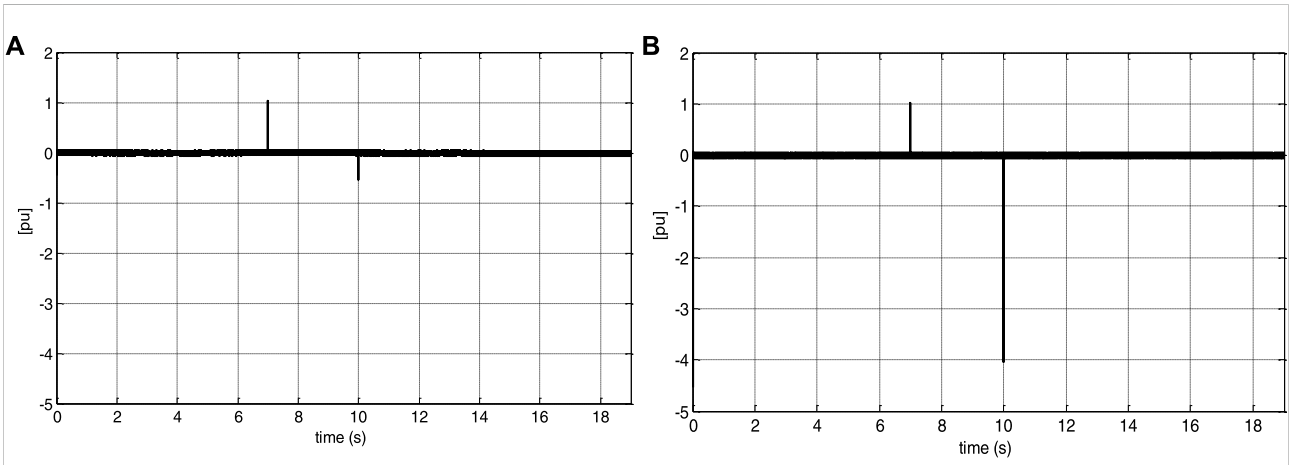

FIGURE 15
Electromagnetic torque tracking error underprediction horizon change: **(A)** for T_{p2} = 15 ms and **(B)** for T_{p2} = 1.5 ms.

Conclusion

A robust nonlinear generalized predictive controller for a DFIG wind turbine system has been devised in this study. A novel finite horizon cost function is introduced into the control law to ensure robustness against aerodynamic torque and parameter fluctuations without the necessity for an aerodynamic torque observer. The active power delivered to the grid varies with wind speed and follows the optimal wind power precisely. The simulation results show that the control architecture is resistant to unknown aerodynamic torques. This supports the suggested control's efficiency and dependability in tracking the projected references. The RNGPC's efficacy and resilience are confirmed by simulation results under a variety of operating conditions and DFIG parameter variations.

Data availability statement

The raw data supporting the conclusions of this article will be made available by the authors, without undue reservation.

Author contributions

All authors listed have made a substantial, direct, and intellectual contribution to the work and approved it for publication.

Conflict of interest

The authors declare that the research was conducted in the absence of any commercial or financial relationships that could be construed as a potential conflict of interest.

Publisher's note

All claims expressed in this article are solely those of the authors and do not necessarily represent those of their affiliated organizations or those of the publisher, the editors, and the reviewers. Any product that may be evaluated in this article or claim that may be made by its manufacturer is not guaranteed or endorsed by the publisher.

References

Aguilar, M. E. B., Coury, D. V., Reginatto, R., and Monaro, R. M. (2020). Multi-objective PSO applied to PI control of DFIG wind turbine under electrical fault conditions. *Electr. Power Syst. Res.* 180, 106081. doi:10.1016/j.epsr.2019.106081

Belkhier, Y., Achour, A., Ullah, N., and Shaw, R. N. (2022). Modified passivity-based current controller design of permanent magnet synchronous generator for wind conversion system. *Int. J. Model. Simul.* 42 (2), 192–202. doi:10.1080/02286203.2020.1858226

Beltran-Pulido, A., Cortes-Romero, J., and Coral-Enriquez, H. (2018). Robust active disturbance rejection control for LVRT capability enhancement of DFIG-based wind turbines. *Control Eng. Pract.* 77, 174–189. doi:10.1016/j.conengprac.2018.06.001

El Daoudi, S., Lazrak, L., El Ouanjli, N., and Ait Lafkih, M. (2021). Applying sliding mode technique for the nonlinear DTC-SPWM control strategy of sensorless squirrel cage asynchronous motor. *Int. J. Dyn. Control* 9 (4), 1633–1644. doi:10.1007/s40435-021-00758-8

Evangelista, C. A., Pisano, A., Puleston, P., and Usai, E. (2016). Receding horizon adaptive second-order sliding mode control for doubly-fed induction generator based wind turbine. *IEEE Trans. Control Syst. Technol.* 25 (1), 73–84. doi:10.1109/tcst.2016.2540539

Gupta, S., and Shukla, A. (2022). Improved dynamic modelling of DFIG driven wind turbine with algorithm for optimal sharing of reactive power between converters. *Sustain. Energy Technol. Assessments* 51, 101961. doi:10.1016/j.seta.2022.101961

Liu, Y., Wang, Z., Xiong, L., Wang, J., Jiang, X., Bai, G., et al. (2018). DFIG wind turbine sliding mode control with exponential reaching law under variable wind speed. *Int. J. Electr. Power & Energy Syst.* 96, 253–260. doi:10.1016/j.ijepes.2017.10.018

Mahmoud, M. S., and Oyedeji, M. O. (2019). Adaptive and predictive control strategies for wind turbine systems: A survey. *IEEE/CAA J. Autom. Sin.* 6 (2), 364–378. doi:10.1109/jas.2019.1911375

Malik, M. Z., Baloch, M. H., Gul, M., Kaloi, G. S., Chauhdary, S. T., and Memon, A. A. (2021). A research on conventional and modern algorithms for maximum power extraction from wind energy conversion system: A review. *Environ. Sci. Pollut. Res.* 28 (5), 5020–5035. doi:10.1007/s11356-020-11558-6

Nosratabadi, S. M., Bornapour, M., and Gharaei, M. A. (2019). Grasshopper optimization algorithm for optimal load frequency control considering predictive functional modified PID controller in restructured multi-resource multi-area power system with redox flow battery units. *Control Eng. Pract.* 89, 204–227. doi:10.1016/j.conengprac.2019.06.002

Ouari, K., Ouhrouche, M., Rekioua, T., and Nabil, T. (2014). Nonlinear predictive control of wind energy conversion system using DFIG with aerodynamic torque observer. *J. Electr. Eng.* 65 (6), 333–341. doi:10.2478/jee-2014-0055

Ouari, K., Rekioua, T., and Ouhrouche, M. (2014). Real time simulation of nonlinear generalized predictive control for wind energy conversion system with nonlinear observer. *ISA Trans.* 53 (1), 76–84. doi:10.1016/j.isatra.2013.08.004

Pradhan, P. P., Subudhi, B., and Ghosh, A. (2022). A new optimal model predictive control scheme for a wind energy conversion system. *Int. J. Numer. Model.* 35 (3), e2976. doi:10.1002/jnm.2976

Schwenzer, M., Ay, M., Bergs, T., and Abel, D. (2021). Review on model predictive control: An engineering perspective. *Int. J. Adv. Manuf. Technol.* 117 (5), 1327–1349. doi:10.1007/s00170-021-07682-3

Soliman, M. S., Belkhier, Y., Ullah, N., Achour, A., Alharbi, Y. M., Al Alahmadi, A. A., et al. (2021). Supervisory energy management of a hybrid battery/PV/tidal/wind sources integrated in DC-microgrid energy storage system. *Energy Rep.* 7, 7728–7740. doi:10.1016/j.egyr.2021.11.056

Song, D., Li, Z., Wang, L., Jin, F., Huang, C., Xia, E., et al. (2022a). Energy capture efficiency enhancement of wind turbines via stochastic model predictive yaw control based on intelligent scenarios generation. *Appl. Energy* 312 (2022), 118773. doi:10.1016/j.apenergy.2022.118773

Song, D., Tu, Y., Wang, L., Jin, F., Li, Z., Huang, C., et al. (2022b). Coordinated optimization on energy capture and torque fluctuation of wind turbines via variable weight NMPC with fuzzy regulator. *Appl. Energy* 312 (2022), 118821. doi:10.1016/j.apenergy.2022.118821

Tamalouzt, S., Belkhier, Y., Sahri, Y., Bajaj, M., Ullah, N., Chowdhury, M., et al. (2021). Enhanced direct reactive power control-based multi-level inverter for DFIG wind system under variable speeds. *Sustainability* 13 (16), 9060. doi:10.3390/su13169060

Tamalouzt, S., Belkhier, Y., Sahri, Y., Ullah, N., Shaw, R.N., and Bajaj, N. (2022). New direct reactive power control based fuzzy and modulated hysteresis method for micro-grid applications under real wind speed, Energy Sources, Part A: Recovery, Utilization, and Environmental Effects. 44:2, 4862–4887. doi:10.1080/15567036.2022.2081741

Wang, H., and Li, Z. S. (2022). Multi-Area load frequency control in power system integrated with wind farms using fuzzy generalized predictive control method. *IEEE Trans. Reliab.*, 1–11. doi:10.1109/tr.2022.3177045

Xiong, L., Li, P., Wu, F., Ma, M., Khan, M. W., and Wang, J. (2019). A coordinated high-order sliding mode control of DFIG wind turbine for power optimization and grid synchronization. *Int. J. Electr. Power & Energy Syst.* 105, 679–689. doi:10.1016/j.ijepes.2018.09.008

Younesi, A., Tohidi, S., and Feyzi, M. R. (2022). An improved long-horizon model predictive control for DFIG in WECS with variable sampling-time. *IET Renew. Power Gen.* 16 (3), 517–531. doi:10.1049/rpg2.12357

Zhang, H., Hao, J., Wu, C., Li, Y., and Sahab, A. (2019). A novel LMI-based robust adaptive model predictive control for DFIG-based wind energy conversion system. *Syst. Sci. Control Eng.* 7 (1), 311–320. doi:10.1080/21642583.2019.1663291

Zhang, Y., Jiao, J., Xu, D., Jiang, D., Wang, Z., and Tong, C. (2019). Model predictive direct power control of doubly fed induction generators under balanced and unbalanced network conditions. *IEEE Trans. Ind. Appl.* 56 (1), 771–786. doi:10.1109/tia.2019.2947396

Zhou, C., Wang, Z., Xin, H., and Ju, P. (2021). A PQ coordination based model predictive control for dfig high-voltage ride through. *IEEE Trans. Energy Convers.* 37, 254–263. doi:10.1109/tec.2021.3088464

Nomenclature

$\boldsymbol{\Omega_t}$ $\boldsymbol{\Omega_r}$ Turbine, generator speed (rd/s)

$\boldsymbol{T_t, T_r}$ Aerodynamic and generator torque(N.m)

$\boldsymbol{\Omega_{r\text{-}ref}}$ Reference generator speed

G Gear ratio

$\boldsymbol{P_{grid\ \text{-}ref}}$ Reference grid active power (W)

η System (wind turbine + DFIG) efficiency

$\boldsymbol{P_r}$, $\boldsymbol{Q_r}$ Active and reactive rotor power (W,Var)

$\mathbf{V_s}$ Stator voltages (v)

$\mathbf{R_r}$, $\mathbf{L_r}$ Per-phase rotor resistance and self-inductance

M, P Mutual inductance, number of pole pairs

$\boldsymbol{J}$, $\boldsymbol{f_r}$ Moment of inertia, coefficient of friction

s,σ Generator slip and dispersion ratio

$\mathbf{T_p}$ Predictive time

ρ_1 Relative degree of output i

frontiers | Frontiers in Energy Research

TYPE Original Research
PUBLISHED 28 September 2022
DOI 10.3389/fenrg.2022.966975

OPEN ACCESS

EDITED BY
Dongran Song,
Central South University, China

REVIEWED BY
Jian Yang,
Central South University, China
Rizk Masoud,
University of Menoufia, Egypt

*CORRESPONDENCE
Elmazeg Elgamli,
Elgamlies@cardiff.ac.uk

SPECIALTY SECTION
This article was submitted to Smart Grids,
a section of the journal
Frontiers in Energy Research

RECEIVED 12 June 2022
ACCEPTED 12 July 2022
PUBLISHED 28 September 2022

CITATION
Jaiswal A, Belkhier Y, Chandra S, Priyadarshi A, Bajaj M, Pushkarna M, Elgamli E, Shouran M and Kamel S (2022), Design and implementation of energy reshaping based fuzzy logic control for optimal power extraction of PMSG wind energy converter.
Front. Energy Res. 10:966975.
doi: 10.3389/fenrg.2022.966975

Design and implementation of energy reshaping based fuzzy logic control for optimal power extraction of PMSG wind energy converter

Ashish Jaiswal[1], Youcef Belkhier[2], Subhash Chandra[1], Anurag Priyadarshi[1], Mohit Bajaj[3], Mukesh Pushkarna[1], Elmazeg Elgamli[4]*, Mokhtar Shouran[4] and Salah Kamel[5]

[1]Department of Electrical Engineering, GLA University Mathura, Mathura, India, [2]Centre for Ocean Energy Research, Maynooth University, Maynooth, Kildare, [3]Department of Electrical Engineering, Graphic Era (Deemed to be University), Dehradun, India, [4]Wolfson Centre for Magnetics, School of Engineering, Cardiff University, Cardiff, United Kingdom, [5]Department of Electrical Engineering, Faculty of Engineering, Aswan University, Aswan, Egypt

Given the greater penetration of wind power, the impact of wind generators on grid electricity reliability imposes additional requirements. One of the most common technologies in wind power generating schemes is the permanent magnet synchronous generator (PMSG) converter. However, the controller calculation is difficult due to the nonlinear dynamical and time-varying characteristics of this type of conversion system. This study develops a unique intelligent controller approach based on the passivity notion that tracks velocity and maintains it functioning at the optimum torque. To address the robustness issues encountered by traditional generator-side converter (MSC) strategies such as proportional-integral (PI), this suggested scheme integrates a passivity-based procedure with a fuzzy logic control (FLC) methodology for a PMSG-based wind power converter. The suggested controller is distinguished by the fact that the nonlinear features are compensated in a damped manner rather than canceled. To achieve the required dynamic, the fuzzy controller is used, which ensures quick convergence and global stability of the closed loop system. The development of the maximum power collected, the lowered fixed gains, and the real-time application of the control method are the primary contributions and novelties. The primary objectives of this project are to manage DC voltage and attain adequate reactive power levels in order to provide dependable and efficient electricity to the grid. The proposed scheme is being used to regulate the MSC, while the grid-side employs a traditional proportional-integral method. The efficiency of the suggested technique is investigated numerically using MATLAB/Simulink software. Furthermore, the processor-in-the-loop (PIL) tests are carried out to demonstrate that the suggested regulator is practically implementable.

KEYWORDS

renewable energy systems, fuzzy logic control, processor-in-the loop (PIL) experiments, nonlinear control, power extraction

Introduction

Sustainable energy source innovations are turning into an expanding option to address the issues of environmental change. One of the most promising types of renewable energy is wind energy. Wind power has been in full industrial growth for some years. Indeed, it has several advantages: first and foremost, it is a non-polluting renewable energy source that helps to improve air quality and the reduction of greenhouse gas emissions. It is also a form of energy that makes use of domestic resources and so helps to energy independence and supply security, its high-power density, and a high potential for electricity generation (Soliman et al., 2021). The role of a wind turbine is to convert the kinetic energy of the wind into electrical energy. Its various elements are designed to maximize this energy conversion. There are several technologies that are used to capture the energy of the wind (vertical axis or horizontal axis), and also, different configurations of a wind turbine system (fixed speed and variable speed). Therefore, wind turbines are considered with variable power generators, connected to the electrical grid. The amount of energy recovered by variable speed wind energy conversion systems (VS-WECS) depends on the accuracy of the maximum power point tracking (MPPT) search and also on the type of generator used. The associated power conversion chains often use a PMSG (Soliman et al., 2021), (Mohammadi et al., 2019). This type of machine allows making it possible to get rid of the problem of the excitation current supply, which is difficult to manage in a conventional synchronous machine (Mohammadi et al., 2019). However, due to unknown modeling inaccuracy, dynamic characteristics, and non-linearities, control system computation for the PMSG remains a difficult task (Wang and Wang, 2020). In the literature, there has been several research studies related to the nonlinear control of PMSG. In the study by Saidi et al. (2019), a tip-speed ratio technique associated with an integral backstepping controller is suggested. A mechanical sensorless control strategy-based nonlinear observer is proposed (Fantino et al., 2016). In the work of Zargham and Mazinan (2019), a super-twisting sliding mode controller is designed. A new direct torque of a fault-tolerant direct-driven PMSG controller is developed (Jlassi and Cardoso, 2019). To achieve direct power control, an optimal voltage vector-based modulated model predictive control is developed in Bigarelli et al. (2020). Further, in the study by Haq et al. (2020), a maximum power extraction-based feed-forward neural network and generalized global sliding mode controller are investigated. Meanwhile, an autonomous PMSG-based wind conversion system is controlled by using a cascade neural networks algorithm (Chandrasekaran et al., 2020). More recently, a nonlinear model predictive control with the fuzzy regulator is proposed in Song et al. (2022a), for the optimization of the energy capture and torque fluctuation of wind turbines. In the study by Song et al. (2022b), a stochastic model predictive yaw control strategy based on intelligent scenario generation is proposed to improve the energy capture efficiency of wind energy converters. A chaos-opposition-enhanced slime mould algorithm to minimize energy cost for the wind turbines on high-altitude sites is developed in Rizk-Allah et al. (2022), the proposed model is established based on rotor radius, rated power, and hub height needed to achieve an optimal design model. However, as stated in Yang et al. (2013), most of such controls are dependent on signals and therefore do not consider the structural properties of the PMSG when building the regulator.

The present article investigates a new control approach based on the passivity notion, a new fuzzy passivity-based control (PBC) to design an optimal controller for the PMSG, which tracks speed and maintains it functioning at the optimal torque. Inherent advantages of the PBC method are that the nonlinear terms are adjusted in a damped manner rather than being eliminated that the assured stability, as well as the promised robustness qualities (Nicklasson et al., 1994), (Belkhier et al., 2022). The study's major goal is to highlight a hybrid control method for VS-WECS, to enable efficient power integration to the grid and increase the PMSG operational speed.

Several techniques have been reported in the literature based on the passivity control method to improve the performance of the PMSG and increase the efficiency of wind energy conversion systems. A sliding mode strategy (SMC) associated with PBC is adopted in Yang et al. (2018a). However, as the authors point out, the provided coupled PBC-SMC controlling employs over six fixed gains, making it hard to find their ideal settings. A passivity-based linear feedback current control approach is developed for a PMSG in Belkhier and Achour (2020a), where the authors proposed PBC with an orientation of the flux, where the desired current is computed by a PI controller. However, the use of the PI implies fixed gains, which brings a significant sensitivity to disturbances that can affect the functioning of the system. In Subramaniam and Joo (2019), a PBC-SMC and fuzzy controller is proposed. However, the suggested combined strategy's controller design is complex due to mathematical constraints; passivity-based linear feedback control is explored in Yang et al. (2018b). However, nonlinear properties and the robustness due to parameter changes of the PMSG have not been evaluated. In Belkhier and Achour (2020b), a passivity-based backstepping is proposed. However, due to mathematical limitations, the controller design of the proposed combination method is complicated.

As it was mentioned before, several aspects were neglected by the works carried out. In order to make more improvements and

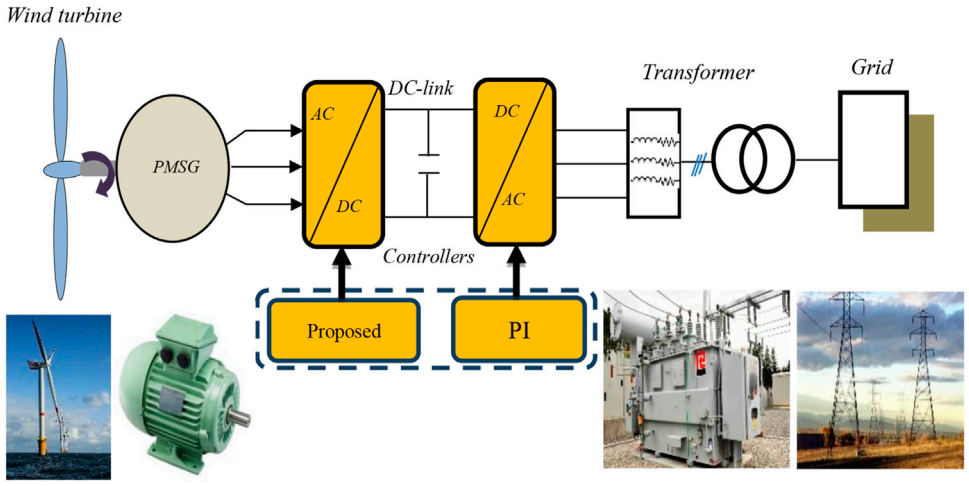

FIGURE 1
Wind power system.

contributions to what was performed. The present work is split into two sections. First, a fuzzy-PBC system is used to ensure that the PMSG receives continuous power from the wind source, increase the PMSG operational speed, and rectify non-linearities, external disturbances, and parametric fluctuations in the PMSG. The second is devoted to applying the classical PI control to regulating the grid-side power and voltage. A special focus is given to the control of the PMSG, by synthesizing the new suggested control scheme while considering the complete dynamic of the PMSG. In addition, the resilience over parameter variations has received considerable consideration. Also, experimental testing of the investigated strategy is conducted using a DSP card, and the results show clearly that the present system is applicable practically.

The contribution and novelty of the present article are summarized as follows:

- A novel control technique based on hybrid fuzzy-PBC for optimum efficiency of the PMSG is presented to ensure a quick convergence of the locked system and energy extraction.
- By simulating the unstructured dynamics of the PMSG, the fuzzy manager is employed for gain adjustment, which meets the requirements produced by incorrect variables to calculate the appropriate dynamics and considerably enhances the resilience of the system.
- Numerous numerical studies are conducted to show how resilient the suggested technique is to parameter changes and outside disruptions. In addition, analytical proof of the closed-stability loop's and exponential convergence has been provided.
- The novelty of the proposed control lies in its structure, which is really very simple and contains only one fixed gain, which is the damping gain of the control, which makes it particularly robust and increases resilience and global stability, as demonstrated in the results section.
- Experimental validation of the proposed control schemes is conducted using processor-in-the loop (PIL) and the results show clearly that the present system is applicable practically.

The current article is arranged in the following manner: *Introduction* establishes the system description. The proposed strategy calculation is discussed in *Introduction*. Concerning *Introduction*, grid-side converter (GSC) voltage and management is presented. In *Introduction*, simulation experimental results are exposed. Finally, *Introduction* finishes with the main findings and recommendations for future research.

System description

Figure 1 shows the setup of the MATLAB/Simulink-based wind energy converter, which includes a wind turbine, PMSG, AC-DC-AC converter, and main electrical network.

Wind power

The wind energy converter model is represented as follows (Fantino et al., 2016; Belkhier et al., 2020):

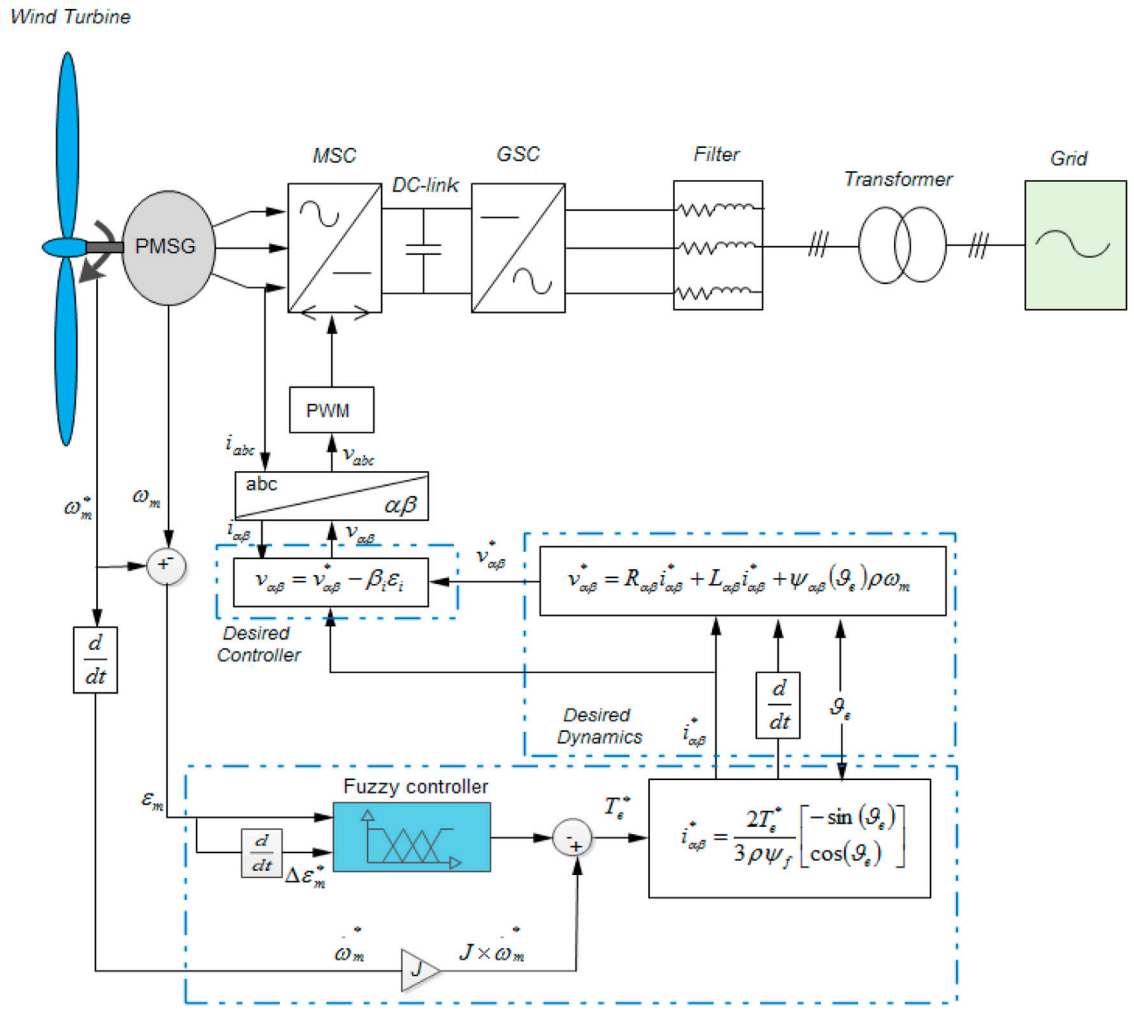

FIGURE 2
Schematic of the proposed controller.

$$P_m = \frac{1}{2}\rho C_p(\beta,\lambda)Av_s^3, \tag{1}$$

$$T_m = \frac{P_m}{\omega_t}, \tag{2}$$

$$C_p(\beta,\lambda) = 0.5\left(\frac{116}{\lambda_i} - 0.4\beta - 5\right)e^{-\left(\frac{21}{\lambda_i}\right)}, \tag{3}$$

$$\lambda_i^{-1} = (\lambda + 0.08\beta)^{-1} - 0.035(1+\beta^3)^{-1}, \tag{4}$$

$$\lambda = \frac{\omega_t R}{v_s}, \tag{5}$$

where P_m depicts the wind power captured, T_m is the wind turbine output torque, A depicts the blades' area, ρ is fluid density, λ is speed ratio, v_s denotes the wind speed, β depicts pitch angle, ω_t depicts turbine speed, R is the blades' radius, and C_p is power coefficient.

Permanent magnet synchronous generator modeling

The PMSG modeling according to αβ-frame is needed to design the proposed technique, which is formulated as (Soliman et al., 2021; Belkhier et al., 2022):

$$L_{\alpha\beta}\frac{di_{\alpha\beta}}{dt} + \psi_{\alpha\beta}(\theta_e)p\omega_m = v_{\alpha\beta} - R_{\alpha\beta}i_{\alpha\beta}, \tag{6}$$

$$C\frac{d\omega_m}{dt} = T_m - T_e\left(i_{\alpha\beta},\theta_e\right) - f_{fv}\omega_m, \tag{7}$$

$$T_e\left(i_{\alpha\beta},\theta_e\right) = \psi_{\alpha\beta}^T(\theta_e)i_{\alpha\beta}, \tag{8}$$

where p denotes the pair pole numbers, J represents the moment of the inertia, $i_{\alpha\beta} = \begin{bmatrix} i_\alpha \\ i_\beta \end{bmatrix}$ indicates the current, T_e indicates electromagnetic torque, $L_{\alpha\beta} = \begin{bmatrix} L_\alpha & 0 \\ 0 & L_\beta \end{bmatrix}$ indicates induction's

stator, f_{fv} indicates viscosity parameter, θ_e indicates electrical angular, $v_{\alpha\beta} = \begin{bmatrix} v_\alpha \\ v_\beta \end{bmatrix}$ indicates stator's voltage, $R_{\alpha\beta} = \begin{bmatrix} R_S & 0 \\ 0 & R_s \end{bmatrix}$ indicates the resistance, $\psi_{\alpha\beta}(\theta_e) = \psi_f \begin{bmatrix} -\sin(\theta_e) \\ \cos(\theta_e) \end{bmatrix}$ indicates linkages' flux, and ω_m indicates motor speed.

Proposed controller computation

Several stages must be validated in order to build the developed technique: at first, the passivity attribute of the PMSG model must be demonstrated so that the suggested approach may be used. Second, the PMSG must be broken down into two passive subsystems with negative feedback. Finally, in order to construct a controller with a simple structure, the non-dissipative variables in the PMSG model must be formulated. Figure 2 depicts the explored strategy computing process, which has two distinct components: the first phase consists in designing the reference current using the computed electromagnetic torque and the high order sliding mode control (HSMC) technique, and the needed current is subsequently calculated using the required torque. In the second portion, the controller law is computed using the created method-based HSMC.

PMSG αβ-model interconnected subsystems decomposition

From Eq. 6, the following relationship is formulated:

$$\sum_e : V_e = \begin{bmatrix} v_{\alpha\beta} \\ -\omega_m \end{bmatrix} \rightarrow Y_e = \begin{bmatrix} i_{\alpha\beta} \\ T_m \end{bmatrix}. \tag{9}$$

From Eqs 7, 8, the following relationship is formulated:

$$\sum_m : V_m = (-T_e + T_m) \rightarrow Y_e = -\omega_m = \frac{(-T_e + T_m)}{Js + f_{fv}}. \tag{10}$$

According to (9) and (10) the upcoming lemma is yield:

Lemma 1: *according to the aforementioned conditions, the PMSG in the dq-model can be decomposed into feedback interconnected two passive subsystems, electrical subsystem* $\sum_e$ *and mechanical subsystem* $\sum_m$.

Proof: from (9), the following PMSG total energy H_e is given as:

$$H_e = \frac{1}{2} i_{\alpha\beta}^T L_{\alpha\beta} i_{\alpha\beta} + \psi_{\alpha\beta}^T i_{\alpha\beta}. \tag{11}$$

The time derivative of H_e along (6), yields:

$$\dot{H}_e = -i_{\alpha\beta}^T R_{\alpha\beta} i_{\alpha\beta} + Y_e^T V_e + \frac{d}{dt}\left(\psi_{\alpha\beta}^T i_{\alpha\beta}\right). \tag{12}$$

Integrating on both sides of (12) along $[0 \quad T_e]$, gives:

$$\underbrace{H_e(T_e) - H_e(0)}_{Stored\ Energy} = -\underbrace{\int_0^{T_e} i_{\alpha\beta}^T R_{\alpha\beta} i_{\alpha\beta} d\tau}_{Dissipated\ Energy} + \underbrace{\int_0^{T_e} Y_e^T V_e d\tau + \left[\psi_{\alpha\beta}^T i_{\alpha\beta}\right]_0^{T_e}}_{Supplied\ Energy}. \tag{13}$$

Here, $H_e(T_e) \geq 0$ and $H_e(0)$ indicate stored energy initially. By Increasing Eq. 13, the following inequality dissipation is formulated:

$$\int_0^{T_e} Y_e^T V_e d\tau \geq \lambda_{min}\{R_{\alpha\beta}\} \int_0^{T_e} \left\| i_{\alpha\beta} \right\|^2 d\tau - \left(H_e(0) + \left[\psi_{\alpha\beta}^T i_{\alpha\beta}\right]_0^{T_e}\right), \tag{14}$$

where $\|.\|$ indicates Euclidian norm's vector.

It is clearly indicated that $\sum_e$ is passive. Then, from $\sum_m$, the transfer function $F_m(s)$ is deduced and formulated as:

$$\mathrm{F}_m(s) = \frac{\mathrm{Y}_m(s)}{\mathrm{V}_m(s)} = \frac{1}{\mathrm{J}s + f_{fv}}. \tag{15}$$

It can be deduced that $\sum_m$ is passive, since $\mathbf{F}_m(s)$ is strictly positive. Thus, the PMSG model is decomposable into two passive subsystems.

PMSG passivity property

Lemma 2: *the model (6)–(8) is passive, when* $Y = [v_{\alpha\beta}^T, T_e]^T$ *and* $X = [i_{\alpha\beta}^T, \omega_m]^T$ *are chosen as the PMSG outputs and inputs,* respectively.

Proof: first, the PMSG Hamiltonian H_m is defined as:

$$H_m\left(i_{\alpha\beta}, \omega_m\right) = \underbrace{\frac{1}{2} i_{\alpha\beta}^T L_{\alpha\beta} i_{\alpha\beta} + \frac{1}{2} i_{\alpha\beta}^T L_{\alpha\beta} i_{\alpha\beta}}_{Electrical\ Energy} + \underbrace{\frac{1}{2} J\omega_m^2}_{Mecanical\ Energy}. \tag{16}$$

Derivative along (6)–8) of H_m, gives:

$$\frac{dH_m\left(i_{\alpha\beta}, \omega_m\right)}{dt} = -\frac{d\left(i_{\alpha\beta}^T R\, i_{dq}\right)}{dt} + y^T v + \frac{d}{dt}\left(\psi_{\alpha\beta}^T i_{\alpha\beta}\right), \tag{17}$$

where $R = \mathrm{diag}\{R_{\alpha\beta}, f_{fv}\}$. Integrating (17) along $[0 \ T_m]$, gives:

$$\underbrace{H_m(T_m) - H_m(0)}_{Stored\ Energy} = -\underbrace{\int_0^{T_m} i_{\alpha\beta}^T R\, i_{\alpha\beta}\, d\tau}_{Dissipated\ Energy} + \underbrace{\int_0^{T_m} y^T v\, d\tau + \left[\psi_{\alpha\beta}^T i_{\alpha\beta}\right]_0^{T_m}}_{Supplied\ Energy}, \tag{18}$$

where $H_m(0)$ is the stored initial energy and $H_m(T_m) \geq 0$. Integrating (18) yields:

$$\int_0^{T_m} y^T v\, d\tau \geq \lambda_{\min}\{R\} \int_0^{T_m} \left\| i_{\alpha\beta} \right\|^2 d\tau - \left(H_m(0) + \left[\psi_{\alpha\beta}^T i_{\alpha\beta}\right]_0^{T_m}\right). \tag{19}$$

Then, relationship M is passive, which is the same for the PMSG.

Controller law design process

According to the model (6)–(8), one can formulate the reference dynamics given as follows:

$$v^*_{\alpha\beta} = L_{\alpha\beta}\frac{di^*_{\alpha\beta}}{dt} + \psi_{\alpha\beta}(\theta_e)p\omega_m + R_{\alpha\beta}i^*_{\alpha\beta}, \tag{20}$$

$$T_m = J\frac{d\omega^*_m}{dt} - T^*_e\left(i^*_{\alpha\beta}, \theta_e\right) - f_{fv}\omega^*_m, \tag{21}$$

where $i^*_{\alpha\beta}$ represents the reference current, $v^*_{\alpha\beta}$ represents the reference voltage, ω^*_m denotes speed of the turbine, and T^*_e denotes the reference torque. To ensure zero error convergence of between the reference and the measured dynamics, it is aimed to compute $v_{\alpha\beta}$. Thus, the error between the desired model (20)–(21) and the measured model (6)–(8) is formulated as:

$$v_{\alpha\beta} - v^*_{\alpha\beta} = L_{\alpha\beta}\frac{d\varepsilon_i}{dt} + R_{\alpha\beta}\left(i^*_{\alpha\beta} - i_{\alpha\beta}\right) \tag{22}$$

$$J\frac{d\omega^*_m}{dt} - T^*_e\left(i^*_{\alpha\beta}, \theta_e\right) - f_{fv}\left(\omega^*_m - \omega_m\right) = 0. \tag{23}$$

Let us define the function $V^*_f(\varepsilon_i)$, which represents the reference energy given as:

$$V^*_f(\varepsilon_i) = \frac{1}{2}\varepsilon_i^T\left(L_{\alpha\beta}\varepsilon_i\right), \tag{24}$$

where $\varepsilon_i = (i^*_{\alpha\beta} - i_{\alpha\beta})$ denotes the tracking error of the current. Derivative of $V^*_f(\varepsilon_i)$ along (22), gives:

$$\dot{V}^*_f(\varepsilon_i) = -\varepsilon_i^T\left(R_{\alpha\beta}\varepsilon_i + \left(v_{\alpha\beta} - v^*_{\alpha\beta}\right)\right). \tag{25}$$

Thus, the controller law is deduced as follows:

$$v_{\alpha\beta} = v^*_{\alpha\beta} - B_i\varepsilon_i, \tag{26}$$

where $B_i = b_i I_2$ and I_2 denotes the matrix identity.

Remark 2: the term $B_i\varepsilon_i$ expressed by Eq. 26 represents the damping term which is injected to make the PMSG strictly passive, where a suitable choice of the gain b_i permits to matrix B_i to improves the tracking error convergence and addresses the parameter disturbances faced by the closed loop.

The proof of the convergence is given as follows:

Considering Eq. 25, where according to $L_{\alpha\beta}$ and the Rayleigh, it yields the inequality given as follows:

$$0 \le \lambda_{\min}\left\{L_{\alpha\beta}\right\}\|\varepsilon_i\|^2 \le V^*_f(\varepsilon_i) \le \lambda_{\max}\left\{L_{\alpha\beta}\right\}\|\varepsilon_i\|^2, \tag{27}$$

where $\lambda_{\max}\{L_{\alpha\beta}\}$ and $\lambda_{\min}\{L_{\alpha\beta}\}$ denotes maximum and minimum eigenvalues of $L_{\alpha\beta}$.

According to dissipation term $R_{\alpha\beta} + B_i$ and the Rayleigh quotient, the derivative of (28) along (26) and (27) yields the inequality given as follows:

$$\dot{V}^*_f(\varepsilon_i) = -\varepsilon_i^T\left(R_{\alpha\beta} + B_i\right)\varepsilon_i \le -\lambda_{\min}\left\{R_{\alpha\beta} + B_i\right\}\|\varepsilon_i\|^2, \ \forall t \ge 0, \tag{29}$$

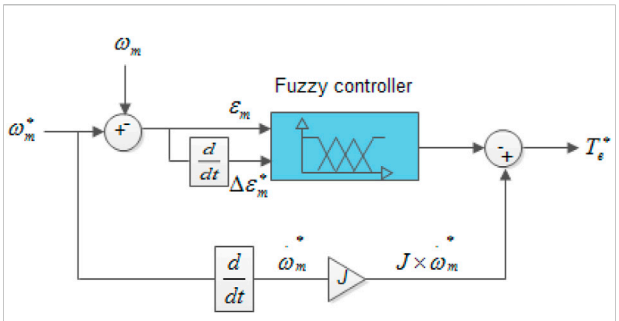

FIGURE 3
Desired torque computation.

where $\lambda_{\min}\{R_{\alpha\beta} + B_i\} > 0$ denotes minimum eigenvalue of the matrix $R_{\alpha\beta} + B_i$.

From (28) and (29), it yields:

$$\dot{V}^*_f(\varepsilon_i) = -r_1 V^*_f(\varepsilon_i), \tag{30}$$

where $r_1 = \frac{\lambda_{\min}\{R_{\alpha\beta}+B_i\}}{\lambda_{\max}\{L_{\alpha\beta}\}} > 0$.

Integrating (30), yields:

$$\dot{V}^*_f(\varepsilon_i) \le V^*_f(0)e^{-r_1 t}. \tag{31}$$

From (28) and (31), we get:

$$\|\varepsilon_i\| \le r_2\|\varepsilon_i\|e^{-r_1 t}, \tag{32}$$

where $r_2 = \sqrt{\frac{\lambda_{\min}\{L_{\alpha\beta}\}}{\lambda_{\min}\{L_{\alpha\beta}\}}} > 0$.

Thus, $\boldsymbol{\varepsilon_i}$ is exponentially decreasing with convergence of $\boldsymbol{r}_1$.

To forces the PMSG works at an optimal torque, the reference current is chosen as follows (Yang et al., 2018a):

$$i^*_{\alpha\beta} = \frac{2T^*_e}{3p\psi_f}\begin{bmatrix} -\sin(\theta_e) \\ \cos(\theta_e) \end{bmatrix}. \tag{33}$$

From Equation 23, the reference torque is formulated as follows:

$$T^*_e = J\frac{d\omega^*_m}{dt} - f_{fv}\left(\omega^*_m - \omega_m\right), \tag{34}$$

where $\varepsilon_m = (\omega^*_m - \omega_m)$ denotes the tracking error between the turbine and PMSG. The suitable dynamic is to reduce this speed tracking error as much as possible. As can be seen from the aforementioned Eq. 34, the desired torque T^*_e has two drawbacks: the dependence of its convergence on the PMSG mechanical parameters (J, f_{fv}), and it is in open-loop (Belkhier et al., 2022). To address these issues, in Belkhier et al. (2020), the term (f_{fv}) was removed, and T^*_e was computed by a PID controller. However, the authors mentioned this strategy still has a drawback with the change of J due to the fixed gains of the PID. Thus, to address this inconvenient, an FLC is introduced to replace the PID loop to solve the problem caused by imprecise

TABLE 1 Fuzzy logic rules.

$\Delta\varepsilon_m$ / ε_m	NB	NS	Z	PS	PB
NB	NB	NB	NS	NS	Z
NS	NB	NB	NS	Z	PS
Z	NS	NS	Z	PS	PS
PS	NS	Z	PS	PB	PB
PB	Z	PS	PS	PB	PB

parameters, to guarantee convergence of ε_m, eliminates the static error, and ensures robustness. The design process of T_e^* is depicted by Figure 3.

The fuzzy manager is used for gain adjustment, which satisfies the requirements induced by inaccurate variables. The fuzzy values are either the speed error ε_m in the instance of the regulator equation calculation in (34) or its derivation. Fuzzy controller rules are exposed in Table 1, which are defined as: zero (Z), negative small (NS), positive small (PS), positive big (PB), positive medium (PM), negative medium (NM), and negative big (NB). To choose the membership functions shown in Figure 4, symmetrical and equally distributed triangular and trapezoidal types are utilized. The mechanism for splitting these functions is provided according to Lee and Takagi (Michael and Takagi, 1993) and Yubazaki et al. (1995). Their approach is predicated on the notion that many membership functions might share a single parameter. The benefit of this approach is that it significantly reduces the number of parameters required by the membership functions. The center of gravity defuzzication approach is used to generate the crisp outputs, and a max–min fuzzy inference is used to produce the decision-making output.

Grid-side model and PI controller

The GSC is modelized as given in Figure 5. The classical PI method is selected to regulate the GSC, which is formulated as (Yang et al., 2018a; Belkhier et al., 2020):

$$\begin{bmatrix} V_d \\ V_q \end{bmatrix} = R_f \begin{bmatrix} i_{df} \\ i_{qf} \end{bmatrix} + \begin{bmatrix} L_f \dfrac{di_{df}}{dt} - \omega L_f i_{qf} \\ L_f \dfrac{di_{qf}}{dt} + \omega L_f i_{df} \end{bmatrix} + \begin{bmatrix} V_{gd} \\ V_{gq} \end{bmatrix}, \quad (35)$$

where ω indicates the angular frequency, V_{gd} and V_{gq} are the grid voltages, i_{df} and i_{qf} indicate the currents, L_f indicates the inductance, V_d and V_q indicate inverter voltages, and R_f indicates resistance of the filter. The mathematical formalism

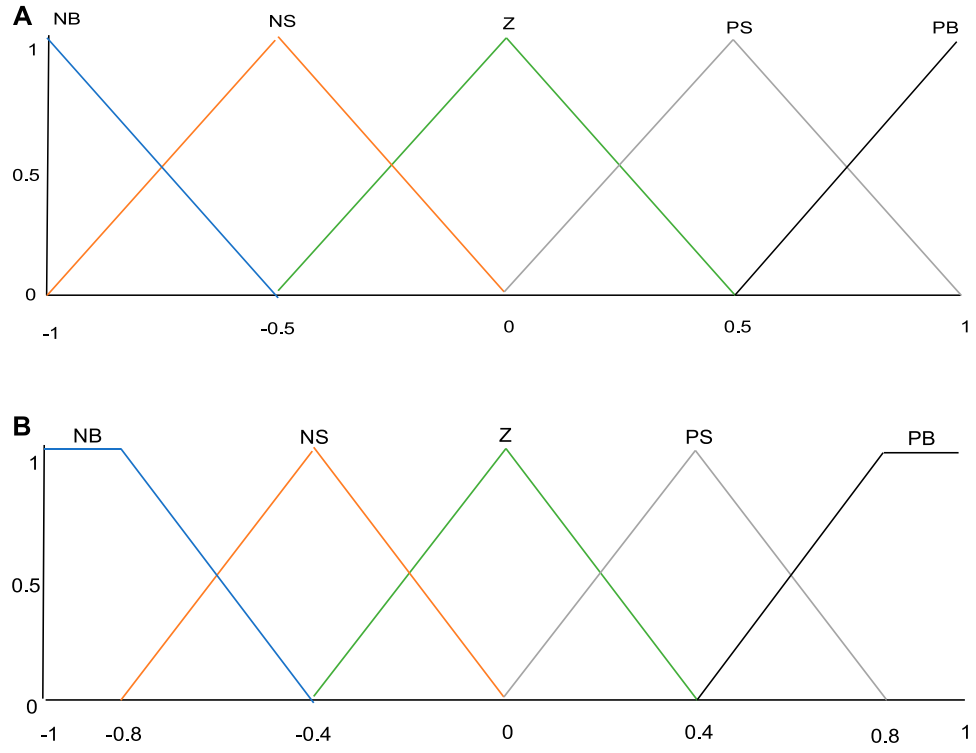

FIGURE 4
Fuzzy rules. **(A)** Function's inputs **(B)** Outputs function.

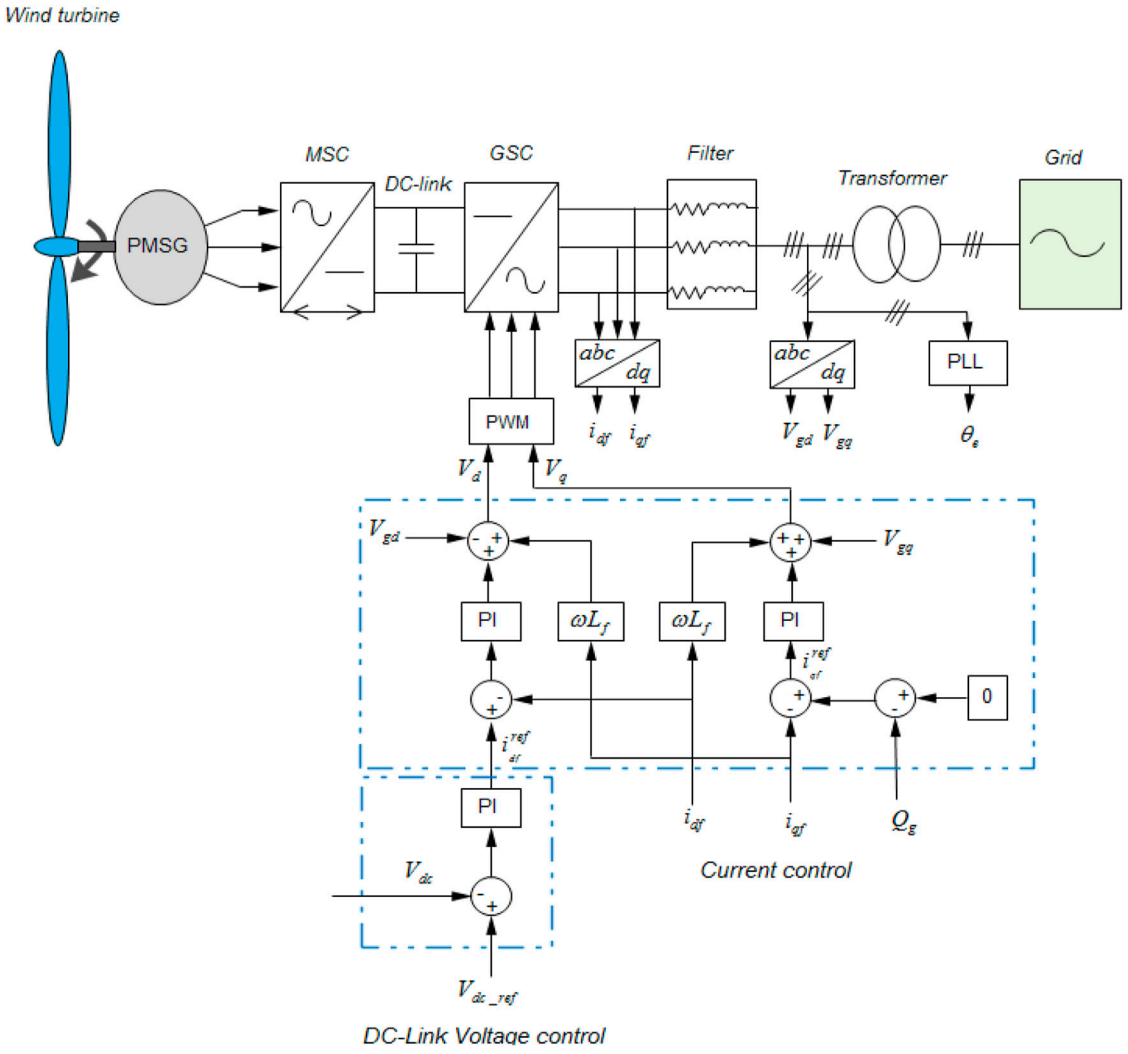

FIGURE 5
GSC PI controller schematic.

for the converter link voltage is given by (Subramaniam and Joo, 2019):

$$C\frac{dV_{dc}}{dt} = \frac{3}{2}\frac{v_{gd}}{V_{dc}}i_{df} + i_{dc}, \tag{36}$$

where C is the DC-link capacitance, i_{dc} is the line current, and V_{dc} is the DC-link voltage. The PI loop designs are as follows:

$$\begin{cases} V_{gd}^{PI} = k_{gp}^{d}\left(i_{df}^{ref} - i_{df}\right) - k_{gi}^{d}\int_0^t \left(i_{df}^{ref} - i_{df}\right)d\tau \\ V_{gq}^{PI} = k_{gp}^{q}\left(i_{qf}^{ref} - i_{qf}\right) - k_{gi}^{q}\int_0^t \left(i_{qf}^{ref} - i_{qf}\right)d\tau \end{cases}, \tag{37}$$

$$i_{qf}^{ref} = k_{dcp}\left(V_{dc\_ref} - V_{dc}\right) - k_{dci}\int_0^t \left(V_{dc\_ref} - V_{dc}\right)d\tau, \tag{38}$$

where $k_{gp}^{d} > 0$, $k_{gi}^{d} > 0$, $k_{gp}^{q} > 0$, $k_{gi}^{q} > 0$, $k_{dcp} > 0$, and $k_{dci} > 0$. The active and reactive powers are given as:

$$\begin{cases} P_g = \frac{3}{2}V_{gd}i_{df} \\ Q_g = \frac{3}{2}V_{gd}i_{qf} \end{cases}. \tag{39}$$

Extensive numerical investigation and experimental validation

For the simulation of the system, the average value of the wind speed is fixed at 12 m/s, and the reference of the wind

TABLE 2 Parameters of the system.

Parameter	Value
Air density (ρ)	1.24 kg/m^2
Stator resistance (R_s)	0.006 Ω
Turbine radius (R)	33.5 m
Stator inductance (L_{dq})	0.3 mH
Pole pairs number (p)	48
Flux linkage (ψ_f)	1.48 Wb
Total inertia (J)	35,000 kg m^2
DC-link capacitor (C)	2.9 F
Grid voltage (V_g)	574 V
DC-link voltage (V_{dc})	1150 V
Grid-filter resistance (R_f)	0.3 pu
Grid-filter inductance (L_f)	0.3 pu

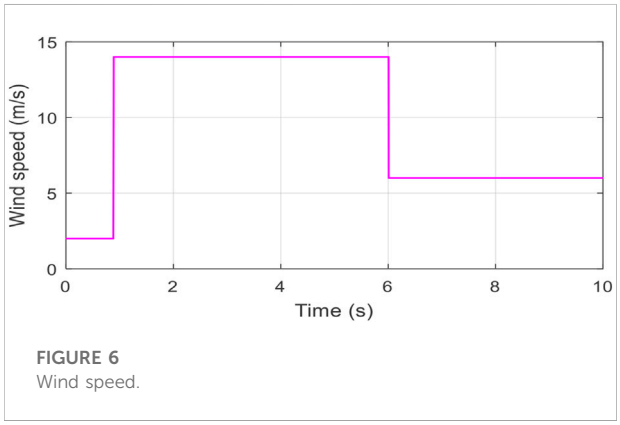

FIGURE 6
Wind speed.

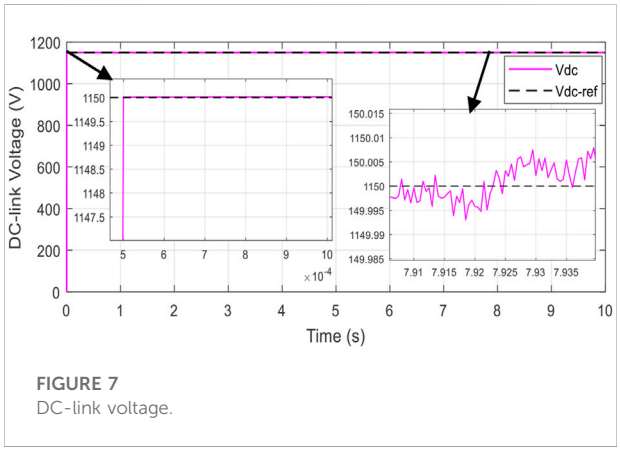

FIGURE 7
DC-link voltage.

turbine speed ref is estimated from the generator. The reference of the reactive power is set to 0 kVAr. The parameter values of the system are given in Table 2. The reference of the DC-bus voltage is set to 1150 V. The network is assumed to have infinite power, which allows the injection of all the production without

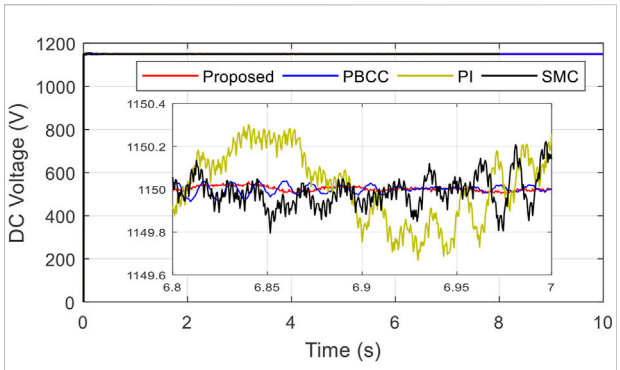

FIGURE 8
DC-link response compared with conventional controls.

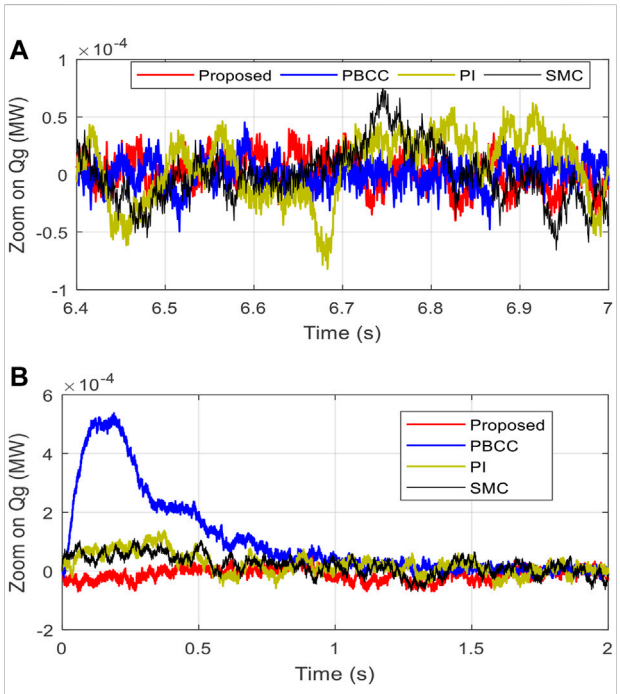

FIGURE 9
Reactive power response of the tested controls.

constraints. The damping value is $b_i = 250$. The fixed gains are $k_{dcp} = 5$, $k_{dci} = 500$, $k^d_{gp} = k^q_{gp} = 9$, and $k^d_{gi} = k^q_{gi} = 200$. For a better analysis of the performance of the adopted strategy, a comparison with other techniques was illustrated, with the conventional (PI) method, passivity-based current control (PBCC) proposed in Belkhier et al. (2020), and the SMC. The suggested approach is put to the test in two situations: First, the suggested regulator is evaluated using the PMSG's starting settings and evaluated to the standard controllers. The next aim is to analyze the resilience of this suggested fuzzy-EBC in the face of fluctuation. Finally,

TABLE 3 Results comparison of the control strategies.

Control	Proposed		PBCC		PI		SMC	
Variation	R_s, J	2 R_s 2J	R_s, J	2 R_s 2J	R_s, J	2 R_s 2J	R_s, J	2 R_s 2J
ε (V_{dc})	±0.005	±0.005	±0.02	±0.04	±0.2	±0.4	±0.2	±0.3
ε (Q_g)	±4e-5	±4e-5	±5e-5	±5.5e-5	±8e-5	±9e-5	±7e-5	±8e-5
Convergence speed (V_{dc})	0.6 s	0.6 s	1 s	1.2 s	1.4 s	1.8 s	1.6 s	1.8 s
Convergence speed (Q_g)	0.6 s	0.6 s	0.6 s	0.8 s	1 s	1.2 s	0.55 s	0.8 s

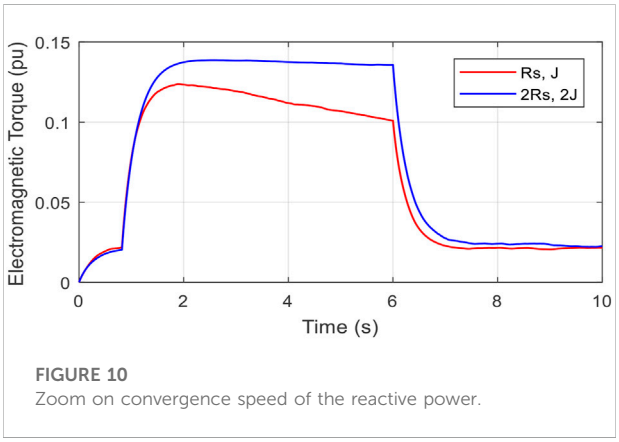

FIGURE 10
Zoom on convergence speed of the reactive power.

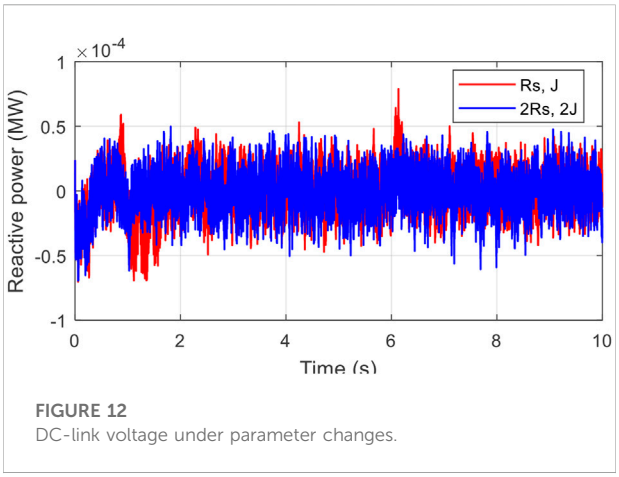

FIGURE 12
DC-link voltage under parameter changes.

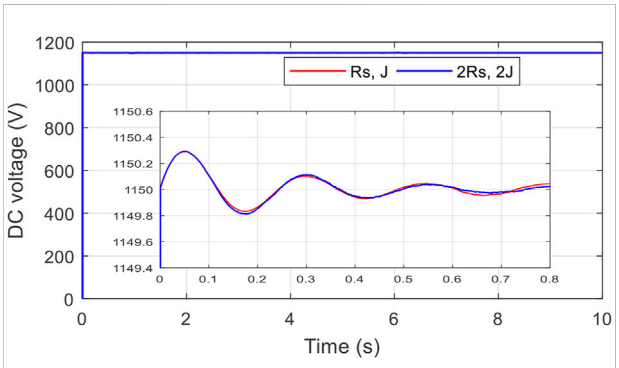

FIGURE 11
Electromagnetic torque under parameter changes.

experimental analysis utilizing PIL testing is performed to establish the practicality of the proposed system.

Fixed parameters performance analysis

Figure 6 indicates the wind velocity profile applied on the conversion mechanism. Figure 7 depicts the DC-bus trailing behavior with exceptionally low error (ε (V_{dc})). The suggested method produces transitory deflates of -0.005 and messes up of +0.005. The DC power reaction owing to suggested fuzzy-PBC, SMC, PBCC, and PI benchmarks is indicated in Figure 8. Transient undershoots of -0.02, -0.2, and -0.2 are recorded with the PBCC, PI, and SMC techniques, respectively, and transient messes up of +0.02, +0.2, and +0.2 are noted with the PBCC, PI, and SMC methodologies, respectively.

Figure 9 depicts the tracking error (ε (Q_g)) caused by the examined fuzzy-EBC, PBCC, PI, and SMC, with intermittent underneath and messes up of -4e-5, -5e-5, -8e-5, -7e-5, and +4e-5, +5e-5, +8e-5, +7e-5, correspondingly. Therefore, the recommended methodology, as shown in Table 3, has the smallest underneath and overreach. Furthermore, the suggested approach (0.3s) outperforms the PBCC (1s), PI (0.6s), and SMC (0.55s) in terms of relatively stable inaccuracy and converging ratio, as demonstrated in Figure 9; Table 3. It is deduced that the suggested PBC guaranteed faster response time, greater productivity, and lower following faults as compared to the standard nonlinear techniques studied.

Parameter changes performance analysis

In the present sub-section, simultaneous changes of +100% R_s and J are applied on the PMSG model to illustrate the robustness properties of the present method. Figure 10 indicates T_e behavior under fixed and varied conditions. It is

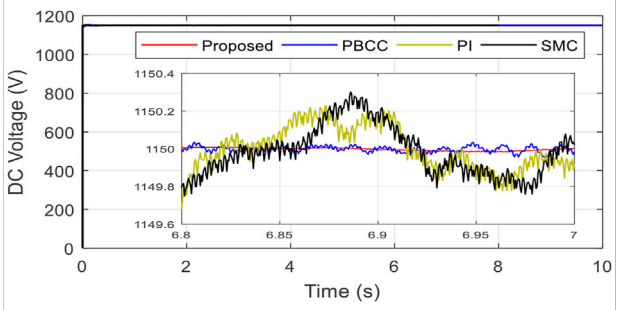

FIGURE 13
Reactive power response under parameter changes.

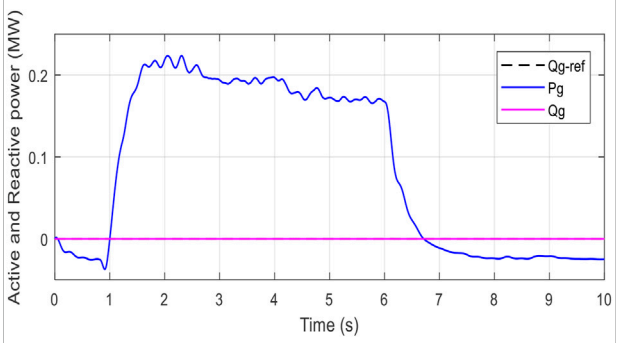

FIGURE 15
Reactive power response of the tested controls under parameter changes.

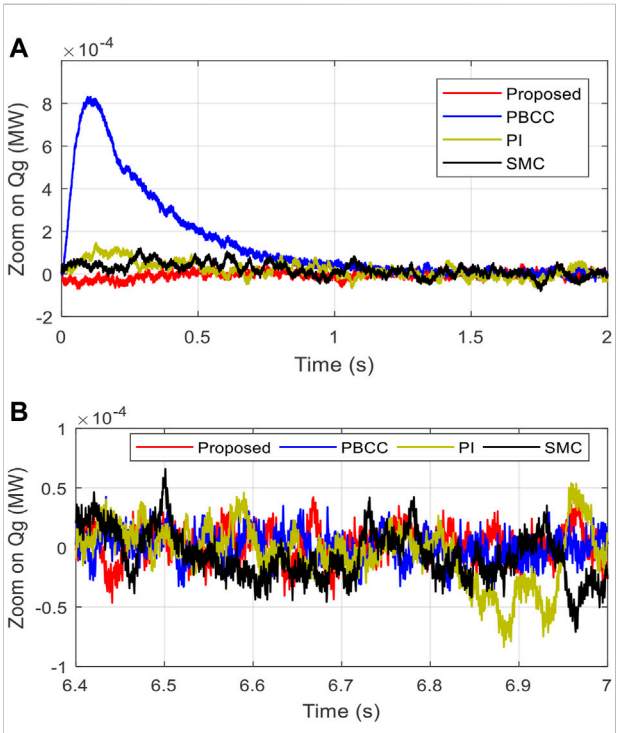

FIGURE 14
DC-link response of the tested controls under parameter changes.

evident that at t = 1–8s, the investigated fuzzy-EBC generate a higher torque with a constant steady-state under variation conditions (0.14 pu) than the one generated under initial parameter conditions (0.12 pu), an increase on the generated T_e of 16.53%. Figure 11 depicts V_{dc} answer caused by the suggested alternative within every scenario, in which error ε (V_{dc}) answer and monitoring inaccuracy equal to 0 are almost observed, that is, 0.05 as per Table 3.

Figure 12 indicates the resemblance monitoring reaction of Q_g to R_s and J perturbations. According to the findings, the suggested fuzzy-EBC demonstrates the same Q g behavior including both variable and fixed attribute values, where the recorded Q_g error ε (Q_g) is approximately the same as in case 1, that is, ±4.5e-5. The measured values of both V_{dc} and Q_g are tabulated in Table. 3.

Figure 13 depicts the V_{dc} response for all the PBCC, PI, SMC, and proposed fuzzy-PBC. As indicated in Table 3, the PBCC has a path loss of ±0.04, the PI has a path loss of ±0.4, and the SMC has a path loss of ±0.3. As shown in Table 3, the suggested technique obviously provides a constant V_{dc} error and greater trajectory tracking rate when opposed to the other competitors, that are either susceptible to combined perturbations of R_s and J. The Q g answer for all of the investigated controllers is indicated in Figure 14.

As per the reported findings, the suggested fuzzy-EBC has a lower tracking error below these variations than PBCC (5.5e-5), PI (9e-5), and SMC (8e-5), as shown in Table 3. Moreover, the suggested fuzzy-PBC clearly outperforms the other alternatives in terms of velocity position error ε (Q_g) although when exposed to simultaneous perturbations, as demonstrated in Figure 14 and Table 3. Hence, based on the actual analysis and Table 4, the suggested alternative outperforms the other comparable methodologies of resilience, quick reaction and rapid converging, and effectiveness. This verified the theoretical findings of *parameter changes performance analysis*. Furthermore, as shown in Figures 15–17, the closed loop operates at full power and integrates an effective electricity to the network.

Experimental testing

The processor-in-the-loop testing (PiL) is the process of testing and validating embedded software on the processor before it is utilized in the electronic control unit (ECU). Algorithms and functions are often created on a PC in a development environment. More details about processor-in-

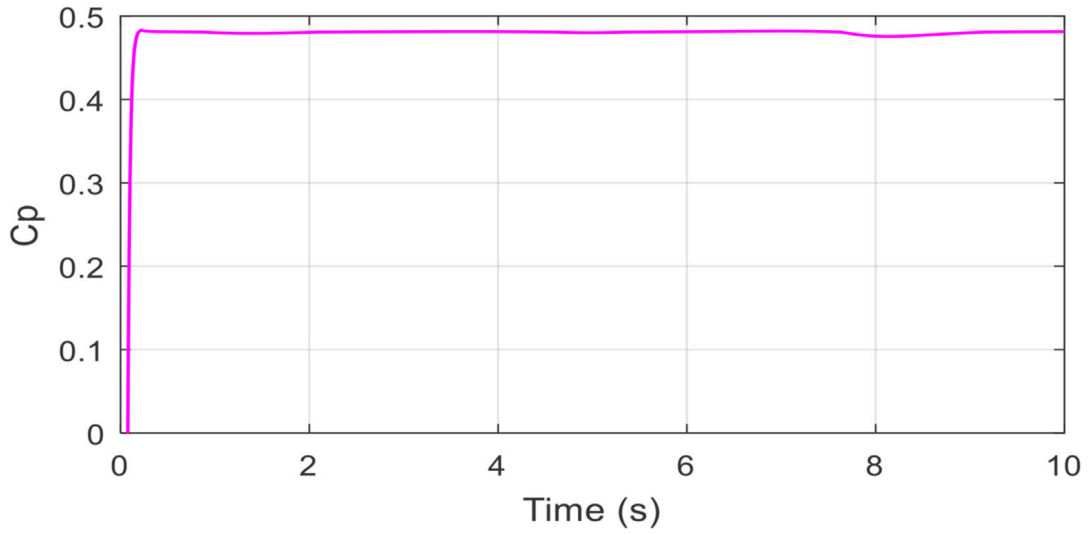

FIGURE 16
Zoom on reactive power response of the tested controls under parameter changes

TABLE 4 Performance comparisons of the tested controls.

Controls	Proposed	PBCC	SMC	PI
Response speed	Extremely fast (0.8e-3 s)	Very fast (1e-3 s)	Fast (1.2e-3 s)	Slow (2e-3 s)
Stability	Highly stable (fluctuations free)	Very stable (fluctuations free)	Stable (with fluctuations)	Poor stability (with fluctuations)
Robustness	High robustness	Robust	Not robust	Not robust
Performance	Higher	Good	Low	Low

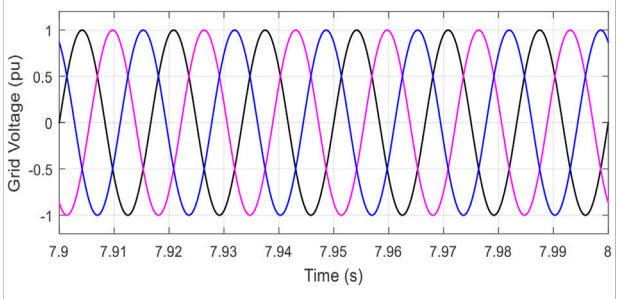

FIGURE 17
Active and reactive powers response.

the loop experimentation are reported in Ullah et al. (2020); Ullah et al. (2021a); Ullah et al. (2021b). PiL tests are run to ensure that the built code also runs on the target CPU. The control algorithms for the PiL test are often run on a device known as an evaluation board. PiL testing is sometimes run on the actual ECU. Both types use the controller's actual processor rather than the PC as in software-in-loop (SiL) testing. The target processor offers the advantage of detecting compiler issues. As a result of the preceding work, the suggested control systems are evaluated utilizing PIL investigation, and the block diagram of the setup is illustrated in Figure 18. In the PIL investigation, the DSP command board is physically interconnected with the simulated converter system. The control board is made up of a double core processor TMS320F379D that was developed using the Simulink planet's simple synthesis approach. Simulink is used to create discontinuous versions of the described devices, and the output or hex file is loaded into the processor's random-access memory (RAM).

In PiL testing, "in-the-loop" indicates that the controller is integrated in physical machine and the program during test's surroundings is emulated. The wind profile utilized in the PIL testing is depicted in Figure 19. Figures 20 and 21, which demonstrate the experimental findings for DC-link voltage, active, and reactive powers obtained using the PIL approach.

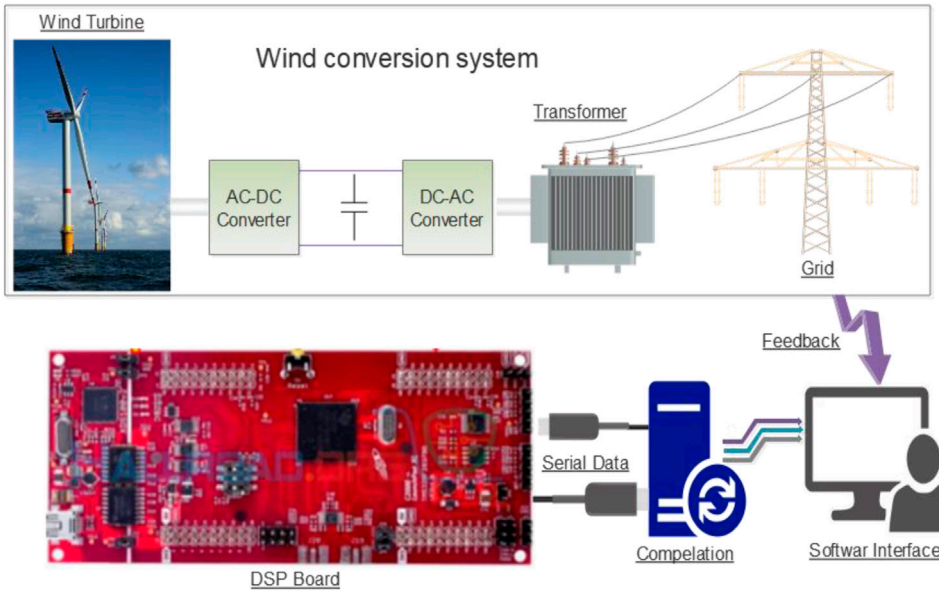

FIGURE 18
Experimental Step.

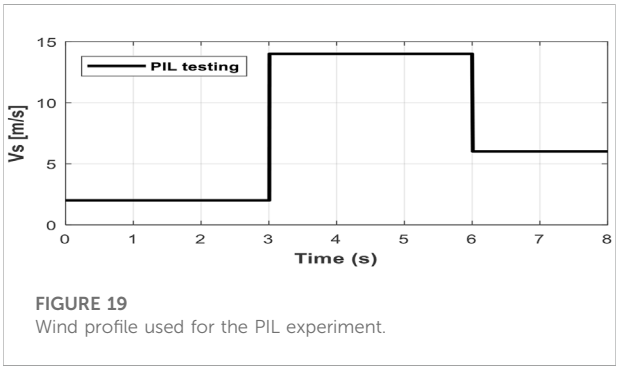

FIGURE 19
Wind profile used for the PIL experiment.

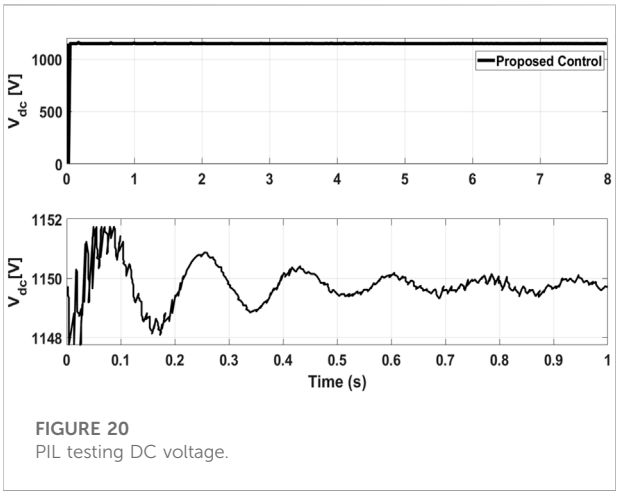

FIGURE 20
PIL testing DC voltage.

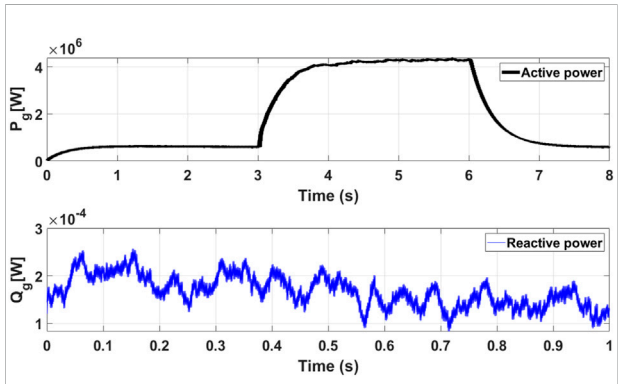

FIGURE 21
PIL testing grid powers.

Based on the provided data, the proposed fuzzy-EBC is definitely applicable in practice.

6 Conclusion

For a PMSG in a wind power converter, a new fuzzy energy-based controller is presented. To obtain the maximum power out of wind energy, utilize the suggested strategy where the entire dynamics of the PMSG is considered when designing the control law. A fuzzy controller is selected to guarantee the overall-rated speed operation of the PMSG, and then compute a higher reference torque. Dynamic

simulations of the studied system under parameter changes have taken special attention, and the results have been compared to conventional methods, which show a quick track of the DC voltage and reactive energy to their set values over the compared controls. All of the conversion system's flaws have been fixed, and the goals have been met. The designed control approach offers optimum performance as well as increased resilience. Moreover, the PIL experiment is conducted to prove that the proposed controller is practically implementable. Future works will be focused on:

- Experimental validation of the proposed control on a real wind energy system.
- The adaptation of the damping fixed gain by introducing an optimization algorithm.

Data availability statement

The original contributions presented in the study are included in the article/Supplementary Material; further inquiries can be directed to the corresponding author.

Author contributions

All authors listed have made a substantial, direct, and intellectual contribution to the work and approved it for publication.

Conflict of interest

The authors declare that the research was conducted in the absence of any commercial or financial relationships that could be construed as a potential conflict of interest.

Publisher's note

All claims expressed in this article are solely those of the authors and do not necessarily represent those of their affiliated organizations, or those of the publisher, the editors, and the reviewers. Any product that may be evaluated in this article, or claim that may be made by its manufacturer, is not guaranteed or endorsed by the publisher.

References

Belkhier, Y., and Achour, A. (2020). Fuzzy passivity-based linear feedback current controller approach for PMSG-based tidal turbine. *Ocean. Eng.* 218, 108156. doi:10.1016/j.oceaneng.2020.108156

Belkhier, Y., Achour, A., Ullah, N., Shaw, R. N., Chowdhury, S., and Techato, K. (2022). Energy-based fuzzy supervisory non integer control for performance improvement of PMSG-Based marine energy system under swell effect and parameter uncertainties. *Renew. Energy* 186, 457–468. doi:10.1016/j.renene.2021.12.126

Belkhier, Y., and Achour, A. Y. (2020). An intelligent passivity-based backstepping approach for optimal control for grid-connecting permanent magnet synchronous generator-based tidal conversion system. *Int. J. Energy Res.* 45, 5433–5448. doi:10.1002/er.6171

Belkhier, Y., Achour, A. Y., Ullah, N., and Shaw, R. N. (2020). Modified passivity-based current controller design of permanent magnet synchronous generator for wind conversion system. *Int. J. Model. Simul.* 42, 192–202. doi:10.1080/02286203.2020.1858226

Bigarelli, L., Benedetto, M. D., Lidozzi, A., Solero, L., Odhano, S. A., and Zanchetta, P. (2020). PWM-based optimal model predictive control for variable speed generating units. *IEEE Trans. Ind. Appl.* 56 (1), 541–550. doi:10.1109/tia.2019.2955662

Chandrasekaran, K., Mohanty, M., Golla, M., Venkadesan, A., and Simon, S. P. (2020). Dynamic MPPT controller using cascade neural network for a wind power conversion system with energy management. *IETE J. Res.*, 1–15. doi:10.1080/03772063.2020.1756934

Soliman, M. S., Belkhier, Y., Ullah, N., Achour, A., Alharbi, Y. M., Al Alahmadi, A. A., et al. (2021). Supervisory energy management of a hybrid battery/PV/tidal/wind sources integrated in DC-microgrid energy storage system. *Energy Reports* 7, 7728–7728.

Fantino, R., Solsona, J., and Busada, C. (2016). Nonlinear observer-based control for PMSG wind turbine. *Energy* 113, 248–257. doi:10.1016/j.energy.2016.07.039

Haq, I. U., Khan, Q., Khan, I., Akmeliawati, R., and Nisar, K. S. (2020). Maximum power extraction strategy for variable speed wind turbine system via neuro-adaptive generalized global sliding mode controller. *IEEE Access* 8, 128536–128547. doi:10.1109/access.2020.2966053

Jlassi, I., and Cardoso, A. J. M. (2019). Fault-tolerant back-to-back converter for direct-drive PMSG wind turbines using direct torque and power control techniques. *IEEE Trans. Power Electron.* 34 (11), 11215–11227. doi:10.1109/tpel.2019.2897541

Michael, A., and Takagi, H. (1993). "Dynamic control of genetic algorithms using fuzzy logic techniques," in Proceedings of the Fifth International Conference on Genetic Algorithms (Morgan Kaufmann), 76–83.

Mohammadi, E., Fadaeinedjad, R., and Nadji, H. R. (2019). Design, electromechanical simulation, and control of a variable speed stall-regulated PMSG-based wind turbine. *Int. J. Green Energy* 16 (12), 890–900. doi:10.1080/15435075.2019.1641714

Nicklasson, P. J., Ortega, R., and Espinosa-Perez, G. (1994). Passivity-based control of the general rotating electrical machine. *Proc. 1994 33rd IEEE Conf. Decis. Control* 4, 4018–4023. doi:10.1109/CDC.1994.411573

Rizk-Allah, R. M., Hassanien, A. E., and Song, D. (2022). Chaos-opposition-enhanced slime mould algorithm for minimizing the cost of energy for the wind turbines on high-altitude sites. *ISA Trans.* 121, 191–205. doi:10.1016/j.isatra.2021.04.011

Saidi, Y., Mezouar, A., Miloud, Y., Kerrouche, K. D. E., Brahmi, B., and Benmahdjoub, M. A. (2019). Advanced non-linear backstepping control design for variable speed wind turbine power maximization based on tip-speed-ratio approach during partial load operation. *Int. J. Dyn. Control* 8, 615–628. doi:10.1007/s40435-019-00564-3

Song, D., Li, Z., Wang, L., Jin, F., Huang, C., Xia, E., et al. (2022). Energy capture efficiency enhancement of wind turbines via stochastic model predictive yaw control based on intelligent scenarios generation. *Appl. Energy* 312, 118773. doi:10.1016/j.apenergy.2022.118773

Song, D., Tu, Y., Wang, L., Jin, F., Li, Z., Huang, C., et al. (2022). Coordinated optimization on energy capture and torque fluctuation of wind turbines via variable weight NMPC with fuzzy regulator. *Appl. Energy* 312, 118821. doi:10.1016/j.apenergy.2022.118821

Subramaniam, R., and Joo, Y. H. (2019). Passivity-based fuzzy ISMC for wind energy conversion systems with PMSG. *IEEE Trans. Syst. Man. Cybern. Syst.* 51, 2212–2220. doi:10.1109/tsmc.2019.2930743

Ullah, N., Farooq, Z., Sami, I., Chowdhury, M. S., Techato, K., and Alkhammash, H. I. (2020). Industrial grade Adaptive control scheme for a micro-grid integrated dual active bridge driven battery storage system. *IEEE Access* 8, 210435–210451. doi:10.1109/ACCESS.2020.3039947

Ullah, N., Sami, I., Chowdhury, M. S., Techato, K., and Alkhammash, H. I. (2021a). Artificial intelligence integrated fractional order control of doubly fed induction generator-based wind energy system. *IEEE Access* 9, 5734–5748. doi:10.1109/ACCESS.2020.3048420

Ullah, N., Sami, I., Jamal Babqi, A., I Alkhammash, H., Belkhier, Y., Althobaiti, A., et al. (2021b). Processor in the loop verification of fault tolerant control for a three phase inverter in grid connected PV system. *Energy Sources, Part A Recovery, Util. Environ. Eff.*, 1–17. doi:10.1080/15567036.2021.2015486

Wang, X., and Wang, S. (2020). Adaptive fuzzy robust control of PMSM with smooth inverse based dead-zone compensation. *Int. J. Control Autom. Syst.* 14 (2), 378–388. doi:10.1007/s12555-015-0010-6

Yang, B., Wu, Q. H., Tiang, L., and Smith, J. S. (2013). *Adaptive passivity-based control of a TCSC for the power system damping improvement of a PMSG based offshore wind farm*. Madrid, Spain: IEEE International Conference on Renewable Energy Research and Applications ICRERA, 1–5.

Yang, B., Yu, H., Zhang, Y., Chen, J., Sang, Y., Jing, L., et al. (2018a). Passivity-based sliding-mode control design for optimal power extraction of a PMSG based variable speed wind turbine. *Renew. Energy* 119, 577–589. doi:10.1016/j.renene.2017.12.047

Yang, B., Yu, T., Shu, H., Qiu, D., Zhang, Y., Cao, P., et al. (2018b). Passivity-based linear feedback control of permanent magnetic synchronous generator-based wind energy conversion system: Design and analysis. *IET Renew. Power Gener.* 12 (9), 981–991. doi:10.1049/iet-rpg.2017.0680

Yubazaki, N., Otani, M., Ashida, T., and Hirota, K. (1995). "Dynamic fuzzy control method and its application to positioning of induction motor," in Proceedings of 1995 IEEE International Conference on Fuzzy Systems (IEEE), 1095–1102.3

Zargham, F., and Mazinan, A. H. (2019). Super-twisting sliding mode control approach with its application to wind turbine systems. *Energy Syst.* 10, 211–229. doi:10.1007/s12667-018-0270-3

frontiers | Frontiers in Energy Research

TYPE Original Research
PUBLISHED 15 November 2022
DOI 10.3389/fenrg.2022.1059132

OPEN ACCESS

EDITED BY
Khalid Mehmood Cheema,
Fatima Jinnah Women University,
Pakistan

REVIEWED BY
Asad Aziz,
Southeast University, China
Arshad Rauf,
Nanjing University of Aeronautics and Astronautics, China
Omar Abu Arqub,
Al-Balqa Applied University, Jordan

*CORRESPONDENCE
Adiqa Kausar Kiani,
adiqa@yuntech.edu.tw

SPECIALTY SECTION
This article was submitted to Smart Grids, a section of the journal Frontiers in Energy Research

RECEIVED 30 September 2022
ACCEPTED 25 October 2022
PUBLISHED 15 November 2022

CITATION
Malik NA, Chang C-L, Chaudhary NI, Khan ZA, Zahoor Raja MA, Kiani AK, Milyani AH and Azhari AA (2022), Parameter estimation of harmonics arising in electrical instruments of smart grids using cuckoo search heuristics. *Front. Energy Res.* 10:1059132. doi: 10.3389/fenrg.2022.1059132

Parameter estimation of harmonics arising in electrical instruments of smart grids using cuckoo search heuristics

Naveed Ahmed Malik[1], Ching-Lung Chang[2], Naveed Ishtiaq Chaudhary[3], Zeshan Aslam Khan[4], Muhammad Asif Zahoor Raja[3], Adiqa Kausar Kiani[3]*, Ahmed H. Milyani[5] and Abdullah Ahmed Azhari[6]

[1]Graduate School of Engineering Science and Technology, National Yunlin University of Science and Technology, Douliou, Taiwan, [2]Department of Computer Science and Information Engineering, National Yunlin University of Science and Technology, Douliou, Taiwan, [3]Future Technology Research Center, National Yunlin University of Science and Technology, Douliou, Taiwan, [4]Department of Electrical and Computer Engineering, International Islamic University Islamabad, Islamabad, Pakistan, [5]Department of Electrical and Computer Engineering, King Abdulaziz University, Jeddah, Saudi Arabia, [6]The Applied College, King Abdulaziz University, Jeddah, Saudi Arabia

The accurate estimation of power signal parameters allows smart grids to optimize power delivery efficiency, improve equipment utilization, and control power flow among generation nodes and loads. However, practically it becomes a challenging task because of the presence of harmonic distortions. In this study, a parameter estimation of the power system harmonics is investigated through swarm intelligence–based optimization strength of the cuckoo search algorithm. The performance evaluation is conducted in detail for different generations and particle sizes and for different signal-to-noise ratios. The simulation results reveal that the cuckoo search optimization heuristic accurately estimates the amplitude and phase parameters of the power system harmonics and is robust against different signal-to-noise ratios.

KEYWORDS

cuckoo search, swarm optimization, harmonics, parameter estimation, smart grid

1 Introduction

The control of the power systems and synchronization of grid-connected electrical devices require parameters of voltage and current signals, such as amplitude, frequency, and phase (Baradarani et al., 2014; Jafarpisheh et al., 2016). Accurate information on these signal parameters allows smart grids to optimize power delivery efficiency, improve equipment utilization, and control power flow among generation nodes and loads (Sun et al., 2019). However, practically the presence of harmonics and inter-harmonic distortions in power signals complicates the situation because the amplitude and phase estimations of harmonics is challenging for evaluating the quality of service characteristics in smart grids (Rivas et al., 2020). Thus, it is imperative to investigate

the development of accurate, robust, and stable estimation methods to mitigate the adverse effects of harmonics in smart grid efficiency.

Different researchers have investigated the domain of estimating power system harmonics and proposed various techniques. For example, Das et al. (2020) developed the ADALINE-based least mean square (LMS) algorithm and compared its performance with the recursive least square, while Elnady et al. (2020) presented the novel smooth variable structure filters for voltage harmonics and voltage imbalance. Santos et al. (2020) introduced the filter bank–based ESPRIT approach for increased efficiency in harmonics detection and estimation. Enayati and Moravej (2017) developed a hybrid estimation scheme by combining recursive least squares with the iterated extended Kalman filter, and Shuai et al. (2018) presented the frequency shifting/filtering method. Xu et al. (Xu and Ding, 2018; Xu and Song, 2020) investigated the parameter estimation of power signals using iterative/recursive methods, such as multi-innovation stochastic gradient (Xu and Ding, 2017), separable multi-synchronous multi-innovation gradient (Xu et al., 2022), separable Newton recursive (Xu, 2022a), separable multi-innovation Newton iterative (Xu, 2022b), and hierarchical principle-based recursive least squares (Xu et al., 2021). Chaudhary et al. introduced fractional gradient-based estimation algorithms for power signals, such as fractional LMS (Chaudhary et al., 2017) and innovative fractional order LMS (Chaudhary et al., 2020), while Zubair et al. (2018) presented the momentum term–based fractional scheme. Mehmood et al. (2020), Mehmood et al. (2021) had applied evolutionary and swarming heuristics for parameter estimation of power signals.

The schemes based on swarm and evolutionary heuristics have established their significance through effective application in solving various challenging optimization tasks (Francesca and Birattari, 2016; Jana et al., 2019; Sabir et al., 2020; AbdelAty et al., 2022; Altaf et al., 2022) such as power system harmonics estimation (Ray and Subudhi, 2012; Elvira-Ortiz et al., 2020; Ray and Subudhi, 2015; Kabalci et al., 2018; doNascimentoSepulchro et al., 2014; Singh et al., 2016). Yang and Deb (2009), Yang and Deb (2014) introduced a metaheuristic inspired by the search mechanism of cuckoo called the cuckoo search optimization (CSO) algorithm. The CSO has been used extensively for effective solutions in a number of engineering and applied problems with many variants (Li and Yin, 2015; Cuong-Le et al., 2021), such as photovoltaic model (Gude and Jana, 2020), social media sentiment analysis (Pandey et al., 2017), path planning (Song et al., 2020), power control in salt reactors (Karahan, 2021), damage detection infrastructures (Tran-Ngoc et al., 2019), chemoinformatics (Houssein et al., 2020), economic load dispatch (Yu et al., 2020), and many others. The effective performance of CSO in illustrated applications motivated us to explore parameter estimation power system harmonics through well-established optimization strength of the CSO. In this study, parameters of power system harmonics are estimated through CSO for different generation and particle size. Detailed and in-depth performance analyses are conducted to check the accuracy, diversity, and robustness of the CSO for harmonics estimation.

The remaining article is set as follows: the estimation model for power system harmonics along with the optimization procedure of CSO is described in Section 2. The results of simulation studies are elaborated in Section 3. The conclusions and future works are listed in Section 4.

2 Materials and methods

The system model for power harmonics signal is first introduced, then the proposed methodology for optimization of the fitness function for the estimation of the harmonic signal is presented in this section. The overall flow diagram of the proposed scheme is presented in Figure 1 by means of different process block structures.

2.1 System model

The general harmonic signal in terms of its constituent parameters (Malik et al., 2022) is defined as

$$s(t) = \sum_{k=1}^{K} \alpha_k \sin\left(\beta_k t + \gamma_k\right) + \delta(t)h(t) = \sum_{j=1}^{J} a_j \sin\left(b_j t + c_j\right) + d(t), \tag{1}$$

and the variables in Eq. 1 are defined as J represents harmonic order, a_j is amplitude, b_j is angular frequency represented as $b_j = 2\pi f_0$ with f_0 as fundamental frequency, c_j is phase, and d is AWGN. Then, by writing a discrete version of Eq. 1 after sampling with period p, $t_n = np$, and by assuming $h(t_n) = h(n)$, Eq. 1 is rewritten as

$$\begin{aligned} h(t_n) &= \sum_{j=1}^{J} a_j \sin\left(b_j t_n + \gamma_k\right) + d(t_n), \\ h(n) &= \sum_{j=1}^{J} a_j \sin\left(\beta_j n + c_k\right) + d(n). \end{aligned} \tag{2}$$

Expanding Eq. 2 through the fundamental trigonometric identity

$$h(n) = \sum_{j=1}^{J} \left[a_j \cos\left(b_j n\right) \sin c_j + a_j \sin\left(b_j n\right) \cos c_j\right] + d(n), \tag{3}$$

with the assumption that

$$u_j = a_j \cos c_j \text{ and } v_j = a_j \sin c_j, \tag{4}$$

using the assumptions given in Eq. 4 into Eq. 3 gives Eq. 5:

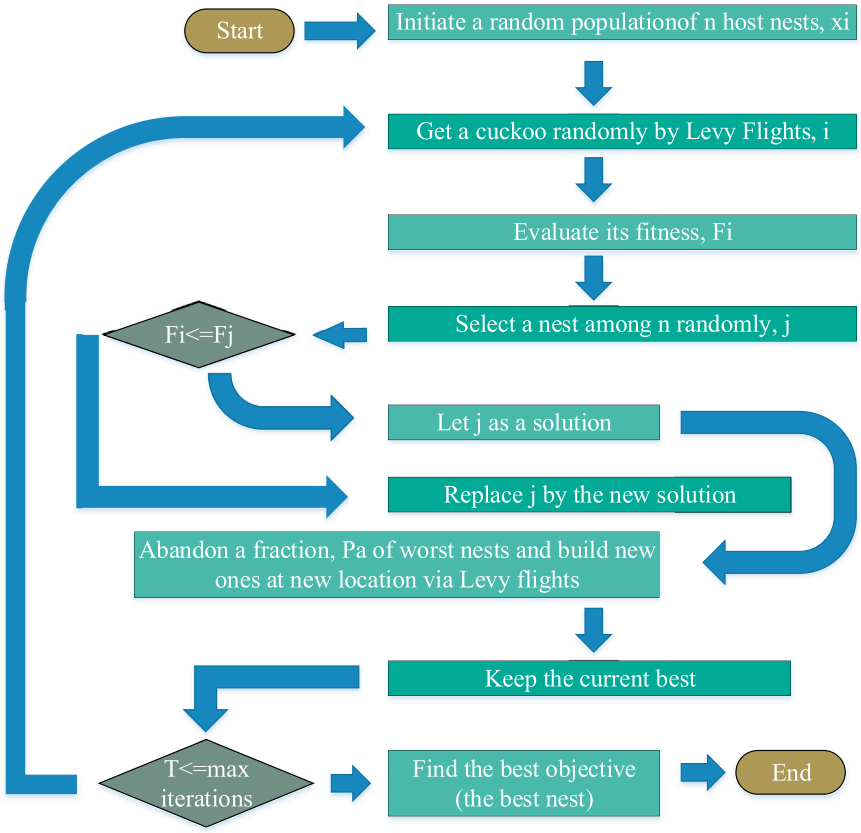

FIGURE 1
Process flow structure of the CSO algorithm.

$$h(n) = \sum_{j=1}^{J}\left[u_j \sin\left(b_j n\right) + v_j \cos\left(b_j n\right)\right] + d(n). \tag{5}$$

The harmonics estimation model with information-vector ψ and parameter-vector ζ is written as

$$\begin{gathered} h(n) = \psi^T(n)\zeta + d(n), \\ \psi(n) = \left[\sin(b_1 n), \cos(b_1 n), \sin(b_2 n), \cos(b_2 n), ..., \sin\left(b_j n\right), \cos\left(b_j n\right)\right], \\ \zeta = \left[u_1, v_1, u_2, v_2, ..., u_j, v_j\right]. \end{gathered} \tag{6}$$

The aim is to estimate the amplitude and phase parameters of the harmonics through minimizing the error-based criterion function defined as

$$\delta(n) = \text{mean}\left[h(n) - \tilde{h}(n)\right]^2 = \left[h(n) - \psi^T(n)\tilde{\zeta}\right]^2, \tag{7}$$

$h(n)$ is the actual signal, $\tilde{h}(n)$ is an estimated harmonic signal calculated through estimated parameter-vector $\tilde{\zeta}$ by using the proposed CSO-based heuristic. The relationship between the intermediate variables and the actual parameters is given by

$$a_j = \sqrt{\left(u_j\right)^2 + \left(v_j\right)^2},\ c_j = \tan^{-1}\frac{v_j}{u_j}. \tag{8}$$

2.2 Optimization method: Cuckoo search optimization algorithm

Yang and Deb (2009), Yang and Deb (2014) introduced a metaheuristic inspired by the search mechanism of cuckoo called CSO with exhaustive applications in different fields of engineering design and optimization. The formulation of the CSO is based on three fundamental concepts: firstly, each cuckoo lays a single egg in a single instance of time, while dumping the respective egg in an arbitrary selected nest; secondly, the nests with the best fitness, i.e., having the best quality of eggs, proceed to the next generations; and thirdly, the number of host nests is fixed, and the probability of discovery of next by the host cuckoo is set between 0 and 1. The basis of these three fundamental steps in the CSO is proposed with the process flow structure as shown in Figure 1.

TABLE 1 Results of parameter estimates of Example 1 for G = 500.

d	p	a_1	a_2	a_3	a_4	a_5	c_1	c_2	c_3	c_4	c_5	δ
30	50	1.5028	0.4903	0.2059	0.1384	0.1010	1.3943	1.0096	0.7530	0.5487	0.5573	9.46E-04
	100	1.4904	0.4991	0.1894	0.1581	0.0975	1.4002	1.0211	0.7449	0.6339	0.5726	9.70E-04
	150	1.5087	0.4904	0.2023	0.1463	0.0967	1.3955	1.0529	0.7615	0.6934	0.6441	8.64E-04
60	50	1.5026	0.4985	0.1989	0.1496	0.0982	1.3965	1.0456	0.7820	0.6432	0.5329	1.02E-05
	100	1.5003	0.5008	0.1978	0.1507	0.1007	1.3967	1.0410	0.7978	0.6495	0.5096	1.79E-05
	150	1.5005	0.5010	0.2018	0.1537	0.1005	1.3956	1.0455	0.7833	0.6221	0.5477	1.38E-05
90	50	1.4988	0.5024	0.1988	0.1486	0.0999	1.3964	1.0468	0.7795	0.6266	0.5078	7.40E-06
	100	1.4988	0.5009	0.1997	0.1483	0.1006	1.3954	1.0426	0.7934	0.6270	0.5264	7.11E-06
	150	1.4991	0.4975	0.2018	0.1504	0.1006	1.3965	1.0449	0.7793	0.6296	0.5074	8.01E-06
		1.5000	0.5000	0.2000	0.1500	0.1000	1.3960	1.0470	0.7850	0.6280	0.5230	0

TABLE 2 Results of parameter estimates of Example 1 for G = 1,000.

d	p	a_1	a_2	a_3	a_4	a_5	c_1	c_2	c_3	c_4	c_5	δ
30	50	1.4952	0.4968	0.2042	0.1611	0.0934	1.4038	1.0503	0.7960	0.5386	0.5653	7.11E-04
	100	1.4977	0.4896	0.1984	0.1546	0.1018	1.3969	1.0433	0.7826	0.6401	0.5742	7.17E-04
	150	1.5014	0.5028	0.2011	0.1480	0.0941	1.3938	1.0509	0.8318	0.6224	0.6175	7.12E-04
60	50	1.5000	0.5000	0.1998	0.1501	0.1000	1.3961	1.0470	0.7862	0.6260	0.5211	7.07E-07
	100	1.4999	0.5004	0.2002	0.1500	0.1001	1.3959	1.0468	0.7881	0.6290	0.5188	8.60E-07
	150	1.5001	0.4998	0.1999	0.1497	0.0997	1.3963	1.0468	0.7855	0.6267	0.5263	8.06E-07
90	50	1.5000	0.5000	0.2000	0.1500	0.1000	1.3960	1.0470	0.7849	0.6280	0.5227	2.65E-09
	100	1.5000	0.5000	0.2000	0.1500	0.1000	1.3960	1.0471	0.7850	0.6280	0.5229	3.54E-09
	150	1.5000	0.5000	0.2000	0.1500	0.1001	1.3960	1.0470	0.7850	0.6281	0.5228	5.67E-09
		1.5000	0.5000	0.2000	0.1500	0.1000	1.3960	1.0470	0.7850	0.6280	0.5230	0

TABLE 3 Results of parameter estimates of Example 1 for G = 1,500.

d	p	a_1	a_2	a_3	a_4	a_5	c_1	c_2	c_3	c_4	c_5	δ
30	50	1.5062	0.5012	0.2063	0.1391	0.1015	1.3967	1.0482	0.7961	0.6084	0.4847	6.81E-04
	100	1.4972	0.5052	0.1938	0.1573	0.1014	1.3949	1.0526	0.7824	0.6144	0.5761	6.08E-04
	150	1.4962	0.5003	0.1958	0.1505	0.0907	1.3955	1.0315	0.8229	0.6524	0.5335	6.34E-04
60	50	1.5000	0.5001	0.1999	0.1501	0.0997	1.3961	1.0472	0.7848	0.6273	0.5270	6.83E-07
	100	1.5000	0.5001	0.1997	0.1498	0.1001	1.3961	1.0467	0.7847	0.6292	0.5218	6.23E-07
	150	1.5000	0.5000	0.2000	0.1498	0.0998	1.3961	1.0467	0.7841	0.6268	0.5203	6.57E-07
90	50	1.5000	0.5000	0.2000	0.1500	0.1000	1.3960	1.0470	0.7850	0.6279	0.5230	6.68E-10
	100	1.5000	0.5000	0.2000	0.1500	0.1000	1.3960	1.0470	0.7850	0.6280	0.5230	7.68E-10
	150	1.5000	0.5000	0.2000	0.1500	0.1000	1.3960	1.0470	0.7850	0.6280	0.5231	7.82E-10
		1.5000	0.5000	0.2000	0.1500	0.1000	1.3960	1.0470	0.7850	0.6280	0.5230	0

Proceeding by the actual behavior of the cuckoo, mathematical models were introduced by Yang et al.; by taking the new candidate solution x_i(t+1) that represents an i-*th* cuckoo at t flight/iteration index and considering the Levy flight, we have the following expression iterative update of CSO as

$$x_i(t+1) = x_i(t) + \alpha \odot Levy(\lambda), \tag{9}$$

TABLE 4 Results of parameter estimates of Example 1 for G = 2000.

d	p	a_1	a_2	a_3	a_4	a_5	c_1	c_2	c_3	c_4	c_5	δ
30	50	1.5024	0.5020	0.2011	0.1462	0.0958	1.3909	1.0393	0.7911	0.6087	0.5671	6.10E-04
	100	1.4909	0.4982	0.2001	0.1471	0.0913	1.3968	1.0594	0.7639	0.5954	0.6038	5.51E-04
	150	1.4930	0.5076	0.2050	0.1453	0.1043	1.3977	1.0479	0.8170	0.5725	0.5632	6.00E-04
60	50	1.5001	0.4999	0.2000	0.1502	0.1001	1.3959	1.0468	0.7849	0.6286	0.5216	5.94E-07
	100	1.5002	0.4999	0.2001	0.1498	0.0999	1.3960	1.0475	0.7848	0.6282	0.5219	5.74E-07
	150	1.5000	0.5003	0.1999	0.1498	0.0999	1.3959	1.0467	0.7848	0.6292	0.5194	6.15E-07
90	50	1.5000	0.5000	0.2000	0.1500	0.1000	1.3960	1.0470	0.7850	0.6280	0.5229	6.59E-10
	100	1.5000	0.5000	0.2000	0.1500	0.1000	1.3960	1.0470	0.7850	0.6280	0.5230	6.67E-10
	150	1.5000	0.5000	0.2000	0.1500	0.1000	1.3960	1.0470	0.7850	0.6280	0.5230	6.59E-10
		1.5000	0.5000	0.2000	0.1500	0.1000	1.3960	1.0470	0.7850	0.6280	0.5230	0

TABLE 5 Results of parameter estimates of Example 2 for G = 500.

d	p	a_1	a_2	a_3	a_4	a_5	c_1	c_2	c_3	c_4	c_5	δ
30	50	1.1894	0.8090	0.2030	0.1721	0.0846	1.3078	0.9609	0.8036	0.6879	0.6185	7.91E-04
	100	1.1887	0.8069	0.1964	0.1717	0.1024	1.3088	0.9683	0.6965	0.7246	0.5261	9.62E-04
	150	1.1867	0.7975	0.1961	0.1844	0.1074	1.3148	0.9610	0.7408	0.6736	0.4660	8.57E-04
60	50	1.2029	0.8000	0.2001	0.1829	0.1022	1.3100	0.9597	0.7827	0.6976	0.5053	1.34E-05
	100	1.2018	0.7972	0.2015	0.1777	0.0971	1.3077	0.9612	0.7884	0.6951	0.5268	1.58E-05
	150	1.1984	0.7962	0.2008	0.1790	0.0979	1.3080	0.9620	0.7898	0.6939	0.5613	2.19E-05
90	50	1.1987	0.7990	0.1996	0.1796	0.0997	1.3095	0.9583	0.7956	0.7191	0.5277	1.14E-05
	100	1.1974	0.7991	0.2004	0.1790	0.0983	1.3075	0.9591	0.7817	0.7046	0.5416	1.01E-05
	150	1.2008	0.7975	0.2042	0.1780	0.1001	1.3100	0.9559	0.7866	0.6948	0.5428	2.01E-05
		1.2000	0.8000	0.2000	0.1800	0.1000	1.3090	0.9590	0.7850	0.6980	0.5230	0

TABLE 6 Results of parameter estimates of Example 2 for G = 1,000.

d	p	a_1	a_2	a_3	a_4	a_5	c_1	c_2	c_3	c_4	c_5	δ
30	50	1.2096	0.8051	0.2019	0.1866	0.0936	1.3101	0.9696	0.8023	0.6930	0.5116	7.02E-04
	100	1.1960	0.8067	0.1974	0.1822	0.1000	1.3079	0.9672	0.7963	0.7429	0.5082	7.32E-04
	150	1.1969	0.8024	0.1955	0.1762	0.1092	1.3089	0.9584	0.8046	0.6871	0.4465	6.98E-04
60	50	1.1998	0.8001	0.1998	0.1802	0.0997	1.3092	0.9590	0.7865	0.6978	0.5212	7.53E-07
	100	1.2000	0.8002	0.1998	0.1800	0.1005	1.3094	0.9586	0.7861	0.7009	0.5285	8.08E-07
	150	1.2001	0.8001	0.2000	0.1802	0.1001	1.3088	0.9593	0.7865	0.6980	0.5252	8.10E-07
90	50	1.2000	0.8000	0.2000	0.1800	0.1000	1.3090	0.9590	0.7850	0.6980	0.5229	1.45E-09
	100	1.2000	0.8000	0.2000	0.1800	0.1000	1.3090	0.9590	0.7848	0.6981	0.5231	2.16E-09
	150	1.2000	0.8000	0.2000	0.1800	0.1000	1.3090	0.9591	0.7851	0.6983	0.5229	4.69E-09
		1.2000	0.8000	0.2000	0.1800	0.1000	1.3090	0.9590	0.7850	0.6980	0.5230	0

here α represents the step size based on the scale of the optimization problem, and generally its value is set equal to unit value in most of the cases and the Levy flight is represented with a random walk procedure on the basis of Levy distribution as

$$Levy(\lambda) \sim u = t^{(-\lambda)}, \tag{10}$$

TABLE 7 Results of parameter estimates of Example 2 for G = 1,500.

d	p	a_1	a_2	a_3	a_4	a_5	c_1	c_2	c_3	c_4	c_5	δ
30	50	1.1985	0.8005	0.2013	0.1755	0.0949	1.3134	0.9585	0.7586	0.6795	0.5023	6.40E-04
	100	1.1909	0.8036	0.1962	0.1757	0.1137	1.3091	0.9548	0.7750	0.6668	0.6236	6.61E-04
	150	1.2013	0.8014	0.1918	0.1790	0.0984	1.3135	0.9679	0.8190	0.7242	0.6072	6.39E-04
60	50	1.2001	0.8000	0.1999	0.1799	0.1000	1.3089	0.9589	0.7858	0.6976	0.5225	6.91E-07
	100	1.1998	0.7997	0.2000	0.1802	0.0999	1.3091	0.9591	0.7847	0.6988	0.5215	6.82E-07
	150	1.1999	0.7999	0.2002	0.1800	0.1001	1.3091	0.9588	0.7866	0.6979	0.5224	6.11E-07
90	50	1.2000	0.8000	0.2000	0.1800	0.1000	1.3090	0.9590	0.7850	0.6980	0.5230	6.71E-10
	100	1.2000	0.8000	0.2000	0.1800	0.1000	1.3090	0.9590	0.7850	0.6980	0.5230	6.73E-10
	150	1.2000	0.8000	0.2000	0.1800	0.1000	1.3090	0.9590	0.7850	0.6980	0.5230	7.60E-10
		1.2000	0.8000	0.2000	0.1800	0.1000	1.3090	0.9590	0.7850	0.6980	0.5230	0

TABLE 8 Results of parameter estimates of Example 2 for G = 2000.

d	p	a_1	a_2	a_3	a_4	a_5	c_1	c_2	c_3	c_4	c_5	δ
30	50	1.1992	0.7993	0.1921	0.1931	0.1024	1.3071	0.9623	0.8177	0.7112	0.5600	5.57E-04
	100	1.1976	0.8012	0.2052	0.1809	0.1048	1.2983	0.9477	0.8055	0.7149	0.5158	5.55E-04
	150	1.2013	0.8022	0.2006	0.1794	0.1015	1.3068	0.9566	0.7844	0.7002	0.6340	6.02E-04
60	50	1.2001	0.8000	0.2002	0.1802	0.0999	1.3092	0.9590	0.7843	0.6989	0.5230	6.11E-07
	100	1.1999	0.8002	0.2000	0.1800	0.1001	1.3090	0.9591	0.7845	0.6993	0.5232	6.04E-07
	150	1.2001	0.8001	0.1998	0.1802	0.0998	1.3090	0.9594	0.7859	0.6976	0.5214	6.33E-07
90	50	1.2000	0.8000	0.2000	0.1800	0.1000	1.3090	0.9590	0.7850	0.6980	0.5230	6.67E-10
	100	1.2000	0.8000	0.2000	0.1800	0.1000	1.3090	0.9590	0.7850	0.6980	0.5230	6.73E-10
	150	1.2000	0.8000	0.2000	0.1800	0.1000	1.3090	0.9590	0.7850	0.6980	0.5230	6.45E-10
		1.2000	0.8000	0.2000	0.1800	0.1000	1.3090	0.9590	0.7850	0.6980	0.5230	0

here λ is a constant taken between 1 and 3, and the Levy flight has an infinite mean and variance. Further details on the mathematical terms, convergence proofs, and applications can be referred from citations mentioned therein: Yang and Deb (2009); Yang and Deb (2014); Li and Yin (2015); Pandey et al. (2017); Tran-Ngoc et al. (2019); Gude and Jana (2020); Houssein et al. (2020); Song et al. (2020); Yu et al. (2020); Cuong-Le et al. (2021); Karahan (2021). Inspired by the optimization performance of the CSO algorithm, we have implemented the CSO for optimization of parameters of the system models presented in Eqs. 1–8. The CSO algorithm was implemented in the presented research based on the routine available at the MATLAB Central File Exchange (Yang, 2022). The optimization strength of the CSO may be enhanced by integrating it with the kernel theory (Arqub, 2016; Arqub, 2018; Arqub, 2020; Arqub and Al-Smadi, 2020; Sweis et al., 2022).

3 Results and discussion

Harmonics estimation of power systems is carried out in this research work by applying the CSO algorithm to two examples, and the results are given in a tabular form with the necessary discussion along with graphs. The simulations are conducted using MATLAB with a sampling frequency of 2 KHz. Three levels of additive white Gaussian noise d with 30 DB, 60 DB, and 90 DB are introduced in the system to check the heftiness of the proposed scheme. The investigation is carried out by considering four generation (G) sizes and three particle (P) sizes in the CSO. The considered values of G are 500, 1000, 1,500, and 2000, while the values of P are 50, 100, and 150.

Example 1: The harmonic signal (Malik et al., 2022) considered in the first simulation study is

$$h(t)=\begin{bmatrix}1.5\sin\left(2\pi f_1 t+1.396\right)+0.5\sin\left(2\pi f_3 t+1.047\right)+0.2\sin\left(2\pi f_5 t+0.785\right)\\+0.15\sin\left(2\pi f_7 t+0.628\right)+0.1\sin\left(2\pi f_{11} t+0.523\right)\end{bmatrix}. \tag{11}$$

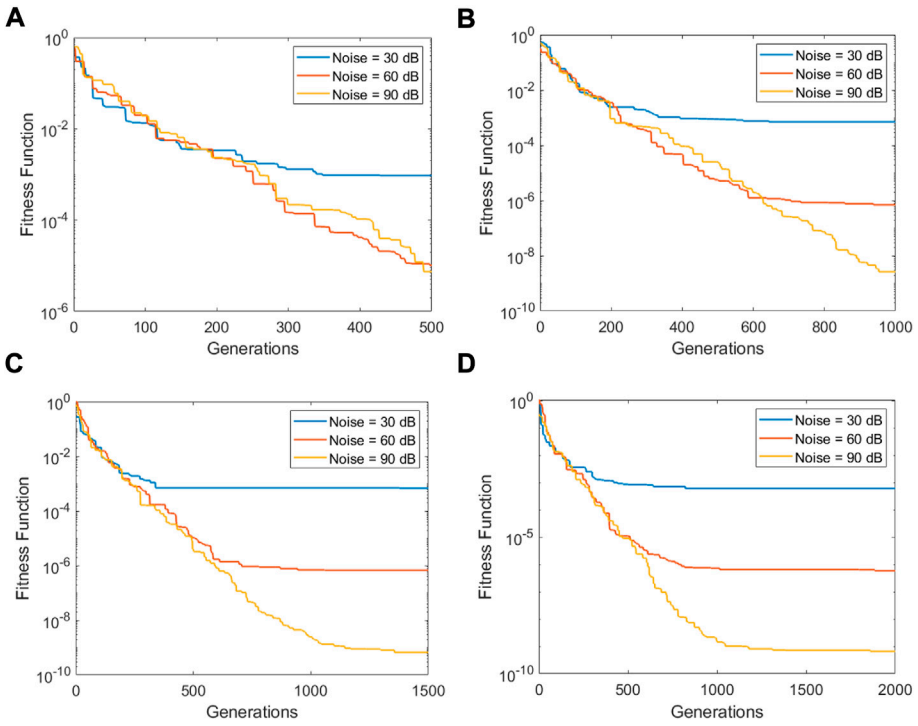

FIGURE 2
Convergence plots of Example 1: **(A)** G = 500, **(B)** G = 500, **(C)** G = 500, and **(D)** G = 500.

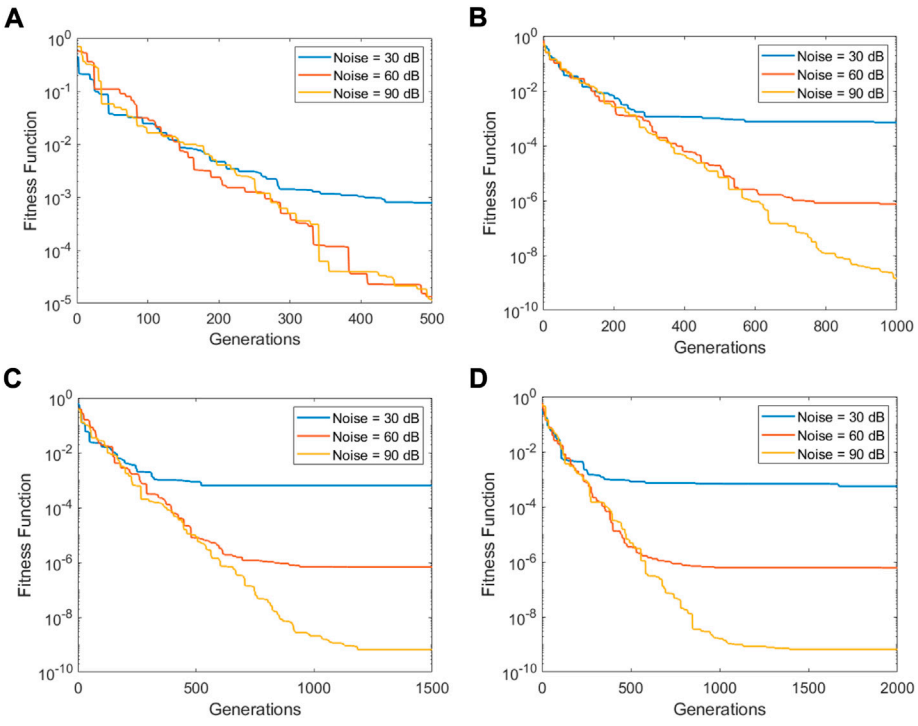

FIGURE 3
Convergence plots of Example 1: **(A)** G = 500, **(B)** G = 500, **(C)** G = 500, and **(D)** G = 500.

Ten parameters are taken under consideration in this problem. Five phase and five amplitude parameters that were taken are given below, while, f_1, f_3, f_5, f_7, and f_{11} are the frequencies with values 50 Hz, 150 Hz, 250 Hz, 350 Hz, and 550 Hz, respectively:

$$\begin{aligned}\boldsymbol{\zeta} &= [a_1, a_2, a_3, a_4, a_5, c_1, c_2, c_3, c_4, c_5] \\ &= [1.50, 0.50, 0.20, 0.15, 0.10, 1.396, 1.047, 0.785, 0.628, 0.523].\end{aligned} \tag{12}$$

Example 2: The harmonic signal considered in the second simulation study is

$$h(t) = \begin{bmatrix} 1.2\sin(2\pi f_1 t + 1.309) + 0.8\sin(2\pi f_3 t + 0.959) + 0.2\sin(2\pi f_5 t + 0.785) \\ +0.18\sin(2\pi f_7 t + 0.698) + 0.1\sin(2\pi f_{11} t + 0.523) \end{bmatrix}. \tag{13}$$

The parameter-vector consisting of five amplitude and five phase parameters is

$$\begin{aligned}\boldsymbol{\zeta} &= [a_1, a_2, a_3, a_4, a_5, c_1, c_2, c_3, c_4, c_5] \\ &= [1.20, 0.80, 0.20, 0.18, 0.10, 1.309, 0.959, 0.785, 0.698, 0.523].\end{aligned} \tag{14}$$

The results of Example 1 in terms of parameter estimates through the CSO along with the MSE value are given in Tables 1–4 for G = 500, 1,000, 1,500, and 2,000, respectively. While the respective results in the case of Example 2 are presented in Tables 5–8. The learning curves for Example 1 are given in Figure 2, while for Example 2, the convergence plots are provided in Figure 3. The results clearly indicate that the CSO gives a better accuracy for 90 dB SNR than it does for 60 dB and 30 dB. Moreover, the accuracy of the CSO for harmonics estimation increases by increasing the generation size.

4 Conclusion

This study exploits a swarm intelligence–based cuckoo search optimization, CSO, heuristic for parameter estimation of power system harmonics. The CSO accurately estimates the amplitude and phase parameters associated with the first, third, fifth, and eleventh harmonic components. Simulation studies conducted on the mean square error–based evaluation metric indicate that the accuracy of the CSO increases with an increase in the generation size, while increasing particle size has not shown a significant rise in the accuracy level. Moreover, the CSO has shown a robust performance in estimating the parameters of power system harmonics for different scenarios of additive white Gaussian noise.

Future studies may investigate the applying of the CSO algorithm for real-time harmonics estimation and for other engineering optimization problems (Phannil et al., 2018; Montoya et al., 2019; Beleiu et al., 2020; Yang et al., 2020; Chaudhary et al., 2021).

Data availability statement

The original contributions presented in the study are included in the article/supplementary material; further inquiries can be directed to the corresponding author.

Author contributions

Conceptualization: NC and MZ; methodology: NM, NC, and MZ; software: NM; validation: ZK, AK, MZ, and NC; resources: AK and CC; writing—original draft preparation: NM; writing—review and editing: NC, ZK, AK, and MZ; supervision: CC and NC; project administration: AM and AA; funding acquisition: AM and AA.

Funding

The Deanship of Scientific Research (DSR) at King Abdulaziz University (KAU), Jeddah, Saudi Arabia has funded this project, under grant no. (KEP-MSc: 122-135-1443).

Conflict of interest

The authors declare that the research was conducted in the absence of any commercial or financial relationships that could be construed as a potential conflict of interest.

Publisher's note

References

AbdelAty, A. M., Fouda, M. E., and Eltawil, A. (2022). Parameter estimation of two spiking neuron models with meta-heuristic optimization algorithms. *Front. Neuroinform.* 16, 771730. doi:10.3389/fninf.2022.771730

Altaf, F., Chang, C. L., Chaudhary, N. I., Raja, M. A. Z., Cheema, K. M., Shu, C. M., et al. (2022). Adaptive evolutionary computation for nonlinear hammerstein control autoregressive systems with key term separation principle. *Mathematics* 10 (6), 1001. doi:10.3390/math10061001

Arqub, O. A., and Al-Smadi, M. (2020). Numerical solutions of Riesz fractional diffusion and advection-dispersion equations in porous media using iterative reproducing kernel algorithm. *J. Porous Media* 23 (8), 783–804. doi:10.1615/jpormedia.2020025011

Arqub, O. A. (2016). Approximate solutions of DASs with nonclassical boundary conditions using novel reproducing kernel algorithm. *Fundam. Inf.* 146 (3), 231–254. doi:10.3233/fi-2016-1384

Arqub, O. A. (2020). Numerical simulation of time-fractional partial differential equations arising in fluid flows via reproducing Kernel method. *Int. J. Numer. Methods Heat. Fluid Flow.* 30, 4711–4733. doi:10.1108/hff-10-2017-0394

Arqub, O. A. (2018). Numerical solutions for the Robin time-fractional partial differential equations of heat and fluid flows based on the reproducing kernel algorithm. *Int. J. Numer. Methods Heat. Fluid Flow.* 28, 828–856. doi:10.1108/hff-07-2016-0278

Baradarani, F., Zadeh, M. R. D., and Zamani, M. A. (2014). A phase-angle estimation method for synchronization of grid-connected power-electronic converters. *IEEE Trans. Power Deliv.* 30 (2), 827–835. doi:10.1109/tpwrd.2014.2362930

Beleiu, H. G., Maier, V., Pavel, S. G., Birou, I., Pică, C. S., and Dărab, P. C. (2020). Harmonics consequences on drive systems with induction motor. *Appl. Sci.* 10 (4), 1528. doi:10.3390/app10041528

Chaudhary, N. I., Latif, R., Raja, M. A. Z., and Machado, J. T. (2020). An innovative fractional order LMS algorithm for power signal parameter estimation. *Appl. Math. Model.* 83, 703–718. doi:10.1016/j.apm.2020.03.014

Chaudhary, N. I., Zubair, S., and Raja, M. A. Z. (2017). A new computing approach for power signal modeling using fractional adaptive algorithms. *ISA Trans.* 68, 189–202. doi:10.1016/j.isatra.2017.03.011

Chaudhary, N. I., Raja, M. A. Z., He, Y., Khan, Z. A., and Tenreiro Machado, J. (2021). Design of multi innovation fractional LMS algorithm for parameter estimation of input nonlinear control autoregressive systems. *Appl. Math. Model.* 93, 412–425. doi:10.1016/j.apm.2020.12.035

Cuong-Le, T., Minh, H. L., Khatir, S., Wahab, M. A., Tran, M. T., and Mirjalili, S. (2021). A novel version of Cuckoo search algorithm for solving optimization problems. *Expert Syst. Appl.* 186, 115669. doi:10.1016/j.eswa.2021.115669

Das, S. R., Ray, P. K., Sahoo, A. K., Balasubramanian, K., and Reddy, G. S. (2020). Improvement of power quality in a three-phase system using an adaline-based multilevel inverter. *Front. Energy Res.* 8, 23. doi:10.3389/fenrg.2020.00023

do Nascimento Sepulchro, W., Encarnação, L. F., and Brunoro, M. (2014). Harmonic state and power flow estimation in distribution systems using evolutionary strategy. *J. Control Autom. Electr. Syst.* 25 (3), 358–367. doi:10.1007/s40313-014-0110-1

Elnady, A., Al-Shabi, M., and Adam, A. A. (2020). Novel filters based operational scheme for five-level diode-clamped inverters in microgrid. *Front. Energy Res.* 8, 11. doi:10.3389/fenrg.2020.00011

Elvira-Ortiz, D. A., Jaen-Cuellar, A. Y., Morinigo-Sotelo, D., Morales-Velazquez, L., Osornio-Rios, R. A., and Romero-Troncoso, R. d. J. (2020). Genetic algorithm methodology for the estimation of generated power and harmonic content in photovoltaic generation. *Appl. Sci.* 10 (2), 542. doi:10.3390/app10020542

Enayati, J., and Moravej, Z. (2017). Real-time harmonics estimation in power systems using a novel hybrid algorithm. *IET Gener. Transm. &amp. Distrib.* 11 (14), 3532–3538. doi:10.1049/iet-gtd.2017.0044

Francesca, G., and Birattari, M. (2016). Automatic design of robot swarms: Achievements and challenges. *Front. Robot. AI* 3, 29. doi:10.3389/frobt.2016.00029

Gude, S., and Jana, K. C. (2020). Parameter extraction of photovoltaic cell using an improved cuckoo search optimization. *Sol. Energy* 204, 280–293. doi:10.1016/j.solener.2020.04.036

Houssein, E. H., Hosney, M. E., Elhoseny, M., Oliva, D., Mohamed, W. M., and Hassaballah, M. (2020). Hybrid Harris hawks optimization with cuckoo search for drug design and discovery in chemoinformatics. *Sci. Rep.* 10 (1), 14439–14522. doi:10.1038/s41598-020-71502-z

Jafarpisheh, B., Madani, S. M., and Shahrtash, S. M. (2016). A new DFT-based phasor estimation algorithm using high-frequency modulation. *IEEE Trans. Power Deliv.* 32 (6), 1–2423. doi:10.1109/tpwrd.2016.2629762

Jana, G., Mitra, A., Pan, S., Sural, S., and Chattaraj, P. K. (2019). Modified particle swarm optimization algorithms for the generation of stable structures of carbon clusters, Cn (n= 3–6, 10). *Front. Chem.* 7, 485. doi:10.3389/fchem.2019.00485

Kabalci, Y., Kockanat, S., and Kabalci, E. (2018). A modified ABC algorithm approach for power system harmonic estimation problems. *Electr. power Syst. Res.* 154, 160–173. doi:10.1016/j.epsr.2017.08.019

Karahan, O. (2021). Design of optimal fractional order fuzzy PID controller based on cuckoo search algorithm for core power control in molten salt reactors. *Prog. Nucl. Energy* 139, 103868. doi:10.1016/j.pnucene.2021.103868

Li, X., and Yin, M. (2015). Modified cuckoo search algorithm with self adaptive parameter method. *Inf. Sci.* 298, 80–97.doi:10.1016/j.ins.2014.11.042

Malik, N. A., Chang, C. L., Chaudhary, N. I., Raja, M. A. Z., Cheema, K. M., Shu, C. M., et al. (2022). Knacks of fractional order swarming intelligence for parameter estimation of harmonics in electrical systems. *Mathematics* 10 (9), 1570. doi:10.3390/math10091570

Mehmood, A., Raja, M. A. Z., Zameer, A., and Chaudhary, N. I. (2021). Design of backtracking search heuristics for parameter estimation of power signals. *Neural comput. Appl.* 33 (5), 1479–1496. doi:10.1007/s00521-020-05029-9

Mehmood, A., Chaudhary, N. I., Zameer, A., and Raja, M. A. Z. (2020). Novel computing paradigms for parameter estimation in power signal models. *Neural comput. Appl.* 32 (10), 6253–6282. doi:10.1007/s00521-019-04133-9

Montoya, F. G., Baños, R., Alcayde, A., and Arrabal-Campos, F. M. (2019). Analysis of power flow under non-sinusoidal conditions in the presence of harmonics and interharmonics using geometric algebra. *Int. J. Electr. Power & Energy Syst.* 111, 486–492. doi:10.1016/j.ijepes.2019.04.032

Pandey, A. C., Rajpoot, D. S., and Saraswat, M. (2017). Twitter sentiment analysis using hybrid cuckoo search method. *Inf. Process. Manag.* 53 (4), 764–779. doi:10.1016/j.ipm.2017.02.004

Phannil, N., Jettanasen, C., and Ngaopitakkul, A. (2018). Harmonics and reduction of energy consumption in lighting systems by using LED lamps. *Energies* 11 (11), 3169. doi:10.3390/en11113169

Ray, P. K., and Subudhi, B. (2012). BFO optimized RLS algorithm for power system harmonics estimation. *Appl. Soft Comput.* 12 (8), 1965–1977. doi:10.1016/j.asoc.2012.03.008

Ray, P. K., and Subudhi, B. (2015). Neuro-evolutionary approaches to power system harmonics estimation. *Int. J. Electr. Power & Energy Syst.* 64, 212–220. doi:10.1016/j.ijepes.2014.07.035

Rivas, A. E. L., da Silva, N., and Abrão, T. (2020). Adaptive current harmonic estimation under fault conditions for smart grid systems. *Electr. Power Syst. Res.* 183, 106276. doi:10.1016/j.epsr.2020.106276

Sabir, Z., Raja, M. A. Z., Guirao, J. L., and Shoaib, M. (2020). A neuro-swarming intelligence-based computing for second order singular periodic non-linear boundary value problems. *Front. Phys.* 8, 224. doi:10.3389/fphy.2020.00224

Santos, E., Khosravy, M., Lima, M. A., Cerqueira, A. S., and Duque, C. A. (2020). ESPRIT associated with filter bank for power-line harmonics, sub-harmonics and inter-harmonics parameters estimation. *Int. J. Electr. Power & Energy Syst.* 118, 105731. doi:10.1016/j.ijepes.2019.105731

Shuai, Z., Zhang, J., Tang, L., Teng, Z., and Wen, H. (2018). Frequency shifting and filtering algorithm for power system harmonic estimation. *IEEE Trans. Ind. Inf.* 15 (3), 1554–1565. doi:10.1109/tii.2018.2844191

Singh, S. K., Sinha, N., Goswami, A. K., and Sinha, N. (2016). Robust estimation of power system harmonics using a hybrid firefly based recursive least square algorithm. *Int. J. Electr. Power & Energy Syst.* 80, 287–296. doi:10.1016/j.ijepes.2016.01.046

Song, P. C., Pan, J. S., and Chu, S. C. (2020). A parallel compact cuckoo search algorithm for three-dimensional path planning. *Appl. Soft Comput.* 94, 106443. doi:10.1016/j.asoc.2020.106443

Sun, J., Aboutanios, E., Smith, D. B., and Fletcher, J. E. (2019). Robust frequency, phase, and amplitude estimation in power systems considering harmonics. *IEEE Trans. Power Deliv.* 35 (3), 1158–1168. doi:10.1109/tpwrd.2019.2936885

Sweis, H., Shawagfeh, N., and Arqub, O. A. (2022). Fractional crossover delay differential equations of Mittag-Leffler kernel: Existence, uniqueness, and numerical solutions using the Galerkin algorithm based on shifted Legendre polynomials. *Results Phys.* 41, 105891. doi:10.1016/j.rinp.2022.105891

Tran-Ngoc, H., Khatir, S., De Roeck, G., Bui-Tien, T., and Wahab, M. A. (2019). An efficient artificial neural network for damage detection in bridges and beam-like structures by improving training parameters using cuckoo search algorithm. *Eng. Struct.* 199, 109637. doi:10.1016/j.engstruct.2019.109637

Xu, L., Chen, F., Ding, F., Alsaedi, A., and Hayat, T. (2021). Hierarchical recursive signal modeling for multifrequency signals based on discrete measured data. *Int. J. Adapt. Control Signal Process.* 35 (5), 676–693. doi:10.1002/acs.3221

Xu, L., and Ding, F. (2018). Iterative parameter estimation for signal models based on measured data. *Circuits Syst. Signal Process.* 37 (7), 3046–3069. doi:10.1007/s00034-017-0705-4

Xu, L., and Ding, F. (2017). Recursive least squares and multi-innovation stochastic gradient parameter estimation methods for signal modeling. *Circuits Syst. Signal Process.* 36 (4), 1735–1753. doi:10.1007/s00034-016-0378-4

Xu, L., Ding, F., and Zhu, Q. (2022). Separable synchronous multi-innovation gradient-based iterative signal modeling from on-line measurements. *IEEE Trans. Instrum. Meas.* 71, 1–13. doi:10.1109/tim.2022.3154797

Xu, L. (2022). Separable multi-innovation Newton iterative modeling algorithm for multi-frequency signals based on the sliding measurement window. *Circuits Syst. Signal Process.* 41 (2), 805–830. doi:10.1007/s00034-021-01801-x

Xu, L. (2022). Separable Newton recursive estimation method through system responses based on dynamically discrete measurements with increasing data length. *Int. J. Control Autom. Syst.* 20 (2), 432–443. doi:10.1007/s12555-020-0619-y

Xu, L., and Song, G. (2020). A recursive parameter estimation algorithm for modeling signals with multi-frequencies. *Circuits Syst. Signal Process.* 39 (8), 4198–4224. doi:10.1007/s00034-020-01356-3

Yang, X. S. (2022). MATLAB Central File Exchange. Avaliable at: https://www.mathworks.com/matlabcentral/fileexchange/29809-cuckoo-search-cs-algorithm September 30, 2022).

Yang, X. S., and Deb, S. (2009). "Cuckoo search via Lévy flights," in Proceedings of the 2009 World congress on nature & biologically inspired computing (NaBIC), Coimbatore, India, December 2009 (IEEE), 210–214. doi:10.1109/NABIC.2009.5393690

Yang, X. S., and Deb, S. (2014). Cuckoo search: Recent advances and applications. *Neural comput. Appl.* 24 (1), 169–174. doi:10.1007/s00521-013-1367-1

Yang, X., Yang, Y., Liu, Y., and Deng, Z. (2020). A reliability assessment approach for electric power systems considering wind power uncertainty. *IEEE Access* 8, 12467–12478. doi:10.1109/access.2020.2966275

Yu, J., Kim, C. H., and Rhee, S. B. (2020). Clustering cuckoo search optimization for economic load dispatch problem. *Neural comput. Appl.* 32 (22), 16951–16969. doi:10.1007/s00521-020-05036-w

Zubair, S., Chaudhary, N. I., Khan, Z. A., and Wang, W. (2018). Momentum fractional LMS for power signal parameter estimation. *Signal Process.* 142, 441–449. doi:10.1016/j.sigpro.2017.08.009

frontiers | Frontiers in Energy Research

TYPE Original Research
PUBLISHED 28 December 2022
DOI 10.3389/fenrg.2022.1097858

OPEN ACCESS

EDITED BY
Salah Kamel,
Aswan University, Egypt

REVIEWED BY
Youcef Belkhier,
Maynooth University, Ireland
Mohammad Ghiasi,
University of Regina, Canada

*CORRESPONDENCE
Younes Boujoudar,
younes.boujoudar@usmba.ac.ma
Hossam Kotb,
hossam.kotb@alexu.edu.eg

SPECIALTY SECTION
This article was submitted to Smart Grids, a section of the journal Frontiers in Energy Research

RECEIVED 14 November 2022
ACCEPTED 12 December 2022
PUBLISHED 28 December 2022

CITATION
Albarakati AJ, Boujoudar Y, Azeroual M, Eliysaouy L, Kotb H, Aljarbouh A, Khalid Alkahtani H, Mostafa SM, Tassaddiq A and Pupkov A (2022), Microgrid energy management and monitoring systems: A comprehensive review. *Front. Energy Res.* 10:1097858. doi: 10.3389/fenrg.2022.1097858

Microgrid energy management and monitoring systems: A comprehensive review

Aiman J. Albarakati[1], Younes Boujoudar[2]*, Mohamed Azeroual[3], Lahcen Eliysaouy[2], Hossam Kotb[4]*, Ayman Aljarbouh[5], Hend Khalid Alkahtani[6], Samih M. Mostafa[7], Asifa Tassaddiq[1] and Alexander Pupkov[8]

[1]Department of Computer Engineering, Faculty of Computer and Information Sciences, Majmaah University, Al'Majmaah, Saudi Arabia, [2]Department of Electrical Engineering, Faculty of Sciences and Technologies Fez, Sidi Mohamed Ben Abdullah University, Fes, Morocco, [3]High School of Technology Meknes, Moulay Ismail University, Meknes, Egypt, [4]Department of Electrical Power and Machines, Faculty of Engineering, Alexandria University, Alexandria, Egypt, [5]Department of Computer Science, School of Arts and Sciences, University of Central Asia, Bishkek, Kyrgyzstan, [6]Department of Information Systems, College of Computer and Information Sciences, Princess Nourah Bint Abdulrahman University, Riyadh, Saudi Arabia, [7]Faculty of Computers and Information, South Valley University, Qena, Egypt, [8]Department of Informatics, Siberian Federal University, Krasnoyarsk, Russia

Microgrid (MG) technologies offer users attractive characteristics such as enhanced power quality, stability, sustainability, and environmentally friendly energy through a control and Energy Management System (EMS). Microgrids are enabled by integrating such distributed energy sources into the utility grid. The microgrid concept is proposed to create a self-contained system composed of distributed energy resources capable of operating in an isolated mode during grid disruptions. With the Internet of Things (IoT) daily technological advancements and updates, intelligent microgrids, the critical components of the future smart grid, are integrating an increasing number of IoT architectures and technologies for applications aimed at developing, controlling, monitoring, and protecting microgrids. Microgrids are composed of various distributed generators (DG), which may include renewable and non-renewable energy sources. As a result, a proper control strategy and monitoring system must guarantee that MG power is transferred efficiently to sensitive loads and the primary grid. This paper evaluates MG control strategies in detail and classifies them according to their level of protection, energy conversion, integration, benefits, and drawbacks. This paper also shows the role of the IoT and monitoring systems for energy management and data analysis in the microgrid. Additionally, this analysis highlights numerous elements, obstacles, and issues regarding the long-term development of MG control technologies in next-generation intelligent grid applications. This paper can be used as a reference for all new microgrid energy management and monitoring research.

KEYWORDS

microgrid, energy management system, control techniques, monitoring system, IoT

1 Introduction

Real-time power flow management is a contemporary topic in scientific literature. It is gaining prominence to boost the intelligence and adaptability of multi-energy systems, such as smart grids, microgrids, smart homes, and hybrid electric vehicles (George and Ravindran, 2019; George and Ravindran, 2020; George et al., 2021). Microgrid (MG) is a small-scale grid that may unite consumers, conventional power sources, distributed renewable energy sources, and energy storage technologies to form a flexible, self-sufficient, and ecologically beneficial system. A microgrid can operate on AC, DC, or a combination of the two (hybrid mode), and it can be connected to the main grid in parallel or as an isolated power island (George and Ravindran, 2019; George and Ravindran, 2020).

In grid-connected mode, microgrids manage the voltage and frequency of the main power grid. The renewable energy sources are operated in maximum power point mode, supplying the system with the maximum electricity. In islanded mode, the microgrid disconnects from the main grid and relies on distributed energy resources (DERs) to supply load (Sen and Kumar, 2018; Ortiz et al., 2019). In all forms of operation, the balance between power supply and demand is one of the most critical factors governing the microgrid. In grid-connected mode, the main grid is necessary to maintain balance. In island mode, the microgrid must balance the load by increasing its generating capacity or distributing the burden (Kang et al., 2021).

Reduced greenhouse gas emissions, reactive power assistance for enhanced voltage profiles, decentralization of energy supply, heat load integration for cogeneration, auxiliary services, and demand response are among the benefits given by MGs. In addition, it reduces transmission and distribution system interruptions and line losses (Hirsch et al., 2018).

RESs have a high investment cost, whereas MGs have various constraints, including optimal energy consumption, control concerns, a lack of system protection and regulatory standards, and consumer privacy (Azeroual et al., 2020). Due to the increasing deployment of RERs that are intrinsically intermittent and the introduction of probabilistic controlled loads into MGs, research has centered on overcoming its energy management issues. To ensure that a MG operates economically, sustainably, and reliably, its EMS includes both supply- and demand-side control and system limits (Ghiasi, 2019). EMS provides various benefits, from generation dispatch to energy savings, reactive power support to frequency management, reliability to loss cost reduction, energy balancing to lower GHG emissions, and customer engagement to customer privacy (España et al., 2021).

Numerous studies have addressed several MG-related subjects, such as reactive power compensation procedures in MGs, control techniques for enhancing microgrid stability, and MG protection and control schemes. In addition, they studied droop control strategies, voltage, frequency regulation methods, and control strategies for inverter-based MGs (Boujoudar et al., 2020; Vaikund and Srivani, 2021).

They investigated the modeling, design, planning, and designs of hybrid microgrids (Ortiz et al., 2019) and an overview of AC and DC microgrids (Andishgar et al., 2017). In addition, they examined energy management control systems for microgrids (Malik et al., 2017; Tayab et al., 2017). In addition, the literature included evaluations of homeostatic control-based energy-efficient micro generation systems (Amrr et al., 2018), methods for MG uncertainty quantification (Ghiasi et al., 2021a), and a review of network technology-based energy efficiency in buildings and micro generation systems (Fotopoulou et al., 2021). Table 1 contains a compilation of reviews of MG's energy management.

Unlike other literature studies, this study presents a comprehensive and critical analysis of microgrid energy management systems and control technologies. In addition, the protection and management of Internet of Things-based microgrid monitoring systems are investigated. Several uncertainty quantification approaches are discussed to handle renewable energy resources' volatile and irregular nature and load demand.

The main goals of this review are to study the development of the MG and EMS as well as to investigate the MG's components, implementation, classification, objective functions, quality, and protection mechanisms. This study discusses both the present technology and the issues that are addressed with MGs and EMSs. This paper includes an extensive literature review covering the most recent developments in the field of networked MGs. The most important parts of this article are summarized here.

1) A comprehensive discussion on the advantages of MGs as well as their architecture, energy management functions, and topologies in MGs.
2) A comprehensive analysis of the bilateral EMS schemes in MMG, taking into account resilience and transactive operations.
3) Energy management system control techniques used with advantages and drawback of each methods.
4) Microgrid monitoring system using IoT based communication and bulk integration of power sources in MGs. Brief explanations of the most used techniques SACADA system and Thingspeak.

The remainder of the paper will be organized in the following manner: In Section 2, we will discuss the Microgrid control structure and demerits as well as its different functionalities and review the control schemes of the MG and the objectives of an EMS. Section 3 will examine the Microgrid Monitoring systems, which provides an overview of these approaches. Section 4 presents the perspective and discussion. Finally, the Conclusion is documented in Section 5.

TABLE 1 The reviews related to energy management of MG.

References	Details
Fotopoulou et al. (2021)	The writers examine the field of microgrid energy management in depth and offer insightful commentary. This article summarizes many uncertainty quantification methodologies to manage the intermittent and unpredictable nature of renewable energy supply and load demand
George et al. (2021)	An in-depth analysis of the various MG controls is presented. Mainly, you can classify them into one of four management structures: centralized, decentralized, distributed, or hierarchical
Soliman et al. (2021)	The capabilities of multiagent systems concerning energy management, MG system operation, security, and stability are thoroughly explored
Sen and Kumar, (2018)	The authors defined a microgrid and painted a detailed picture of current microgrid motivators, practical applications, challenges, and future potential
Kumar and Saravanan, (2017)	The research delves further into the protection issues and potential solutions related to three distinct types of microgrid architectures: alternating current (AC), direct current (DC), and hybrid. Both AC and DC microgrid protection methods are evaluated, as are the challenges inherent to defending microgrids in both configurations
Albarakati et al. (2021)	The authors comprehensively analyze MG control systems, categorizing them based on features like protection, energy conversion, integration, benefits, and limitations. Both simple and complex methods of control for efficient energy use in MG applications are discussed

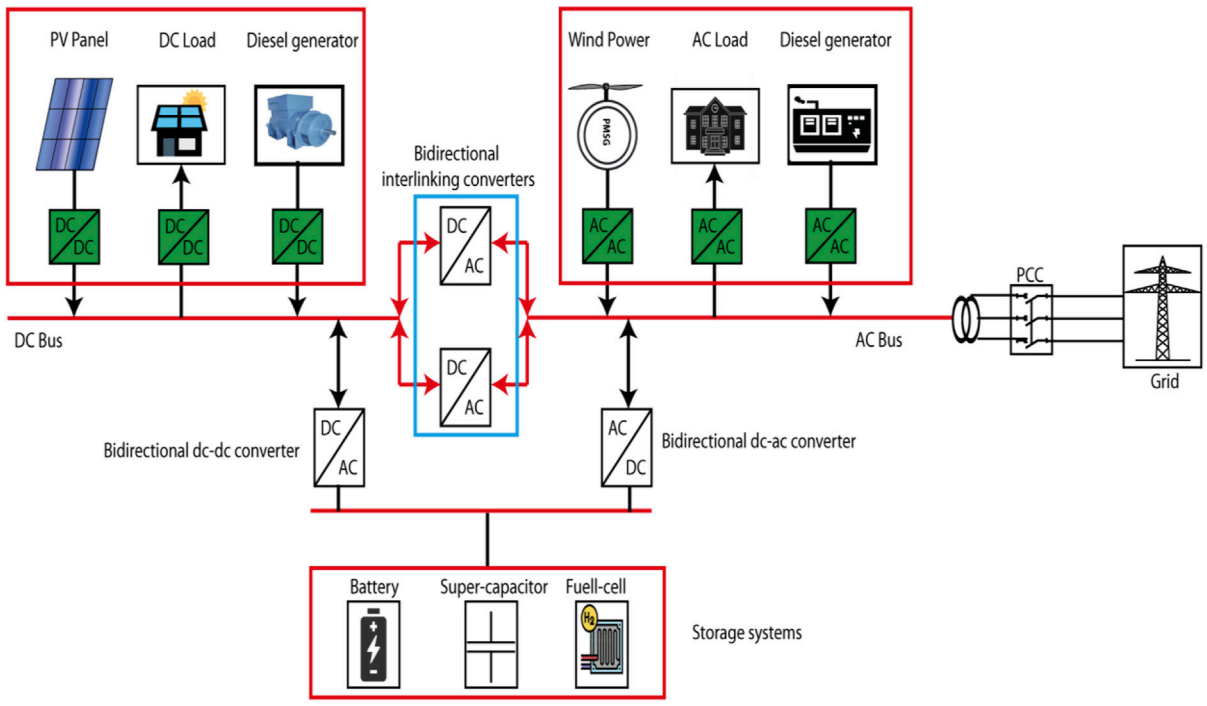

FIGURE 1
The microgrid structure.

2 Microgrid control structure

"A computer system comprising a software platform providing basic support services and a set of applications providing the functionality needed for the effective operation of electrical generation and transmission facilities to assure adequate security of energy supply at minimum cost" (Coelho et al., 2017) is how the International Electrotechnical Commission defines an EMS in the standard IEC 61970 on EMS application program interface in power systems management.

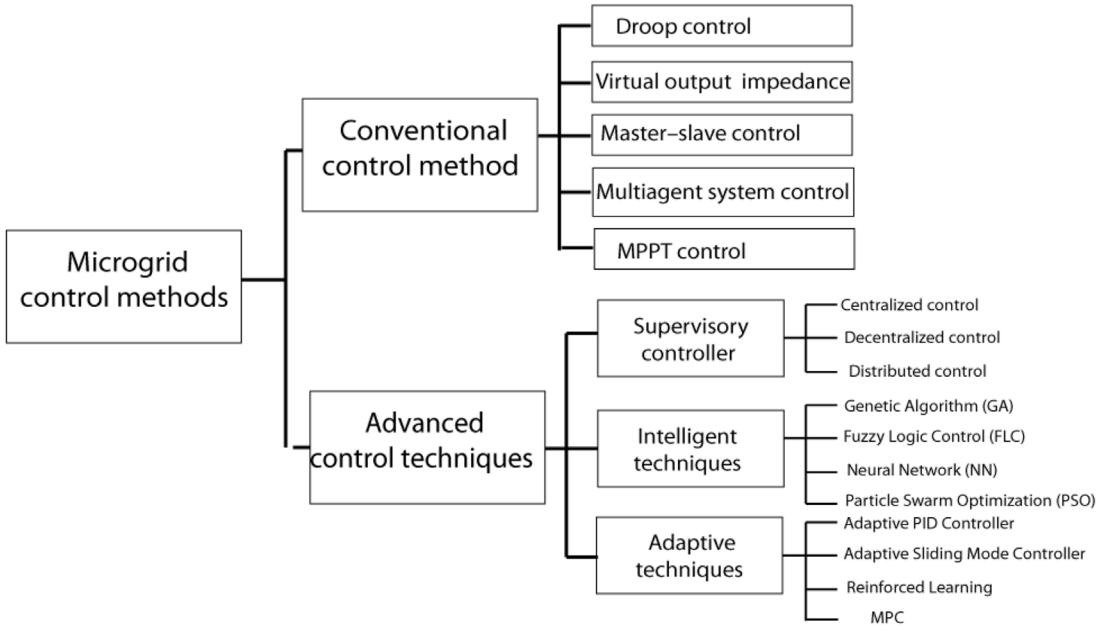

FIGURE 2
Classification of microgrid control techniques.

These features are typical of an MG EMS, including decision-making strategy modules. Optimal decisions are transmitted to each generating, storing, and loading unit thanks to DERs/load forecasting, control, supervisory, energy management, and data acquisition modules, among others (Dagar et al., 2021).

MGs can be controlled in ways other parts of the distribution system cannot, making this an important area of study and application. It isn't easy to centrally manage MGs due to their dual functionality (grid-connected and islanded as represented in Figure 1) (Al Alahmadi et al., 2021). Therefore, separate management systems are often developed for each operation mode. Because there are typically multiple DERs and loads connected to a microgrid, coordination challenges arise. When applied consistently, MG control is highly successful (Su and Wang, 2012).

Therefore, a necessary control technique is needed to allow a seamless transition and automation in the event of a sudden disconnection. This is essential for achieving the goal mentioned above regarding power flow between MGs and the power system. In addition, a suitable control strategy is necessary to handle the stochastic generating behavior of DG units in MGs.

The main object of the control strategy is to ensure the microgrid balance during all changes in meteorological conditions and load demands. Stabilizations of voltage and frequency transduce the microgrid balance. Therefore, all proposed techniques in the literatures use frequency or voltage control to ensure the microgrid balance as described.

Below, we will break down the several types of traditional control that can be used to boost MG systems' effectiveness and dependability to the delight of their clientele.

Various control techniques outlined in Figure 2 (Albarakati et al., 2021) present MG control types typically employed in MG to improve MG's power and operations. The microgrid control regulates reactive power and MG output voltage.

2.1 Conventional microgrid control techniques

Conventional control methods have been utilized extensively in MGs to maintain voltage and frequency stability and regulation, especially during network failures. MG management is a multi-objective, complicated control system encompassing multiple technical domains, periods, and physical levels. Several areas of interest include load power sharing, voltage/frequency and power quality regulation, market participation, short- and long-term scheduling, etc. (Singh et al., 2020; Singh et al., 2021).

To appropriately handle these challenges, a hierarchical control scheme has been designed and widely regarded as a standard method for efficient MGs management. For example, (Han et al., 2016), describes secondary control for energy management functions and third-level control for multiple MG interactions. Hierarchical control has three levels of control: tertiary, secondary, and primary. Due to the need to

TABLE 2 The conventional control approaches in the microgrid.

Control method	Parameters	Technique	Advantages
Virtual output impedance Mahmoud et al. (2017)	Voltage, reference, voltage impedance, active, and reactive power	Summation of virtual output impedance to balance reactive and Q power-sharing	Provides proper active and reactive power sharing transient response with no frequency variations
Droop control Kaur et al. (2016)	Voltage, frequency, active, and reactive power	Balanced load current sharing is achieved under-voltage v/s current droop characteristics by modifying output voltage and frequency	Allows active power-sharing of DERs, which improves system stability and flexibility by eliminating the need for a communication link in decentralized control
Multiagent system (MAS)-based control Ahmethodzic and Music, (2021)	Voltage, current, frequency, and power	The MS or load can function as a separate agent, communicating with others in the system to coordinate efforts and share knowledge	Economics and voltage regulation are at the heart of EMS. makes MG controls more robust, secure, and adaptable; addresses MG coordination control issues
Maximum Power Point Tracking (MPPT) control Sahri et al. (2021)	DC/DC converter, solar irradiance, temperature, load power, voltage, and current	The DC/DC converter between the PV panel and the batteries can regulate normal operations like MPP looking	Determine the output RESs' maximum power given irradiance, temperature, and load profiles; act as a converter to fine-tune the duty cycle and input impedance of control signals; boost the effectiveness of renewable energy installations

TABLE 3 Comparisons related procedures (De Santis et al., 2017; Albarakati et al., 2021)].

Method	Parameter	Applications	Advantages
Adaptive PID Controller De Santis et al. (2017)	Voltage and courant	An adaptive PID controller's gain parameter is determined through optimal tuning	Simple to implement; does not necessitate system dynamics to be realized; There are only three variables to optimize
Adaptive Sliding Mode Controller Hussein and Shamekh, (2019)	Voltage and frequency; power quality control	Changing the control structure allows the approach to track the system output within predetermined limitations. low tracking error in steady-state	Fast dynamic response; non-linear controller; robustness under system parameter changes and external and internal aberrations
Model predictive control Umuhoza et al. (2017)	MG operations control the inverter output voltage references of power electronic converters for consistent power-sharing	Fast dynamic response; can accommodate restrictions; no modulator and variable switching frequency; no pulse width modulator is required	A lot of computational power is required

maintain real-time frequency and voltage stability in the case of a disruption, primary control levels are considered the most challenging (Zahraoui et al., 2021):

Local electricity, voltage, and current are regulated at the main level. It often executes control operations over interface PCs by adhering to the configuration points specified by upper-level control.

- Secondary level: In the current system, secondary control is positioned above primary control. Along with other things, it handles harmonic compensation, voltage imbalance, and voltage/frequency restoration. Additionally, it is in charge of synchronizing and exchanging electricity with the main grid and other MGs.
- Tertiary management seeks to incorporate intelligence throughout the entire system. Thus, tertiary control will optimize the MG operation in light of competing interests, particularly efficiency and economics. In order to carry out the optimization activities, Information and Communication Technology (ICT) is a significant enabling tool, as it facilitates the acquisition of knowledge from both the MG side and the external grid. Decision-Making (DM) algorithms are used to examine data and decide what steps to take next.

The conventional control approaches in the microgrid are summarized in Table 2.

2.2 Advanced MG control techniques

Improved control performance is a common goal for MG control systems. Hence, sophisticated control techniques are routinely used in these systems. These methods include, for

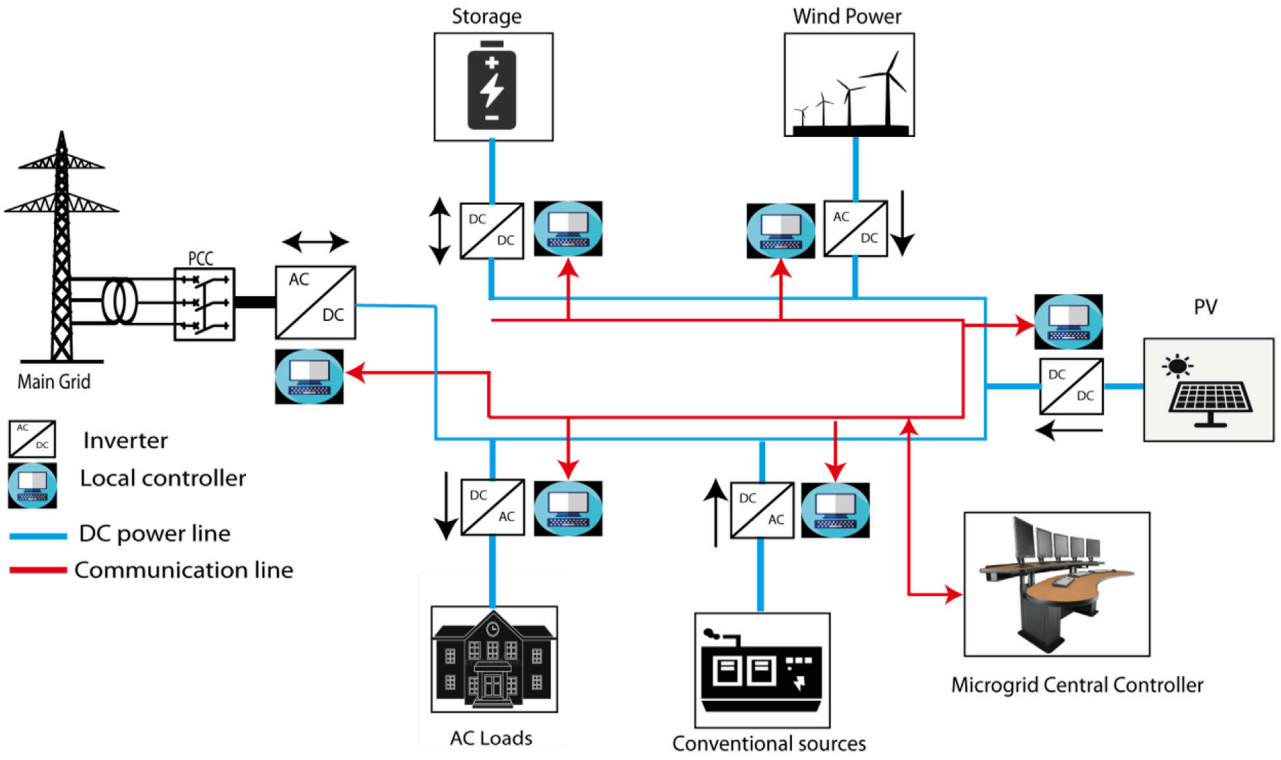

FIGURE 3
Architecture of centralized control.

instance, intelligent and adaptive approaches to optimizing the parameters involved in control systems to generate resilient controllers. In the following, we will go over some methods that can be used for MG management. Supervisory controllers in MG energy management can be categorized into three subfields: centralized, decentralized, and distributed. The objective is to improve system performance by adding intelligence while delivering critical functions like power quality monitoring. The relevant group of supervisory controllers is discussed in the next section (Tayab et al., 2017).

2.2.1 Centralized control scheme

The brain of the operation, so to speak, is what we mean when we talk about centralized control schemes. A centralized control management system makes it easy to build and monitor the system in real-time to provide a safe environment. The MG component data and an external grid for the optimization process are necessary for effective operation. We investigated the concept of secondary control for a centralized MG controller in (Jimeno et al., 2011). Hierarchical control, which includes the system's primary, secondary, and tertiary levels, provides an explanation for the MGs' centralized control (Atawi and Kassem, 2017).

Centralized microgrid controls are illustrated as a hierarchical network in Figure 3. One Central Processing Unit (CPU) makes all the important decisions in a centralized control setup. It communicates them to the rest of the system's components based on data and calculations it has received from those components. The MG's main controller handles every single control and measurement. Local Controllers (LC) obey orders and depend on the MGCC (microgrid central controller) when operating in grid-connected mode but operate autonomously in islanded mode.

2.2.2 Decentralized controls

Decentralized MG administration (Figure 4) has emerged in MG systems, enhancing flexibility and scalability. Due to its plug-and-play functionality, this controller gives great operational flexibility and avoids a single point of failure. Due to decentralization, frequency and voltage regulation, DER coordination, and energy management may all be decentralized (Roslan et al., 2019). In decentralized control, local controllers are primarily responsible for optimizing their production for demand satisfaction and exportation to grids, given current market prices. Multi-Agent Systems (MAS) for decentralized energy management represent an intriguing aspect of supervisory controller research (Sahoo et al., 2021). A MAS is a

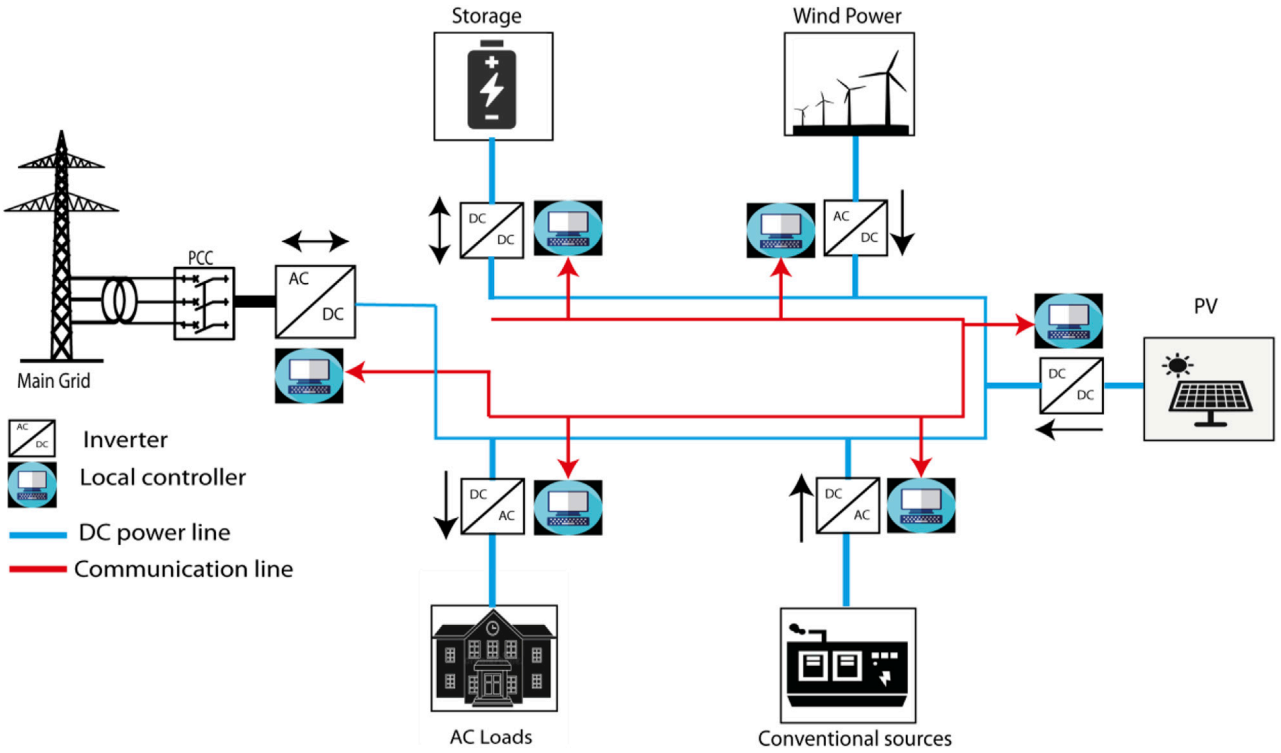

FIGURE 4
Architecture of decentralized control.

system composed of several intelligent agents that give local information and interact with one another to pursue various objectives (Khorsandi et al., 2014; Sabri et al., 2019) autonomously. Moreover, a MAS for real-time MG operation is implemented, focusing on generation scheduling and demand-side management, as described in (Al-Saadi et al., 2021). Consequently, there are numerous approaches to the MAS method for the decentralized control of MGs, as explained in detail in (Roslan et al., 2022).

2.2.3 Distributed controls

The distributed control scheme for microgrid management and stability can be described as a method in which local controllers connect with a central controller *via* communication and networking channels. The central controller is in charge of system monitoring and control, while the local controllers are in order of the other MG components individually (Raya-Armenta et al., 2021).

The following are some of the many advantages of taking this strategy:

- Enhanced sturdiness.
- Improved decision making and system analysis.
- A common control law that can be easily implemented at the central and local levels.
- System monitoring and real-time communication.

According to some studies, the tertiary control level in an MG system may be dispersed. During the deployment of distributed control to compensate for a voltage imbalance in the crucial bus, a current study found power quality disturbances on the generator side and the local bus.

2.3 Microgrid intelligent techniques

A range of intelligent solutions in power system applications can increase control system performance and power source stability. Furthermore, as the number of DG units in MGs increases, so does the complexity of fine-tuning the system's control settings. Many complex strategies have also been employed to control such parameters in MGs, considering economic load dispatch in MG systems (Azeroual et al., 2022). EMS solutions based on artificial intelligence have been used to increase the efficiency and performance of MG systems, allowing them to fulfill demand while generating the most energy

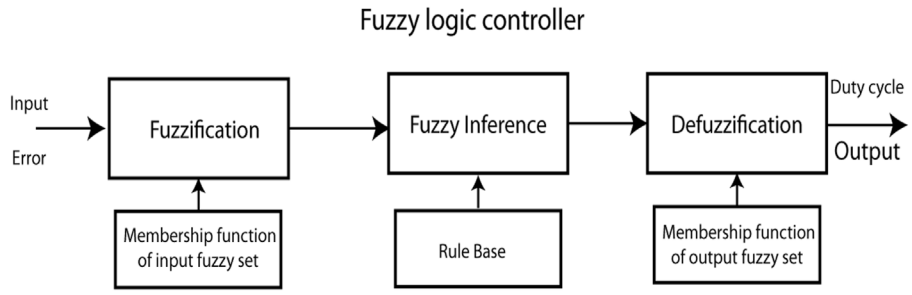

FIGURE 5
Fuzzy logic control system.

(Chaudhary et al., 2021). Fuzzy logic and neural network techniques consider anticipated values and improve battery lifetime and grid energy trading. These methods are the most commonly employed in microgrid energy management (Pan et al., 2021).

2.3.1 Artificial neural network controller

Data is sent to the central processor *via* a neural network controller at a delayed rate, much like the human brain. A closed-loop design is used to transfer information to each other while minimizing the error or intended function. The fundamental architecture contains an input/output layer, activation function, weights, and hidden later. Allowing for greater flexibility and a simpler implementation for a variety of operating situations, neural networks are a more intelligent and self-learning controller. MG's stability is further aided by neural networks' resilient behavior and swift decision-making capabilities while they are working. In the area of research, Neural Networks (NNs) have gotten a lot of interest. ANNs are among the most successful strategies for optimizing, controlling, and identifying system parameters (Justo et al., 2013).

Furthermore, in MG systems, NNs can tackle difficulties with non-linear data techniques in large-scale systems. Fault tolerance, stability systems, prediction, parametric optimization and identification, self-learning, and load sharing are all examples of NN applications. Furthermore, in grid-connected mode, the main utility grid determines and maintains the nominal voltage and frequency of the entire system. The ANC is used to control the bidirectional DC-DC converter by generating the duty cycle to keep the DC Bus voltage at the reference voltage value in the DC microgrid (Ali and Choi, 2020).

2.3.2 Fuzzy logic controller

The original proposal of the fuzzy theory may be found in (Zia et al., 2018), which was created to provide numerical values for intangible ideas. Fuzzy-logic reasoning is used in the design of a controller in a fuzzy-control system. So-called fuzzy logic aims to create a gray area between zero and one by breaking down logical problems into smaller, more manageable chunks. Figure 5 is a schematic representation of the foundations upon which fuzzy logic control rests. Fuzzification, membership, rule base, fuzzy inference, and defuzzification are all part of the FLC. Distributed control systems have recently incorporated fuzzy logic controllers to choose optimal distributed controller parameters for MG system performance (Rangu et al., 2020). Fuzzy Logic Control (FLC) is an interesting method for MG systems. Many researchers have explored the potential of fuzzy logic methods for resolving the parameters of MG systems. The automatic definition of a fuzzy rule for a fuzzy controller is proposed in (Singh et al., 2022), based on the Tabu search algorithm scheme. A study presented a GA-based fuzzy gain scheduling technique for load frequency regulation in power systems. The GA will construct a fuzzy system without any manual input from the user, saving time and effort that would otherwise be spent on designing and writing fuzzy rules (Hafsi et al., 2022).

The foundations of fuzzy logic control are depicted in Figure 5 as a schematic. The FLC includes fuzzification, membership, rule base, fuzzy inference, and defuzzification.

2.4 Microgrid adaptive techniques

In recent years, adaptive control strategies have been a popular research area. These strategies can be used to maintain system stability, robustness convergence, and optimization in MG applications. Furthermore, these strategies are primarily employed in MG applications to solve and cater to uncertainty parameters and disturbance occurrences. The following section examines a few adaptive approaches often used in MG applications to regulate voltage and frequency variations and hence attain optimum power generation values as summarized in Table 3.

3 Microgrid monitoring system

The monitoring system checks all the equipment's real-time running status and controls all the equipment to ensure it is safe and stable. Ensuring that the monitor system is always up to date is essential. We ensure that the system is always running in real-time through the software and hardware in this micro-grid.

3.1 IoT

Future network technology, known as the IoT connects information about people, things, and processes to the Internet to create, gather, exchange, and use data. The IoTdid not appear overnight; it has been there for a while. Many other names have referred to it, and as technology develops, so do its technologies and ideas. Machine-to-Machine (M2M) and Radio frequency Identification (RFID) are two examples of good ideas (object intelligence communication). Everything is connected to the Internet through a concept known as the "Internet of Things." However, why should items be connected to the Internet, not how should they be connected to the Internet? The ultimate objective of the Internet of Objects is to intelligently connect everything in our environment to the Internet, automate it with minimal human involvement, and then deliver knowledge and improved services to people through information fusion across several connections. For assessing and disseminating the resulting information, it is essential to connect human, physical, geographic, and intangible data (Siddique et al., 2019).

The term "Internet of Things" describes a notion that integrates real objects and labor. Put another way, it includes everything we come into contact with daily, such as people, machines, electrical equipment, bicycles, glasses, watches, clothing, cultural artifacts, animals, and plants. A solid connection to the information network, intelligent interfaces, and physical and virtual entities with distinct identifiers and attributes are other components of the IoT (Roy et al., 2020).

IoT devices may interact with and respond to objects, environments, data, and environmental information as active participants in business, news, and social activities. Whether a human is directly involved, an object responds autonomously to a physical event in the real world or runs a process that creates a service or starts a certain activity. The interface of the service type enables Internet-based communication with such smart devices and searches for or exchanges data relevant to the status of the items while taking security and privacy concerns into account (Hu et al., 2021).

Microgrids' dependability, stability, security, and environmental sustainability are all guaranteed by the IoT. With the help of the Internet of Things, a futuristic network technology, data generated by people, things, processes, and other objects can be produced, gathered, shared, and used. IoT technologies have recently gained popularity due to their development and use in SMG applications. Bidirectional connectivity, self-healing, decentralization, and smart metering are crucial IoT technologies. A flexible and intelligent EMS must monitor and control all SMG variables in real-time (Vermesan et al., 2011).

3.2 Microgrid monitoring system using IoT

MG energy management systems will become substantially more efficient due to collecting and analyzing data from power sources *via* IoT. Additionally, utilities may perform operational duties such as shortening outage investigation times, optimizing load balancing, optimizing line voltage, finding faults, decreasing service costs, and restoring services more quickly. Additionally, using IoT technology for smart homes, Energy Storage Systems (ESS), Electric Vehicles (EVs), charging stations, and variable loads increases the flexibility and dependability of the SMG (Ahmad et al., 2017). As seen in Figure 6, IoT may improve energy efficiency by managing Demand Response (DR), collecting data, sharing, and trading energy. An optimum DSM system built on the IoT is necessary to address energy conservation and management challenges. This technique should provide a continuous energy supply while preventing power surges in the future (Zamfir et al., 2016).

The microgrid is equipped with various sensors for data collection (current, voltage, power, temperature). The data collected from these sensors is analyzed in real-time to determine the optimal control strategy based on current conditions (occupancy, energy consumption-production, and weather conditions data). Additionally, this data must be saved for subsequent study, notably to build predictive control techniques (Elmouatamid et al., 2019). In addition, multiple platforms that incorporate IoT technologies are installed for data collecting, processing, and visualization, and with the upcoming generation of wireless. In the present day, a smart microgrid is all about electronic communication networks, electronic billing systems, and smart meters. The smart microgrid will be equipped with automated distribution and secure DER administration and generation on the road to 5G. Automatic power generation and distribution *via* real-time load balancing and massively distributed generation services (Sedhom et al., 2021) is the focus of a smart microgrid in the 5G age. The IoT is used in various applications, including smart grid, microgrids, intelligent buildings, and intelligent control devices, to monitor and track essential information about the target environment. Numerous studies have used IoT solutions for energy management and system monitoring in a microgrid (Sylcloud Smart Micro Grid, 2022).

Reference (Khan et al., 2018) proposes a communication platform that may operate in both central and dispersed modes in the event of a communication hierarchy failure. This research

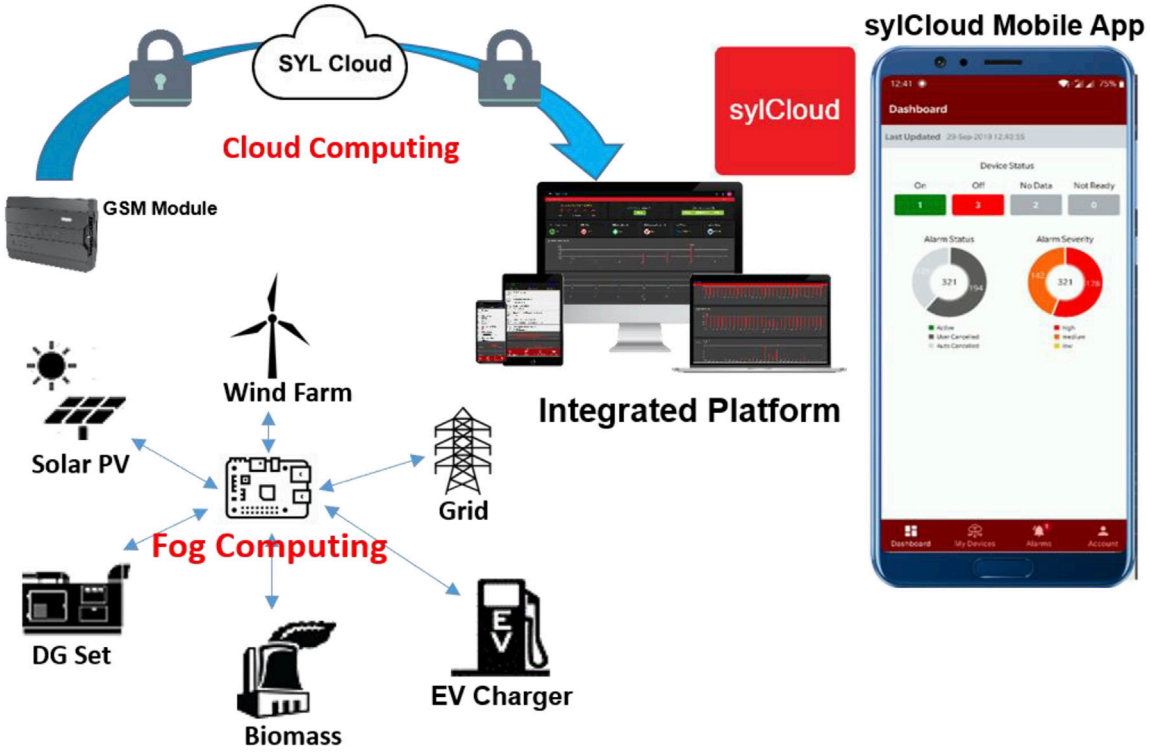

FIGURE 6
Applications of IoT in intelligent power grids (Khatua et al., 2020).

explores the effect of a hybrid communication system with communication delay on the MMG EMS. In other words, the hierarchical communication system supports the EMS in reducing MMG's operating expenses.

The authors of (Draft, 2016) demonstrate the importance of the IoTin building and deploying intelligent microgrids, including their benefits, difficulties, and hazards and several processes, techniques, and procedures for controlling and protecting intelligent microgrids.

In (Ali and Choi, 2020), the authors study the real-time features of security mechanisms for IoT connectivity. In addition, the influence of IoT protocols on the real-time needs of smart grid operations are investigated (protection, control, and monitoring).

The authors of (Moghimi et al., 2018) employed an IoT system to monitor company energy use. The monitoring platform incorporated various technologies, including digital instrumentation, communication networks, software, and databases, with the aims of central administration, decentralized control, and remote monitoring.

In (Ghiasi et al., 2022), authors have created a remote energy monitoring system based on the IoT to control, plan, optimize, and conserve energy in smart grids and homes. A system that efficiently collects energy resource information in the house reduces energy wastage and provides information for analyzing energy consumption patterns.

In (Kondoro et al., 2021), the authors propose an EMS based on an advanced IoT system. The framework system was implemented in the building to unify and standardize the things that comprise the built environment. Appropriate guidelines are developed with intelligent energy management and smart Buildings' available mode of operation.

The authors of (Khoa et al., 2021) present a real-time monitoring system using web server technology for the microgrid. The Arduino embedded system was used as a control core, and an Ethernet network module was used for the data acquisition and the wireless transmission.

In this study, an IoT system was used to measure, track, and record a few power quality (PQ) aspects of a microgrid system (Ku et al., 2017). PQ parameters are measured in the hardware unit by three PZEM-004T modules that have non-invasive Current Transformer (CT) sensors installed. The sensors' data is gathered simultaneously by an Arduino WeMos D1 R1 ESP8266 microcontroller and transmitted to the server through the Internet.

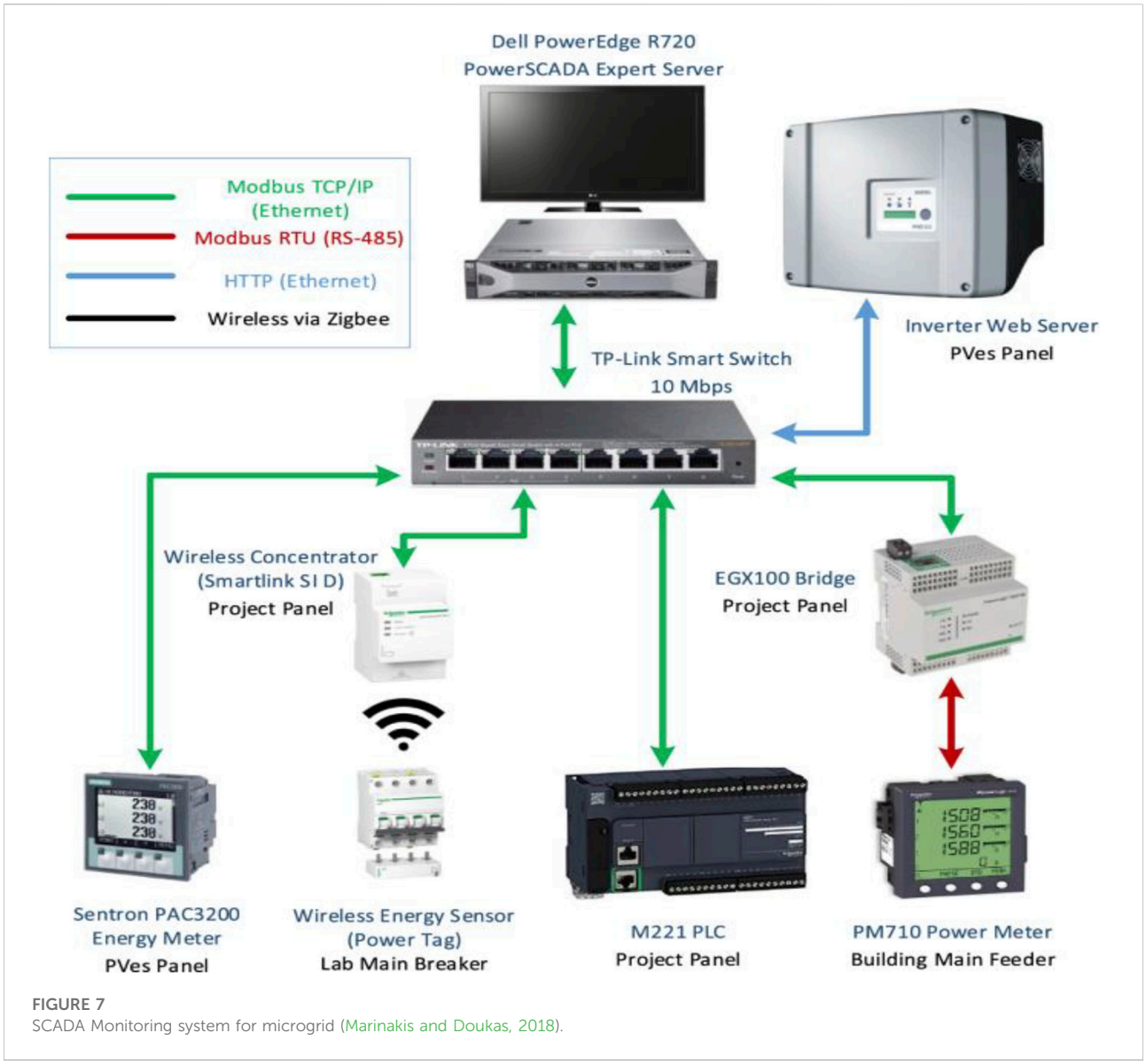

FIGURE 7
SCADA Monitoring system for microgrid (Marinakis and Doukas, 2018).

3.3 Microgrid monitoring system using SCADA

A Supervisory Control and Data Acquisition (SCADA) system is another option for microgrid monitoring and energy management in small and large-scale buildings (Residential, Commercial and Industrial). A SCADA system comprises two components: a hardware system for data collection, communication, control, and operation, and a software system for data storage, elaboration, visualization, optimization, and careful management (Figure 7). The SCADA system, a type of middleware used in intelligent monitoring systems, is discussed in this section. The SCADA system is mostly used to read bundled microgrid data. The SCADA system accesses the microgrid data before saving it in the MySQL database (Marinakis and Doukas, 2018).

Four major kinds of SCADA hardware functions exist. The first is the Remote Terminal Unit (RTU), whose primary role is to gather data for the SCADA system. The second role is the communication platform, which facilitates the establishment of data links between devices (Zhuang et al., 2017). The third function is the Programmable Logic Controller (PLC), which is needed to ensure that the MG operates properly in grid-connected and island modes (Khoa et al., 2021).

The Human Machine Interface (HMI), a software component of the SCADA system, is critical for controlling and monitoring. The SCADA component's conventional structure is server-client, with the primary SCADA application

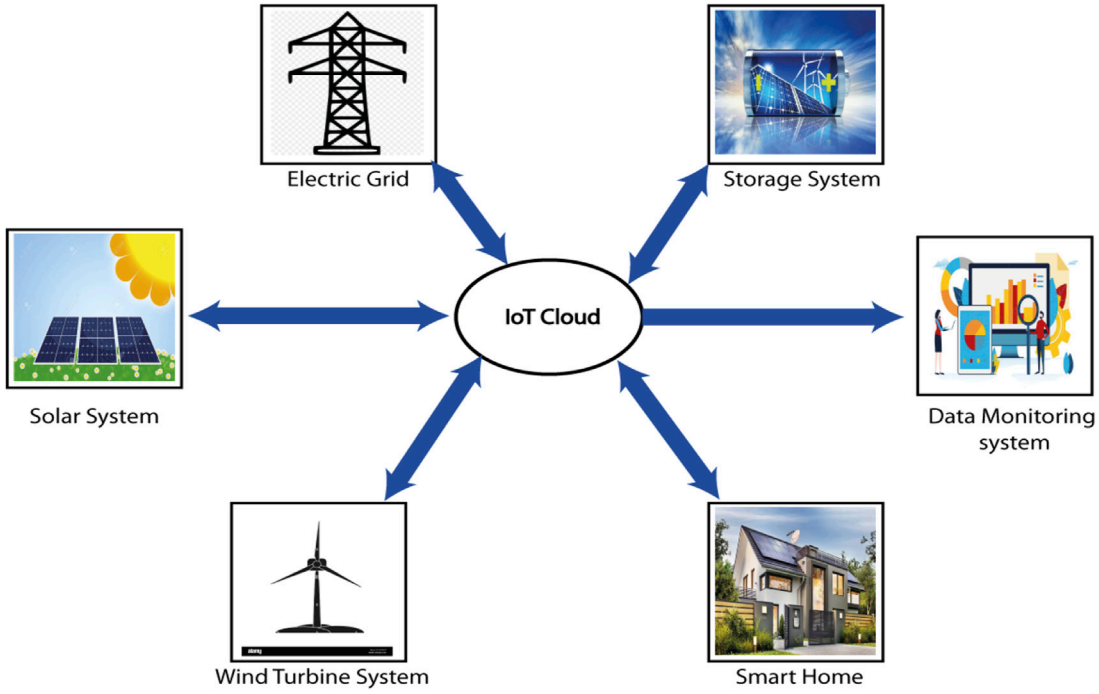

FIGURE 8
Microgrid monitoring using Cloud computing.

operating on the server and the HMI running on the client. Numerous articles examined various aspects of SCADA use in MGs. By comparison, this work is unusual because it employs all four SCADA elements to accomplish a new aim of intelligent energy management (Ali et al., 2021).

3.4 Microgrid monitoring system using cloud computing

Another approach to microgrid monitoring is based on the communication between powers sources and the monitoring platform using the cloud. The measured data is sent directly to the cloud by measurement unit as shown in Figure 8.

Cloud computing and the IoT have evolved independently thus far. Non-etheless, their integration into microgrids has demonstrated significant reciprocal benefits. The cloud, in particular, can provide an efficient and practical option for administering IoT services and offering some applications to help in data analysis. Many researchers have been used this structure of monitoring due to its benefits in high-quality data transmission (Ghiasi et al., 2021b).

The authors in (Kermani et al., 2020) present a real-time design of efficient monitoring and control of grid power systems using the remote cloud server to improve the universal control and response time, with a new security approach in access to user authentication.

The authors of (Gupta and Rastogi, 2021) provide a cloud computing platform for microgrid power management. The strategy links the system's current computer and storage capabilities with external computing devices, enhancing data processing and interaction and providing a cost-effective and rapid mechanism for microgrids to meet their computational requirements.

The authors in (Gui and MacGill, 2018) use a low-cost IoT-based innovative communication platform to implement an optimal energy management technique for microgrid systems. The suggested system's energy monitoring and control architecture is built on a cloud-based Remote Monitoring Unit (RMU) that communicates *via* a Message Queuing Telemetry Transport (MQTT) server and Thingspeak Middleware.

Thingspeak is a cloud-based IoT analytics platform that lets users visualize and analyze real-time data streams. It can do online data stream analysis and processing and immediately visualize data presented by system gateways. Thingspeak is frequently used in IoT systems that require analytics for prototyping and proof of concept (Khatua et al., 2020). Thingspeak is an IoT platform that stores data delivered by apps or devices *via* channels. You have numerous options for

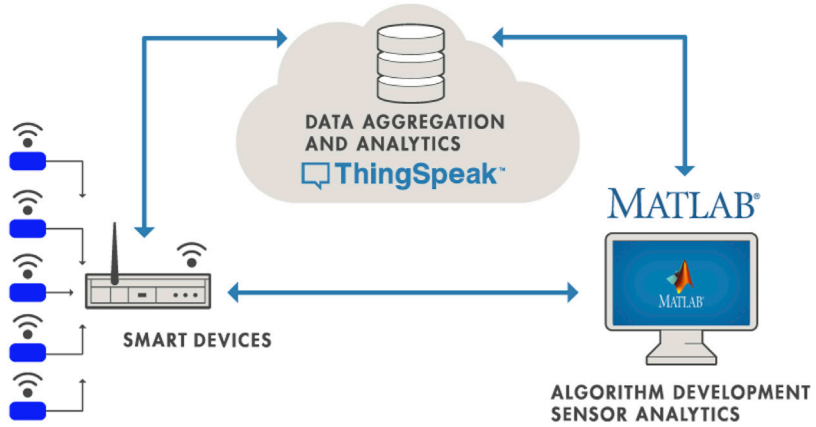

FIGURE 9
The architecture of IoT connectivity with Thingspeak.

writing data to your Thingspeak platform: HTTP requests through the REST API, MQTT. Thingspeak is frequently used in IoT systems that require analytics for prototyping and proof of concept (Figure 9).

Due to the development of the connection between Matlab and Thingspeak by adding the IoT Matlab toolbox. Thingspeak is the most used platform during the simulation of the power system at Matlab/Simulink. The quality of communication and microgrid monitoring depends on the sensors used for measurement (Bera et al., 2014).

To make an intelligent distribution system functional, many networks and devices must come together to create a dependable system. The IoT and smart meters are the significant components that will transform the traditional link between consumer and operator into an innovative interdependent system capable of quicker and more reliable communication (Karthick et al., 2021). In recent years, disc-type meters have been phased out in favor of electronic integrated circuit embedded meters, which distribution utility companies effectively employ to provide consumers with authentic and electronic invoicing (Chen et al., 2019). The requirement for enhanced flexible billing and management of billing information in the case of two-way power flow necessitates intelligent meter technology. In commercial and industrial settings, smart meter technology gives customers daily market values for their energy use (Mehrizi-Sani and Iravani, 2010). Historically, Automated Meter Reading (AMR) technology collected data on customers' and utilities' energy use, resulting in a one-way flow of energy and communication. The AMR, a recent advancement in Advanced Metering Infrastructure (AMI), enables bidirectional communication and power flow between the meter and the central control system (Mohanty et al., 2016).

A smart grid is a novel approach to transmission and distribution, and intelligent meters play a critical role in connecting with consumers and collecting data as an essential element of the smart grid. The smart meter comprises three major components: network management, advanced metering element, and data management unit (Vuddanti and Salkuti, 2021). The smart meter has a memory chip that enables users to monitor their energy consumption using a software interface, allowing it to communicate in two directions (Zheng et al., 2013). The smart meter regulates the functioning of the distribution system's switches and recloses, ensuring an efficient and reliable delivery system. Due to the smart meter's two-way communication capability and energy interface, it is possible to regulate distribution infrastructure by sending directives to the control center, a process known as distribution automation at the load end (Guo et al., 2015). The benefit of the smart meter is that it enables central control to intervene quickly when tampering occurs, based on the accessible rapid report supplied by the smart meter as part of the data collection process (Barai et al., 2015). This contributes to reducing power theft while also enhancing the security of the power system. The availability of daily billing information to consumers enables them to regulate their loads and save money using the smart meter (Avancini et al., 2021).

4 Perspective and discussion

This work presents an extensive literature analysis of the issues of stability, control, and power management of AC, DC, and hybrid AC/DC microgrids. According to the research, AC and DC microgrids are both very common. Still, hybrid AC/DC microgrids are gaining popularity due to their lower conversion losses, greater reliability, and increased efficiency. The microgrids use a hierarchical control architecture that features main, secondary, and tertiary controllers in the chain of command. The primary control,

often known as the LC, is built into the DER to guarantee dependable operation by preserving stable voltage and frequency levels and regulating power. Secondary control regulates microgrid communication protocols to improve power quality by reducing steady-state voltage and frequency mistakes created by primary control. The main control caused these faults. The tertiary management manages the power flow between the main grid and the microgrid to ensure that the system operates cost-effectively. Nevertheless, possibilities to develop improved planning, operation, and control strategies. It is possible to do extensive studies in these areas to improve microgrids' development, operation, and control.

- The microgrids require accurate system modeling for efficient planning and operation. Considering the stochastic character of the integrated DGs in microgrids, a new or enhanced model can be designed to reduce planning and operation expenses.
- It is possible to redesign or develop several advanced control approaches, such as adaptive control, model predictive control, robust control, and optimum control, to ensure that microgrids have efficient DC and AC buses voltage management and concurrent power sharing.
- Integrating renewable sources in microgrids lowers the overall inertia of DC microgrids, decreasing the microgrids' voltage control performance. Even though certain control strategies have been established to deal with such a scenario, more work should be undertaken in this regard because the DC microgrid is becoming a system based entirely on renewable energy.
- In the future, MGs may use various energy sources, such as large-scale decentralized resources, to be flexible and fit their needs. The way energy is made and moved could change because of energy storage systems.
- Future MGs could improve at finding faults and fixing themselves, which would cut down on recovery time, get more loads back online, and find gaps between research and implementation.
- The IoT makes it easier for real-time platforms to form and connect
- decentralized and transactional energy markets in a very important way. From their previous research, the authors also know that two-way energy exchanges between customers and producers will likely be the most difficult in the future. However, new technologies are likely to solve this problem.
- Deep learning, like ANN, could be used in MGs instead of classical and mathematical methods to achieve dynamic changes in energy flow, lower GHG emissions, and better protection for MGs. Blockchains and smart contracts should be used in MGs to ensure that energy transactions and DER operations are safe (Zahraoui et al., 2021).

5 Conclusion

This article examines recent research on the various energy management techniques proposed for microgrids, including classical, heuristic, and intelligent algorithms. Additionally, this article discusses the design of microgrids, their many classifications, the components of a microgrid, the communication technologies utilized, and the auxiliary services necessary in a microgrid. It addresses significant energy management applications, data management, and control structure. Additionally, this article provides a brief examination of monitoring methods used for the data analysis of the microgrid. The EMS is vital to the MG's proper operation. An overview of MG control and various energy management schemes has been studied to optimize and stabilize the MG's functioning while optimizing the use of renewable energy resources. The developed hardware and software for the computer control and monitoring system for electricity generation allows the process to provide continuous user access to sensor data regardless of the state of the external power supply, to unify the approach to data collection *via* the use of an intermediate data aggregation node, and to provide convenient access to data processing *via* a diverse set of client interfaces. The impacts of the integration of electric vehicles on microgrid stability and balance and microgrid energy management during cybersecurity attacks represent the topics of our future works.

Data availability statement

The original contributions presented in the study are included in the article/supplementary material, further inquiries can be directed to the corresponding author.

Author contributions

All authors listed have made a substantial, direct, and intellectual contribution to the work and approved it for publication.

Conflict of interest

The authors declare that the research was conducted in the absence of any commercial or financial relationships that could be construed as a potential conflict of interest.

Publisher's note

References

Ahmad, F., Alam, M. S., and Asaad, M. (2017). Developments in xEVs charging infrastructure and energy management system for smart microgrids including xEVs. *Sustain. cities Soc.* 35, 552–564. doi:10.1016/j.scs.2017.09.008

Ahmethodzic, L., and Music, M. (2021). Comprehensive review of trends in microgrid control. *Renew. Energy Focus* 38, 84–96. doi:10.1016/j.ref.2021.07.003

Al Alahmadi, A. A., Belkhier, Y., Ullah, N., Abeida, H., Soliman, M. S., Khraisat, Y. S. H., et al. (2021). Hybrid wind/PV/battery energy management-based intelligent non-integer control for smart DC-microgrid of smart University. *IEEE Access* 9, 98948–98961. doi:10.1109/access.2021.3095973

Al-Saadi, M., Al-Greer, M., and Short, M. (2021). Strategies for controlling microgrid networks with energy storage systems: A review. *Energies* 14 (21), 7234. doi:10.3390/en14217234

Albarakati, A. J., Boujoudar, Y., Azeroual, M., Jabeur, R., Aljarbouh, A., El Moussaoui, H., et al. (2021). Real-time energy management for DC microgrids using artificial intelligence. *Energies* 14 (17), 5307. doi:10.3390/en14175307

Ali, M. A., Barakat, M. M., Abokhalaf, M. M., Fadel, Y. H., Kandil, M., Rasmy, M. W., et al. (2021). Micro-grid monitoring and supervision: Web-based SCADA approach. *J. Electr. Eng. Technol.* 16 (5), 2313–2331. doi:10.1007/s42835-021-00762-0

Ali, S. S., and Choi, B. J. (2020). State-of-the-art artificial intelligence techniques for distributed smart grids: A review. *Electronics* 9 (6), 1030. doi:10.3390/electronics9061030

Amrr, S. M., Alam, M. S., Asghar, M. J., and Ahmad, F. (2018). Low cost residential microgrid system based home to grid (H2G) back up power management. *Sustain. Cities Soc.* 36, 204–214. doi:10.1016/j.scs.2017.10.016

Andishgar, M. H., Gholipour, E., and Hooshmand, R. A. (2017). An overview of control approaches of inverter-based microgrids in islanding mode of operation. *Renew. Sustain. Energy Rev.* 80, 1043–1060. doi:10.1016/j.rser.2017.05.267

Arsad, A. Z., Hannan, M. A., Lipu, M. H., Rahman, S. A., Ker, P. J., Mansor, M., et al. (2022). Rule-based fuzzy controller for solid-state transfer switch towards fast sensitive loads transfer. *IEEE Trans. Industry Appl.* 58, 1888–1898. doi:10.1109/tia.2022.3146100

Atawi, I. E., and Kassem, A. M. (2017). Optimal control based on maximum power point tracking (MPPT) of an autonomous hybrid photovoltaic/storage system in microgrid applications. *Energies* 10 (5), 643. doi:10.3390/en10050643

Avancini, D. B., Rodrigues, J. J., Rabêlo, R. A., Das, A. K., Kozlov, S., and Solic, P. (2021). A new IoT-based smart energy meter for smart grids. *Int. J. Energy Res.* 45 (1), 189–202. doi:10.1002/er.5177

Azeroual, M., Boujoudar, Y., Iysaouy, L. E., Aljarbouh, A., Fayaz, M., Qureshi, M. S., and Markhi, H. E. (2022). Energy management and control system for microgrid based wind-PV-battery using multiagent systems. *Wind Eng.* 46, 0309524X221075583. doi:10.1177/0309524X221075583

Azeroual, M., Lamhamdi, T., El Moussaoui, H., and El Markhi, H. (2020). Intelligent EMS of a smart microgrid using multiagent systems. *Archives Electr. Eng.*, 23–38.

Barai, G. R., Krishnan, S., and Venkatesh, B. (20152015). *IEEE electrical power and energy conference (EPEC)*. IEEE, 138–145.Smart metering and functionalities of smart meters in smart grid-a review

Bera, S., Misra, S., and Rodrigues, J. J. (2014). Cloud computing applications for smart grid: A survey. *IEEE Trans. Parallel Distributed Syst.* 26 (5), 1477–1494. doi:10.1109/tpds.2014.2321378

Boujoudar, Y., Azeroual, M., El Moussaoui, H., and Lamhamdi, T. (2020). Intelligent controller based energy management for stand-alone power system using artificial neural network. *Int. Trans. Electr. Energy Syst.* 30 (11), e12579. doi:10.1002/2050-7038.12579

Chaudhary, G., Lamb, J. J., Burheim, O. S., and Austbø, B. (2021). Review of energy storage and energy management system control strategies in microgrids. *Energies* 14 (16), 4929. doi:10.3390/en14164929

Chen, Y. Y., Lin, Y. H., Kung, C. C., Chung, M. H., and Yen, I. H. (2019). Design and implementation of cloud analytics-assisted smart power meters considering advanced artificial intelligence as edge analytics in demand-side management for smart homes. *Sensors* 19 (9), 2047. doi:10.3390/s19092047

Coelho, V. N., Cohen, M. W., Coelho, I. M., Liu, N., and Guimarães, F. G. (2017). Multiagent systems applied for energy systems integration: State-of-the-art applications and trends in microgrids. *Appl. energy* 187, 820–832. doi:10.1016/j.apenergy.2016.10.056

Dagar, A., Gupta, P., and Niranjan, V. (2021). Microgrid protection: A comprehensive review. *Renew. Sustain. Energy Rev.* 149, 111401. doi:10.1016/j.rser.2021.111401

De Santis, E., Rizzi, A., and Sadeghian, A. (2017). Hierarchical genetic optimization of a fuzzy logic system for energy flows management in microgrids. *Appl. Soft Comput.* 60, 135–149. doi:10.1016/j.asoc.2017.05.059

Dileep, G. (2020). A survey on smart grid technologies and applications. *Renew. energy* 146, 2589–2625. doi:10.1016/j.renene.2019.08.092

Draft, A. U. (2016). *Issues paper on smart cities and infrastructure*.

Elmouatamid, A., Ouladsine, R., Bakhouya, M., El Kamoun, N., Zine-Dine, K., and Khaidar, M. (2019). "A model predictive control approach for energy management in micro-grid systems," in *2019 international conference on smart energy systems and technologies (SEST)* (IEEE), 1–6.

España, N., Barco-Jiménez, J., Pantoja, A., and Quijano, N. (2021). Distributed population dynamics for active and reactive power dispatch in islanded microgrids. *Int. J. Electr. Power & Energy Syst.* 125, 106407. doi:10.1016/j.ijepes.2020.106407

Fotopoulou, M., Rakopoulos, D., Trigkas, D., Stergiopoulos, F., Blanas, O., and Voutetakis, S. (2021). State of the art of low and medium voltage direct current (Dc) microgrids. *Energies* 14 (18), 5595. doi:10.3390/en14185595

George, A., and Ravindran, A. (2019). "Distributed middleware for edge vision systems," in *2019 IEEE 16th international conference on smart cities: Improving quality of life using ICT & IoT and AI (HONET-ICT)* (IEEE), 193–194.

George, A., Ravindran, A., Mendieta, M., and Tabkhi, H. (2021). Mez: An adaptive messaging system for latency-sensitive multi-camera machine vision at the iot edge. *IEEE Access* 9, 21457–21473. doi:10.1109/access.2021.3055775

George, A., and Ravindran, A. (2020). "Scalable approximate computing techniques for latency and bandwidth constrained IoT edge," in *International summit smart city 360°* (Cham: Springer), 274–292.

Ghiasi, M., Dehghani, M., Niknam, T., Kavousi-Fard, A., Siano, P., and Alhelou, H. H. (2021). Cyber-attack detection and cyber-security enhancement in smart DC-microgrid based on blockchain technology and Hilbert Huang transform. *Ieee Access* 9, 29429–29440. doi:10.1109/access.2021.3059042

Ghiasi, M. (2019). Detailed study, multi-objective optimization, and design of an AC-DC smart microgrid with hybrid renewable energy resources. *Energy* 169, 496–507. doi:10.1016/j.energy.2018.12.083

Ghiasi, M., Niknam, T., Dehghani, M., Siano, P., Haes Alhelou, H., and Al-Hinai, A. (2021). Optimal multi-operation energy management in smart microgrids in the presence of ress based on multi-objective improved de algorithm: Cost-emission based optimization. *Appl. Sci.* 11 (8), 3661. doi:10.3390/app11083661

Ghiasi, M., Wang, Z., Mehrandezh, M., Jalilian, S., and Ghadimi, N. (2022). Evolution of smart grids towards the Internet of energy: Concept and essential components for deep decarbonisation. *IET Smart Grid*. doi:10.1049/stg2.12095

Ghosal, A., and Conti, M. (2019). Key management systems for smart grid advanced metering infrastructure: A survey. *IEEE Commun. Surv. Tutorials* 21 (3), 2831–2848. doi:10.1109/comst.2019.2907650

Gui, E. M., and MacGill, I. (2018). Typology of future clean energy communities: An exploratory structure, opportunities, and challenges. *Energy Res. Soc. Sci.* 35, 94–107. doi:10.1016/j.erss.2017.10.019

Guo, Y., Tan, C. W., Hu, S., and Weaver, W. W. (2015). "Modeling distributed denial of service attack in advanced metering infrastructure," in *2015 IEEE power & energy society innovative smart grid technologies conference (ISGT)* (IEEE), 1–5.

Gupta, B. K., and Rastogi, V. (2021). Integration of technology to access the manufacturing plant via remote access system-A part of Industry 4.0. *Mater. Today Proc.* 56, 3497–3505. doi:10.1016/j.matpr.2021.11.135

Hafsi, O., Abdelkhalek, O., Mekhilef, S., Soumeur, M. A., Hartani, M. A., and Chakar, A. (2022). Integration of hydrogen technology and energy management comparison for DC-Microgrid including renewable energies and energy storage system. *Sustain. Energy Technol. Assessments* 52, 102121. doi:10.1016/j.seta.2022.102121

Han, Y., Li, H., Shen, P., Coelho, E. A. A., and Guerrero, J. M. (2016). Review of active and reactive power sharing strategies in hierarchical controlled microgrids. *IEEE Trans. Power Electron.* 32 (3), 2427–2451. doi:10.1109/tpel.2016.2569597

Hirsch, A., Parag, Y., and Guerrero, J. (2018). Microgrids: A review of technologies, key drivers, and outstanding issues. *Renew. Sustain. Energy Rev.* 90, 402–411. doi:10.1016/j.rser.2018.03.040

Hu, J., Shan, Y., Guerrero, J. M., Ioinovici, A., Chan, K. W., and Rodriguez, J. (2021). Model predictive control of microgrids–An overview. *Renew. Sustain. Energy Rev.* 136, 110422. doi:10.1016/j.rser.2020.110422

Hussein, T., and Shamekh, A. (2019). Design of PI fuzzy logic gain scheduling load frequency control in two-area power systems. *Designs* 3 (2), 26. doi:10.3390/designs3020026

Jimeno, J., Anduaga, J., Oyarzabal, J., and de Muro, A. G. (2011). Architecture of a microgrid energy management system. *Eur. Trans. Electr. Power* 21 (2), 1142–1158. doi:10.1002/etep.443

Justo, J. J., Mwasilu, F., Lee, J., and Jung, J. W. (2013). AC-microgrids versus DC-microgrids with distributed energy resources: A review. *Renew. Sustain. energy Rev.* 24, 387–405. doi:10.1016/j.rser.2013.03.067

Kang, K. M., Choi, B. Y., Lee, H., An, C. G., Kim, T. G., Lee, Y. S., et al. (2021). Energy management method of hybrid AC/DC microgrid using artificial neural network. *Electronics* 10 (16), 1939. doi:10.3390/electronics10161939

Karthick, T., Chandrasekaran, K., and Jeslin., D. N. J. (2021). Design of IoT based smart compact energy meter for monitoring and controlling the usage of energy and power quality issues with demand-side management for a commercial building. *Sustain. Energy, Grids Netw.* 26, 100454. doi:10.1016/j.segan.2021.100454

Kaur, A., Kaushal, J., and Basak, P. (2016). A review on microgrid central controller. *Renew. Sustain. Energy Rev.* 55, 338–345. doi:10.1016/j.rser.2015.10.141

Kermani, M., Carnì, D. L., Rotondo, S., Paolillo, A., Manzo, F., and Martirano, L. (2020). A nearly zero-energy microgrid testbed laboratory: Centralized control strategy based on SCADA system. *Energies* 13 (8), 2106. doi:10.3390/en13082106

Khan, K. R., Rahman, A., Nadeem, A., Siddiqui, M. S., and Khan, R. A. (2018). "Remote monitoring and control of microgrid using smart sensor network and Internet of thing," in *2018 1st international conference on computer applications & information security (ICCAIS)* (IEEE), 1–4.

Khatua, P. K., Ramachandaramurthy, V. K., Kasinathan, P., Yong, J. Y., Pasupuleti, J., and Rajagopalan, A. (2020). Application and assessment of internet of things toward the sustainability of energy systems: Challenges and issues. *Sustain. Cities Soc.* 53, 101957. doi:10.1016/j.scs.2019.101957

Khoa, N. M., Dai, L. V., Tung, D. D., and Toan, N. A. (2021). An advanced IoT system for monitoring and analysing chosen power quality parameters in micro-grid solution. *Archives Electr. Eng.* 70 (1).

Khorsandi, A., Ashourloo, M., and Mokhtari, H. (2014). A decentralized control method for a low-voltage DC microgrid. *IEEE Trans. Energy Convers.* 29 (4), 793–801. doi:10.1109/tec.2014.2329236

Kondoro, A., Dhaou, I. B., Tenhunen, H., and Mvungi, N. (2021). Real time performance analysis of secure IoT protocols for microgrid communication. *Future Gener. Comput. Syst.* 116, 1–12. doi:10.1016/j.future.2020.09.031

Ku, T. Y., Park, W. K., and Choi, H. (2017). "IoT energy management platform for microgrid," in *2017 IEEE 7th international conference on power and energy systems (ICPES)* (IEEE), 106–110.

Kumar, K. P., and Saravanan, B. (2017). Recent techniques to model uncertainties in power generation from renewable energy sources and loads in microgrids–a review. *Renew. Sustain. Energy Rev.* 71, 348–358. doi:10.1016/j.rser.2016.12.063

Mahmoud, M. S., Alyazidi, N. M., and Abouheaf, M. I. (2017). Adaptive intelligent techniques for microgrid control systems: A survey. *Int. J. Electr. Power & Energy Syst.* 90, 292–305. doi:10.1016/j.ijepes.2017.02.008

Malik, S. M., Ai, X., Sun, Y., Zhengqi, C., and Shupeng, Z. (2017). Voltage and frequency control strategies of hybrid AC/DC microgrid: A review. *IET Generation, Transm. Distribution* 11 (2), 303–313. doi:10.1049/iet-gtd.2016.0791

Marinakis, V., and Doukas, H. (2018). An advanced IoT-based system for intelligent energy management in buildings. *Sensors* 18 (2), 610. doi:10.3390/s18020610

Mehrizi-Sani, A., and Iravani, R. (2010). Potential-function based control of a microgrid in islanded and grid-connected modes. *IEEE Trans. Power Syst.* 25 (4), 1883–1891. doi:10.1109/tpwrs.2010.2045773

Moghimi, M., Jamborsalamati, P., Hossain, J., Stegen, S., and Lu, J. (2018). "A hybrid communication platform for multi-microgridEMSoptimization," in *2018 IEEE 27th international symposium on industrial electronics (ISIE)* (IEEE), 1215–1220.

Mohanty, S. P., Choppali, U., and Kougianos, E. (2016). Everything you wanted to know about smart cities: The Internet of things is the backbone. *IEEE Consum. Electron. Mag.* 5 (3), 60–70. doi:10.1109/mce.2016.2556879

Ortiz, L., Orizondo, R., Águila, A., González, J. W., López, G. J., and Isaac, I. (2019). Hybrid AC/DC microgrid test system simulation: Grid-connected mode. *Heliyon* 5 (12), e02862. doi:10.1016/j.heliyon.2019.e02862

Pan, Y., Sangwongwanich, A., Yang, Y., and Blaabjerg, F. (2021). Distributed control of islanded series PV-battery-hybrid systems with low communication burden. *IEEE Trans. Power Electron.* 36 (9), 10199–10213. doi:10.1109/tpel.2021.3063111

Rangu, S. K., Lolla, P. R., Dhenuvakonda, K. R., and Singh, A. R. (2020). Recent trends in power management strategies for optimal operation of distributed energy resources in microgrids: A comprehensive review. *Int. J. Energy Res.* 44 (13), 9889–9911. doi:10.1002/er.5649

Raya-Armenta, J. M., Bazmohammadi, N., Avina-Cervantes, J. G., Saez, D., Vasquez, J. C., and Guerrero, J. M. (2021). Energy management system optimization in islanded microgrids: An overview and future trends. *Renew. Sustain. Energy Rev.* 149, 111327. doi:10.1016/j.rser.2021.111327

Roslan, M. F., Hannan, M. A., Ker, P. J., Mannan, M., Muttaqi, K. M., and Mahlia, T. I. (2022). Microgrid control methods toward achieving sustainable energy management: A bibliometric analysis for future directions. *J. Clean. Prod.* 348, 131340. doi:10.1016/j.jclepro.2022.131340

Roslan, M. F., Hannan, M. A., Ker, P. J., and Uddin, M. N. (2019). Microgrid control methods toward achieving sustainable energy management. *Appl. Energy* 240, 583–607. doi:10.1016/j.apenergy.2019.02.070

Roy, S., Baldi, S., and Fridman, L. M. (2020). On adaptive sliding mode control without a priori bounded uncertainty. *Automatica* 111, 108650. doi:10.1016/j.automatica.2019.108650

Sabri, Y., El Kamoun, N., and Lakrami, F. (2019). "A survey: Centralized, decentralized, and distributed control scheme in smart grid systems," in *2019 7th mediterranean congress of telecommunications (CMT)* (IEEE), 1–11.

Sahoo, B., Routray, S. K., and Rout, P. K. (2021). AC, DC, and hybrid control strategies for smart microgrid application: A review. *Int. Trans. Electr. Energy Syst.* 31 (1), e12683. doi:10.1002/2050-7038.12683

Sahri, Y., Belkhier, Y., Tamalouzt, S., Ullah, N., Shaw, R. N., Chowdhury, M. S., et al. (2021). Energy management system for hybrid PV/wind/battery/fuel cell in microgrid-based hydrogen and economical hybrid battery/super capacitor energy storage. *Energies* 14 (18), 5722. doi:10.3390/en14185722

Sedhom, B. E., El-Saadawi, M. M., El Moursi, M. S., Hassan, M. A., and Eladl, A. A. (2021). IoT-based optimal demand-side management and control scheme for smart microgrid. *Int. J. Electr. Power & Energy Syst.* 127, 106674. doi:10.1016/j.ijepes.2020.106674

Sen, S., and Kumar, V. (2018). Microgrid control: A comprehensive survey. *Annu. Rev. control* 45, 118–151. doi:10.1016/j.arcontrol.2018.04.012

Siddique, A. B., Munsi, M. S., Sarker, S. K., Das, S. K., and Islam, M. R. (2019). Voltage and current control augmentation of islanded microgrid using multifunction model reference modified adaptive PID controller. *Int. J. Electr. Power & Energy Syst.* 113, 492–501. doi:10.1016/j.ijepes.2019.05.065

Singh, K., Amir, M., Ahmad, F., and Khan, M. A. (2020). An integral tilt derivative control strategy for frequency control in multimicrogrid system. *IEEE Syst. J.* 15 (1), 1477–1488. doi:10.1109/jsyst.2020.2991634

Singh, K., Amir, M., Ahmad, F., and Refaat, S. S. (2021). Enhancement of frequency control for stand-alone multi-microgrids. *IEEE Access* 9, 79128–79142. doi:10.1109/access.2021.3083960

Singh, S. K., Matwankar, C. S., Jee, M., and Alam, A. (2022). MRAS-based current estimator for DC-DC converters considering time-variant load impedance. *J. Power Electron.* 22 (2), 210–221. doi:10.1007/s43236-021-00353-2

Soliman, M. S., Belkhier, Y., Ullah, N., Achour, A., Alharbi, Y. M., Al Alahmadi, A. A., et al. (2021). Supervisory energy management of a hybrid battery/PV/tidal/wind sources integrated in DC-microgrid energy storage system. *Energy Rep.* 7, 7728–7740. doi:10.1016/j.egyr.2021.11.056

Su, W., and Wang, J. (2012). Energy management systems in microgrid operations. *Electr. J.* 25 (8), 45–60. doi:10.1016/j.tej.2012.09.010

Sylcloud Smart Micro Grid *Sylcloud smart micro grid*. Available at: https://sylcloud.com/smartmicrogrid (Accessed March 26 2022).

Tayab, U. B., Roslan, M. A. B., Hwai, L. J., and Kashif, M. (2017). A review of droop control techniques for microgrid. *Renew. Sustain. Energy Rev.* 76, 717–727. doi:10.1016/j.rser.2017.03.028

Umuhoza, J., Zhang, Y., Zhao, S., and Mantooth, H. A. (2017). "An adaptive control strategy for power balance and the intermittency mitigation in battery-PV energy system at residential DC microgrid level," in *2017 IEEE applied power electronics conference and exposition (APEC)* (IEEE), 1341–1345.

Vaikund, H., and Srivani, S. G. (2021). Trends inEMSfor smart microgrid—An overview. *Adv. Signal Data Process.*, 15–28.

Vermesan, O., Friess, P., Guillemin, P., Gusmeroli, S., Sundmaeker, H., Bassi, A., and Doody, P. (2011). IoTstrategic research roadmap. *Internet things-global Technol. Soc. trends* 1, 9–52.

Völker, B., Reinhardt, A., Faustine, A., and Pereira, L. (2021). Watt's up at home? Smart meter data analytics from a consumer-centric perspective. *Energies* 14 (3), 719. doi:10.3390/en14030719

Vuddanti, S., and Salkuti, S. R. (2021). Review of energy management system approaches in microgrids. *Energies* 14 (17), 5459. doi:10.3390/en14175459

Zahraoui, Y., Alhamrouni, I., Mekhilef, S., Basir Khan, M. R., Seyedmahmoudian, M., Stojcevski, A., et al. (2021). Energy management system in microgrids: A comprehensive review. *Sustainability* 13 (19), 10492. doi:10.3390/su131910492

Zamfir, M., Florian, V., Stanciu, A., Neagu, G., Preda, Ş., and Militaru, G. (2016). "Towards a platform for prototyping IoT health monitoring services," in *International conference on exploring services science* (Cham: Springer), 522–533.

Zheng, J., Gao, D. W., and Lin, L. (2013). "Smart meters in smart grid: An overview," in *2013 IEEE green technologies conference (GreenTech)* (IEEE), 57–64.

Zhuang, J., Shen, G., Yu, J., Xiang, T., and Wang, X. (2017). The design and implementation of intelligent microgrid monitoring system based on WEB. *Procedia Comput. Sci.* 107, 4–8. doi:10.1016/j.procs.2017.03.047

Zia, M. F., Elbouchikhi, E., and Benbouzid, M. (2018). Microgrids energy management systems: A critical review on methods, solutions, and prospects. *Appl. energy* 222, 1033–1055. doi:10.1016/j.apenergy.2018.04.103

Nomenclature

AMI Advanced metering infrastructure
ANN Artificial neural network
AMR Automated Meter Reading
CANADA Supervisory control and data acquisition
CT Current transformer
DER Distributed energy resources
DG Distributed generators
DR Demand response
EMS Energy management system
ESS Energy storage system
ESS Energy Storage Systems
FL Fuzzy logic
GA Genetic algorithm
GHG Greenhouse gas
HMI Human machine interface
IoT Internet of things
LC Local controller
M2M Machine to machine
MAS Multiagent system
MG Microgrid
MGCC Microgrid central controller
MMG Multi-microGrid
MQTT Message queuing telemetry transport
PID Proportional–integral–derivative
PLC Programmable logic controller
PQ Power quality
PSO Particle swarm optimization
RER Renewable energy resource
RMU Remote monitoring unit
RTU Remote terminal unit
SMG Smart grid

frontiers | Frontiers in Energy Research

TYPE Original Research
PUBLISHED 28 December 2022
DOI 10.3389/fenrg.2022.1043593

OPEN ACCESS

EDITED BY
Kashif Mehmood,
Southeast University, China

REVIEWED BY
Sheeraz Iqbal,
University of Azad Jammu and Kashmir, Pakistan
Muhammad Asad,
Dalhousie University, Canada
Omar Abu Arqub,
Al-Balqa Applied University, Jordan

*CORRESPONDENCE
Naveed Ishtiaq Chaudhary,
chaudni@yuntech.edu.tw

SPECIALTY SECTION
This article was submitted to Smart Grids, a section of the journal Frontiers in Energy Research

RECEIVED 13 September 2022
ACCEPTED 17 October 2022
PUBLISHED 28 December 2022

CITATION
Munawar S, Khan ZA, Chaudhary NI, Javaid N, Raja MAZ, Milyani AH and Azhari AA (2022), Novel FDIs-based data manipulation and its detection in smart meters' electricity theft scenarios. *Front. Energy Res.* 10:1043593. doi: 10.3389/fenrg.2022.1043593

Novel FDIs-based data manipulation and its detection in smart meters' electricity theft scenarios

Shoaib Munawar[1], Zeshan Aslam Khan[1], Naveed Ishtiaq Chaudhary[2]*, Nadeem Javaid[3], Muhammad Asif Zahoor Raja[2], Ahmad H. Milyani[4] and Abdullah Ahmed Azhari[5]

[1]Department of Electrical and Computer Engineering, International Islamic University, Islamabad, Pakistan, [2]Future Technology Research Center, National Yunlin University of Science and Technology, Yunlin, Taiwan, [3]Department of Computer Science, COMSATS University Islamabad, Islamabad, Pakistan, [4]Department of Electrical and Computer Engineering, King Abdulaziz University, Jeddah, Saudi Arabia, [5]The Applied College, King Abdulaziz University, Jeddah, Saudi Arabia

Non-technical loss is a serious issue around the globe. Consumers manipulate their smart meter (SM) data to under-report their readings for financial benefit. Various manipulation techniques are used. This paper highlights novel false data injection (FDIs) techniques, which are used to manipulate the smart meter data. These techniques are introduced in comparison to six theft cases. Furthermore, various features are engineered to analyze the variance, complexity, and distribution of the manipulated data. The variance and complexity are created in data distribution when FDIs and theft cases are used to poison SM data, which is investigated through skewness and kurtosis analysis. Furthermore, to tackle the data imbalance issue, the proximity weighted synthetic oversampling (ProWsyn) technique is used. Moreover, a hybrid attentionLSTMInception is introduced, which is an integration of attention layers, LSTM, and inception blocks to tackle data dimensionality, misclassification, and high false positive rate issues. The proposed hybrid model outperforms the traditional theft detectors and achieves an accuracy of

Abbreviations: *ADASYN*, adaptive synthetic; *ADASYNENN*, adaptive synthetic edited nearest neighbor neural network; *AMI*, advanced metering infrastructure; *ANFIS*, adaptive neural fuzzy inference system; *ANN*, artificial neural network; *AUC*, area under the curve; *DSN*, deep siamese network; *DWMCNN*, day week month convolutional neural network; *ETD*, electricity theft detection; *FDI*, false data injection; *FIS*, fuzzy interface system; *FPR*, false positive rate; *FRESH*, feature extraction and scalable hypothesis; *GRU*, gated recurrent unit; *KNN*, K-nearest neighbor; *LLE*, locally linear embedded; *NAN*, neighborhood area network; *NCA*, neighborhood component analysis; *NTLs*, non technical losses; *PCA*, principal component analysis; *ProWsyn*, proximity weighted synthetic oversampling; *RE*, reconstruction error; *RESNet*, residual network; *SAGAN*, self attention generative adverserial neural network; *SCADA*, supervisory control and data acquisition; *SMs*, smart meters; *SMOTE*, synthetic minority oversampling technique; *TPR*, true positive rate; 1 – *DCNN*, 1 dimensional convolutional neural network.

0.95%, precision 0.97%, recall 0.94%, F1 score 0.96%, and area under-the-curve (AUC) score 0.98%.

KEYWORDS

inception module, AttLSTM, false data injection, electricity theft detection, time series data

1 Introduction

Smart grids are serially interconnected networks having resilient features of unity power factor, self-healing, system monitoring, load balancing, and two-way communication. The communication channel is a delicate part of the power network. Network stability is interrupted when it is interfaced with a wrong information flow (Rawat and Bajracharya, 2015). Various types of cellular technologies, wireless sensor protocols, WLAN, and WAN are used for the purpose of communication in smart grids (Parikh et al., 2010), (Djennadi et al., 2021a). The world is moving towards the development of smart grids for efficient and reliable smart energy where different types of energy-production sources are integrated for optimal and reliable operations (Cai et al., 2017), (Djennadi et al., 2021b). The survival of societies is based on economic growth and an uninterrupted electrical energy supply. Losses are of two types: technical losses (TLs) and non technical losses (NTLs) (Jeyaraj et al., 2020), (Guo et al., 2018). An almost as large portion of the losses in the electrical system are NTLs. TLs are the inherent losses of the electrical power system, whereas NTLs occur due to the problems of double tapping, by-passing of smart meters (SMs), and tampering with SM readings, etc., in order to under-report the consumed electrical energy (Buzau et al., 2019), (Somefun et al., 2019). The deployment of smart grids can easily regulate customers' consumption behavior. Detection of NTLs secures the smart grids against anomalies and optimal flow of energy is managed (Rodriguez et al., 2017), (Arqub, 2018).

Advanced metering infrastructure (AMI) is an intelligent infrastructure to detect NTLs, however, it is a hardware-based architecture with multiple architectural flaws. False Data injections (FDIs) of novel nature are used to manipulate in SMs data, which are difficult to investigate and detect by AMI architecture. FDIs are novel techniques, which are used to manipulate the data of SM readings to gain illegal financial benefit. AMI collects the data with the help of a neighborhood area network (NAN). NAN is a useful architecture designed to manage energy in order to forecast short-term load and to investigate the optimal energy scheduling by the utility providers (UPs) (Depuru et al., 2011), (Arqub, 2020). Traditional grids use supervisory control and data acquisition (SCADA) in order to monitor grid operations and ensure security (Yasakethu and Jiang, 2013), (Sweis et al., 2022). Conventional machine learning techniques are used for the detection of NTLs, however, techniques such as support vector machine (SVM), random forest (RF), and 1D-convolutional neural network (1D-CNN) have low detection accuracy in classification scenarios (Glauner et al., 2016). Henceforth, classifiers with high detection and low false positive rate (FPR) are required to mitigate the problem of misclassification.

1.1 Motivation

Electricity theft is extant worldwide. Utility providers look for problems in their consumers' premises due to NTLs. Consumers opt for various electricity theft techniques in order to under-report their consumption. Some of these techniques are (Rawat and Bajracharya, 2015) tampering with the data with shunt devices (Parikh et al., 2010), double tapping of SMs, and (Djennadi et al., 2021a) electronic faults. These traditional approaches capture the behavior of NTLs where various hand-drafted mechanisms are developed due to a lack of clear mathematical formulations. Developing such solutions for each individual theft case is very expensive and time-consuming due to their relience on expert knowledge. In order to tackle such issues we propose a deep-learning based architecture that self-learns features of the observed data and automatically detects NTLs. Such architecture is operated in less time in order to mitigate the need for experts and excessive costs. Moreover, false data injection techniques (FDIs) are introduced in this paper, which can be used in real-time applications to manipulate SM readings. These manipulating techniques are highly intensive in nature and they can manipulate the data accordingly to the consumer's choice. So highlighting the detection of such intensive techniques improves the detection scenarios and minimizes the chances of theft. Consideration of such FDIs in detection scenarios minimizes NTLs, and manipulated patterns found with attributes of such theft traces can easily be identified as theft. Moreover, an efficient model should be used to detect and segregate fraudulent and benign consumers in such scenarios with minimal FPR. Minimal FPR is an effective parameter and minimizes excessive on-site costs for verification of fraudulent consumers.

2 Literature review

This section provides an overview of the existing literature related to electricity theft detection (ETD) in smart grids.

In (Takiddin et al., 2020), an ensemble detector is proposed, which is a combination of deep auto encoders with attention-gated recurrent units (GRU) and feed-forward neural networks. Similarly, (Kocaman and Tümen, 2020) proposes an LSTM classifier for the detection of malicious customers. Data selection, normalization, and weights updating mechanisms are used as preprocessing mechanisms in both of the proposed solutions. Architectures of the LSTM classifier contain LSTM cells, dropout layers, relu activation function, and softmax classifier. Precision, accuracy, and recall matrix is used to evaluate the performance of the proposed models.

Study in (Li et al., 2019) uses a convolutional neural network and random forest (CNN-RF) as a novel hybrid classifier for the detection of NTLs. CNN is used as a down-sampler to extract key features of the time series data. The featured data is inputted to RF for further classification in order to identify anomalous consumers. Similarly (Javaid et al., 2021a), uses adaptive synthesis (ADASYN) for the provision of balanced data. A hybrid module of CNN and LSTM is proposed to detect ill-intent within consumers' profiles. CNN is used to extract abstract features from weekly time series data, however, LSTM is trained on the inputted data of the CNN. Integration of CNN-LSTM is named deep siamese network (DSN), which segregates honest and thieving customers. In (Pereira and Saraiva, 2021), data augmentation techniques are analysed to evaluate the performance of various minority over-sampler techniques. A pool of data augmentation techniques enlisting cost-sensitive learning, random over-sampling, K-medoids over-sampling, cluster-based over-sampling, and synthetic minority over-sampling technique (SMOTE) are used to balance the imbalanced data. The balance data is inputted to CNN. The performance of CNN is evaluated on each of the data augmentation techniques, respectively. Furthermore, CNN is used as a binary classifier for data classification, and area under the curve (AUC) is used as a performance matrix to evaluate the classifier's performance. Literature in (Blazakis et al., 2020) uses an adaptive neural fuzzy inference system (ANFIS), which is a combination of artificial neural network (ANN) and fuzzy set theory in order to investigate NTLs. ANFIS utilizes back propagation learning of ANN and sugeno fuzzy inference system (FIS) to detect maliciousness in time series data of SMs. To maximize the efficiency of the classifier, neighborhood component analysis (NCA) is used to select the optimal ranking of the important features such as mean, medium, entropy, and load factor. Furthermore, accuracy, precision, F1 score, and AUC score are used to evaluate the performance of the classifier.

Similarly, in (Himeur et al., 2021) an ensemble model based on genetic optimization is developed to detect anomaly. SMOTE, a data over-sampling technique, is used to balance the data distribution. Afterward, features of the anomalous consumers are extracted using principal component analysis (PCA) along with the data dimensionality reduction. The abstract information of customers' behavior is extracted using AdaBoost technique and architectural optimization of the deep neural network is analysed through genetic algorithms. Moreover (Hussain et al., 2021), presents a novel supervised learning solution, which is an integration of catboost and SMOTETOMEK algorithms. Data preprocessing is tackled by K-nearest neighbor (KNN) in order to fill missing values, while data augmentation is carried out using SMOTETOMEK in order to mitigate biasness towards a majority class. Furthermore, to extract key features of highly dense time series data feature extraction and scalable hypothesis (FRESH) is used. The extracted data is inputted into catboost classifier for classification and a tree-SHAP algorithm is used as a decision-maker for theft identification. Study in (Cheng et al., 2021) proposes RF based classifier for the detection of an anomaly in a time series data. To reduce heavily dense time series data K-means method is used, whereas, a neural network of day, week, and month convolutional neural network (DWMCNN) is used to analyse the SMs' consumption data and to extract key features. To evaluate the performance AUC score is used as a performance metric. In order to segregate the honest and fraudulent consumers (Javaid et al., 2021b) proposes two supervised learning models. One of the models is an integration of self-attention generative adversarial network (SAGAN) and CNN. Important features of the time series data are extracted using the locally linear embedding technique (LLE) technique and to tackle the class imbalance issue adaptive synthetic edited nearest neighbor (ADASYNENN) is utilized. Furthermore, an ensemble model ERNET is developed, which consists of an efficient net residual network (ResNet) and gated recurrent unit (GRU). ResNet and GRU hybrid model is used as a second classifier to detect NTLs. Robust learning rate and data imbalance issues are tackled with root mean square propagation (RMSProP) and SMOTE edited the nearest neighbor, respectively.

Various proposed solutions have been presented in the literature, however, slow computations in RNN, the need for bulk training data in the case of CNN, performance declination in AFNIS due to the provision of less training data, and non-availability of intrinsic evaluation metric for SAGAN, we propose the AttentionLSTMInception model to overcome all these issues. Moreover, the Attention layer memorizes the large sequence of data. LSTM has more additional units which can hold information longer. An additional number of parameters such as learning rate, input and output biases, updating of weights, and backpropagation make the model more flexible. The inception module is added for better utilization of the computing resources in order to avoid excessive computational load. These are deeper networks, which are used for dimensionality reduction with stacked convolutions. Furthermore, the proposed hybrid model utilizes the attributes of long-term memorization of information and backpropagation of LSTM, data filtering for dimensionality reduction of CNN, and cognitive attention towards the prominent features of the attention layers, we

are integrating them to introduce a novel hybrid model AttenLSTMInception for the detection of NTLs. The proposed hybrid model tackles issues of long-term memory dependencies, vanishing grading, under-fitting, over-fitting, and high FPR.

2.1 Paper organization

The rest of the paper is organized as follows. **Section 3** provides a list of contributions and their mapped solutions. **Section 4** determines the importance of feature engineering. **Section 5** and **Section 6** provide a detailed study of the system model and its workings, respectively. **Section 7** highlights performance evaluation and **section 8** is simulations results. Finally, a conclusion is drawn in **section 9**.

3 List of contributions

The contributions of the study are enlisted as follows.

- Diversity and dense variability in data distribution confuse the classification scenario and require special filtering mechanisms, which are tackled in this paper.
- Novel false data injection techniques (FDIs) are investigated, which manipulate the SMs data extremely and remained still undetectable in literature.
- A problem of high FPR due to extensive misclassification is tackled, which causes financial overburdens.
- To tackle data reductionality issues, inception, attention, and filtering mechanisms are introduced to hybridize the existing classifying architectures.
- In order to retain long-term memorization, the inputted data is overlapped through segmented attributes of sliding windows to adopt cognitive learning of the data.
- Data synthesizing through ineffective balancing techniques mimic resembled, overlapped, and replicated data, which is tackled by introducing a novel proximity-weighted synthetic oversampling (ProWsyn) technique.

3.1 Dataset

SMs installed on consumer premises record the electricity consumption for the consumed energy. Consumed energy is recorded in the form of time series data. In this paper, a realistic dataset, named as state grid corporation of China (SGCC) is used which contains 42,372 consumers. We are considering 6 months of data from 1500 benign consumers only for data classification and manipulation due to the limited resources of our machine (Punmiya and Choe, 2019). Our machine specifications are intel(R) core (TM) M-5y10c, CPU@ 0.80 GHz 1.00GHz, RAM 4 GB. Moreover, the simulator is google CoLab. The dataset contains a few missing readings, which are due to the mal-operation and malfunctioning of the sensors deployed over the installed SMs. Such erroneous readings create ambiguity over the classification scenario and ultimately result in a low detection rate. A straightforward approach to eliminating such readings disrupts the time series data's sequence and integrity. Considering optimal data filling techniques and operating such techniques over the perspective rows provide refined and complete consumption data of each consumer. A 24-h time series data for every consumer is recorded by an SM. A unique consumer ID is assigned to each consumer. A label is indexed for the identification of honest and fraudulent consumption. A binary representation of 0 and 1 is used where 0 represents benign class data and 1 represents fraudulent class data. Due to the rarity of theft class data, we are proposing false data injection techniques (FDIs) to manipulate the benign class data in order to synthesize fraudulent class data. FDIs are proposed in comparison to theft cases (Sha et al., 2022), which are shown in **Eqs. 1**, **2**. Moreover, the dataset is online available at: https://github.com/henryRDlab/ElectricityTheftDetection.

3.2 Data preprocessing

Electricity consumption time series data is a series of numeric values, which is monitored by the installed SMs on the consumers' premises. Such time series data contain missing values and outliers due to the mal-operation and malfunctioning of the deployed SMs. Filling in the missing values and removing the outliers are necessary steps. A simple Imputer technique is used to fill in the missing values and to remove the outliers. To fill in the missing values, a mean-based strategy is operated row-wise. Furthermore, data normalization is carried out to normalize the data into a specific range. The normalized data is the input data, which is then transformed and scaled to carry out further operations.

3.3 Data augmentation

The problem of skewness towards the majority class by the classifier is a serious issue, which needs proper attention. To tackle the data imbalance issue, synthetic data is synthesized by oversampling minority class data. Weight value-based approaches transform the data into equal distribution, however, most of the techniques synthesize inappropriate data, which ultimately results in a poor distribution of the classes. To overcome such problems, this paper proposes a proximity-weighted synthetic oversampling technique (ProWsyn) (Islam and Belhaouari, 2022). ProWsyn targets the minority class samples to balance the data. The proximity information of

TABLE 1 Mapping of limitations and proposed solutions.

Sr	Limitation Identified	Solution Number	Proposed Solution	Validations
L1	Misclassification due to the dense variability of the distributed data	S1	Addition of Inception module for filtering abstract features	V1: Table 2
L2	Lack of theft class data samples	S2	Synthesizing through novel FDIs	V2: Eq.1
L3	High FPR	S3	Hybrid model architecture to tackle extensive misclassification	V3: Figure 6
L4	Problem of short term information memorization	S4	Data segmentation and overlapping	V4: Figure 1
L5	Imbalance data and model's skewness towards the majority class	S5	ProWsyn data resampling technique	V5: Algorithm 2

each sample is measured based on the distance from the decision boundary. Distance-based proximity helps to generate the effective weights for the minority class samples. Such effective weights of the minority samples normalize the data distribution, which mitigates the skewness of the model towards the majority class samples. The data is balanced and synthetic samples are generated. ProWsyn is a clustering-based technique, which operates in two steps.

- In the first step, the distance between the residing position of the sample and the decision boundary is monitored for each of the minority samples. All the samples are partitioned (P) upon the splitting.
- In the second step, the partitioned data samples are assigned a proximity level (L).

The proximity level is directly proportional to the distance. A smaller proximity level gives more important samples, whereas, a greater proximity level gives less important samples. Algorithm 2 shows the operating mechanism of the ProWsyn technique.

In step 1 of Algorithm 2, input parameters are defined. Step 2 considers new sampling based on EU. New samples are synthesized and considered if EU of the corresponding sample is less than the corresponding cluster and weight of the sample is updated accordingly. However, if the EU is greater it is ignored. Finally, in step 3, the number of honest consumers and fraudulent consumers is balanced.

$$\begin{cases} FDI_1 = \dfrac{mean(E) * random(0.1-0.9)}{E} \\ where E > 1 \leq mean \\ FDI_2 = \sqrt{(mean(E))} * random(0.1-0.9) \\ FDI_3 = \sqrt{(E)} * random(0.1-0.9) \\ FDI_4 = mean(E) - (\gamma) \\ where\ \gamma\ is\ a\ constant\ consumption\ and \\ \gamma \leq mean \\ FDI_5 = E - \gamma_i \\ where\ i = 0, \ldots, E_{max} \\ FDI_6 = E(t-d) = 0\ if\ t < d\ and\ 1\ if\ t \geq d \\ where\ t, d\ is\ time\ and\ difference,\ respectively. \end{cases} \quad (1)$$

Step 1: Defining fraudulent and honest consumers:
Input: Honest Consumers H_{E_c}, *Fradulent Consumers* F_{E_c} Sample S_i, Euclidean distance *EU*, Decision Boundary DB, Weight *W*

Step 2: Introducing FDIs:
$F_{E_c} > H_{E_c}$;
S_i *if EU is geater ignore* S_i;
update W;
consider S_i *if EU is less*;
skip: and go to next sample
Step 3: Balancing :
$F_{E_c} = H_{E_c}$
STOP
Output:Target (Proximity S_i *having EU >), Skip (Proximity* S_i *having EU <)*

Algorithm 1. Data Augmentation using proWsyn Technique.

$$\begin{cases} T1(E_t) = E_t * random(0.1, 0.9) \\ T2(E_t) = E_t * E_t(E_t = random(0.1, 0.9)) \\ T3(E_t) = E_t * random[0, 1] \\ T4(E_t) = mean(E_t) * random(0.1, 1.0) \\ T5(E_t) = mean(E_t) \end{cases} \quad (2)$$

4 Feature engineering

The data distribution analysis is presented in Table 2. Effective classification is based on the data's nature. Complex data is very difficult to be learned and classified by weak models. Such complexity is based on the variance among the data samples that need special attention before deploying any model to tackle the classification problem. Various types of features are engineered, which include min, max, standard

TABLE 2 Data distribution analysis.

Data Manipulation Scheme	Kurtosis	Skewness
FDIs	6	46
Theft Cases	1	10

deviation, mean, root mean square error, skew, kurtosis, quantile, and rolling mean. Mean, min, max and standard deviation are basically the stochastical features, whereas, root mean square error, skew, kurtosis, quantile, and rolling mean are the static features based on the dynamics of the time series data. Stochastical features show the randomness and variations in the data, which helps to know the complexity of the distributed data. Whereas, the root mean square responds to the provision of the actual information of variations and distribution in the data. Skewness factor (S_k) judges the symmetry and resemblance of the data. In literature, it is represented as three-point plotting. One point is a central point and the other two lies on the left and the right of the central point, respectively. A symmetric distribution is the same to the left and right of the central point. Mathematically it can be represented as:

$$\left\{ S_k = \frac{\sum_{j=1}^{M} (Wj - W^{-})^3 / (M)}{q^3}, \right. \tag{3}$$

The kurtosis parameter helps to investigate the problems associated with the outliers and the data's distribution. It shows the difference between each and every point within the data whether it is symmetric or un-symmetric. Mathematically, it can be represented as:

$$\left\{ Kurtosis = \frac{\sum_{j=1}^{M} (Wj - W^{-})^4 / (M)}{q^4} - 3, \right. \tag{4}$$

Where W^{-} is the mean, q is the standard deviation and M is the number of data samples. Positive kurtosis represents a heavy-tailed distribution, whereas, negative kurtosis is a light tailed distribution. Normal data distribution has a zero kurtosis. Quantile concludes the shape of the distribution. It distributes the observations in the same number of samples based on the probability distribution.Rolling mean (R_m) is a computing window, which computes the mean on a piece of the data slab. The rolling window rolls on continuous time series data and computes for a subset. The computed subset is the rolling average for that specific slab of the data. It basically accesses the stability within the data distribution. Mathematically, it is represented as (Blanca et al., 2013):

$$\left\{ R_m = \frac{E_t + E_{t-1} + E_{t-2} + \cdots + E_{t-n} + 1}{M}, \right. \tag{5}$$

4.1 Data manipulation

Novel FDI techniques are proposed in comparison to six theft cases for data manipulation (Pamir et al., 2022a).

- FDI 1 under-reports the consumption by manipulating the SM's data as shown in **Figure 1A**. The total consumption is aggregated into a mean. A random number is multiplied by the aggregated mean, which ranges between (0.1–0.9). The product is divided by a number greater than 1 and less than a number equal to the aggregated mean, which vanishes the consumed energy reading and limits it to a zero reading.
- FDI2 targets the mean and a random number's product, which is squarely rooted in order to inject false reading by manipulating SM's consumption data. This data subjectively minimizes the consumption of energy almost by 1/2 of the total consumed energy as shown in **Figure 1B**.
- FDI3 is the periodic bulk manipulation of the total consumed energy over monthly and weekly based. It is a specific defined time period manipulation. The square-rooted consumption is multiplied by a random number ranging between (0.1–0.9) in order to get more financial benefits as shown in **Figure 2A**.
- FDI4 is a two-phase manipulation. One is mean-based manipulation and the second one is a constant numeric number subtraction-based manipulation. The mutual difference between both strategies the SM's consumption data under-reports the original consumption as shown in **Figure 2B**.
- FDI5 is the manipulation of the SM's data during off-peak and off-peak hours. A γ factor is a difference-based manipulation variable, which is represented by a simple numeric number. The variable is subtracted from the recorded readings to under-report the consumed energy as shown in **Figure 3A**.
- FDI6 is a unit-step function-based manipulation at the consumer's end. It manipulates the consumption with a choice to operate it at any time stamp or periodically. It can steal 100% of the consumed energy in the extreme. However, in the case of equilibrium, a 50% of the theft is expected. During such modes of manipulation, the consumption is limited to 0 or 1 where 1 shows the original consumption and 0 shows the manipulated consumption as shown in **Figure 3B**.

4.2 Model's architecture

The input data is segmented into various data subsets in form of slabs through a dynamic sliding window. The dynamic

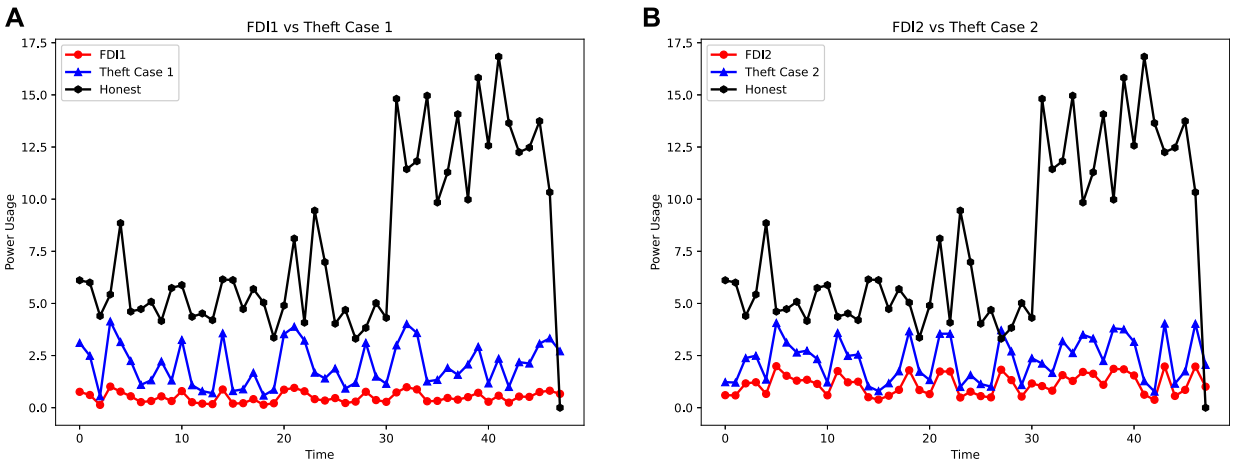

FIGURE 1
(A) Theft Case 1 vs. FDI 1. **(B)** Theft Case 2 vs. FDI 2.

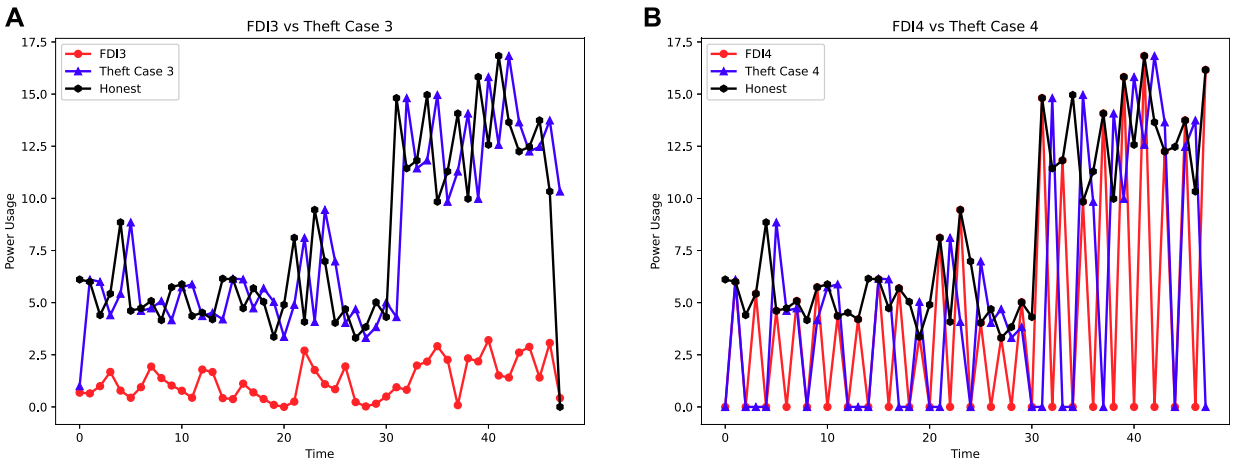

FIGURE 2
(A) Theft Case 3 vs. FDI 3. **(B)** Theft Case 4 vs. FDI 4.

sliding widow overlaps the input data by 50%. Data's subsets contain resizing strategy over k = 20 where 10 previous and 10 next records are buffered. Every next sliding slab selects the data starting from the data point residing on the 10th index of the previous slab. The data is resized in similar fashion until the very end of the array is reached. The same phenomenon is repeated consecutively for the oncoming next slab. The 50% overlapping of the data is a linear traversal of the data, which minimizes the complexity of the dense time series data and finds an optimized data resizing strategy for the input data. The developed hybrid model is a delicately structured architecture, which is a multivariate model and inspired by the long-term short-term memory and fully convolutional network (LSTM-FCN). In order to retain recurrent information of the time series data the modules are integrated in parallel where the LSTM module is connected to an inception time network with additional layers of attention (Abbasimehr and Paki, 2022). Novel FDI techniques are proposed in comparison to six theft cases for data manipulation (Dua et al., 2022). AttenLSTMInception model is a multivariate resolution feature of the time series data. The ultimate goal is to capture and analyse the variance between the classes' data. In order to retain the information LSTM-Inception model contains two residual blocks. Information propagation between the residual blocks is initiated by an ultimate short linear connection where inputs are added to the next block. Such schematics mitigate the vanishing gradient problem due to the direct flow of the gradient. Stacking the inception modules, the first inception component is named

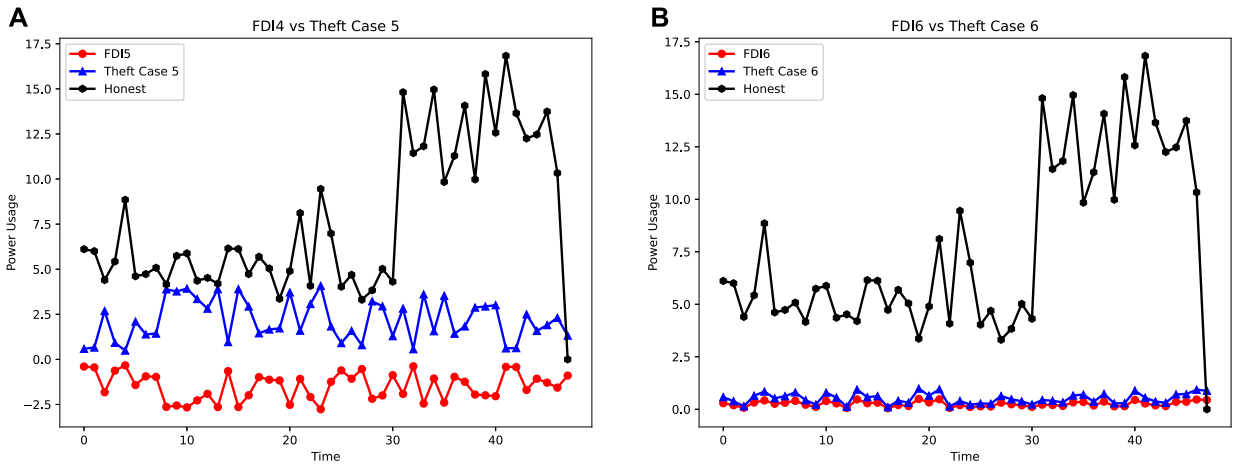

FIGURE 3
(A) Theft Case 5 vs. FDI 5. **(B)** Theft case 6 vs. FDI 6.

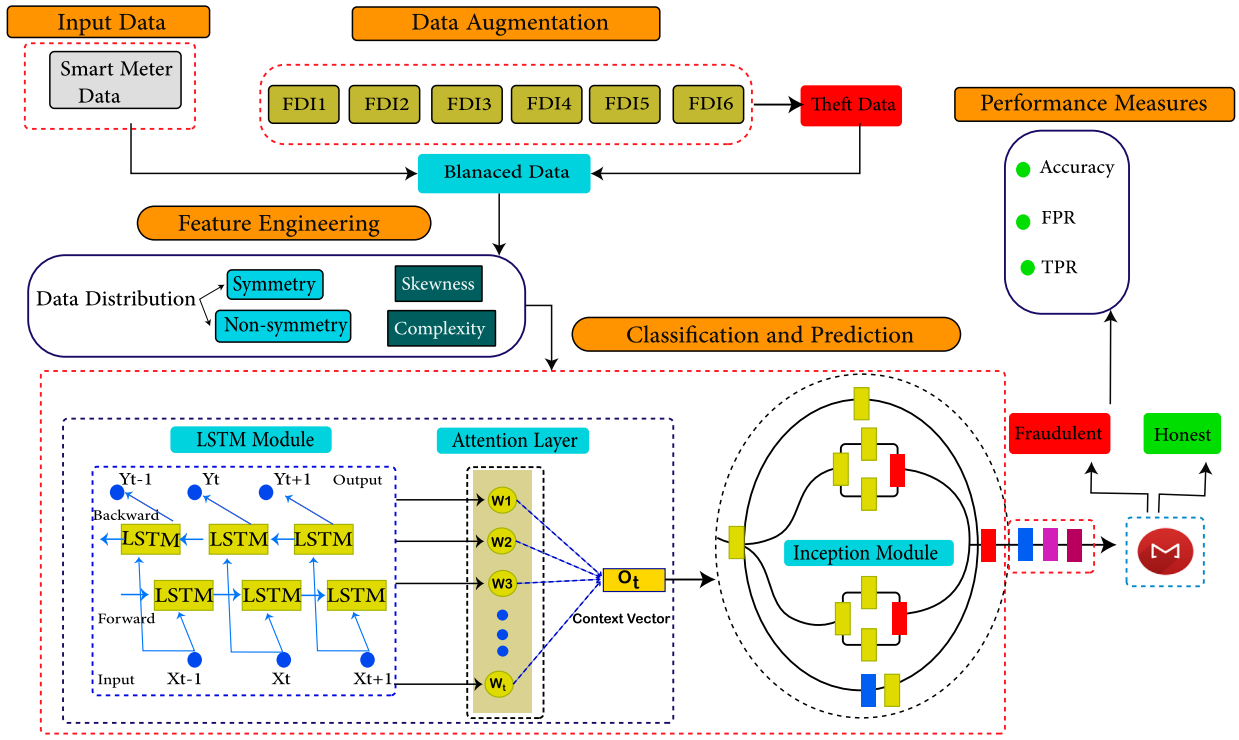

FIGURE 4
The proposed system model.

the bottleneck layer, which performs sliding operation over the data. Such layers reduce the data's dimensionality due to the sliding operation of the filters. Integrating networks in such scenarios mitigate the over-fitting issue, model's complexity, and complex dimensionality. It is necessary to mention that the bottleneck technique maximizes filter length in terms of pulling, which helps in reducing the computational complexity. The max-pooling generates sequential attributed data, which is concatenated with the inception modules' output. The hierarchical latent features are extracted *via* stacking and backpropagation mechanisms. The global pooled output of the inception module and AttenLSTM block are concatenated, which

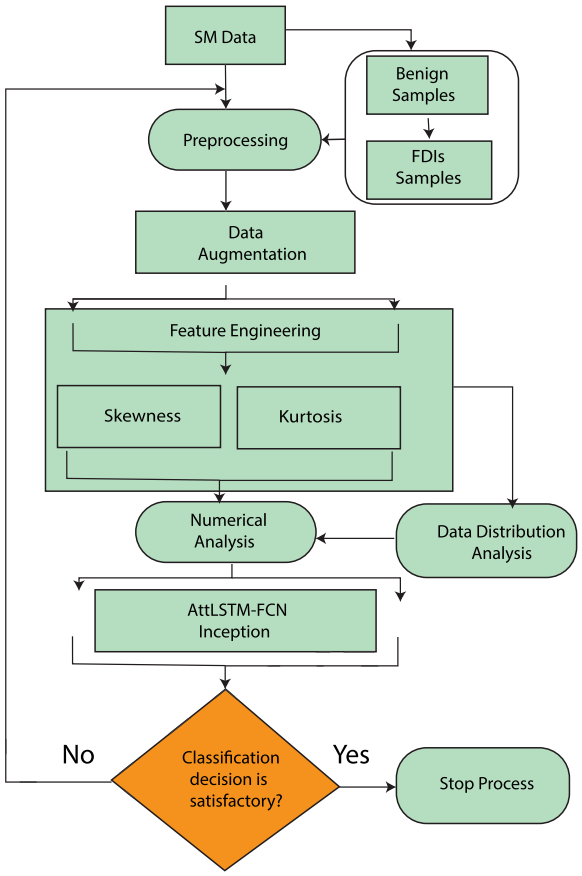

FIGURE 5
Working of flowchart.

Step 1: Defining fraudulent and honest consumers:
Input: Honest Consumers H_{E_c}, Fradulent Consumers F_{E_c}
Step 2: Introducing FDIs:
$FDI1 = \frac{mean(E)*random(0.1-0.9)}{E}$;
$FDI2 = \sqrt{(mean(E_c))}*random(0.1-0.9))$;
$FDI3 = \sqrt{(E_c)}*random(0.1-0.9)$;
$FDI4 = mean(E) - (\gamma)$;
$FDI5 = E - \gamma_i$;
$FDI6 = E(t-d) = 0 \ if \ t < d \ and \ 1 \ if \ t >= c$;
Step 3: Data Augmentation and Concatenation:
$Concat(\ FFDI1 \ + \ FDI2 \ + \ FDI3 \ + \ FDI4$
$+ \ FDI5 \ + \ FDI6 \ )$
$F_{E_c} = FDI_i + \ldots + FDI_n$: $where \ i = 1,\ldots,6.$
$E_{C_T} = H_{E_c} \ + \ F_{E_c}$
Step 4: Data Equilibrium:
$H_{E_c} \ = \ F_{E_c}$;
$F_{E_c} \ > \ H_{E_c}$; $apply \ proWsyn \ to \ H_{E_c}$.
$H_{E_c} \ = \ F_{E_c}$.
Step 5: Feature Engineering:
$E_{C_T} = H_{E_c} \ + \ F_{E_c}$
$skewness(mean(E_{C_T}))$
$kurtosis(mean(E_{C_T}))$
Step 6: Classification
Output: $E_c \ \varepsilon \ F_{X_c}$;
$E_c \ \varepsilon \ H_{X_c}$

Algorithm 2. AttenLSTMInception based Electricity Theft Detection Scheme.

is connected to the inception layer and classification operator function.

5 Proposed system model

The limitations with the proposed solutions are presented in Table 1. While the system model in Figure 4 represents our proposed solution for the aforementioned limitations. It is divided into five sections (1) Data preprocessing (2) Data manipulation (3) Data augmentation (4) Feature engineering and (5) Classification. The data distribution analysis is presented in Table 2.

- Initially in section (1), data is preprocessed where the missing values and outliers are filled and removed by the simple Imputer technique, respectively. A row-wise operation is carried out on the data to tackle such issues.
- In data manipulation section (2), consumers are defined based on their provided SM's readings, which are labeled with a binary representation of 0 and 1, where 0 stands for honest consumers and 1 for fraudulent consumers. Honest consumer data is manipulated in order to synthesize fraudulent consumers' data by applying FDI techniques. Data is synthesized due to the rare availability of the theft class data. Synthesized data by such FDI techniques show fraudulent consumers' data. The defined FDI techniques result in six variants for each benign sample.

- In section (3), data balancing is required in order to mitigate the Model's biasness and skewness towards a majority class. Dense skewness poisons the model's classification, which tends to increase the false positive rate (FPR). A data augmentation technique is required to mitigate such issues (Ullah et al., 2021), (Asif et al., 2021a), (Asif et al., 2021b), (Kabir et al., 2021). ProWsyn based data augmentation strategy is applied in the proposed work to balance fraudulent and benign class samples.
- In section (4), the balanced data is observed by the feature engineering module where the data's nature and distribution

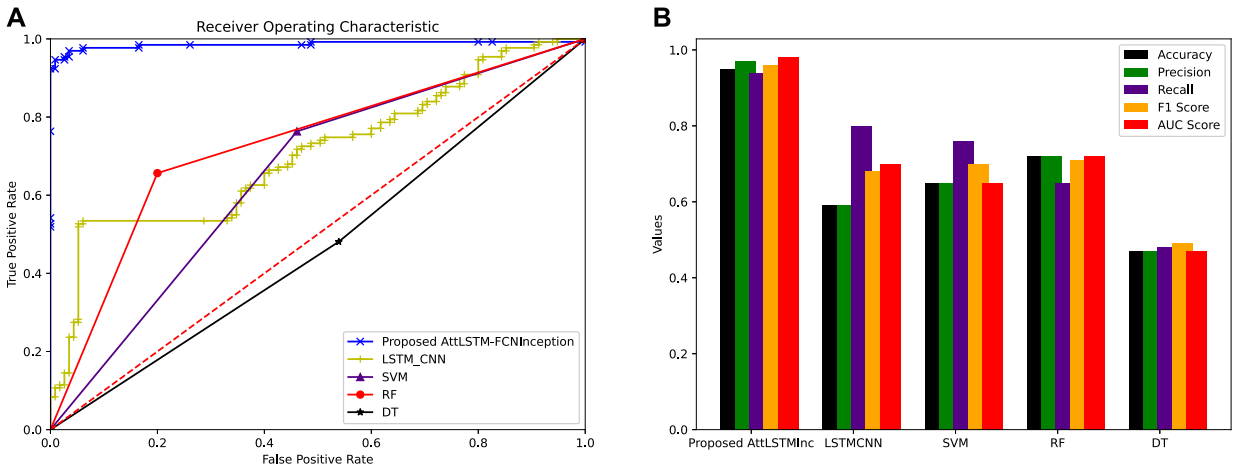

FIGURE 6
(A) Performance analysis of the benchmark and proposed model **(B)** Performance comparison.

are studied. Stochastical features, which contain mean, min, max, and standard deviation are generated to study the data's distribution. In addition, the skewness factors, kurtosis, quantile, root mean square and rolling features are engineered, which shows the distribution symmetry and its deviation. Such investigating factors result in deciding the model's complexity and deepness for the classification scenario. Highly skewed, defused and un-symmetric data needs a heavily featured classifying model for effective class segregation and classification.

- In section (5), to classify the samples effectively a hybrid model AttLSTM-FCNInception model is adopted, which is an integration of attention layers (Pustokhin et al., 2020), LSTM module (Yu et al., 2019) and Inception (Yang et al., 2019). Two of the Inception modules and attention layers are integrated into LSTM. The model is fed with the affine preprocessed data, which is suitable to tackle complex and un-symmetric data. **Algorithm 1** defines a summary of the whole system model.

6 Working of the system model

The working of the whole classification scenario is defined in **Figure 5**.

- Initially in step 1, the SMs' time series data is analyzed and benign samples are considered only due to non-availability of the theft class samples.
- In step 2, the benign class data is manipulated by six FDIs, and six new variants are synthesized for a single benign sample. Such variants for a single benign sample disrupt the data balancing, which requires balancing techniques to balance the data.
- In step 3, a ProWsyn minority class oversampling technique is opted to balance the data. Each sample is considered on a proximity basis where EU distance is measured by assigning weights to the samples. The nearest sample of the cluster to the decision boundary is weighted greater, whereas, the sample with a large EU distance from the perspective cluster is weighted less. The assigned weights help to mitigate the issues of misclassification and high FPR.
- In step 4, various features are engineered in order to investigate the complexity and distribution of the data. Two major mean-based synthesized features are targeted to investigate the complexity and distribution of the data. Kurtosis and skewness are the mean-based engineered features, which visualize the data's symmetry and far-tailed numeric outliers.
- In step 5, in order to enhance the data memorization, a sliding window segments the data with a 50% overlap, which carries the previous and next step information segments of the input data. Such translation of the available information flows back and forth, which increases the memorization capability of the model.
- In step 6, the segmented data is fed to a hybrid AttenLSTMInception model for classification. The fed data is classified and fraudulent consumers are detected with a low FPR, effectively.

7 Performance evaluation

ETD is a binary classification problem where benign and fraudulent classes are represented as positive and negative, respectively. In a binary classification scenario, the positive class

TABLE 3 Performance comparison of the proposed and existing models.

Classifier	Accuracy	Precision	Recall	F1 Score	AUC Score
Proposed AttLSTMInception	0.95	0.97	0.94	0.96	0.98
LSTMCNN	0.59	0.59	0.80	0.68	0.70
SVM	0.65	0.65	0.76	0.70	0.65
RF	0.72	0.72	0.65	0.71	0.72
DT	0.47	0.47	0.48	0.49	0.47

is labeled as 0 and the negative is labeled as 1. Precision, detection rate (DR), accuracy, AUC, and F1 score are used to evaluate the performance of the model. AUC is the area under the curve with two distinguishing parameters, TPR and FPR. TPR is the detection sensitivity of the model and FPR is the specificity. A comparative investigation between the accurate identification of true positive samples and true negative samples constructs AUC. Four parametric attributes are collectively mapped to measure the sensitivity and specificity of the model. Sensitivity is DR and specificity is the FPR of the model. Mathematically, it can be represented as (Jones and Athanasiou., 2005):

$$DR = \frac{TP}{TP + FN} \quad , \tag{6}$$

$$FPR = \frac{TN}{TN + FN} \quad , \tag{7}$$

Where TP, TN, FP, and FN represent true positive, true negative, false positive, and false negative, respectively. TP, TN, FP, and FN are the confusion matrix attributes, which investigate binary classification.

8 Simulation results

In order to compare the proposed AttLSTMInception model with the existing models DT, RF, SVM, and LSTMCNN, a comparative analysis is shown in **Figure 6A**, **Figure 6B**. Accuracy, precision, recall, F1 score, and AUC are the performance parameters, which are considered to investigate the performance of the models. The results in **Table 3** show that the proposed model outperforms the rest of the models. The effective performance of the proposed model is due to the attention and inception modules. The attention module mimics cognitive attention, which focuses on the prominent and important features rather than non-useful data. The inception module adds the properties of efficient computations and dimensionality reduction by using multiple data filtering sizes. The addition of the inception module tackles the problem of over-fitting and computational complexity. RF (Nguyen and Phan, 2021), SVM (Lin et al., 2021), DT, and LSTMCNN (Hasan et al., 2019) perform very badly. They cannot perform on complex time series data and cause overfitting issues. Furthermore, the performance of the proposed model is enhanced by using dropout regularization and adam optimization. **Figure 6** shows the AUC of various models against the proposed model. The proposed model outperforms the rest of the models. Initially, the proposed model classifies the time series data of the honest and fraudulent consumers with zero FPR, however, at an AUC score of 0.92 a minimal FPR is reported. The slight change in reporting FPR is due to the increased data complexity. LSTMCNN performs efficiently with a slight FPR, however, it reduces its performance over the increased complexity of the data. **Figures 6A,B** shows that the low FPR is achieved by the proposed model as compared to other models, which means that the fraudulent and honest consumers are accurately classified. Similarly, the AUC score of the conventional machine learning techniques SVM (Pamir et al., 2022b), RF, and DT (Munawar et al., 2021) is very bad and reports high FPR. **Figure 6** shows the accuracy, precision, recall, F1 scores, and AUC scores of the models. It can be seen that the proposed model outperforms the rest of the models in each of the performance parameters.

9 Conclusion and future work

In this paper, novel FDIs techniques are proposed in comparison to theft cases. The proposed FDIs manipulate the data severely as compared to the theft cases. The variations and complexity in data distribution caused by the proposed FDIs and theft cases are investigated through data distribution techniques. The analysis shows that the proposed FDIs are severe in nature while manipulating data of SMs' as compared to theft cases. FDIs observe minimal skewness and complexity in data distribution as compared to the theft cases data. Furthermore, six variants are synthesized for each of the honest consumers. A novel data balancing technique, ProWsyn is used to balance the data. Moreover, the attLSTMInception model is proposed, which is an integration of LSTM, attention layers, and inception modules. The proposed model outperforms the rest of the existing models and achieves an accuracy of 0.95%, precision 0.97%, recall 0.94%, F1 score 0.96%, and AUC score 0.98%. In future work, we will investigate the extraction of abstract features for dimensionality reduction and the addition of more memory modules for long-term dependencies of the data in our proposed model to reduce FPR furthermore.

Data availability statement

The original contributions presented in the study are included in the article/Supplementary Materials, further inquiries can be directed to the corresponding author.

Author contributions

Conceptualization, SM and NJ; methodology, SM; software, SM; validation, NJ; writing—original draft preparation, SM; writing—review and editing, NJ, ZK, NC, and MR; supervision, ZK and NC; project administration, MR, AM, and AA; funding acquisition, AM and AA. All authors have read and agreed to the published version of the manuscript.

Funding

This research work was funded by Institutional Fund Projects under grant no. (IFPIP: 1555-135-1442). Therefore, authors gratefully acknowledge technical and financial support from the Ministry of Education and King Abdulaziz University, DSR, Jeddah, Saudi Arabia.

Conflict of interest

The authors declare that the research was conducted in the absence of any commercial or financial relationships that could be construed as a potential conflict of interest.

The handling editor, KM declared a past co-authorship with the author(s), NC and AM.

Publisher's note

All claims expressed in this article are solely those of the authors and do not necessarily represent those of their affiliated organizations, or those of the publisher, the editors and the reviewers. Any product that may be evaluated in this article, or claim that may be made by its manufacturer, is not guaranteed or endorsed by the publisher.

References

Abbasimehr, H., and Paki, R. (2022). Improving time series forecasting using LSTM and attention models. *J. Ambient. Intell. Humaniz. Comput.* 13 (1), 673–691. doi:10.1007/s12652-020-02761-x

Arqub, O. A. (2020). Numerical simulation of time-fractional partial differential equations arising in fluid flows via reproducing Kernel method. *Int. J. Numer. Methods Heat. Fluid Flow.* 30, 4711–4733. doi:10.1108/hff-10-2017-0394

Arqub, O. A. (2018). Numerical solutions for the Robin time-fractional partial differential equations of heat and fluid flows based on the reproducing kernel algorithm. *Int. J. Numer. Methods Heat. Fluid Flow.* 28, 828–856. doi:10.1108/hff-07-2016-0278

Asif, M., Kabir, B., Ullah, A., Munawar, S., and Javaid, N. (2021). "Towards energy efficient smart grids: Data augmentation through BiWGAN, feature extraction and classification using hybrid 2DCNN and BiLSTM," in *International conference on innovative mobile and internet services in ubiquitous computing* (Cham: Springer), 108–119.

Asif, M., Ullah, A., Munawar, S., Kabir, B., Khan, A., and Javaid, N. (2021). "Alexnet-AdaBoost-ABC based hybrid neural network for electricity theft detection in smart grids," in *Conference on complex, intelligent, and software intensive systems* (Cham: Springer), 249–258.

Blanca, M. J., Arnau, J., Lopez-Montiel, D., and Bendayan, R. (2013). Skewness and kurtosis in real data samples. *Methodol. (Gott).* 9 (2), 78–84. doi:10.1027/1614-2241/a000057

Blazakis, K. V., Kapetanakis, T. N., and Stavrakakis, G. S. (2020). Effective electricity theft detection in power distribution grids using an adaptive neuro fuzzy inference system. *Energies* 13 (12), 3110. doi:10.3390/en13123110

Buzau, M. M., Tejedor-Aguilera, J., Cruz-Romero, P., and Gómez-Expósito, A. (2019). Hybrid deep neural networks for detection of non-technical losses in electricity smart meters. *IEEE Trans. Power Syst.* 35 (2), 1254–1263. doi:10.1109/tpwrs.2019.2943115

Cai, Y., Li, Y., Cao, Y., Li, W., and Zeng, X. (2017). Modeling and impact analysis of interdependent characteristics on cascading failures in smart grids. *Int. J. Electr. Power & Energy Syst.* 89, 106–114. doi:10.1016/j.ijepes.2017.01.010

Cheng, G., Zhang, Z., Li, Q., Li, Y., and Jin, W. (2021). Energy theft detection in an edge data center using deep learning. *Math. Problems Eng.* 2021, 1–12. doi:10.1155/2021/9938475

Depuru, S., Reddy, S. S., Wang, L., and Devabhaktuni, V. (2011). Electricity theft: Overview, issues, prevention and a smart meter based approach to control theft. *Energy policy* 39 (2), 1007–1015. doi:10.1016/j.enpol.2010.11.037

Djennadi, S., Shawagfeh, N., and Arqub, O. A. (2021). A fractional Tikhonov regularization method for an inverse backward and source problems in the time-space fractional diffusion equations. *Chaos, Solit. Fractals* 150, 111127. doi:10.1016/j.chaos.2021.111127

Djennadi, S., Shawagfeh, N., Osman, M. S., Gómez-Aguilar, J. F., Arqub, O. A., and Abu Arqub, O. (2021). The Tikhonov regularization method for the inverse source problem of time fractional heat equation in the view of ABC-fractional technique. *Phys. Scr.* 96 (9), 094006. doi:10.1088/1402-4896/ac0867

Dua, N., Singh, S. N., Vijay, B. S., Kumar Challa, S., and Challa, S. K. (2022). Inception inspired CNN-GRU hybrid network for human activity recognition. *Multimed. Tools Appl.*, 1–35. doi:10.1007/s11042-021-11885-x

Glauner, P., Augusto Meira, J., Valtchev, P., Radu, S., and Franck, B. (2016). *The challenge of non-technical loss detection using artificial intelligence: A survey*. arXiv preprint arXiv:1606.00626.

Guo, Y., Yang, Z., Feng, S., and Hu, J. (2018). "Complex power system status monitoring and evaluation using big data platform and machine learning algorithms: A review and a case study," in *Complexity 2018*.

Hasan, M., Toma, R. N., Nahid, A-A., Islam, M. M., and Kim, J-M. (2019). Electricity theft detection in smart grid systems: A CNN-LSTM based approach. *Energies* 1217, 3310. doi:10.3390/en12173310

Himeur, Y., Ghanem, K., Abdullah, A., Bensaali, F., and Amira, A. (2021). Artificial intelligence based anomaly detection of energy consumption in buildings: A review, current trends and new perspectives. *Appl. Energy* 287 (2021), 116601. doi:10.1016/j.apenergy.2021.116601

Hussain, S., Mustafa, M. W., Jumani, T. A., Khan Baloch, S., Alotaibi, H., Khan, I., et al. (2021). A novel feature engineered-CatBoost-based supervised machine learning framework for electricity theft detection. *Energy Rep.* 7 (2021), 4425–4436. doi:10.1016/j.egyr.2021.07.008

Islam, A., and Belhaouari, S. B. (2022). *Atiq ur rahman, and halima bensmail. "K nearest neighbor OveRsampling approach: An open source python package for data augmentation*. Software Impacts, 100272.

Javaid, N., Gul, H., Baig, S., Shehzad, F., Xia, C., Guan, L., et al. (2021). Using GANCNN and ERNET for detection of non technical losses to secure smart grids. *IEEE Access* 9 (2021), 98679–98700. doi:10.1109/access.2021.3092645

Javaid, N., Jan, N., and Umar Javed, M. (2021). An adaptive synthesis to handle imbalanced big data with deep siamese network for electricity theft detection in smart grids. *J. Parallel Distributed Comput.* 153, 44–52. doi:10.1016/j.jpdc.2021.03.002

Jeyaraj, P. R., Edward, P. R. S. N., Kathiresan, A. C., and Siva, P. A. (2020). Smart grid security enhancement by detection and classification of non-technical losses employing deep learning algorithm. *Int. Trans. Electr. Energ. Syst.* 30 (9), e12521. doi:10.1002/2050-7038.12521

Jones, C. M., and Athanasiou., T. (2005). Summary receiver operating characteristic curve analysis techniques in the evaluation of diagnostic tests. *Ann. Thorac. Surg.* 79 (1), 16–20. doi:10.1016/j.athoracsur.2004.09.040

Kabir, B., Ullah, A., Munawar, S., Asif, M., and Javaid, N. (2021). "Detection of non-technical losses using MLP-GRU based neural network to secure smart grids," in *Conference on complex, intelligent, and software intensive systems* (Cham: Springer), 383–394.

Kocaman, B. T., and Tümen, V. (2020). Detection of electricity theft using data processing and LSTM method in distribution systems. *Sādhanā* 451, 286–10. doi:10.1007/s12046-020-01512-0, no.

Li, S., Han, Y., Yao, X., Song, Y., Wang, J., and Zhao, Q. (2019). Electricity theft detection in power grids with deep learning and random forests. *J. Electr. Comput. Eng.* 2019, 1–12. doi:10.1155/2019/4136874

Lin, G., Feng, X., Guo, W., Cui, X., Liu, S., Jin, W., et al. (2021). Electricity theft detection based on stacked autoencoder and the undersampling and resampling based random forest algorithm. *IEEE Access* 9 (2021), 124044–124058. doi:10.1109/access.2021.3110510

Munawar, S., Asif, M., Kabir, B., Ullah, A., and Javaid, N. (2021). "Electricity theft detection in smart meters using a hybrid Bi-directional GRU Bi-directional LSTM model," in *Conference on complex, intelligent, and software intensive systems* (Cham: Springer), 297–308.

Nguyen, T. H. T., and Phan, Q. B. (2021). "Electricity theft detection in power grid with a hybrid convolutional neural network-support vector machine model," in *The 5th international conference on future networks & distributed systems*, 24–30.

Pamir, N. J., Javaid, S., Asif, M., Umar Javed, M., Adamu, S. Y., Aslam, S., et al. (2022). Synthetic theft attacks and long short term memory-based preprocessing for electricity theft detection using gated recurrent unit. *Energies* 15 (8), 2778. doi:10.3390/en15082778

Pamir, N. J., Qasim, U., Adamu, S. Y., Alkhammash, E. H., and Hadjouni, M. (2022). *Non-technical losses detection using autoencoder and bidirectional gated recurrent unit to secure smart grids*. IEEE Access.

Parikh, P. P., Kanabar, M. G., and Sidhu, T. S. (2010). "Opportunities and challenges of wireless communication technologies for smart grid applications," in *IEEE PES general meeting* (IEEE), 1–7.

Pereira, J., and Saraiva, F. (2021). Convolutional neural network applied to detect electricity theft: A comparative study on unbalanced data handling techniques. *Int. J. Electr. Power & Energy Syst.* 131, 107085. doi:10.1016/j.ijepes.2021.107085

Punmiya, R., and Choe, S. (2019). Energy theft detection using gradient boosting theft detector with feature engineering-based preprocessing. *IEEE Trans. Smart Grid* 10 (2), 2326–2329. doi:10.1109/tsg.2019.2892595

Pustokhin, D. A., Pustokhina, I. V., Dinh, P. N., Van Phan, S., Gia, N. N., Joshi, G. P., et al. (2020). An effective deep residual network based class attention layer with bidirectional LSTM for diagnosis and classification of COVID-19. *J. Appl. Statistics*, 1–18. doi:10.1080/02664763.2020.1849057

Rawat, D. B., and Bajracharya, C. (2015). "Cyber security for smart grid systems: Status, challenges and perspectives," in *SoutheastCon 2015*, 1–6.

Rodriguez, V., Esther, J. D. S., Oregi, I., Bilbao, M. N., and Gil-Lopez, S. (2017). Detection of non-technical losses in smart meter data based on load curve profiling and time series analysis. *Energy* 137, 118–128. doi:10.1016/j.energy.2017.07.008

Sha, Y., Faber, J., Gou, S., Liu, B., Li, W., Schramm, S., et al. (2022). An acoustic signal cavitation detection framework based on XGBoost with adaptive selection feature engineering. *Measurement* 192 (2022), 110897. doi:10.1016/j.measurement.2022.110897

Somefun, T. E., Awosope, C. O. A., and Chiagoro, A. (2019). Smart prepaid energy metering system to detect energy theft with facility for real time monitoring. *Int. J. Electr. Comput. Eng.* 9 (5), 4184. doi:10.11591/ijece.v9i5.pp4184-4191

Sweis, H., Shawagfeh, N., and Arqub, O. A. (2022). Fractional crossover delay differential equations of Mittag-Leffler kernel: Existence, uniqueness, and numerical solutions using the Galerkin algorithm based on shifted Legendre polynomials. *Results Phys.* 41, 105891. doi:10.1016/j.rinp.2022.105891

Takiddin, A., Ismail, M., Zafar, U., and Serpedin, E. (2020). Robust electricity theft detection against data poisoning attacks in smart grids. *IEEE Trans. Smart Grid* 12 (3), 2675–2684. doi:10.1109/tsg.2020.3047864

Ullah, A., Munawar, S., Asif, M., Kabir, B., and Javaid, N. (2021). "Synthetic theft attacks implementation for data balancing and a gated recurrent unit based electricity theft detection in smart grids," in *Conference on complex, intelligent, and software intensive systems* (Cham: Springer), 395–405.

Yang, S., Lin, G., Jiang, Q., and Lin, W. (2019). A dilated inception network for visual saliency prediction. *IEEE Trans. Multimed.* 22 (8), 2163–2176. doi:10.1109/tmm.2019.2947352

Yasakethu, S. L. P., and Jiang, J. (2013). "Intrusion detection via machine learning for SCADA system protection," in *1st international symposium for ICS & SCADA cyber security research 2013 (ICS-csr 2013)*, 1, 101–105.

Yu, Y., Si, X., Hu, C., and Zhang, J. (2019). A review of recurrent neural networks: LSTM cells and network architectures. *Neural Comput.* 31 (7), 1235–1270. doi:10.1162/neco_a_01199

frontiers | Frontiers in Energy Research

TYPE Original Research
PUBLISHED 16 January 2023
DOI 10.3389/fenrg.2022.1009812

OPEN ACCESS

EDITED BY
Salah Kamel,
Aswan University, Egypt

REVIEWED BY
Youcef Belkhier,
Maynooth University, Ireland
Muhammad Asad,
Dalhousie University, Canada

*CORRESPONDENCE
Yuanqing Xia,
xia_yuanqing@bit.edu.cn

SPECIALTY SECTION
This article was submitted to Smart Grids, a section of the journal Frontiers in Energy Research

RECEIVED 02 August 2022
ACCEPTED 21 October 2022
PUBLISHED 16 January 2023

CITATION
Samad MA, Xia Y, Manzoor T, Mehmood K, Saleem A, Milyani AH and Azhari AA (2023), Composite model predictive control for the boost converter and two-phase interleaved boost converter.
Front. Energy Res. 10:1009812.
doi: 10.3389/fenrg.2022.1009812

Composite model predictive control for the boost converter and two-phase interleaved boost converter

Muhammad Adnan Samad[1], Yuanqing Xia[1]*, Tayyab Manzoor[2], Kashif Mehmood[3], Adeel Saleem[3], Ahmad H. Milyani[4] and Abdullah Ahmed Azhari[5]

[1]Key Laboratory of Intelligent Control and Decision of Complex Systems, School of Automation, Beijing Institute of Technology, Beijing, China, [2]School of Automation Science and Engineering, South China University of Technology, Guangzhou, China, [3]Department of Electrical Engineering, Fergana Polytechnic Institute, Fergana, Uzbekistan, [4]Department of Electrical and Computer Engineering, Center of Research Excellence in Renewable Energy and Power Systems, King Abdulaziz University, Jeddah, Saudi Arabia, [5]The Applied College, King Abdulaziz University, Jeddah, Saudi Arabia

This article compares the conventional model predictive control (MPC) and active disturbance rejection control (ADRC) with a novel MPADRC technique for controlling a non-minimum phase behavior in the DC–DC boost converter. The control of the boost converter is challenging as it is nonlinear, and it shows non-minimum phase behavior in a continuous conduction mode (CCM). Moreover, in this article, the comparison is presented for the boost converter and the two-phase interleaved boost converter using MPC and ADRC, and the effectiveness of the interleaving technique is shown. Finally, it is proved that the interleaving method has much more efficiency and less output ripple than the simple boost converter. To conclude, a novel technique has been introduced that combines both the techniques, that is, MPC and ADRC, in the outer and inner loop with a boost converter, respectively, and the response is clearly the best when compared to the said techniques individually. The overall impact of this technique includes the advantages of both the techniques, that is, the use of MPC allows us to optimize the current value by predicting the future values, and the use of ADRC ensures that the disturbance factor is well tackled and cancels the effect caused by all the disturbances including ignored quantities as well.

KEYWORDS

boost converter, interleaved boost converter, model predictive control (MPC), active disturbance rejection control (ADRC), MPADRC

1 Introduction

1.1 Literature review

Boost converters are mainly used to get a higher regulated output voltage from a lower unregulated input voltage. To implement it and fully understand its step response,

first, the simple boost converter is implemented in MATLAB using a state space model and analyzed. Upon analysis, the step response parameters, that is, rise time, settling time, percentage overshoot, and steady-state error are found to be highly undesirable, so there should be a technique, that is, a controller that should be used in conjunction with a boost converter to make its step response parameters better. In search of a controller, initially, PID (proportional integral derivative), PD, and PI controllers were found to be appropriate and used, but later on, the results, that is, step response parameters obtained using PID, PD, and PI, were also found to be the non-optimal ones, so the search for a better controller continued. Finally, MPC (model predictive controller) and ADRC (active disturbance rejection control) were found to be the best among all, while PID did not consider the future associations of the current control strategies. On the other hand, MPC unambiguously computes the predicted output over some horizon. The control of simple boost converters using the unconstrained nonlinear optimization technique to tune the parameters of PID is an advancement as compared to conventional techniques in many research articles but still has a chance to increase the efficiency. In recent days, there have been many research studies that cover all of these advancements. Nowadays, MPC is considered a new control technique for DC–DC converters. It can be used to obtain a better step response and step response parameters. The main theme of MPC is to predict future output by looking into present or past input values (Murali et al., 2010; Rossiter, 2022).

Recently, many used techniques incorporate detailed mathematical modeling to control these types of converters, but the need of the hour is to explore some other techniques as well that can predict, estimate, and reject the future disturbances (Chen et al., 2016) as ADRC. It was first introduced and discovered by Han (1999) and Han (2009) to work on both internal and external disturbances by estimating their mutual effect *via* an ESO (extended state observer), and much literature is presented on the said technique (Zhou et al., 2009; Zheng et al., 2012; Huang and Xue, 2014; Madoński and Herman, 2015; Feng and Guo, 2017). ADRC is also used recently to control these types of converters, and there have been different ADRC techniques from linear to high control gain and generalized ADRC (Saif and Ahmad, 2019).

State space representation is the most used representation for DC–DC converters to implement their step response, especially in MPC. First, the control problem is formulated, and then it is taken as the optimal problem to solve it using a predictive controller. The main objective is to regulate the output voltage despite changes in the input voltage or load resistance (Wang, 2009). Although the boost converter is very useful in many power applications, the interleaving technique has also become more effective than a simple boost converter. Basically, an interleaved boost converter is made by combining more than one boost converter. Moreover, the interleaving method is more suitable than the simple boost converter topology. The main objectives of interleaving are to improve the efficiency, reduce the component size, and reduce the current ripple and obviously the transient response. The benefits of interleaving are high power ability, improved efficiency, modularity, reduced size, and reliability, but there is a trade-off that the number of overall components will be increased (Kosai et al., 2009). The poor dynamic response caused by the use of conventional PI control requires a voltage feedforward compensator with MPC (Li et al., 2017; Li et al., 2018). To overcome this problem, the advanced technique ADRC is proposed in this work.

As compared to low-power applications, the use of interleaving for high-power applications has many advantages like increasing the output power and decreasing the output ripple, but the current sharing between the parallel paths is really worth considering (Lee et al., 2000).

The interleaving technique has many more advantages as compared to a conventional boost converter, that is, a slight modification in an interleaved boost converter can result in a voltage gain far better than a conventional boost converter (Gustavo et al., 2010). With these features, the interleaved boost converter is considered the best converter used in many applications. It is most suitable where a large step-up power is demanded in which the renewable energy resource application is on the top list.

Some more applications of the interleaving technique include high-power applications. It is a multidevice interleaved boost converter (MDIBC) that basically forms an interface between fuel cells and hybrid electric vehicles. The main advantages of this technique include the reduction of input ripple current, the ripples of output voltage, and finally the size of the passive components with high efficiency as compared to the other available techniques (Omar et al., 2012). Moreover, the interleaving technique can include a minimum of two boost converters in parallel up to n, where n can be any integer level according to the requirements of the controller and plant.

Some more optimization techniques like predictive function control can be used to regulate the temperature-efficient energy consumption (Nassima et al., 2021). Furthermore, the limitation of a proportional integral (PI) controller can be resolved by using some advanced expert approaches (Ahmed et al., 2022; Kim et al., 2014). For tuning the control parameters, there is a need for advanced optimization techniques so that we can get better system response parameters (Khan et al., 2022). Finally, the comparison of PID and ADRC is presented in Han (2009), which clearly shows the effectiveness of ADRC on PID and its shortcomings.

1.2 Contribution

While talking about DC converters, specifically a non-minimum phase system like boost converters, much work has

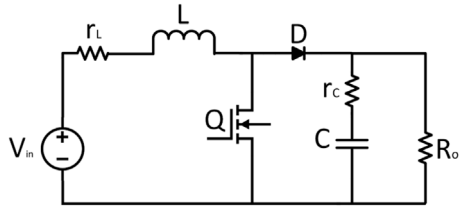

FIGURE 1
DC/DC boost converter.

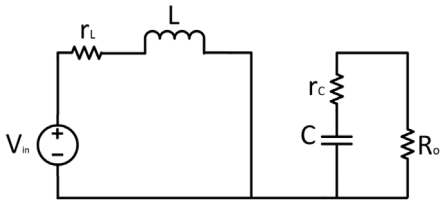

FIGURE 2
ON state.

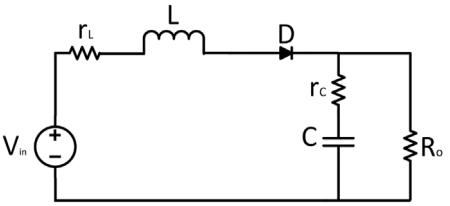

FIGURE 3
OFF state.

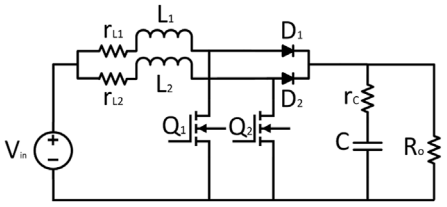

FIGURE 4
Two-phase interleaved boost converter.

been carried out in terms of its use in stepping up techniques and its control using conventional and some advanced techniques. In this work, the two-way approach has been used; first, not only the boost converter but also the two-phase boost converter is used to attain maximum efficiency. Second, the proposed work uses two control techniques, namely, the MPC and the ADRC,

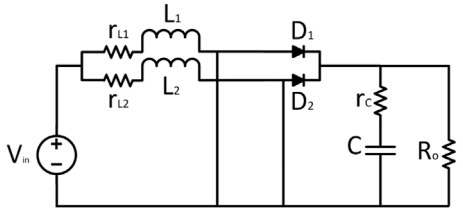

FIGURE 5
Q1 and Q2 are ON.

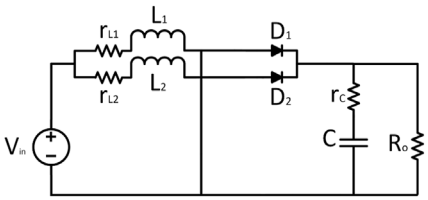

FIGURE 6
Q1 is ON and Q2 is OFF.

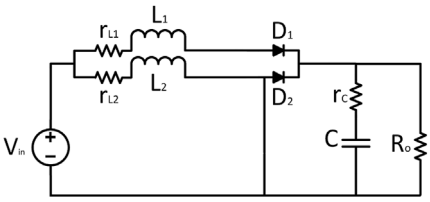

FIGURE 7
Q1 is OFF and Q2 is ON.

in the outer and inner loops, respectively. The results clearly show that controlling these types of converters alone by using any technique has less efficiency as compared to using a novel MPADRC technique.

1.3 Organization and notations

The article is organized in the following way: **Section 1** gives the introduction and literature review. **Section 2** covers the detailed mathematical modeling of boost and interleaved boost converters. **Section 3** briefly states the problem that is going to be solved. **Section 4** outlines the control and design approach opted for this research. Finally, the simulation is presented in **Section 5** which shows and proves the effectiveness of this proposed controller design. In the end, the conclusion and future work are presented in **Section 6**.

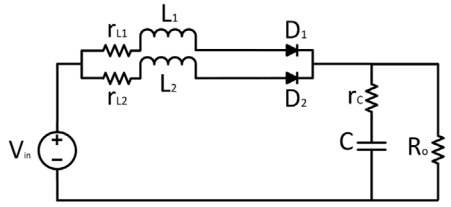

FIGURE 8
Q1 and Q2 are OFF.

2 Mathematical modeling

2.1 Mathematical modeling of the DC/DC boost converter

The basic circuit diagram of a DC/DC boost converter, which can enhance the voltage level, is shown in **Figure 1**. The basic topology consists of a voltage source, an inductor, a switch, a diode, and a capacitor with an output load in parallel. There can be different possibilities to implement this type of converter (reference). Some techniques (reference) can easily handle its both modes of conduction, that is, CCM and DCM, and some have only taken CCM for the sake of simplicity (reference). This research only includes CCM for the sake of simplicity. In addition, the parasitic resistances for both the inductor and capacitor are also included. The different states associated with the DC/DC boost converter are shown in **Figures 2**, **3**, representing the ON state and OFF state, respectively. During the ON state, the inductor current increases, and during the OFF state, this inductor current decreases to fulfill the load requirements. Initially, KCL and KVL have been used to formulate the basic current and voltage equations, and then, for averaging, the state space modeling is being used and expressed as follows:

$$\frac{dx(t)}{dt} = \begin{cases} A_1 x(t) + Bv(t), & S = 1, \\ A_2 x(t) + Bv(t), & S = 0 \end{cases}, \tag{1}$$

$$y(t) = C.x(t), \tag{2}$$

where

$x(t) = \begin{bmatrix} i_L(t) & v_o(t) \end{bmatrix}$ and

$v(t) = \begin{bmatrix} v_{in}(t) & i_o(t) \end{bmatrix}$. Also, the matrices A_1, A_2, and B are given by $A_1 = \begin{bmatrix} -\frac{r_L}{L} & 0 \\ 0 & -\frac{1}{RC} \end{bmatrix}$, $A_2 = \begin{bmatrix} -\frac{r_L}{L} & -\frac{1}{L} \\ \frac{1}{C} & -\frac{1}{RC} \end{bmatrix}$, and $B = \begin{bmatrix} \frac{1}{L} & 0 \\ 0 & 0 \end{bmatrix}$.

Finally, averaging and combining the state space representation for ON time and OFF time as given in the following equation, $A = A_1 d + A_2(1-d)$, $B = B_1 d + B_2(1-d)$, $C = C_1 d + C_2(1-d)$, and $D = D_1 d + D_2(1-d)$, yield

$$A = \begin{bmatrix} -\frac{r_L}{L} & -(1-d)\frac{1}{L} \\ (1-d)\frac{1}{C} & \frac{-1}{RC} \end{bmatrix},$$

$$B = \begin{bmatrix} \frac{1}{L} & 0 \\ 0 & 0 \end{bmatrix},$$

where v_{in} is the input voltage, v_c is the voltage across the capacitor, v_o is the output voltage, i_L is the inductor current, L is the inductance, C is the capacitance, and R is the load resistance.

2.2 Mathematical modeling of the DC/DC interleaved boost converter

2.2.1 Two-phase interleaved boost converter

Nowadays multiphase converter topologies are in high demand as they can be very useful, especially in high-performance applications. This research work includes the interleaving technique to increase efficiency and reduce the input and output ripples as compared to simple topologies. Moreover, improvement in switching stress and low EMI can also be achieved. Starting from two to n boost converters, they can be connected in parallel to form an n-phase interleaved boost converter. Initially, a two-phase interleaved boost converter is presented in detail with two switches and four states.

The basic circuit diagram of a two-phase interleaved DC/DC boost converter is shown in **Figure 4**. The basic topology consists of two boost converter stages in parallel. Again, the CCM for the sake of simplicity is being taken into consideration, and the parasitic resistances for both the inductor and capacitor are also included.

The different states associated with the DC/DC boost converter are shown in **Figures 5–8** representing the four states, respectively. Then, using basic rules of KCL and KVL and depending upon switch states, the current and voltage equations of all states have been formulated, and the average state space is modeled as follows, while the matrices A1, A2, A3, A4, and B of all four states, respectively, are given by

$$A_1 = \begin{bmatrix} -\frac{R_{L_1}}{L_1} & 0 & 0 \\ 0 & -\frac{R_{L_2}}{L_2} & 0 \\ 0 & 0 & -\frac{1}{R_{oC}} \end{bmatrix},$$

$$A_2 = \begin{bmatrix} -\frac{R_{L_1}}{L_1} & 0 & 0 \\ 0 & -\frac{R_{L_2}}{L_2} & -\frac{1}{L_2} \\ 0 & \frac{1}{C} & -\frac{1}{R_{oC}} \end{bmatrix},$$

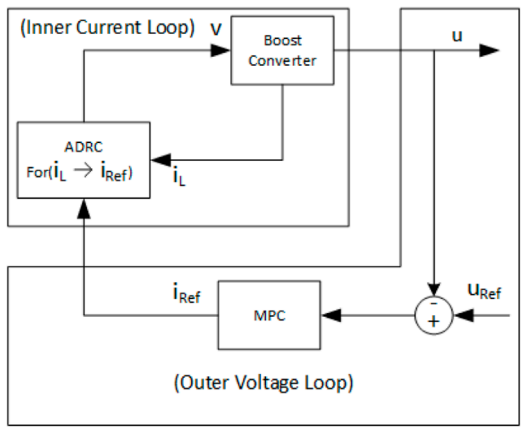

FIGURE 9
Main control approach.

$$A_3 = \begin{bmatrix} -\frac{R_{L_1}}{L_1} & 0 & -\frac{1}{L_1} \\ -\frac{R_{L_2}}{L_2} & 0 & 0 \\ \frac{1}{C} & 0 & -\frac{1}{R_{oC}} \end{bmatrix},$$

$$A_4 = \begin{bmatrix} -\frac{R_{L_1}}{L_1} & 0 & -\frac{1}{L_1} \\ 0 & -\frac{R_{L_2}}{L_2} & -\frac{1}{L_2} \\ \frac{1}{C} & \frac{1}{C} & -\frac{1}{R_{oC}} \end{bmatrix},$$

$$B = \begin{bmatrix} \frac{1}{L_1} & 0 \\ \frac{1}{L_2} & 0 \\ 0 & 0 \end{bmatrix}.$$

Finally, averaging and combining the state space representation for all the states using
$A = [A_1 + A_3]^*d + [A_2 + A_4]^*(1/N - d)$ yields

$$A = \begin{bmatrix} -\frac{R_{L_1}}{L_1}0 & -\frac{1}{2L_1} \\ -D\frac{R_{L_2}}{L_2} & (D-1)\frac{R_{L_2}}{L_2} \quad (D-1)\frac{1}{L_2} \\ \frac{1}{2C} & (2D+1)\frac{1}{C} \quad -\frac{1}{R_{oC}} \end{bmatrix},$$

$$B = \begin{bmatrix} \frac{1}{L_1} & 0 \\ \frac{1}{L_2} & 0 \\ 0 & 0 \end{bmatrix},$$

where v_{in} is the input voltage, v_c is the voltage across the capacitor, v_o is the output voltage, i_{L_1} and i_{L_2} are the inductor currents with L_1 and L_2 as the inductances, respectively, C is the capacitance, and R is the load resistance.

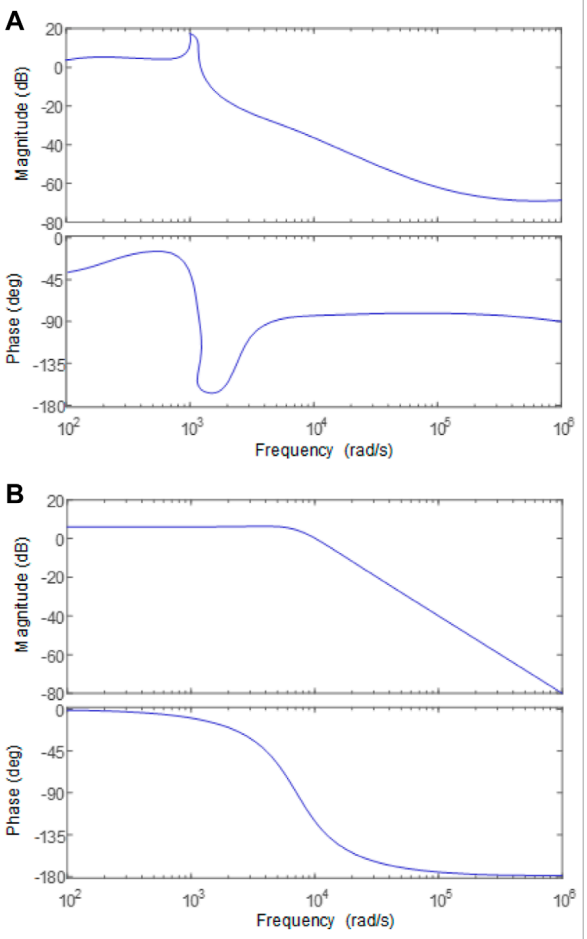

FIGURE 10
(A) Bode diagram without a controller. **(B)** Bode diagram with a controller.

3 Problem statement

While talking about DC/DC converters, the output should regulate to follow the given reference, while the input voltage or the output load keeps changing. In the presented case of the boost converter and interleaved boost converter, the input to the converter is the unregulated DC voltage, and the output is the regulated DC voltage. One more prominent and challenging factor while controlling these types of converters is its non-minimum phase behavior that tries to destabilize the close loop response due to the right half plane zero in its transfer function, which is mainly because of the inductor attached to the input. This specific type of system shows an inverse phenomenon as the output initially moves in the opposite direction of the reference (Forouzesh et al., 2017). In many practical applications, the uncertainties in different parameters,

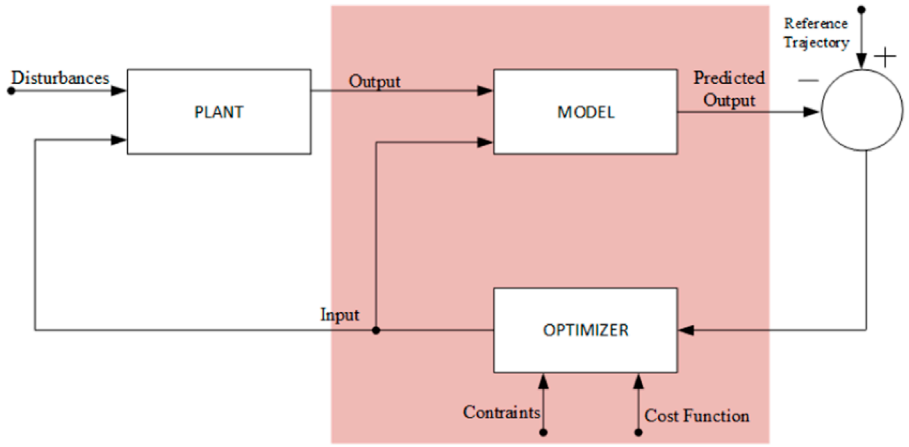

FIGURE 11
MPC block diagram.

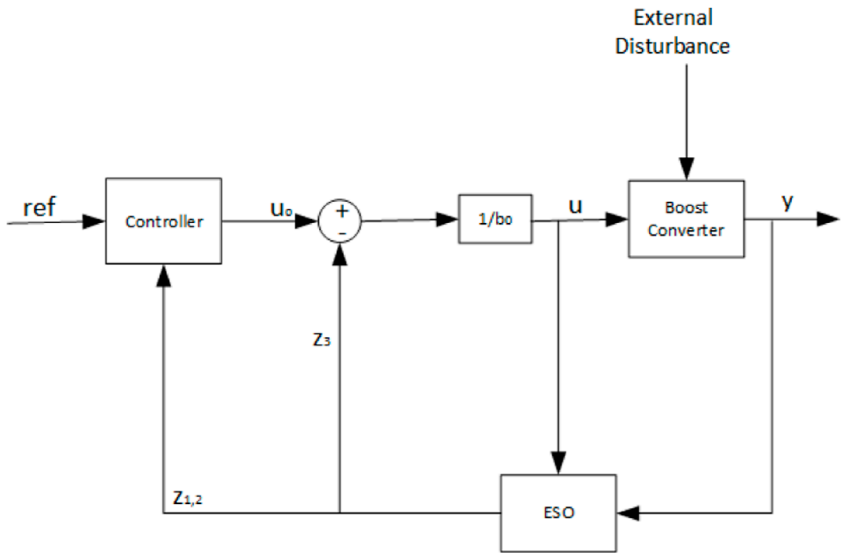

FIGURE 12
Structure of the ADRC.

especially ESR contributes to the poor performance, and the importance of ESR (effective series resistance) in DC boost converters is detailed in Yao et al. (2016). The steady-state error due to ESR of an inductor is more prominent than that due to the ESR of a capacitor. In short, the main objective of this study is to regulate the output voltage under input and load variations as quickly as possible while eliminating the steady-state error using model predictive control along with ADRC.

TABLE 1 Initial values.

Parameter	Value
Input voltage	12V
Output voltage	24V
Duty ratio	0.5
Switching frequency	20Khz
Load resistance	100Ω
Inductance	50mH
Conductance	1,000μF

4 Control and design approach

This section incorporates the controller and its novel design while using the model predictive controller and ADRC in the outer and inner loops, respectively. The detailed control diagram is shown in **Figure 9**. Initially, an objective function is defined, and then this function is minimized based on the control law techniques. As it can be seen in the figure, the control includes two loops: the inner ADRC loop for tracking the current to its reference and the outer MPC loop for producing a reference current. Thus, the ADRC scheme for the inner loop is designed to track the current according to $\lim_{k\to\infty} i_L(k) = i_{ref}$, while the outer loop is an addition to further tune the response by taking the collective advantage of ADRC and MPC. For stability check and to see the effectiveness of the proposed controller, the Bode diagram of the plant without any controller and with an MPADRC controller is analyzed in **Figure 10**. The Bode diagram of the DC–DC boost converter without any controller is shown in **Figure 10A**, and the Bode diagram of the said converter with the proposed controller is shown in **Figure 10B**.

4.1 Model predictive controller

The standard MPC technique solves a finite horizon problem and an optimal control problem based on a linear prediction model of the process (Bemporad et al., 2002; Mayne, 2014). In the field of power supplies, the use and interest of MPC keep growing as it has the ease of handling multivariable systems, introducing input/output constraints, and an intuitive design process (Vazquez et al., 2014; Karamanakos et al., 2014). Moreover, the MPC is an efficient control technique that works on the principle of receding horizon control (Belda and Vosmik, 2016; Judewicz et al., 2016). The major benefits of MPC include the following: it can control the MIMO system, it can well handle the input/output constraints, and it can make an advanced prediction of the model response. For all the aforementioned benefits, the applications of MPC have been investigated in different sectors such as power electronic converters, aerospace, renewable energy, and food processing. (Vazquez et al., 2014; Anang and Leksono, 2016; Raziei and Jiang, 2016; Zhao et al., 2017). A general block diagram of MPC is shown in **Figure 11**.

In this work, the MPC scheme is proposed in the outer loop, especially to control the current for controlling the DC–DC boost and multistage interleaved boost converters. The main purpose of using MPC is to control the output voltage by controlling the switch.

The main procedure of MPC is to formulate an objective function according to system dynamics and constraints and then minimize at each step over a set prediction horizon, which increases by one sampling interval at each step.

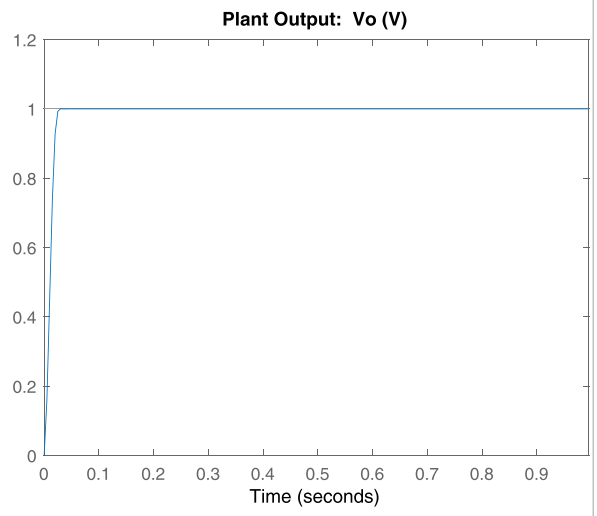

FIGURE 13
Plant output using MPADRC.

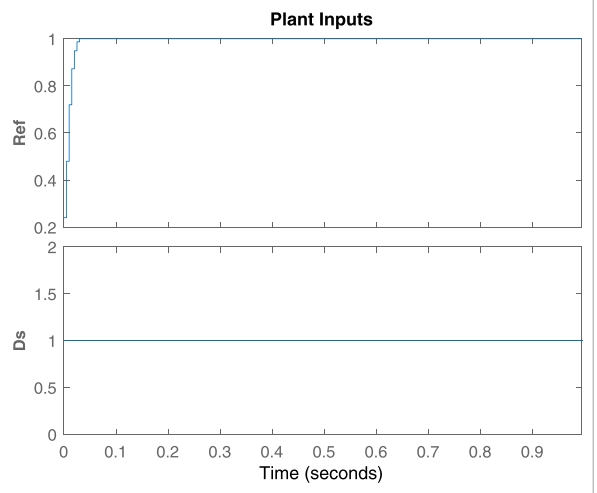

FIGURE 14
Plant inputs.

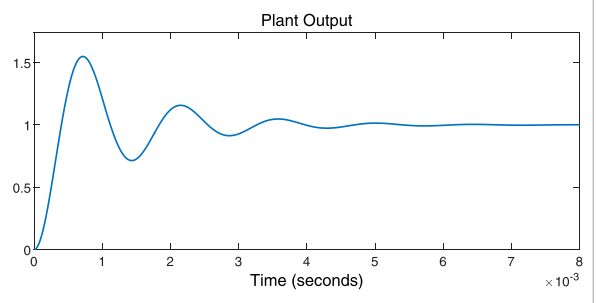

FIGURE 15
Plant output using the ADRC controller only.

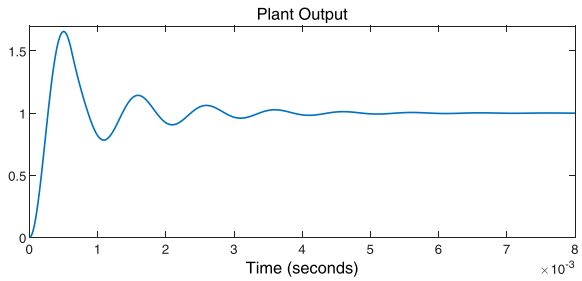

FIGURE 16
Interleaved plant output using the ADRC controller only.

4.2 Active disturbance rejection control

Active disturbance rejection control (ADRC) is first introduced by Jingqing Han in the 1980s as an unconventional design strategy. Since then, it has been considered an effective control strategy in the absence of proper models and in the presence of model uncertainty. Its effectiveness is shown in Han (2009) over conventional PID. In this study, ADRC is implemented in the inner loop to control the voltage of these DC converters and to generate a current reference to further feed into the inner loop for current tracking. The disturbance on load basically brings an error to the input in summer with the reference value, and then ADRC is applied to correct the error by adjusting its parameters as shown in **Figure 12**, where y is the output of the ADRC control and z is the estimates of different states. The nominal model used in this case can be of the *n*th order, where n is the order of the system to be controlled. The need of the hour is to check the deviation from the nominal suggested structure, and each and every deviation will be considered a disturbance. The extended state observer (ESO) is used to estimate the state and the "total disturbance."

4.3 Objective function

This is the main part in controlling any type of plant. When working on the objective function, the deviation should be well taken care of for the variables from the predicted value to the desired value over the set horizon *N*. The input to be controlled at any time instant kTs can be easily obtained by minimizing the particular function while taking into consideration the optimization variable, that is, specifically, the sequence of switching states over the entire horizon $U(k) = [u(k)u(k+1)\ldots u(k+N-1)]^T$. Thus, the optimal solution is represented by U^* which can be calculated by minimizing the objective function; $u^*(k)$ is applied at the input of the converter and used as the first element of the whole sequence. This procedure is repeated at the consecutive sampling instants based on the newly measured values, and the remaining elements are discarded. In this work, the control problem is obtained and formulated as a current regulation problem, which mainly accounts for the deviation of the inductor current from its set reference, which is defined as follows:

$$i_{L,err}(k) = i_{L,ref} - i_L(k). \tag{3}$$

While working on these types of objective functions, there can be several possibilities to describe the error, that is, the average value of the current or the RMS value of the current can be considered. In this particular work, the average current error is used as described in the following section.

4.3.1 Average current error

At any particular time-step k, the average current error over the prediction interval N^*Ts can be represented by

$$i_{L,\,\mathrm{err,avg}}(k) = \frac{1}{N*T_s}\int_{kT_s}^{(k+N)T_s} \left| i_{L,\,\mathrm{err}}(t \mid k) \right| dt. \tag{4}$$

Using the fact that the current slope remains constant in between the sampling instants and changes only at the sampling instants, the aforementioned integral can be rewritten as follows:

$$i_{L,err,avg}(k) = \frac{1}{N}\sum_{\ell=k}^{k+N-1} \frac{i_{L,\mathrm{err}}(\ell \mid k) + i_{L,\,\mathrm{err}}(\ell+1 \mid k)}{2}. \tag{5}$$

Based on these equations, the objective function can be written as follows:

$$J_{avg}(k) = \sum_{\ell=k}^{k+N-1} \frac{1}{N}\left| \bar{i}_{L,erx}(\ell \mid k) \right|. \tag{6}$$

4.4 Optimization problem

After describing the objective function, the optimization problem can be formulated and solved at each sampling instant, and it has the form,

$$\text{minimize } J(k), \tag{7}$$

subject to the mathematical model of the converters. The aforementioned optimization problem is solved using these possible combinations of the switching state, that is, (u = 0 or u = 1) over the entire prediction horizon *N*, which yields the switching sequences U. For each switching sequence, that is, 2 power *N*, the evolution of the variables of concern is formulated, and the objective function is evaluated. The most cost-effective switching sequence is chosen as the optimal one, U^*. Hence, the control input at time-step k is obtained by minimizing the corresponding objective function, and it is given by

$$U^*(k) = \arg\min J(k). \tag{8}$$

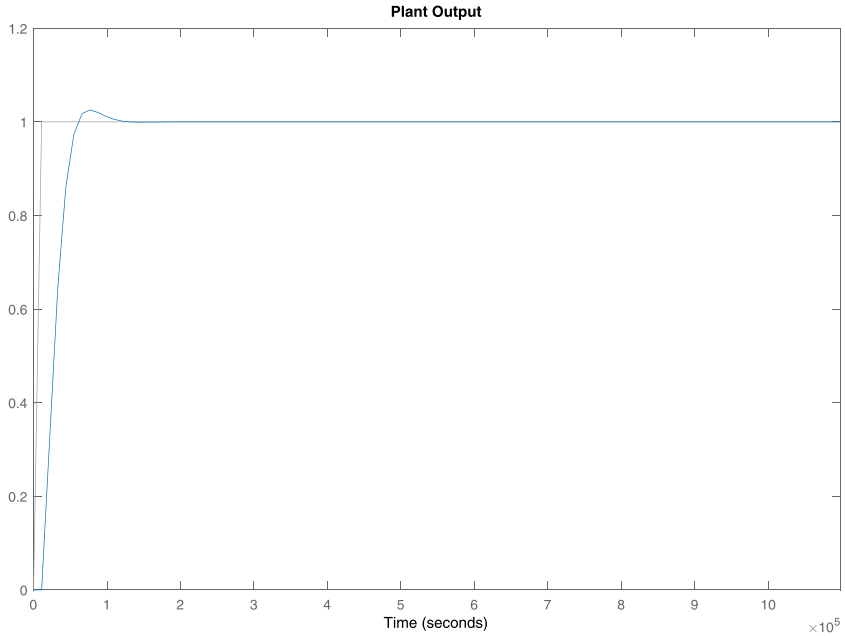

FIGURE 17
Plant output using the MPC controller only.

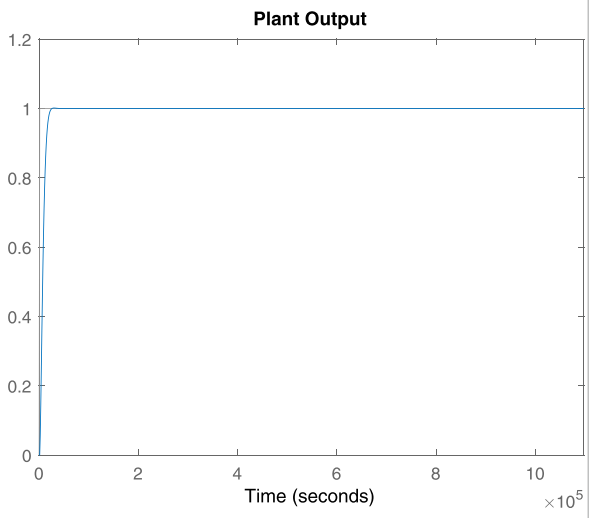

FIGURE 18
Interleaved plant output using the MPC controller only.

5 Simulation results

To investigate the effectiveness of the proposed novel MPADRC, the following simulations in the presence of disturbances are carried out. The initial values of all the parameters are shown in Table 1, and the target condition is to track the set point value with less overshoot and improved steady-state error.

To show the effectiveness of the proposed MPADRC scheme, the input also includes the disturbance parameter in Figure 14. Also, the respective output is shown in Figure 13. The effectiveness of the proposed scheme is shown in comparison to the previous conventional schemes.

Furthermore, the response of ADRC to both the boost and two-phase interleaved boost converters is shown in Figures 15, 16, respectively. Meanwhile, the responses of MPC to both the boost and two-phase interleaved boost converters are shown in Figures 17, 18, respectively, to further show the improved result of the proposed composite scheme MPADRC for the boost converter.

To demonstrate the accuracy, we can readily see and compare the results of the said and the proposed schemes for boost and interleaved boost converters.

The tracking performance of MPADRC is already shown in Figure 13. It is obvious that the tracking performance of the boost converter under the proposed controller is better than that of the other two methods while used individually.

As shown in Figures 13–18, it is evident that the proposed algorithm MPADRC for the boost converter is much more accurate and has less ripples than others.

6 Conclusion

A novel MPADRC technique that is basically a combination of MPC and ADRC as the outer loop and the inner loop,

respectively, is presented for a non-minimum phase behavioral boost converter. Also, its effectiveness is shown with the said techniques individually as used previously. Moreover, the response of interleaving is shown in this article, especially for the two-phase interleaved converter, and one can readily observe the difference between a simple boost converter and an interleaved boost converter. The work motivates the control of DC converters using advanced optimization techniques rather than conventional techniques. Moreover, the future work will include the higher phases of the interleaving technique and also some other converters, that is, buck, SEPIC, and Cuk converters.

Data availability statement

The original contributions presented in the study are included in the article/Supplementary Materials; further inquiries can be directed to the corresponding author.

Author contributions

The main idea, simulation, analysis, and writing of this manuscript were carried out by MS and supervised by YX and TM, KM, and AS carried out literature review, overall layout formatting, and proofreading, while AM and AA provided substantial and intellectual contributions.

Acknowledgments

The Deanship of Scientific Research (DSR) at King Abdulaziz University (KAU), Jeddah, Saudi Arabia has funded this project, under grant no. (KEP-MSc: 122-135-1443), and supported by National Natural Science Foundation of China under Grant 61836001.

Conflict of interest

The authors declare that the research was conducted in the absence of any commercial or financial relationships that could be construed as a potential conflict of interest.

The handling editor SK is currently organizing a research topic with the author KM.

Publisher's note

All claims expressed in this article are solely those of the authors and do not necessarily represent those of their affiliated organizations, or those of the publisher, the editors, and the reviewers. Any product that may be evaluated in this article, or claim that may be made by its manufacturer, is not guaranteed or endorsed by the publisher.

References

Ahmed, A., Nasim, U., Youcef, B., Abdulrahman, B., Hend, A., and Asier, I. (2022). Expert knowledge based proportional resonant controller for three phase inverter under abnormal grid conditions. *Int. J. Green Energy* 2022, 1–17. doi:10.1080/15435075.2022.2107395

Anang, S. H., and Leksono, E. (2016). "Model predictive control design and performance analysis of a pasteurization process plant," in Proceedings of International Conference on Instrumentation, Control and Automation (ICA), Bandung, Indonesia, 81–87.

Belda, K., and Vosmik, D. (2016). Explicit generalized predictive control of speed and position of PMSM drives. *IEEE Trans. Ind. Electron.* 63 (6), 3889–3896. doi:10.1109/tie.2016.2515061

Bemporad, A., Morari, M., Dua, V., and Pistikopoulos, E. N. (2002). The explicit linear quadratic regulator for constrained systems. *Automatica* 38 (1), 3–20. doi:10.1016/s0005-1098(01)00174-1

Chen, W. H., Yang, K., Guo, L., and Li, S. (2016). Disturbance-observer-based control and related methods-an overview. *IEEE Trans. Ind. Electron.* 63 (2), 1083–1095. doi:10.1109/tie.2015.2478397

Feng, H., and Guo, B. Z. (2017). Active disturbance rejection control: Old and new results. *Annu. Rev. Control* 44, 238–248. doi:10.1016/j.arcontrol.2017.05.003

Forouzesh, M., Siwakoti, Y. P., Gorji, S. A., Blaabjerg, F., and Lehman, B. (2017). Step-up DC–DC converters: A comprehensive review of voltage boosting techniques, topologies, and applications. *IEEE Trans. Power Electron.* 32 (12), 9143–9178. doi:10.1109/tpel.2017.2652318

Gustavo, A. L. H., Silva, R. N. A. L., Praca Luiz, P. P., Barreto, H. S. C., and Oliveira, D. S. (2010). Interleaved boost converter with high voltage gain. *IEEE Trans. Power Electron.* 25 (11), 2753–2761. doi:10.1109/tpel.2010.2049379

Han, J. (2009). From PID to active disturbance rejection control. *IEEE Trans. Ind. Electron.* 56 (3), 900–906. doi:10.1109/tie.2008.2011621

Han, J. (1999). Nonlinear design methods for control systems. *IFAC Proc. Vol.* 32 (2), 1531–1536. doi:10.1016/s1474-6670(17)56259-x

Huang, Y., and Xue, W. (2014). Active disturbance rejection control: Methodology and theoretical analysis. *ISA Trans.* 53 (4), 963–976. doi:10.1016/j.isatra.2014.03.003

Judewicz, M. G., Gonzalez, S. A., Echeverria, N. I., Fischer, J. R., and Carrica, D. O. (2016). Generalized predictive current control (GPCC) for grid-tie three-phase inverters. *IEEE Trans. Ind. Electron.* 63 (7), 4475–4484. doi:10.1109/tie.2015.2508934

Karamanakos, P., Geyer, T., Oikonomou, N., Kieferndorf, F. D., and Manias, S. (2014). Direct model predictive control: A review of strategies that achieve long prediction intervals for power electronics. *EEE. Ind. Electron. Mag.* 8 (1), 32–43. doi:10.1109/mie.2013.2290474

Khan, S. A., Ansari, J. A., Chandio, R. H., Munir, H. M., Alharbi, M., and Alkuhayli, A. (2022). AI based controller optimization for VSC-MTDC grids. *Front. Energy Res.* 10, 1008099. doi:10.3389/fenrg.2022.1008099

Kim, S. K., Park, C. R., Kim, J. S., and Lee, Y. I. (2014). A stabilizing model predictive controller for voltage regulation of a DC/DC boost converter. *IEEE Trans. Control Syst. Technol.* 22, 2016–2023. doi:10.1109/tcst.2013.2296508

Kosai, H., McNeal, S., Jordan, B., Scofield, J., Ray, B., and Turgut, Z. (2009). Coupled inductor characterization for a high performance interleaved boost converter. *IEEE Trans. Magn.* 45, 4812–4815. doi:10.1109/tmag.2009.2024639

Lee, P. W., Lee, Y. S., Cheng, D. K. W., and Liu, X. C. (2000). Steady state analysis of an interleaved boost converter with coupled inductors. *IEEE Trans. Ind. Electron.* 47 (4), 787–795. doi:10.1109/41.857959

Li, P., Liu, R., and Ma, X. (2017). "Adaptive indirect model predictive control schemes for boost converters," in 36th Chinese Control Conference (CCC), 26-28 July 2017 (Dalian, China: IEEE), 9203–9207.

Li, P., Ruiyu, L., Tianying, S., Jingrui, Z., and Zheng, F. (2018). Composite adaptive model predictive control for DC-DC boost converters. *IET Power Electron.* 11 (10), 1706–1717. doi:10.1049/iet-pel.2017.0835

Madoński, R., and Herman, P. (2015). Survey on methods of increasing the efficiency of extended state disturbance observers. *ISA Trans.* 134, 18–27. doi:10.1016/j.isatra.2014.11.008

Mayne, D. Q. (2014). Model predictive control: Recent developments and future promise. *Automatica* 50 (12), 2967–2986. doi:10.1016/j.automatica.2014.10.128

Murali, N., Shriram, K. V., and Muthukumar, S. (2010). Model predictive control of boost converter with RLE load. *Int. J. Comput. Appl.* 11 (3), 0975–8887.

Nassima, O., Lehouche, H., Youcef, B., and Achour, A. (2021). Indoor temperature regulation and energy consumption inside a working office in building system using a predictive functional control. *Energy Sources, Part A Recovery, Util. Environ. Eff.* doi:10.1080/15567036.2021.2017517

Omar, H., Van Mierlo, J., and Lataire, P. (2012). Analysis, modeling, and implementation of a multidevice interleaved DC/DC converter for fuel cell hybrid electric vehicles. *IEEE Trans. Power Electron.* 27 (11), 4445. doi:10.1109/TPEL.2012.2183148

Raziei, S. A., and Jiang, Z. (2016). "Model predictive control for complex dynamic systems," in Proceedings of IEEE National Aerospace and Electronics Conference (NAECON) and Ohio Innovation Summit (OIS), Dayton, USA, 193–200.

Rossiter, J. A. (2022). *Model based predictive control*. Boca Raton, FL, USA: CRC Press.

Saif, A., and Ahmad, A. (2019). Active disturbance rejection control of DC–DC boost converter: A review with modifications for improved performance. *IET Power Electron.* 12 (8), 2095–2107. doi:10.1049/iet-pel.2018.5767

Vazquez, S., Leon, J., Franquelo, L. G., Rodriguez, J., Young, H. A., Marquez, A., et al. (2014). Model predictive control: Areview of its applications in power electronics. *EEE. Ind. Electron. Mag.* 8 (1), 16–31. doi:10.1109/mie.2013.2290138

Wang, L. (2009). *Model predictive control system design and implementation using MATLAB*. Berlin, Germany: Springer.

Yao, K., Tang, W., Xiaopeng, B. I., and Lyu, J. (2016). 'An online monitoring scheme of DC-link capacitor's ESR and C for a boost PFC converter. *IEEE Trans. Power Electron.* 29 (7), 5944–5951. doi:10.1109/tpel.2015.2496267

Zhao, H., Wu, Q., Wang, J., Liu, Z., Shahidehpour, M., and Xue, Y. (2017). Combined active and reactive power control of wind farms based on model predictive control. *IEEE Trans. Energy Convers.* 32, 1177. doi:10.1109/TEC.2017.2654271

Zheng, Q., Gao, L. Q., and Gao, Z. (2012). On validation of extended state observer through analysis and experimentation. *J. Dyn. Syst. Meas. Control* 134 (2), 024505. doi:10.1115/1.4005364

Zhou, W., Shao, S., and Gao, Z. (2009). A stability study of the active disturbance rejection control problem by a singular perturbation approach. *Appl. Math. Sci.* 3 (10), 491–508.

frontiers | Frontiers in Energy Research

TYPE Review
PUBLISHED 17 March 2023
DOI 10.3389/fenrg.2023.1114230

OPEN ACCESS

EDITED BY
Jose Luis Domínguez-García,
Energy Research Institute of Catalonia, Spain

REVIEWED BY
Srikanth Goud B,
Anurag Group of Institutions, India
Manohar Mishra,
Siksha O Anusandhan University, India

*CORRESPONDENCE
M. S. P. Subathra,
subathra@karunya.edu
Nallapaneni Manoj Kumar,
mnallapan2-c@my.cityu.edu.hk
Sanchari Deb,
sanchari.deb@warwick.ac.uk

SPECIALTY SECTION
This article was submitted to Smart Grids, a section of the journal Frontiers in Energy Research

RECEIVED 02 December 2022
ACCEPTED 23 February 2023
PUBLISHED 17 March 2023

CITATION
Varghese P R, Subathra MSP, George ST, Kumar NM, Suviseshamuthu ES and Deb S (2023), Application of signal processing techniques and intelligent classifiers for high-impedance fault detection in ensuring the reliable operation of power distribution systems.
Front. Energy Res. 11:1114230.
doi: 10.3389/fenrg.2023.1114230

Application of signal processing techniques and intelligent classifiers for high-impedance fault detection in ensuring the reliable operation of power distribution systems

Rini Varghese P[1], M. S. P. Subathra[2]*, S. Thomas George[3], Nallapaneni Manoj Kumar[4,5,6]*, Easter Selvan Suviseshamuthu[7] and Sanchari Deb[8]*

[1]Department of Electrical and Electronics Engineering, School of Engineering and Technology, Karunya Institute of Technology and Sciences, Coimbatore, Tamil Nadu, India, [2]Department of Robotics Engineering, School of Engineering and Technology, Karunya Institute of Technology and Sciences, Coimbatore, Tamil Nadu, India, [3]Department of Biomedical Engineering, School of Engineering and Technology, Karunya Institute of Technology and Sciences, Coimbatore, Tamil Nadu, India, [4]School of Energy and Environment, City University of Hong Kong, Kowloon, Hong Kong SAR, China, [5]Department of Electrical Engineering, Graphic Era (Deemed to be University), Dehradun, Uttarakhand, India, [6]Center for Research and Innovation in Science, Technology, Engineering, Arts, and Mathematics (STEAM) Education, HICCER—Hariterde International Council of Circular Economy Research, Palakkad, Kerala, India, [7]Center for Mobility and Rehabilitation Engineering Research, Kessler Foundation, West Orange, NJ, United States, [8]School of Engineering, University of Warwick, Coventry, United Kingdom

High-impedance fault (HIF) is always a threat and the biggest challenge in the power transmission and distribution system (PTDS). For a PTDS to operate effectively, HIF diagnosis is essential. However, given the HIF's nature and the involved complexity, detection, identification, and fault location are difficult. This will be even more complicated in conventional PTDSs as they are inefficient and highly vulnerable. Given the importance and urgent need for HIF diagnosis in PTDS, this study reviews state-of-the-art HIF phenomenon and detection techniques and proposes the use of "various signal processing techniques for fault feature extraction" and " different classifiers for identifying HIF." First, HIF current/voltage signals are analyzed using signal processing techniques, which include the discrete wavelet transform (DWT), pattern recognition, Kalman filtering, TT transform, mathematical morphology (MM), S transform (ST), fast Fourier transform (FFT), principal component analysis (PCA), linear discriminant analysis (LDA), and wavelet transforms, such as dual-tree, maximum overlap discrete wavelet transform (MODWT), and lifting wavelet transform (LWT). Second, the various HIF and non-HIF faults are classified using intelligent classifiers. The intelligent classifiers include artificial neural networks (ANNs), probabilistic neural networks (PNNs), genetic algorithms (GAs), fuzzy logic, adaptive neuro-fuzzy interface system, support vector machine (SVM), extreme learning machine (ELM), adaptive resonance theory, random forests (RFs), decision trees (DTs), and convolution neural networks (CNNs). In addition to the comparative discussion of various classifier techniques, their evaluation criterion and performance are prioritized. Third, this review also studied different test systems, such as radial distribution network, mesh distribution

network, IEEE 4 node, IEEE 13 node feeder, IEEE 34 node feeder, IEEE 39 node feeder, IEEE 123 node feeder, Palash feeder, and test microgrid systems, to assess the pertinence of various HIF detection schemes and the behavior along with methods to locate the HIF. Overall, we believe this review would serve as a comprehensive compendium of advanced techniques for HIF diagnosis in different test systems.

KEYWORDS

high-impedance fault, power system protection, signal processing, artificial neural networks, feature extraction, HIF detection, intelligent classifier, electrical test systems

1 Introduction

Faults are often observed in electrical power transmission and distribution systems (PTDSs). The faults in a PTDS will distract the current from the intended path (Ali et al., 2014; Russell and Benner, 1995). The fault causes an irregular condition that decreases the strength of insulation between the conductors (Russell and Benner, 1995; Theron et al., 2018). There are numerous fault types, among which high-impedance faults (HIFs) are critical. HIF occurs when a conductor touches a tree with a high impedance or when a broken conductor touches the ground (Chen et al., 2013; Aljohani and Habiballah, 2020a). The HIF draws non-predictable currents from the distribution network, sometimes leading to arcing (Chen et al., 2013). This is visually represented and shown in Figure 1. Such faults can impose fire risks and cause an electrical shock that endangers electrical system operators, engineers, live stocks, and individuals' lives (Aljohani and Habiballah, 2020a; Sultan et al., 1994). In industrial applications, HIF detection is inevitable to ensure the safety of working persons and equipment and continuity in the service for critical loads. Thus, HIF detection and diagnosis are vital to ensure safety and continuous PTDS operation. However, its detection is quite challenging because HIFs are often not recorded as faults; hence, the reported cases are fewer than the observed ones (Ali et al., 2014). As the fault current draws less current, it remains unnoticed and persists for days. Owing to small fault currents, HIFs are difficult to detect using traditional protection relays and should be addressed through algorithms. HIF depends on various factors, such as the ground surface type, humidity, type of conductor, environmental conditions, and voltage degree, of which surface humidity and surface materials are the most influenced (Sedighizadeh et al., 2010). Many HIFs have similar features that can be represented because of differences in the arc parameters, such as conductance and time constant (Vyshnavi and Prasad, 2018; Chen et al., 2016). Low impedance fault (LIF) (Kavaskar and Mohanty, 2019; Kannan and Rathinam, 2012) is short-circuiting, followed by a high current that is sensed by a breaker.

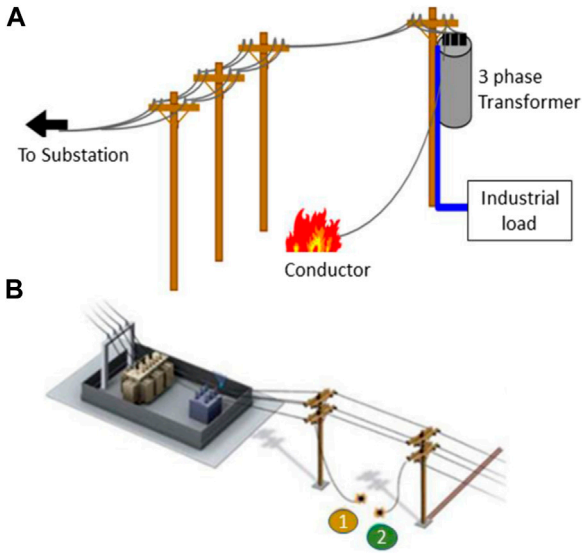

FIGURE 1
HIF in the downed conductor. **(A)** Arcing in the downed conductor. **(B)** Source end and load end conductors (Roberts et al., 2001; Suliman and Ghazal, 2019).

Arc type fault (HIF) usually occurs when a current-carrying conductor touches the ground or with another conductor through a high-impedance medium for a short time. HIF is a disturbance in a power system of approximately 15–25 kV that blocks the current required to trip the overcurrent relay (Ali et al., 2014; Calhoun et al., 1982). The voltage–current characteristics are highly dependent on various materials (Ali et al., 2014), including tree branches, lawns, gravel, stout gravel, asphalt, concrete, crushed stone, board blocks, and cement (Russell et al., 1988). Furthermore, deteriorated insulators due to cracks, dust, humidity, and ice, among others, are some of the main triggers of HIF in PTDSs (Langeroudi and Abdelaziz, 2020). The long-term persistence of HIF is undesirable for profitable and smooth operations (Langeroudi and Abdelaziz, 2020). Various faults and incorrect operations can cause blackouts (Kjølle et al., 2006). Various vulnerable surfaces to HIF with the corresponding fault currents as indicated by Sedighizadeh et al. (2010) and Tengdin et al. (1996) are wet sand 15A, dry sod 20A, dry grass 25A, wet sod 40A, wet grass 50A, reinforced concrete 75A, dry asphalt <1A, and dry sand <1A. HIFs are sub-classified into active and passive faults (Jota and Jota, 1999). Active faults possess fault currents below the threshold values of protection relays accompanied by an electric arc. An electric arc does not follow passive faults. They are challenging to detect as there is no indication of the energization of the conductor and can be detected by phase unbalance analysis. The studies evaluated that approximately 10% of the distribution faults in power systems are HIF, of which 25%–32% of the down

FIGURE 2
(A) Ice and a tree causing HIF in unbroken conductors (Theron et al., 2018). **(B)** HIF arcing on grass (Sedighizadeh et al., 2010) and concrete (Carpenter et al., 2005). **(C)** Unbroken conductors (Louis, 2015).

conductors are not detected with overcurrent relays (Sultan and Swift, 1992). Hence, the detection and isolation of HIF become important. Studies show that conventional protection methods identify only 17.5% of staged HIFs, but the introduction of hybrid energies to distribution grids made the HIF detection demand necessary. An efficient detection method of HIF became necessary to eliminate false tripping and stabilize the power supply. Unlike other faults that endanger electrical appliances, HIF threatens human life. The formation of flammable gases after a HIF interception, which is near flammable material, can cause a fire or explosion. HIF can be caused by a broken or unbroken conductor. Figure 2 shows ice and a tree causing HIF in unbroken and broken conductors (Theron et al., 2018).

As shown by Gururajapathy et al. (2017), faults in power systems can be broadly classified into symmetrical or asymmetrical faults and balanced or unbalanced faults, among which unbalanced loads are more frequent and can be categorized as series and shunt faults. Series faults are caused by broken conductors or otherwise unbalanced series impedances. These faults can be recognized by an increase in voltage and frequency and a reduction in the current of the faulty feeder. However, in the shunt fault, there will be a fall in frequency and voltage and a rise in current, which is common in power systems. The percentage of occurrence in the power system for a single-line-to-ground fault (SLGF) is 70% which, is less severe. In line-to-line fault (LLF), it is 15%, and the severity is less. In LLF, it is 10% and less severe, whereas the triple-line-to-ground fault (LLLGF) is more severe, and occurrence is only 5%. When any phase of the transmission system comes in contact with the ground or neutral wire, an SLGF occurs due to wind and tree falling, among others. In LLF, the occurrence can be due to heavy wind or when two conductors contact each other, which can happen in overhead and underground systems. The variation of impendence spreads over a wide range in this case, and it is difficult to predict the upper and lower limits. Double-line-to-ground fault (DLGF) occurs when a tree falls on the two phases of the transmission system connecting the ground, which is considered asymmetric and a severe event if not cleared in a certain time. LLLGF is symmetrical owing to equipment failure or a tower falling on the transmission line. This is considered a serious situation as the voltages become zero, and the current may be too high. Low fault current resulting from contact with the high-impedance surface, asymmetry (Sultan et al., 1994) resulting from the presence of silica on the contact surface, randomness (Benner et al., 1989) resulting from rapid electrical discharges and floating conductors on the surface of the field, and non-linearity resulting from the different soil layer resistivity (Ali et al., 2014) are the key characteristics of the HIF. The non-linearity results from the fact that the HIF characteristic curve of the voltage–current is non-linear. Low-frequency components are present in the voltage and current waveform due to the non-linearity of HIF, which can range up to 600 Hz for current and 300 Hz for voltage. The fault current has different waveforms, and a disparity in the peak value and shape is called asymmetry for the positive and negative half periods. HIF is called an arcing fault because it is preceded by an arc, producing a few cycles of conduction followed by cycles of non-conduction. The current HIF value increases for a few cycles and holds a constant value. The current range changes over time, making it non-stationary. Random values are both the current magnitude during conduction and non-conduction periods. Arc results in the present waveform's high-frequency components, and because of the non-linearity of the HIF waveform, it contains harmonics. HIF normally occurs at medium voltages and becomes severe at low voltages and less severe at a high voltage above 25 kV. HIF is influenced by several factors, such as feeder configuration, voltage level, weather conditions, and load type (Louis, 2015). HIF detectors find it hard to detect conductors in run-out conditions or undergo severe weather conditions, tree contacts, and a history of excessive breakage. Researchers working on HIF detection concentrated on lab-based staged fault studies. Owing to the critical nature of the faults, industry and academia focus more on simulations and software studies. Early and accurate fault detection will reduce interruption time and increase the safety and reliability of the power system. Advanced signal processing techniques depend on specialized knowledge and the accuracy of the measured data. The modern power system is currently challenged by the growing volumes of data of different natures, the need for data storage, the introduction of distributed generations, and technological advancements. However, the simulation techniques are still in their developing state. During the signal processing analysis, the hidden characteristics of the measured data are revealed, such as randomness, non-linearity, and asymmetry. Machine learning techniques can acquire hidden data from the measured data, thus providing a promising way to meet the challenges in the power system. These fault characteristics are

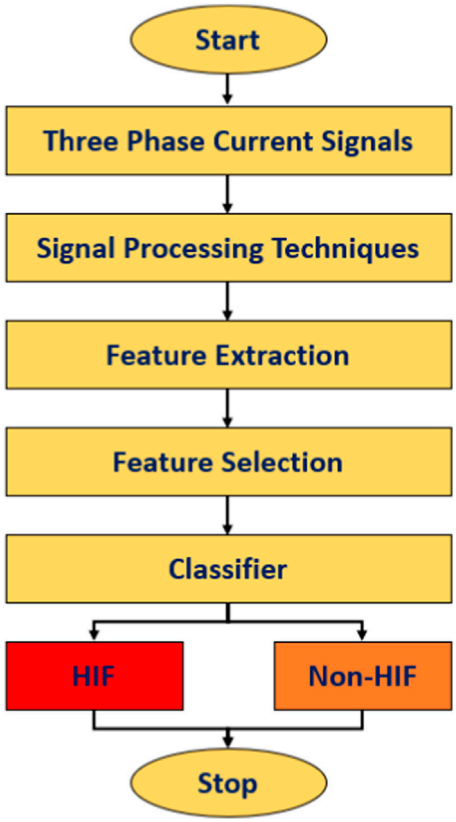

FIGURE 3
Steps involved in pattern classification of HIF detection.

used by the classifiers to discriminate HIFs from other disturbances.

2 HIF detection

The power system network generally has a healthy state and a faulty state. The fault identification task has three main steps: measurements (current, voltage, current and voltage, and magnetic field intensity), feature extraction, and classification (Carr, 1981). Signal processing techniques are frequently used to increase the effectiveness of HIF detection techniques. The signal processing techniques' characteristics extracted their hidden characteristics and measured the three-phase voltage/current signals for HIF detection, improving versatility, stability, and economy. Based on these extracted features, the classifier discriminates whether the HIF event occurred.

Figure 3 shows the basic steps involved in HIF detection using signal processing techniques. The signal processing techniques commonly used for HIF detection schemes are discrete wavelet transform (DWT) (Elkalashy et al., 2007a; Elkalashy et al., 2008; Elkalashy et al., 2007b; Ibrahim et al., 2010a), principal component analysis (PCA) (Sarlak and Shahrtash, 2008), linear discriminant analysis (LDA) (Sarlak and Shahrtash, 2008), continuous wavelet transform (CWT), extended Kalman filter (EKF) (Soheili et al., 2018), time–time transform (TTT) (Nikoofekr et al., 2013), dual-tree complex wavelet transform (DTWT) (Moravej et al., 2015), S transform (ST) (Routray et al., 2016), maximum overlap discrete wavelet transform (MODWT) (Kar and Samantaray, 2017), fast Fourier transform (FFT) (Bin Sulaiman et al., 2017), Stockwell transform (Balser et al., 1982), mathematical morphology filters (MMF) (Sekar and Mohanty, 2018), and lifting wavelet transform (LWT) (Narasimhulu et al., 2020). The description of these signal processing tools used in HIF detection techniques is discussed in Section 2.3, emphasizing time-domain analysis, frequency-domain analysis, and time–frequency-domain analysis. The selected features are extracted from the input signal and then compared to a threshold value in signal processing techniques for HIF detection. Setting the threshold value is challenging because HIF would not be detected if the threshold is set too high. If it is set to an extremely low value, the relay will trip even with light disturbances. This issue can be resolved by introducing intelligent classifiers along with signal processing techniques.

Commonly used intelligent classifiers in signal processing-based HIF detection techniques are probabilistic neural network (PNN) (Samantaray et al., 2008), artificial neural network (ANN) (Baqui et al., 2011), adaptive resonant theory (ART) neural network and Fuzzy ARTMAP (Nikoofekr et al., 2013), extreme learning machines (ELMs) (Reddy et al., 2013), genetic algorithm (GA) (Xie et al., 2013a), support vector machine (SVM) (Bhongade and Golhani, 2016), adaptive neuro-fuzzy inference system (ANFIS) (Veerasamy et al., 2018), decision tree (DT) (Sekar and Mohanty, 2018), random forest (RF) (Sekar and Mohanty, 2020), convolution neural network (CNN) (Fan and Yin, 2019), and fuzzy logic control (FLC) (Suliman and Ghazal, 2019) explained in Section 4. These intelligent classifiers improved the efficiency, speed, and accuracy of signal processing-based procedures by detecting HIFs without the use of threshold settings.

The practical detection of HIFs was explained by Kistler et al. (2019), who used two relay-based HIF detection algorithms. The former uses the odd-harmonic contents of phase current, whereas the latter uses the inter-harmonic contents. The first algorithm uses total odd harmonic content from phase currents using the FIR filter. A threshold value was set, and the odd harmonic contents were compared. If the difference is more significant than the threshold, the counter increments, and the alarm is set. The second algorithm uses the sum of the difference of inter harmonic content that uses a reference and compares it to the measured sum of difference currents to detect the increase in the sum of difference currents during an HIF. The second algorithm was more successful for HIF detection, mainly on grassy surfaces, and slightly less for fully contact good insulators that do not cause an arc. The algorithm's performance was tested in a live conductor by the Electric Power Research Institute and PPL electric utilities (SEL, 2007).

Mitigation of forest fires and human safety issues were addressed by Gashteroodkhani et al. (2021) through the practical detection of HIFs. Two strategies for fault current detection, one based on the non-harmonic content of fault currents and the other on the odd-harmonic content of fault currents, are explained and evaluated in a hardware-in-the-loop (HIL) platform employing a real-time digital simulator (RTDS). With 1,736 relay events reported, the first algorithm detected 95% of the HIFs, whereas the second detected only 5% of HIFs. The test system chosen was from a distribution network in the Northern Nevada area with a 14.4-kV three-phase

three-wire feeder. Chakraborty and Das (2019) explained that smart meters are installed for voltage measurements compared with a threshold value to detect the presence of HIFs. It is tested in six different situations of three broken and three unbroken conductors. The method is implemented along with a single-phase energy meter capable of detecting the presence of HIFs, voltage sag-swells, capacitor/load switching (Panigrahi et al., 2018; Prasad et al., 2022), transformer and feeder energization (Biswal et al., 2022), power electronic loads, arc furnace loads, and distributed generators (DG). The method gives satisfactory results in HIF detection. The detection methods proposed in previous studies (Lima et al., 2018; Yang et al., 2006; Sedighi et al., 2005a; Abdelgayed et al., 2017; Wang et al., 2019) also experimented on real-time systems discussed in the various sections of the manuscript. Discrimination of HIF along with cross-country faults was explained by Ashok and Yadav (2021). A simulation model of the IEEE 13-bus system is used to obtain the three-phase current signals, and MODWPT is used for feature extraction. The real-time field data from Chhattisgarh State Power Transmission Network are collected and tested using the same algorithm. Classification of HIF, non-HIF boundary fault conditions, capacitor switching, reactor string switching, load switching, power swing effects, the effect of noise, lightly load conditions, and electric arc furnace effects in PTDSs is done. The classification is conducted by setting a threshold value for the energy envelop index. The response time of the proposed method for each case is recorded, which is less than 14.3 m. When compared with earlier studies (Ghaderi et al., 2017; Sedighizadeh et al., 2010; Vyshnavi and Prasad, 2018, this study gives an insight into various test systems used for testing various HIF detection methods and studies the nature of HIF, which is discussed in Section 3.

2.1 Measurements

Measurements such as current measurement, voltage measurement, and both current-voltage measurements extract features for fault analysis. An HIF is accompanied by the intermittence of arc (Chen et al., 2013). The arcing fault contains low- and high-frequency components in the current frequency spectrum. The low frequency-based technique results in lower-order harmonics with even, odd, and intermittent harmonics extracted for HIF detection. High frequency-based techniques show short variations in the HIF current.

Voltage measurement is performed by extracting three-phase voltage signals proposed by Ali et al. (2014) during the HIF phenomenon in an underground distribution network. Bakar et al. (2014) performed a voltage measurement at the primary substation and compared fault features with the database generated from the simulation. The method has a single measurement and multiple branches that can detect multiple faulty sections. Detection of HIFs by voltage measurement is efficient only when there is a voltage drop between the relay and fault location. The proposed method by Wang et al. (2018) used the discriminant vector of negative and zero sequence current and voltage in the substation.

Current and voltage measurement has improved reliability compared to the latter measurements. Magnetic field intensity measurement increases the cost and complexity of the detection technique (Bahador et al., 2018).

2.2 Signal processing techniques and feature extraction

Signal processing techniques are widely used to improve the effectiveness of high-impedance defect detection approaches. Signal processing techniques extract the hidden properties of observed three-phase signals for HIF detection, enhancing adaptability, stability, and cost-effectiveness. More informative data are obtained using various analyses based on these extracted data, such as time-domain analysis, frequency-domain analysis, and time–frequency analysis (Chen et al., 1990; Sarlak and Shahrtash, 2013). Table 1 gives a detailed comparison of various signal processing techniques for HIF detection using intelligent classifiers.

2.3 Domain analysis

2.3.1 Time-domain analysis

The time-domain analysis uses the measure of zero-sequence voltage and current for feature extraction of HIF. The time-domain analysis is based on arc current waveform. Time-domain takes out the temporary irregularities in the HIF waveform, making the system computationally complex (Lee and Bishop, 1985).

Nezamzadeh-Ejieh and Sadeghkhani (2020) proposed that Kullback–Leibler divergence extracts the non-linearity and asymmetry characteristics of two half-cycles of the current waveform from the substation in a time-domain detection of HIF. The method is tested in 13-node and IEEE 34 systems (the Institute of Electrical and Electronics Engineers). Without any harmonic component analysis or training set, the method can identify an HIF by calculating the energization of feeders, voltage swag, and swell.

Mathematical morphology (MM) is a signal processing technique applied to issues in the power system illustrated in the literature (Sekar and Mohanty, 2018; Panigrahi et al., 2018). MM uses simple arithmetic operations, such as set theory and integral geometry, and due to its simple calculations, the processing time is less.

The basic functions in MM are dilation and erosion (Kavaskar and Mohanty, 2019). MM is non-linear, and it is time-domain processing of the signal widely used to extract high- and low-frequency signals. Here, the proposed MM, along with data mining DT, is used for HIF detection. Statistical features are extracted, which serve as input to DT and RF for discriminating with non-HIF conditions (load switching, capacitor switching, and inrush current).

The morphology gradient filter extracts statistical features from the features. A rule set is created using RF, which will accept the crisp inputs using a fuzzy-based algorithm proposed by Sekar and Mohanty (2020). This method detects HIFs and normal events with high dependability. The chosen sampling rate was 60 samples/cycle, requiring less memory space and less computational time.

TABLE 1 Comparison of various signal processing techniques for HIF detection using intelligent classifiers.

Ref. No.	Feature extraction approach	Classifier	Test system	Year	Remarks
Samantaray et al. (2009a)	Adaptive extended Kalman filter (AEKF)	Feedforward neural network and PNN	i) Radial distribution feeder, 15 kV ii) Mesh distribution network, 15 kV	2009	Detection time, 0.01 s PNN classification rate is 99.11%, whereas for FNN, it is 96.51%
Cui et al. (2017)	Discrete Fourier transform (DFT) and Kalman filter	Pattern recognition	Benchmark test system 25 kV	2017	An effective feature set algorithm is introduced to the feature extracted and compared with Naive Bayes, support vector machine, KNN, J48, and RF, of which J48 and RF give better results
Bhongade and Golhani (2016)	DWT	Support vector machine	Radial distribution system, 400 kV	2017	The traveling wave method is used for locating the fault. Good accuracy as the % error is below 1.22%
Chen et al. (2014)	DWT-MRA	Simple detection criterion	IEEE 13-node test	2014	Efficient and fast method. Economical since voltage signal measurement is needed
Yeh et al. (2019)	DWT	Digital signal processor	Distribution network at Southern California Edison, 12 kV	2019	Detection time 32.9 m. Effective and flexible method. Tested on real-time data
Akorede and Katende (2010)	DWT	Pattern classifier	The radial distribution network, 11 kV	2010	Moving window approach. Two-class classification only
Baqui et al. (2011)	DWT	ANN	Radial distribution, 13.8 kV, Basque Country (Spain)	2011	Discriminates HIF, LIF, and switching events. Multilayer perceptron network and Levenberg–Marquardt backpropagation algorithm are the learning algorithms used
Ali et al. (2014)	DWT	Short distance algorithm and matching approach	38-Node underground distribution, 132/11 kV, Malaysia	2014	Locating time required is less compared to conventional methods
Xie et al. (2013a)	Dual-tree complex wavelet transforms	PNN	IEEE 34-node test feeder	2014	PNN requires no iteration. Detection time 1.5 m. The error of detection of 1.4%
Ibrahim et al. (2008)	DWT	Moving window-based pattern recognition	JMARTY model 500 kV, Egypt	2007	Simple, accurate, and fast technique. EHV transmission lines
Tag Eldin et al. (2009)	DWT	An algorithm based on a recursive method (Clark's transformation)	ATP/EMTP model for real CCVT, 500 kV, 150 km, 500 kV transmission line	2009	Accurately detect HIF detection in EHV transmission lines. Independent of the HIF model. Detects HIF in ¾th of a cycle
Lai et al. (2005)	DWT and pattern recognition	Nearest neighboring rule	25 kV power distribution networks i) Distribution network with a single branch of a non-linear load ii) Radial distribution network iii) Meshed network	2005	Error range 2.52% and 45.4%. It will not indicate the physical properties of the output coefficient
Xie et al. (2013b)	Extended Kalman filter	Support vector machine	Radial distribution feeder, 13.8 kV	2009	Classification accuracy of 98%. Excellent results under noisy conditions also
Wali et al. (2018)	FFT	Power spectrum (PS) technique	Radial distribution feeder, 13.8 kV	2018	Detection accuracy of 100%, simple technique, requires less time because training is not needed
Tawafan et al. (2012)	FFT	ANFIS	Radial distribution feeder, 13.8 kV	2012	Mean squared value of 0.084. ANFIS is based on subtractive clustering. The classification rate is above 96.4%
Yeh et al. (2014)	FFT and Walsh–Hadamard transforms (WHTs)	Threshold and shape of the magnitude and phase responses of orthogonal transforms	Official websites of DOE/EPRI National Database Repository of Power System Events	2015	Detection time is 0.033 s. The performance of the method is correct and precise
Narasimhulu et al. (2020)	LWT	ANN	Radial distribution network, 400 kV	2020	Efficiency is 98%. Superior to GA-fuzzy, GSA-ANN, and ALO

(Continued on following page)

TABLE 1 (*Continued*) Comparison of various signal processing techniques for HIF detection using intelligent classifiers.

Ref. No.	Feature extraction approach	Classifier	Test system	Year	Remarks
Sekar and Mohanty (2017)	MM	DT	IEEE 13, IEEE 34-node feeder	2017	Detection time 30 m, accuracy 98.33%
Gautam and Brahma (2013)	MM	Implemented on overcurrent relay	IEEE 13-node test feeder	2012	Detection time 1 s. The success rate of detection and classification is 100%
Panigrahi et al. (2018)	MM	Detection algorithm	IEEE PSRC Working Group D15	2020	Detection time 0.8 s
Kavaskar and Mohanty (2019)	MM	Simple rule-based algorithm	EPDS 11 kV radial distribution, Chennai	2019	Detection time 80 m
					Security and dependability 100%
					HIF, LIF, load, and capacitor switching are classified
Sarlak and Shahrtash (2013)	MM	SVM	Palash feeder in southwestern Tehran, radial distribution	2013	HIF indicator is introduced, which is based on magnetic field strength signals
Sekar and Mohanty (2018)	MM	DT	EPDS 11 kV radial distribution system, Chennai	2018	Detection time 30.66 m
					Accuracy 99.34%
Sekar and Mohanty (2020)	Morphology gradient (MG)	Fuzzy rule base	EPDS distribution, Chennai, 33 kV	2020	Accuracy of 99.3%. Less computation time
Gadanayak and Mallick (2019)	MODWT	Knot-based EMD	CERTS microgrid system	2019	Detection time is 0.12 s Accuracy of 100%. The current from the proposed algorithm cannot be used in a mesh network
Kar and Samantaray (2017)	MODWT	DT	Test microgrid system	2017	Classification accuracy of 99.77%. Highly reliable for microgrid distribution systems. The test is also performed in islanded mode
Sarlak and Shahrtash (2011)	Multi-resolution MG	MLPNN	Palash feeder in the southwest of Tehran, simulation, distribution	2011	Superior to other feature extraction techniques like DWT, DFT, discrete s-transform (DST), discrete time–time (DTT) transform. Security 92.8%, dependability 96.4%
Sarlak and Shahrtash (2008)	PCA and LDA	SVM	IEEE four-node test feeders	2008	Better accuracy of 97.5% compared to Bayes and Parzen classifiers
Samantaray et al. (2009b)	S and TT transform	PNN and FNN	i) Three-phase radial distribution feeder ii) Three-phase mesh network. Both have 15 kV	2009	The classification rate of PNN is 98.02% as it is 94.04% for FNN for the radial network. The testing time is 0.3 s for FNN and 0.01 s for PNN
Lima et al. (2019)	Stockwell transform	Probabilistic analysis	Brazilian utility, 13.8 kV real distribution	2019	Accuracy rate of 94.4%. Detection time is 166 m. Tested on six different surfaces, and detection time is measured
Mishra et al. (2016)	Stockwell transform	ANN and SVM	Radial and Mesh distribution system, 138 kV	2016	Comparison of ANN with SVM. ANN in the radial network gives 93.7% accuracy as SVM with 86.25% in the mesh network
Naik and Yadav (2018)	DFT	Fuzzy interface system	IEEE 15-bus system	2018	Effective classification of HIF, symmetrical and unsymmetrical faults in less than 8.33 m
K. Chaitanya and Yadav (2020)	EWT-SVD	SVM	Modified IEEE 13-node system	2020	Classification accuracy of 99% for 60 dB noisy environment
Chaitanya et al. (2020)	Variational mode decomposition (VMD)	SVM	IEEE 13-node system	2020	Effective classification of HIF, LIF, and non-faulty conditions with a classification accuracy of 99% and response time for LIF is 16.67 m, and that for HIF is 166.7 m
Routray et al. (2016)	Stockwell transform	ANN	Radial distribution system, 138 kV	2015	Accuracy of 98.75%

(Continued on following page)

TABLE 1 (*Continued*) Comparison of various signal processing techniques for HIF detection using intelligent classifiers.

Ref. No.	Feature extraction approach	Classifier	Test system	Year	Remarks
Ghaderi et al. (2015)	Time freq. analysis	SVM	The test was conducted in a real-time, high-current research laboratory	2013	Simple, reliable, and efficient. Accuracy of 93.6%
Nikoofekr et al. (2013)	TT transform	ART neural networks and Fuzzy ARTMAP	Palash feeder in the southwest region of Tehran	2013	Accuracy of 99.18%. Five-class classification
Yang et al. (2006)	Wavelet transform	Pattern recognition-based ANN	Tai-16 distribution feeder system 11.4 kV from Taishi substation	2006	Detection rate of 81%. More accurate than unintelligent algorithms
			Yunlin		
Hubana et al. (2018)	DWT	ANN	i) Two-bus test distribution system of the city of Mostar (Bosnia and Herzegovina), 35/10 kV	2018	A two-bus system gives a classification accuracy of 92.5%, and an eight-bus system gives 90.19%. Highly effective with good noise removal capability
			ii) Eight-bus system with the same specifications, including underground cables, substations		
Lima et al. (2018)	STFT	Blackman–Harris window, spectrogram analysis	Brazilian utility, 13.8 kV, real distribution	2018	Tested in simulated data and real-time oscilloscopic data, which gave the best results
Gashteroodkhani et al. (2020)	TT	Deep belief neural network	IEC microgrid 61,850-7-420, 25 kV	2020	Tested in grid-connected as well as an islanded mode of operation. The accuracy of the proposed system for fault detection is 99.8%, and fault classification is 99.32%
Abdelgayed et al. (2017)	DWT	DT and KNN	CERTS microgrid system	2017	The experimental result of DT is 100%, and that of KNN is 95%
Gashteroodkhani et al. (2019)	TT and S transform	SVM	Transmission line, 230 kV	2019	Fault identification is 98%

The adaptive extended Kalman filter (AEKF) estimates the harmonic components in fault currents for non-linear loading conditions (Samantaray et al., 2009a). The harmonic components estimated by the technique are fundamental, third, fifth, seventh, eleventh, and thirteenth harmonics. Based on the Kalman filtering principle, Girgis et al. (1990) built an approach based on the time-varying existence of the fundamental and harmonic components to obtain the best estimate of the time variations of the harmonic components. Faridnia et al. (2012) presented a partial co-relation function for HIF detection from voltage and current relays. The method is tested in a radial feeder system with two HIF models in PSCAD/EMTDC. Twelve indices-based correlation function is implemented and tested on a wide data set to obtain accurate results for HIF detection.

2.3.2 Frequency-domain analysis

Frequency-domain analysis extracts harmonics in the current spectrum. In the current spectrum, an HIF event will produce low- and high-frequency components. Low-frequency components are based on non-linearity results, whereas high-frequency components are based on sudden and random changes in a non-stationary HIF current waveform. FFT extracts the current signal data after the simulation is applied to a power spectrum (PS) technique that can detect an HIF and distinguish it from non-faulty conditions, such as capacitor banks, non-linear loads, and linear loads, which have the same features (Wali et al., 2018). FFT is used to calculate the impulse response of the frequency domain (Scott, 1994). Aucoin and Russell (1982) utilized high-frequency current components to detect HIF. The low-frequency spectrum is compared with the harmonics of the current waveform measured in the primary substation over a week (Emanuel et al., 1990).

2.3.3 Time–frequency domain

The wavelet methods are more potent as they extract the frequency and instant or position for signal analysis. Time–frequency analysis (TFA) could effectively detect discontinuities, repeated patterns, and non-stationary aspects of signals. It measures the energy of the signal at each moment of time and frequency coordinates. TFA has been successfully applied to various power system applications, such as the evaluation of power efficiency, security of power systems, and pathfinding for disturbances of capacitor switching.

Lima et al. (2018) proposed a method that uses a short-time Fourier transform for feature extraction that extracts harmonic components of phase current as of the magnitude and phase of the third harmonic component and magnitude of second and fifth harmonics to identify the presence of HIFs. The window length chosen is directly proportional to frequency resolution and inversely proportional to time resolution. The sampling frequency is 15.6 kHz. A Brazilian distribution feeder of 13.8 kV is used to

evaluate the methodology. A Blackman–Harris window with five cycles is chosen for this method, and the spectrum analysis is performed. The method was tested in sand, asphalt, gravel, grass, cobblestones, and local soil. The detection time is less than 200 ms.

The ST is an extended wavelet transform class based on Gaussian window shifting and scalable localizing. The S transform has absolute phase information and good time–frequency resolution for all frequencies. Unlike wavelet transformation, the ST is extremely resistant to noise (Mishra et al., 2016). Morlet wavelet transform differentiates between HIFs and regular switching events and investigates faults for different surfaces, including Portland cement, wet soil, and grass (Huang and Hsieh, 1999). DWT decomposes time-domain signals into different harmonics in the time–frequency domain, and the extracted features are used to train ANN (Baqui et al., 2011). The mother wavelet of Daubechies is superior to others, such as Morlet, symet, and rbior, as it can accurately detect low-amplitude signals. The method was also verified on various wet and dry surfaces.

The proposed method uses DWT, and high- and low-frequency voltage components at various system points are measured (Santos et al., 2017). The energy spectrum of the detailed and approximation coefficient is calculated. The method is evaluated using a 13.8-kV Brazilian distribution feeder with a signal-to-noise ratio (SNR) of 60 dB, and the two-time varying resistances HIF model is used. The method requires no monitoring devices and information about the feeder and load parameters. The method is reliable and efficiently identifies the HIF with a 70% search field reduction obtained.

Wavelet transform decomposes and extracts the features, PCA performs feature selection, and the Bayesian classifier discriminates the HIF with normal events (Sedighi et al., 2005a). Various tests were conducted on wet and dry surfaces. A pattern recognition system is proposed and is simulated using EMTP software. A real-time experiment is performed in Qeshm island, Iran, and an HIF is created in 8,209 m and 8,446 m locations from the site. The sampling rate of the data is 24.67 kHz, and the classifier success rate is 97.6%.

In (Li and Li, 2005) arc fault detection with automatically modified time windows to differentiate arc fault from non-arc fault is done using wavelet packet transform-based. At level 3 decomposition, db10 is used at a sampling frequency of 12.5 kHz. The window length in this study is 1/2 cycle (1.25 ms in 400 Hz for an airplane). The size of the moving window is 1/4 cycle (0.625 m in 400 Hz), such that $\Delta t = 0.625$ m. The proposed method is powerful with simple calculations.

Michalik et al. (2006) proposed an approach in which a wavelet-based measurement is performed for zero-sequence voltage and current signals. This method gave fast and reliable HIF detection and location and obtained better performance compared to conventional methods. ANN is used for classification, and the decision module is implemented in real-time using a single neuron. The proposed method gives good results with low-impedance permanent ground faults.

Lazkano et al.'s (2004) method is based on the decomposition of three-phase unbalanced current data utilizing wavelet transform techniques. Arc phenomena linked with an HIF can be detected due to the WT's time-frequency characteristic, and the signal is broken down into frequency sub-bands. The Db4 mother wavelet was chosen for the four-level decomposition of the arc current signal. A 20-kV Tuejar feeder of Spain is selected and simulated to test the proposed method, which gives satisfactory results.

De Alvarenga Ferreira and Mariano Lessa Assis (2019) illustrated a novel approach for HIF detection in smart grids using multi-resolution signal decomposition to decompose the DWT coefficient. The HIF model used for testing is the Kizilcay arc model. The IEEE 13-node test feeder simulated in PSCAD/EMTP is used to evaluate the proposed method. Level 3 decomposition with db8 mother wavelet function is adopted for the proposed work. Various conditions are illustrated with HIF and non-HIF conditions, such as capacitor switching. The method provides robust, fast, and reliable HIF detection.

Features of Earth faults due to leaning trees are extracted from the phase currents and voltages using the DWT (Elkalashy et al., 2007b; Elkalashy et al., 2007a; Elkalashy, 2007). The detailed coefficient of current and voltage is used, whose product is taken to compute power. A positive polarity of power gives a healthy feeder, and negative polarity gives a faulty feeder. The method has been tested on a leaning tree in a laboratory setup.

The wavelet-based algorithm is used to detect HIF detection (Michalik et al., 2007). The algorithm works great for ground fault currents above 3A, irrespective of phase and location. The method is tested in the Next-Generation Power Technology Center and KEPCo, South Korea. The sampling rate is 10k Hz, and the detection time ranges from 0.2 to 0.7s depending on the distance.

Stockwell's transform extracts the parameters in both the time and frequency domains proposed by Lima et al. (2019) that select the statistical features discussed in Table 1. The simulated data and real-time field data (from the substation) provide the two databases for the method validation that can discriminate an HIF with other power system disturbances. The method is efficient and accurate in action.

Balser et al. (1982) utilized Hilbert transform (HT) for HIF detection in transmission lines in which an uncompensated line, series compensated line, single-pole tripping situation, and a load change are tested. The method is simulated in MATLAB/SIMULINK, and the data sampling rate is 1 kHz. An HIF detector is placed in certain locations that indicate whether a fault occurred. The method gives good accuracy and consistency. The HIF detection method using optimal transient extracting transform (OTET) was proposed by Prasad et al. (2022) and can be used in grid-connected and islanded mode systems, and is also reliable in unbalanced and harmonic contaminated signals. Biswal et al. (2022) reconstructed the features extracted from the current signals using the Savitzky–Golay filter (SGF) using the matrix pencil method (MPM), and the Teager energy of the error is estimated. The proposed method is verified in the Aalborg test feeder and modified IEEE 30-bus test systems and proven with an accuracy of 98.6%.

3 Test systems

In this section, various test systems are discussed for HIF detection. The various standard test systems were selected and simulated using MATLAB/SIMULINK, PSCAD, EMTP-RV, EMTP-ATP, and a real-time laboratory setup to investigate the performance of the different algorithms for HIF location and detection. Faults at the distribution system are a priority because

TABLE 2 Comparison of various test systems.

Test system with ratings	Methodology used	Remarks
IEEE PSRC distribution of radials 11 KV (Panigrahi et al., 2018)	MM employs morphology gradient, and the statistical features are obtained from dilation and erosion	Identify HIF occurrence in 0.08 s
Radial 13.8 kV distribution feeder (Wali et al., 2018)	FFT extracts features, which are then subjected to power spectrum analysis	Power spectrum identifies the HIF occurrence with 100% accuracy
Radial 13.8 kV distribution feeder (Tawafan et al., 2012)	FFT extracts features, and the classifier used is ANFIS.	The success rate of detecting HIF cases was 97.8%, and that of non-HIF cases was 99%
Radial distribution system, 115 kV feeder (Wang et al., 2018)	VCCP-based disturbance detection approach	The wavelet correlation coefficient was calculated for various surfaces and was less than 0.966 for a healthy feeder
Radial distribution system, 138 kV (Soheili et al., 2018)	Two approaches were compared. 1) Kalman filter and RF and 2) DT with FFT	RF proved to be the best, with 93.56% accuracy and 94.56% dependability
Radial distribution network, 13.8 kV (Veerasamy et al., 2018)	Feature extraction by CWT and DWT	Accuracy 100%
Radial distribution system, 138 V (Routray et al., 2016)	Stockwell transform with ANN	Accuracy 98.75%
Radial distribution system, 138 kV (Mishra et al., 2016)	Stockwell transform for feature extraction. ANN and SVM as classifier	For the ideal case, ST with ANN and ST with SVM give 100% accuracy, whereas with SNR 30 dB, ST with ANN gives 93.7% and ST with SVM gives 92.15% accuracy
Radial distribution system, 15 kV (Samantaray et al., 2008)	S transform and TT transform with PNN and FNN	PNN with ST features provides a classification rate of up to 98.06%. PNN with features from TT transform provides a classification rate of up to 98.05%. FNN and S transform combination gives 93.04%, and that with TT transform gives 94.16% accuracy
Radial distribution system, 33 kV (Sarwagya et al., 2018)	Measuring the residual voltage at the substation and negative sequence current flowing through the feeders	The presence of the HIF is detected at 3 s
Distribution system, 12.5 kV (Shahrtash and Sarlak, 2006)	Pattern recognition-based algorithm and DT as the classifier	For different values of the sampling frequency, data window, and preprocessing time interval, the accuracy of the method is 99.4%
Radial distribution network with 63 kV (Vahidi et al., 2010)	DWT extracts the features, and ANN is the classifier used along with the denoising method	Accuracy is 99%
Medium voltage distribution system from the city of Mostar with two-bus and eight-bus systems of 33 kV (Hubana et al., 2018)	Voltage phase difference algorithm and a combination of DWT with ANN	Two-bus systems, the accuracy obtained is 92.5%, whereas the eight-bus system is 90.19%
Electric power distribution system, Chennai, 33 kV (Sekar and Mohanty, 2020)	MG with fuzzy rule base algorithm	Accuracy is 99.3%, and the computational time required is less
Mesh distribution network, 25 kV (Samantaray et al., 2009a)	AEKF with PNN and FNN	The accuracy rate of PNN is 99.11% compared to FNN with 96.51%
Mesh distribution network, 138 kV (Soheili et al., 2018)	Two approaches were compared. 1) Kalman filter and RF and 2) DT with FFT	RF proved to be the best with 93.56% accuracy and 94.56% dependability
Mesh distribution network, 25 kV (Lai et al., 2005)	DWT and pattern recognition	Error range 2.52% and 45.4%. It will not indicate the physical properties of the output coefficient
Mesh distribution network, 138 kV (Mishra et al., 2016)	Stockwell transform for feature extraction. ANN and SVM as classifiers	For the ideal case, ST with ANN and ST with SVM give 100% accuracy, whereas with SNR 30 dB, ST with ANN gives 81% and ST with SVM gives 86% accuracy
Mesh distribution network, 15 kV (Samantaray et al., 2008)	S transform and TT transform with PNN and FNN	The accuracy of the mesh network with S transform and FNN is 92.86%, and that with TT transform and FNN is 93.55%. S transform and PNN combination gives 97.85% accuracy, and TT transform with PNN gives 97.09%
IEEE 13-node test systems, 4.16 kV (Fan and Yin, 2019)	CNN and transfer learning algorithm	The accuracy obtained was 95.06%
IEEE 13-node test systems, 4.16 kV (Silva et al., 2020)	Wavelet packet-based feature extraction along with EuFNN classifier	97.14% accuracy

(Continued on following page)

TABLE 2 (*Continued*) Comparison of various test systems.

Test system with ratings	Methodology used	Remarks
IEEE 13-node test systems, 4.16 kV (Sarwar et al., 2020)	PCA, Fisher discriminant analysis, binary and multi-class SVM	Security and dependability of 100%
IEEE 13-node test systems, 4.16 kV (Soheili et al., 2018)	FFT approach and harmonic analysis of the sum of all three-phase currents	Detection time is 1.5 s
IEEE 13-node test systems, 4.16 kV (Sekar and Mohanty, 2017)	MM and DT	The detection time is 30 m. Performance indices are 99%. Accuracy is 98.33%
IEEE 13-node test systems, 4.16 kV (Gautam and Brahma, 2013)	MM that can be implemented on a conventional over current relay	The success rate of detection and classification is 100%
IEEE 13-node test systems (Chen et al., 2014)	DWT with MRA	Fast, economical, and efficient
IEEE 13-node test systems (Wang et al., 2019)	Variational mode decomposition (VMD) and Teager–Kaiser energy operators (TKEOs)	Calculation time is 0.0028 s
IEEE 34-node test system, 24.9 kV (Moravej et al., 2015)	Dual-tree complex wavelet transforms for feature extraction and PNN for classification	PNN requires no iteration. Detection time 1.5 m. The error of detection is 1.4%. The proposed algorithm gives an accuracy of 98.88%
IEEE 34-node test system, 24.9 kV (Fan and Yin, 2019)	CNN and transfer learning algorithm	The accuracy of CNN obtained is 99.52%
IEEE 34-node test, 24.9 kV (Sekar and Mohanty, 2017)	MM and DT	The detection time is 30 m. Performance indices are 99%. Accuracy is 98.33% at lightly loaded conditions
IEEE 34-node test, 24.9 kV (Wang et al., 2019)	Variational mode decomposition (VMD) and Teager–Kaiser energy operators (TKEOs)	Calculation time is 0.0028 s
IEEE 13-node test systems (Chen et al., 2014)	DWT with MRA	Fast, economical, and efficient
IEEE four-node test feeder, 12.47 kV (Sarlak and Shahrtash, 2008)	PCA and LDA with SVM	Accuracy is 97.5% compared to Bayes and Parzen classifiers
IEEE-123 distribution feeder, 4.16 kV (Tonelli-Neto et al., 2017)	DWT with a fuzzy interference system and Fuzzy ARTMAP neural network combination based on Dempster–Shafer evidence theory	The accuracy of FANN is 97.69%, and that of FIS is 99.25%
Palash feeder, Tehran, 63 kV (Sarlak and Shahrtash, 2011)	TT transform, ART neural networks, and Fuzzy ARTMAP	Accuracy of 99.18%. Five-class classification
Palash feeder, Tehran, 63 kV (Sarlak and Shahrtash, 2013)	MM and SVM	Security of 96.9% and dependability of 97.2%
Palash feeder, Tehran, 63 kV (Nikoofekr et al., 2013)	Multi-resolution MG and MLPNN	Superior to other feature extraction techniques, such as DWT, DFT, DST, and DTT. Security of 92.8%, dependability of 96.4%
Palash feeder, Tehran, 63 kV (Soheili et al., 2018)	FFT approach and harmonic analysis of the sum of all three-phase currents	Detection time is 1.13 s
CERTS microgrids, 480 V (Gadanayak and Mallick, 2019)	MODWT and Knot-based EMD	Classification accuracy of 99.77%. The mean detection time is 0.12 s
Test microgrid system, 120 kV (Kar and Samantaray, 2017)	MODWT and DT	The detection time is 0.12 s. Accuracy of 100%
IEC standard microgrid, 25 kV (Gashteroodkhani et al., 2020)	Deep-belief neural network with time–time transform	Accuracy of 99.74% and 99.46% radial network with grid-connected and islanded modes, respectively, and 100% for mesh topology in both modes of operation
Test microsystem (CERTS), 13.8 kV (Abdelgayed et al., 2017)	DWT, DT, and k-nearest neighbor	The experimental result of DT is 100%, and that of KNN is 95%
JMARTY model test system, 500 kV (Eldin et al., 2007)	DWT and moving window-based pattern recognition	Simple, accurate, and fast technique for EHV transmission lines. The algorithm can be applied to an already existing digital relay microprocessor
JMARTY model test system, 500 kV (Ibrahim et al., 2008)	DWT and moving window-based pattern recognition	Simple, accurate, and fast technique for EHV transmission lines. The algorithm can be applied to an already existing digital relay microprocessor
Tai-16 feeder, 11.4 kV (Yang et al., 2006)	Wavelet transforms and pattern recognition-based feature extraction with backpropagation ANN	The detection rate is 81%

(Continued on following page)

TABLE 2 (*Continued*) Comparison of various test systems.

Test system with ratings	Methodology used	Remarks
Benchmark system, 25 kV (Cui et al., 2017)	The signal processing technique of DFT and Kalman filtering estimation and classifiers such as Native Bayer's, SVM (Gaussian kernel), KNN, RF, and J48 are compared	RF and J48 proved to be the best, with 99% accuracy for both
Test system, 38 nodes, 132 kV (Ali et al., 2014)	DWT for feature extraction and matching approach technique is used for classification	Identify the faulty section in four or five iterations

the risk is greater relative to HIFs at the transmission level. An acceptable test system is selected for a suitable case study for simulation purposes and performance validation of the proposed methods. Proper data signals from the power system must be obtained under various possible operating scenarios to validate the proposed approaches. For technological and economic reasons, field fault testing on actual power systems is known to be difficult, with field test findings often having certain limitations. PDS must be correctly modeled because of these reasons. Table 1 gives a detailed discussion of various signal processing techniques for HIF detection using intelligent classifiers with various test systems used. Table 2 gives a comparison of various test systems used in HIF detection.

3.1 Radial distribution network

Shahrtash and Sarlak (2006) used a pattern recognition-based approach for HIF detection with DT as the classifier. The power distribution system is illustrated in which the system voltage is 12.5 kV, the short circuit level (at the infinite bus) is 866 MVA, and a time constant of 45 ms is shown in Figure 4A. The following data about transmission lines are given inductance of transmission line of 825 nH/m, resistance of transmission of 313 Ω/m, and line length of 33 km. The loads connected are a capacitor load rated 4.08 MVAr, transformer (10/0.4 kV) connected in delta-star, three-phase thyristor converter as harmonic load, and nominal load current of 630 A. The best results are obtained in even, odd, and in-between harmonics below 400 Hz. The classification factor is based on entropy, which is the effectiveness of an attribute in classifying data. A total of 2,583 and 1,331 cases were used for training and testing purposes, respectively. For different values of the sampling frequency of 2 kHz, a data window size of 2 cycles, and a pre-processing-time interval of 30 cycles, the accuracy of the proposed method was 99.4%.

Vahidi et al. (2010) used the DWT technique to extract the features, and ANN classifies the faulty cases with other power system disturbances. A three-phase radial distribution network is modeled using the PSCAD/EMTDC software used as the test system. The power system frequency is 50 Hz, and the power is supplied at 63 kV from a 30-MVA transformer (wye/delta). The transformers and line parameters are shown in Figure 4C. Line currents during the HIF have high-frequency components and are used for feature extraction. The extracted features are decomposed into two levels of detailed and approximation coefficients at six cycles. The performance of the DWT-based denoising technique depends on the threshold value γ, which can be divided into hard thresholding and soft thresholding. A large value of γ will shrink most of the coefficients to zero and for small values, denoising outcomes are inefficient. The extracted data are trained and compared with six different types of mother wavelet transforms: haar, coif2, dmey, db9, bior2.6, and sym8. Sym8 gives the best performance and accuracy. The sampling rate chosen is 20 kHz. A multi-layer perceptron neural network (MLPNN) with a Levenberg–Marquardt algorithm is used. The effect of SNR on the proposed algorithm is also studied. The HIF model is introduced to buses 2 and 3 to mimic the HIFs that exist on different ground conditions, such as sand, wet soil, dry soil, asphalt, and grass, giving an accuracy of 99%.

The system tested by Tawafan et al. (2012) is a 115-kV distribution feeder comprised of a substation, and three radial network distribution feeders are shown in Figure 4B. The generator is 30 kV and 10 MV connected to the 30/13.8-kV and 10-MV transformers. The 6-pulse rectifier is used for the representation of the non-linear load. The simulation models are created using PSCAD, and the sampling rate is 15.36 kHz. FFT is the feature extraction technique used, with an algorithm based on the adaptive neural Takagi–Sugeno–Kang (TSK) fuzzy modeling scheme, where the HIF detection is performed by taking the amplitude of the ratio of the second and odd harmonics to fundamental harmonics of the current signals that serve as input to ANFIS. The fundamental harmonics are decreased when the fault has occurred. A total of 570 cases are taken, among which 138 cases are HIFs and 432 are non-HIFs. The mean squared error value of the model is 0.1163, and based on the output of ANFIS, if the HIF current is greater than 0.6 it indicates HIF conditions and if it is less than 0.4; it is non-HIF conditions. The detection accuracy of HIF cases is 97.8%, and non-HIFs is 99%. The method was proposed by Soheili et al. (2018). The harmonic components of the third, fifth, seventh, eleventh, and thirteenth HIF current are preprocessed in an EKF, and 12 features are extracted. These features of one-, two-, and three-cycle windows are considered the input to train the RF. RF is trained with 20,580 and 8,820 data sets. The SNR chosen is 20 dB. Two separate, three-phase sources are connected through transformers to a transmission line of length 100 km. The transmission lines are 138 kV, and the transformers are 50 MVA, supplying at 138/25 kV to the distribution network (Figure 4D).

The distribution feeders (pi sections of 20 km each) work at 25 kV and are connected with shunt capacitors, linear loads, and a 2-MVA 6-pulse rectifier load (non-linear load). The resistance, inductance, and capacitance of positive and zero sequences of transmission lines are as follows: R_1 = 0.01273 Ω/km, X_1 = 0.9337 mH/km, C_1 = 0.0012 lF/km and R_0 = 0.3864 Ω/km, X_0 = 4.1264 mH/km, and C_0 = 0.0075 lF/km, respectively. The resistance, inductance, and capacitance of distribution lines (pi-section) are R_1 = 0.2568 Ω/km, X_1 = 2.0 mH/km, and C_1 = 0.0086, respectively. The total percentage impedance of the transformers is 6.75%. The

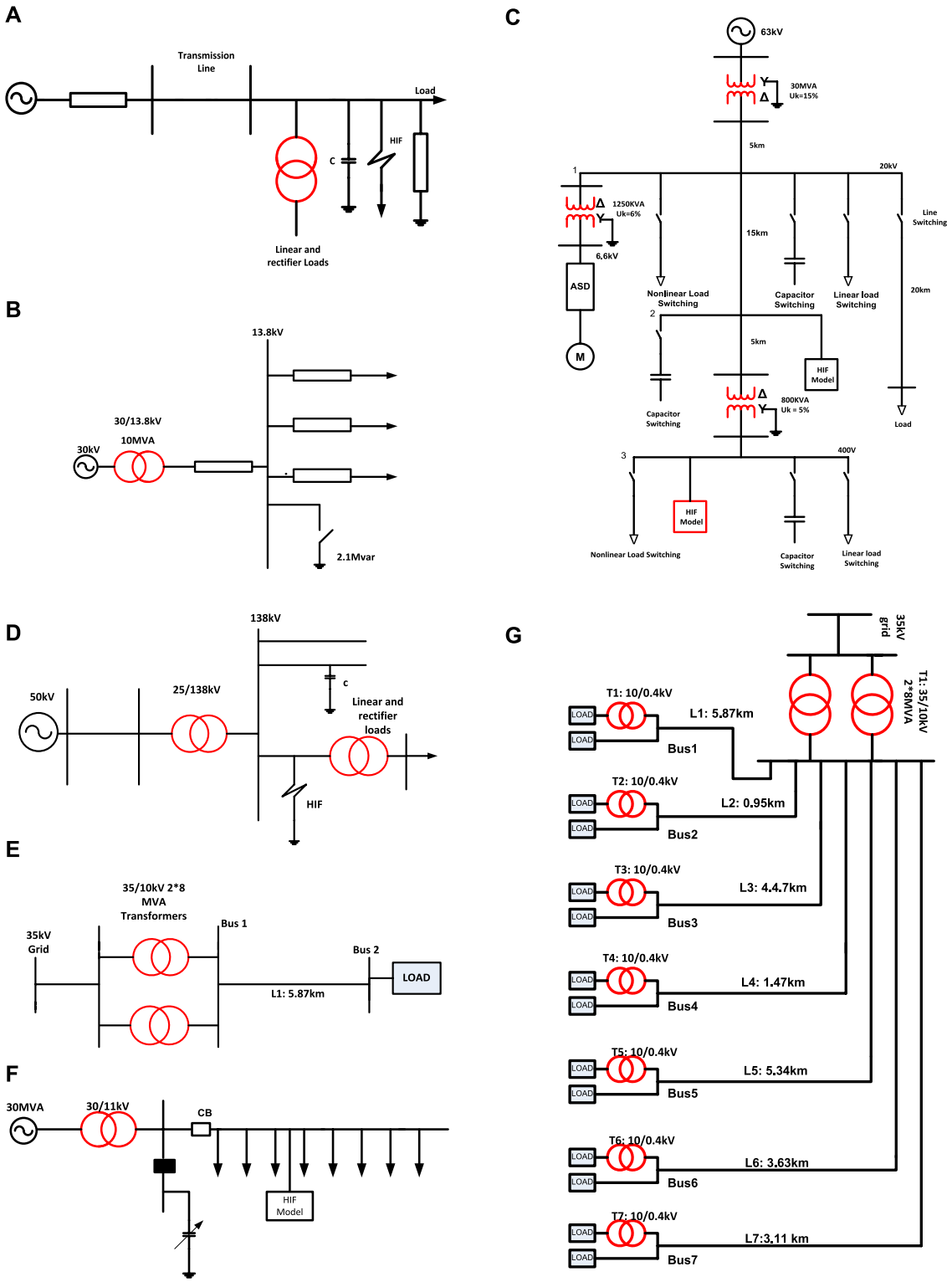

FIGURE 4
(Continued)

simulation models are developed using PSCAD (EMTDC), and the sampling rate chosen is 1.0 kHz on a 50-Hz base frequency (20 samples per cycle). RF proved to be the best, with 93.56% accuracy and 94.56% dependability. A multi-feeder radial distribution system was proposed by Sarwagya et al. (2018) to detect and segregate HIFs. It consists of a 30-MVA, 33-kV

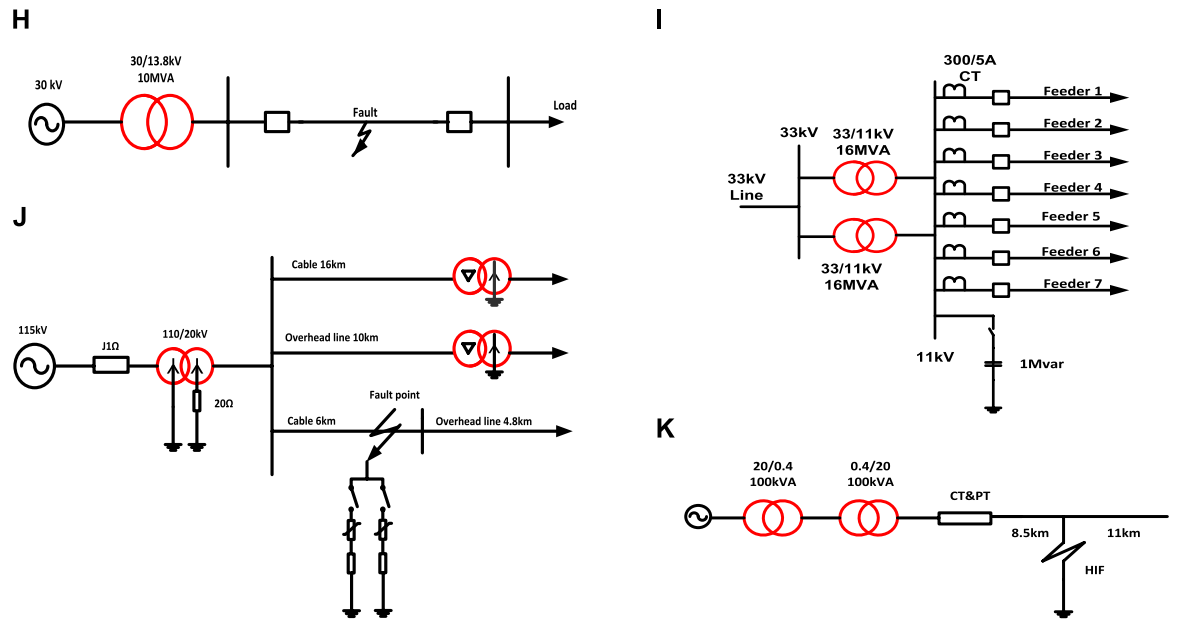

FIGURE 4
(Continued). **(A)** Radial 12.5 kV distribution feeder. **(B)** Three-phase distribution feeder. **(C)** Radial distribution network with three buses. **(D)** Single-line diagram of radial distribution 138 kV Feeder. **(E)** Single-line representation of a 2-bus system from the city of Mostar. **(F)** Typical IEEE PSRC radial distribution. **(G)** Single-line representation of an eight-bus system from the city of Mostar. **(H)** Radial 13.8 kV distribution feeder single-line diagram. **(I)** Single-line diagram of EPDS Chennai. **(J)** Radial 115 kV distribution feeder. **(K)** Representation of a 20-kV typical radial feeder system in Qeshm Island, Iran.

substation, and five numbers of 11 kV radial distribution feeders. The positive-sequence impedance of the distribution line is 0.3 + j0.25 Ω/km. The discrimination of the HIF is performed based on two criteria. The first is based on the maximum value of the one-cycle sum of superimposed components of negative-sequence current for faulty feeder identification, and the second is based on the one-cycle sum of superimposed components of residual voltage for HIF detection. The substation bus provides the residual voltage. The negative sequence current of all the feeders is compared, and the maximum value of the negative sequence will be for the feeder where HIF has occurred. The HIF is accurately detected in 3 s with the proposed method. The performance of the method with HIF during unbalanced loading, unbalanced loading conditions, capacitor switching, and occurrence of an HIF in various feeders is analyzed. Sarlak and Shahrtash (2011) compared two approaches for HIF identification: the voltage phase difference algorithm and a combination of DWT and ANN. The test system chosen is from Bosnia and Herzegovina, a distribution system like in Europe. The article includes two test systems: a two-bus feeder system and the other is an eight-bus system. The two-bus system is a simple one with a main transformer of 35/10 kV, whereas the latter one is more complex, consisting of 8 feeders fed from 35/10 kV, with underground cables and a transformer at the end consumers rating at 10/0.4 kV. Figures 4E, G represent two- and eight-bus systems, respectively. The sampling frequency is 3.2 kHz. The first method DWT is applied to the measured voltage signals. Each voltage has four detailed coefficients and one approximation coefficient. An algorithm is proposed in which DWT signals are combined, representing a signature for symmetrical and unsymmetrical faults. These data are then used to train and test the ANN. A total of 1,600 cases are simulated, including non-faulty conditions and three types of fault conditions. The method gives an accuracy of 100% for the 20–600 Ω range of fault resistances and at different fault locations. In the second method, a voltage measurement is performed, and the Hilbert transform is applied to obtain the best features. The best feature is an instantaneous frequency, which represents the time rate of change of the instantaneous phase angle. The phase difference is calculated by the difference between the instantaneous phases of voltage signals. The voltage phase difference algorithm calculates the PD during normal and fault conditions. At normal working operation, the phase difference will be 120^0, and during each fault condition, the phase difference will be different. This parameter is used to detect and classify the fault. With 2,000 cases in two-bus systems, the accuracy obtained is 92.5%, whereas the eight-bus system showed 90.19%. Panigrahi et al. (2018) used the IEEE Power System Relaying Committee Working Group at medium voltage levels. A simple 11-kV radial distribution feeder with eight nodes is shown in Figure 4F. MATLAB/SIMULINK program is selected and modeled, and the line impedance (positive sequence) is chosen as 0.3 Ω/km + j 0.25 Ω/km. At a distance of 5 km, nodes are isolated from each other, in which nodes 1, 3, 5, and 7 are connected to linear capacity loads of 1 MVA each at power factor 0.9/phase, and nodes 2, 4, 6, and 8 are linked to linear capacity loads of 2 MVA each at power factor 0.9/phase. The method discussed the MM gradient for HIF

detection and classified HIF, LIF, capacitor switching, and load switching (balanced and unbalanced).

The proposed method measures the three-phase voltage at a relay location and evaluates the residual voltage. The morphology gradient is used to extract the irregularities in the voltage signal. The extracted feature index is determined from the zero-energy index at NC and compared with a predefined threshold value. The extracted feature index value will jump slightly for HIF, LIF, and other disturbances for faulty conditions. An HIF is created at nodes 1, 4, and 9, and the occurrence will be for 1 s. The method accurately detects HIF occurrence in 0.8 s. The test system model proposed by Wali et al. (2018) is a 13.8-kV radial distribution feeder simulated by MATLAB/SIMULINK under different scenarios, such as linear load, non-linear load, and several other conditions. Figure 4H shows a single-line representation, a three-phase transformer, and a 13.8-kV distribution network. The non-linear load is represented by a 6-pulse rectifier that creates non-linear features in the feeder. The method used for HIF detection is FFT for feature extraction, and the power spectrum technique is used to identify the fault, which gives an accuracy rate of 100%, the time required is less, and that does not require any level of training. FFT extracts the feature of the current signal from the faulty feeder, and the power spectrum of the time signal is determined using the function FFT. If PS is less than 0.005, then a HIF occurs. HIF of 250 cases and other power system disturbances of 750 cases have been analyzed in this study. The method distinguishes events due to capacitor banks, non-linear loads, linear loads, and HIF.

The test system used for HIF detection (Veerasamy et al., 2018) consists of a grid source of 50 MVA/30 kV, a distribution transformer (12 MVA, 30 kV/13.8 kV), a common bus of 13.8 kV, and five radial type distribution feeders, integrated into the load facility. An Emanuel two-diode model consisting of two variable DC voltage sources of 1–10 kV connected to anti-parallel diodes by non-linear resistors of 50–500 Ω is considered an HIF model with non-linear arc characteristics. The method is proposed by extracting the features using CWT and DWT and classifying the extracted features by ANFIS. CWT gives the region at which the fault has occurred, and DWT can locate it by calculating the standard deviation (SD) using a five-level decomposition. The extracted SD values of different fault conditions with different values of fault resistance from the detailed and approximation coefficients are obtained, which are used to train classifiers FLS and ANFIS. Various faults, such as symmetrical, unsymmetrical, and HIFs, were tested using MATLAB/SIMULINK. The classification rate of ANFIS is 100%, which proved more effective than FLS. Wang et al. (2018) proposed that an HIF detection algorithm identifies the non-linear voltage–current characteristic profiles (VCCP) for identifying an HIF in the MV distribution system. During HIF, the zero-sequence current is less than the positive-sequence current. The slope of the VCCP is the numerical difference between voltage data from current sample data, and the least square linear fitting method is proposed. The wavelet correlation coefficient (WCC) is considered to improve the reliability of the algorithm. If WCC is greater than 0.966, the metered data are from a faulty feeder, and if less than the value, it is a healthy feeder. The radial distribution system is the test system in Figure 4J that uses EMTP/ATP program. The typical Mayr arc model is simulated and drawn in series with constant resistance using a switcher and parallel branches. The simulation time stage was set at 2 μs field-metered data from KEPCo, South Korea, and HIF experiments were performed on a 22.9-kV no-load overhead feeder to check the simulations. As it is a no-load feeder, the zero-sequence current and phase voltage were used at a faulty feeder outlet to correctly estimate the fault point voltage and fault branch current. The faults have been tested on various dry surfaces. The algorithm showed excellent results in real-time digital simulator tests. The test system proposed by Sedighi et al. (2005b) for HIF tests and data collection is a radial feeder of 20 kV at Qeshm Island, Iran, as shown in Figure 4K. The feeder is energized from another 20-kV feeder by two distribution transformers (20/0.4 kV, 100 kV A) connected back-to-back. The HV and LV connections of the transformers are delta/star connected. The HV sides of the transformers are connected to feeders, and the LV sides are connected to the low-voltage switch. Three-phase voltages and currents were monitored and recorded using Hall effect current transformers, potential transformers (PT), power analyzers, and computers. The sampling rate of the recorded data was 24,670 kHz for each test, and the overall recorded time was 15 s. The method used for HIF detection uses WT for feature extraction with a three-level decomposition of current signals. The first method uses GA for feature vector reduction, and the Bayes classifier is used for classification. In the first method, coefficients of three-level decomposition are used for feature extraction. They are divided into 10, 5, and 5 segments. In GA, each segment is mapped to a 20-dimensional space. A space with 20 dimensions is mapped to a space with five dimensions. The Bayes classifier is used to classify the mapped space. In the second method, WT transforms are also applied for the current signals, PCA is used for feature vector reduction, and NN is the classifier. The coefficients of three-level decomposition are used for feature extraction, divided into 10, 5, and 5 segments. Means of the absolute value of each segment were chosen as features, and the extracted signals were mapped to a 20-dimensional space. Using PCA, space was reduced to a 7-dimensional space. A perceptron NN using backpropagation discriminates between HIF, isolator leakage current, and other power system transients. Sekar and Mohanty (2020) stated that morphology gradient extracts the features of which a rule is set by RF and then fed to a fuzzy rule-based algorithm for HIF detection. The electric power distribution system (EPDS) was modeled using MATLAB/SIMULINK. A three-phase shunt capacitor of 1 Mvar has been connected to the busbar to improve power quality and output. The inrush current of a transformer produces an asymmetrical current signal that may serve as a transient signal generated by switching that may be like the HIF current waveform. An induction motor is connected as a load to study the motor operation impacts. The EPDS uses linear and non-linear loads to simulate the loading scenario, as shown in Figure 4I. One cycle window length of the current signal is measured, the impulsive feature of the signal is extracted, and a rule set is created from the statistical features of RF. The sampling frequency is 1,000 Hz, and the signal length is 0.5 s. The periodic signal has third- and fifth-order harmonics, and other harmonics that are negligible make the filter closer to HIF detection. The method effectively detects an HIF from other power system disturbances.

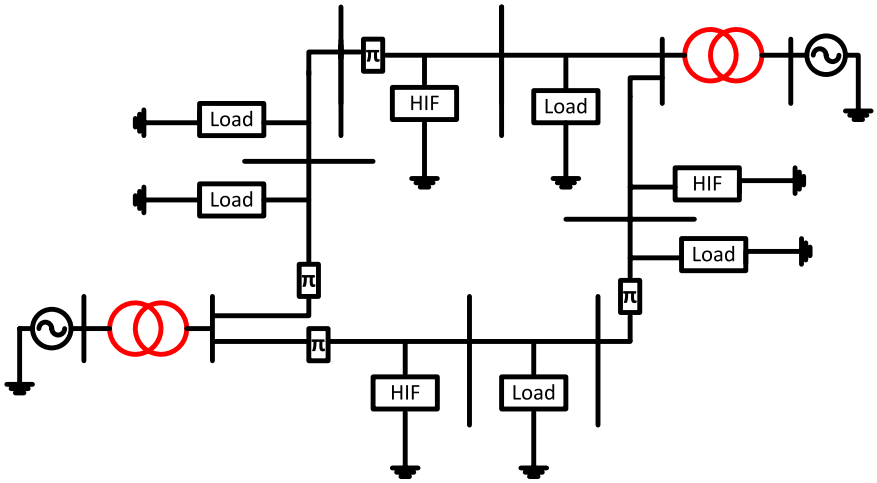

FIGURE 5
Three-phase meshed network.

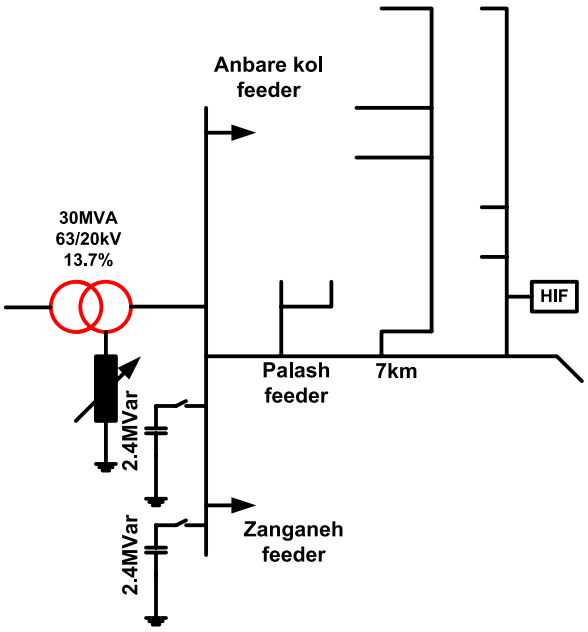

FIGURE 6
Palash feeder single-line diagram.

3.2 Mesh distribution network

The test system proposed by Lai et al. (2005) consists of two 50 MVA generators with 25 kV lines, two transformers, and linear and non-linear loads. In DWT, db4 was chosen as the mother wavelet, with a downsampling frequency chosen as 9,600 Hz, used to extract the detailed and approximation coefficients from the signals of the HIF and non-fault. The current and voltage signals at a targeted circuit breaker are measured. The RMS values of the measured quantities at various frequencies are analyzed and given as input to the nearest neighbor to classify fault signals. The HIF and non-HIF cases (1,000 cases each) were simulated with HIF and LIF models. The range of total error corresponding to the RMS value of the voltage wavelet coefficient is from 2.52% to 45.4% and will not indicate the physical properties of the output coefficient.

Samantaray et al. (2008) reported that S transform and TT extract the features, and FNN and PNN classify the faulty and non-faulty conditions of the HIF. The ST features are extracted from the HIF and normal fault current signals for half-cycle current signals after fault inception. The energy and SD of time and frequency information are considered feature sets. These features are used to train and test the FNN for radial and mesh networks. TT transform also extracts energy and SD of the TT-counter and time index after fault inception for the first half-cycle of the fault current. A total of 500 cases are simulated for training and testing the classifier. The system is modeled in MATLAB/SIMULINK, and the sampling rate chosen is 1 kHz. The PNN classification is based on the distribution values of the probability density function. The classification rate of a radial network with PNN using ST features is up to 98.06%. PNN with TT transform features gives a classification rate of up to 98.05%. The accuracy of the FNN and S transform combination is 93.04%, and the accuracy of the TT transform is 94.16%. The proposed method is also tested in a mesh network. The accuracy of the mesh network with S transform and FNN is 92.86%, and that with TT transform and FNN is 93.55%. The S transform and PNN combination gives 97.85% accuracy, and the TT transform and PNN combination gives 97.09% accuracy.

The HIF detection method used by Samantaray et al. (2009a) is a combination of AEKF with FNN and PNN. The schematic diagram of the test system chosen is given in Figure 5. The base voltage of the distribution network is 25 kV, and the generator is 10 MVA, 15 kV capacity. The harmonic components estimated by the AEKF are fundamental, third, fifth, seventh, eleventh, and thirteenth harmonics for the HIF and NF under non-linear loads. The AEKF calculates the harmonic component within half a cycle of the fault occurrence, with the peak of the estimated harmonic component considered that inputs to PNN and FNN. The PNN

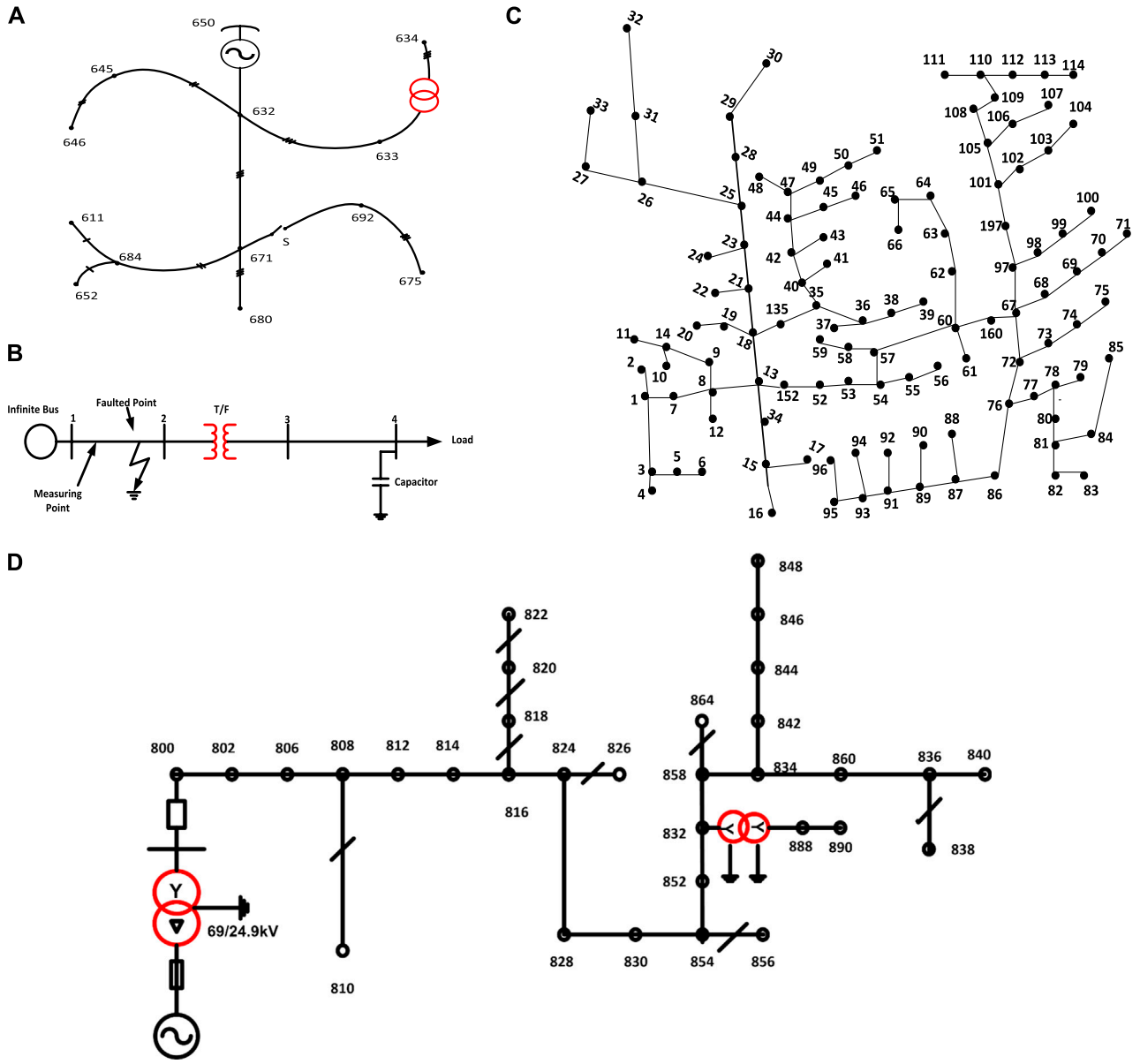

FIGURE 7
(A) Single-line diagram of the IEEE 13-node system. **(B)** Single-line representation of the IEEE four-node test system. **(C)** IEEE-123 distribution feeder. **(D)** IEEE 34-node test system.

classification is based on the probability density function's distribution values. PNN is analyzed using a data set with an SNR of 20 dB, 300 data sets for training, and 200 data sets for testing. For the classification, PNN takes 0.1 s time, whereas FNN takes 0.2 s. Fault and non-fault conditions with non-linear switching (a six-pulse rectifier is used) are checked using various models of MATLAB/SIMULINK, and the sampling rate chosen is 1.6 kHz. The accuracy rate of PNN is 99.11% compared with FNN having 96.51%.

The detection of HIF described by Routray et al. (2016) uses a test system with a generator of 50 MVA supplying 138 KV of voltage to the utility sector through a transmission line 100 km long, and a 138/25-kV star/delta transformer is considered for testing the method. The method uses ST for feature extraction and ANN for discriminating the HIF with load switching, capacitor switching, and NC. The time and frequency information is extracted from the S matrix, and the amplitude factor is calculated from current signals. A total of 4,010 cases were considered, of which 60% is used for training and 40% for testing. The overall accuracy of classifiers for normal fault is 98.75%, 96.4%, 94.06%, and 92.60% for normal (without noise) and noisy conditions.

Samantaray (2012) studies two test systems: one with a radial feeder mentioned in Figure 5 and the other with a mesh feeder given in Figure 7C. The test system studied is connected to a 50-MVA generator and a transformer of 138/25 kV from a transmission line of 138 kV and a length of 100 km. Loads are connected with linear

and non-linear loads. The resistance, inductance, and capacitance of positive and zero sequences of transmission lines are R_1 = 0.01273 Ω/km, X_1 = 0.9337 mH/km, C_1 = 0.0012 lF/km and R_0 = 0.3864 Ω/km, X_0 = 4.1264 mH/km, and C_0 = 0.0075 lF/km, respectively. The resistance, inductance, and capacitance of distribution lines (pi-section) are R_1 = 0.2568 Ω/km, X_1 = 2.0 mH/km, and C_1 = 0.0086, respectively. The total percentage impedance of the transformers is 6.75%. The simulation models are developed using PSCAD (EMTDC), and the sampling rate chosen is 1.0 kHz on a 50-Hz base frequency (20 samples per cycle). RF proved to be the best, with 93.56% accuracy and 94.56% dependability. On the distribution feeder, the HIF faults are generated at 25 kV, 20 km, pi section. Different simulation conditions are also considered, such as three-phase loadings, single-phase loadings, transformer energizations, shunt capacitor switching, and HIF by varying DC voltage sources. Two combinations of the HIF detection technique are proposed: the first is an EKF and RF and the latter is DT with FFT. The harmonic components of the third, fifth, seventh, eleventh, and thirteenth HIF current are preprocessed in an EKF, and 12 features are extracted. These features of one-, two-, and three-cycle windows are considered in this work. Considering the two-cycle window and with SNR set at 20 db. The simulation models are developed using PSCAD (EMTDC), and the sampling rate chosen is 1.0 kHz. RF is trained with 20,580 data sets, and 8,820 data sets are tested. RF proved to be the best, with 93.56% accuracy and 94.56% dependability compared with DT.

Mishra et al. (2016) used S transform with ANN and SVM to discriminate the HIF from other power system disturbances. A total of 4,000 cases, including HIF, normal, load switching, capacitor switching, and normal faults, are taken. Features are extracted from three-phase currents measured from the bus, and the best feature vector is selected. MLPNN with backpropagation NN and SVM along with ST is used, with 60% data for training and 40% for testing. The distribution model with a radial pattern of a 50-MVA generator is connected to a 100-km-long transmission line and a 138/25-kV star/delta transformer to supply 138 kV voltage to the utility sector. For the ideal case, ST with ANN and ST with SVM give 100% accuracy, whereas with SNR 30 dB, ST with ANN gives 93.7% and ST with SVM gives 92.15% accuracy. For the ideal case with the mesh network, ST with ANN and ST with SVM give 100% accuracy, whereas with SNR 30 dB, ST with ANN gives 81% and ST with SVM gives 86% accuracy.

3.3 Palash feeder, Tehran

Detection of the HIF using a combination of MLPNN based on multi-resolution morphological gradient features of the current waveform is described by Sarlak and Shahrtash (2011). The MMG features of the current signals (for three half-cycles) of broken and unbroken conductors are considered, and the features from DFT, DTT, DST, and DWT are compared. The morphology gradient is the difference between the dilation and erosion functions. Data acquisition is performed using the ION7650 meter, and the input port of the meters is connected to the outputs of the current transformers at the 63/20-kV substation. The sampling rate of the current waveform is 1.6 kHz. A disturbance detection module is based on MMG-extracted features of any subwindow with a predefined threshold. Three MLPNNs (A, B, and C) are trained individually by applying the time-based features obtained from the first, second, and third sub-windows. Then, their decisions are concatenated to make the final decision. The proposed algorithm gives security of 96.3% and dependability of 98.3%.

Nikoofekr et al. (2013) used a test system from Tehran, Iran, which has a 63/20-kV transformer feeder with 30 MVA apparent power, and the HV side has been grounded with a zigzag transformer and variable resistance adjusted at 29.5 Ω. Moreover, two 2.4-MVAR capacitor banks are connected through the HV circuit breakers. The ION 7,650-meter tests the HIF current and non-HIF current signals, such as insulator leakage current (ILC) and harmonic load current, with a sampling rate of 64 samples per cycle at the site. The method uses ST for phase correction in CWT, which localizes the phase and amplitude spectrum. TT transform extracts the features of the measured signals. Five different ART neural networks are used to classify the HIF and tested with broken conductors in asphalt, concrete, gravel surfaces and unbroken conductor on trees and under no fault conditions. This study uses five types of ART networks, namely, ART1, ART2, ART2-A, Fuzzy ART, and Fuzzy ARTMAP. The different features extracted were energy, SD, and median absolute deviation. The performance of the ART network is based on the vigilance parameter ρ whose value ranges from 0 to 1. For lower values of ρ, the classification is rough, and categories are less, and for higher values of ρ the categories are more, and classification is fine. In the basic ART training process, the input pattern is delivered to the input layer, which activates F2 neurons *via* bottom-up weights. Because the F2 layer is a competitive layer, the neurons compete with each other to learn the input vector, and the larger neuron wins. All other F2 units' activations (outputs) are set to zero. Then, the top-down weights of the winner neuron are sent back to the F1 layer. Figure 6 shows the Palash feeder in Tehran. From the total 6,437 data taken, 60% were used for training and 40% for testing. The result of the network shows an accuracy of ART1 of 91.61%, ART2 of 98.65%, ART2-A of 99%, Fuzzy ART of 99.18%, and Fuzzy ARTMAP of 99.18%.

MMG is the feature extraction used by Sarlak and Shahrtash (2013) and tested on the Palash feeder in the Southwestern Tehran distribution network, as shown in Figure 6. An HIF indicator is installed in various poles that detect HIF at various locations. The HIF indicators are installed in the feeder based on the processing of the magnetic-field strength signal. The fitness evaluation combines three goals: accuracy, number of training samples, and the weighting factor. The impulse response of magnetic response in the frequency domain is calculated in terms of the electric hertz vector. By simulation, a 978-feature vector for the HIF and 852 non-HIF is calculated. The dependability and security of the proposed system are best above the 20 db SNR. To evaluate the proposed method, MMG extracts a magnetic field strength signal, which is given to SVM for classification. The proposed algorithm has 96.9% security and 97.2% dependability.

The real-time experiments are performed in the Palash feeder, Tehran (Soheili et al., 2018). The modified FFT approach is used to detect the HIF concerning non-linear loads. In the proposed method, the measured three-phase current is analyzed by FFT. These currents are continuously

monitored for non-linear loads, abnormal conditions, and HIF detection. HIF currents during non-linear loading conditions and different ground types are recorded. The proposed algorithm has divided the output into three levels: 0, 0.5, and 1. NC, pickup, and HIF, respectively, are represented by these levels. Various scenarios in the simulated data are considered, including high current three-phase feeder, low current three-phase feeder, low current single-phase feeder, and capacitor switching events. The distribution network is energized *via* a 63-kV/20-kV three-phase transformer with a rated power of 30 MVA. Data recording has been conducted using the ION 7650, with a sampling rate of 64 samples per cycle (3.2 kHz). The various surfaces where real-time experiments are conducted are concrete with 20 cm in no-load conditions, concrete with 10 cm in 55% full load conditions, and asphalt with 2 cm under 55% full load conditions. The HIF detection time of the proposed method was 1.13 s.

3.4 IEEE test systems

There are various IEEE test systems, such as the single-line diagram of the IEEE 13-node system (Figure 7A), the single-line representation of the IEEE four-node test system (Figure 7B), the IEEE-123 distribution feeder (Figure 7C), and the IEEE 34-node test system (Figure 7D).

3.4.1 IEEE 13-node systems

The illustration given by Gautam and Brahma (2013) used an HIF detection tool using MM that can be implemented along with the conventional overcurrent relays in the substation. Both IEEE 13- and IEEE 34-node test feeders are used to validate the approach. Closing Opening Difference Operation effectively detects a disturbance in waveforms. A low sampling rate of 3,840 Hz (64 samples per cycle) was chosen to reduce computing time. The dilation and erosion function of MM and its difference will effectively detect the disturbance in the waveform. Voltage waveforms measured at substations are used in the procedure. The fault detection time is less than 1 s, and the method is fast and reliable. The two-test system gives 100% accuracy in detecting and classifying unbroken, broken conductors, capacitor switching, and load switching. A modified FFT approach based on HIF detection is proposed by Soheili et al. (2018), in which non-linear loading conditions are also considered. At node 630 of the IEEE 13-node system, the type of feeder, point of common coupling (PCC), and the current rate are considered, and the recording devices are installed at this node to resemble the real-world scenario. The feeder connected between 650 and 632 is considered the three-phase high current feeder with 300 A, 606 m long. The feeder between 692 and 675 is considered a low-current three-phase feeder with 80 A. The main factors considered include high and low three-phase currents and low current single-phase feeders. The scheme successfully distinguishes the HIF with load switching and capacitor bank switching in 1.15 s. Wang et al. (2019) used variational mode decomposition (VMD) and Teager–Kaiser energy operators (TKEOs) to identify the HIF. The method is tested in radial, IEEE 13-node, IEEE 34-node, and test microgrid systems, as well as experimental field tests. Three-phase current signals are measured, and VMD is performed on transient zero sequence currents (TZSCs) to obtain the intrinsic mode functions (IMFs). Then, the IMFs with the largest kurtosis value were selected as the characteristic IMFs. Second, the characteristic IMFs are calculated to obtain TKEOs and divided into subintervals of TKEOs waveform to calculate the time entropy values. The HIF detection criterion is when the time entropy value is 0; then, CS or LS has occurred. When the entropy value is not 0, it is judged as an HIF. The calculation time taken is 0.0028 s.

A data-driven technique includes PCA, Fisher discriminant analysis, and binary and multi-class SVM for HIF detection. Compared with PCA, FDA can classify and locate the HIF successfully (Sarwar et al., 2020). PCA utilizes Hotelling's T^2 statics for HIF discrimination (see Eq. 1). The IEEE 13-node system is used for testing:

$$T_{\alpha}^{2} = \frac{m(n+1)(n-1)}{n(n-m)F_{\alpha}(m,n-m)}, \tag{1}$$

where $F_{\alpha}(m, n\text{-}m)$ is the F distribution with m; $(n–m)$ is the degree of freedom; $T_2 \leq T^2{}_{\alpha}$ means no-fault condition; and $T_2 > T^2{}_{\alpha}$ means faulty condition.

The SVM uses a discriminant function to differentiate various classes. Non-linear classification is based on a kernel function from kernelized SVM. Figure 7A shows the single-line diagram of the IEEE 13-node system. Multiclass SVM gives the best results, with dependability and security at 100%. Silva et al. (2020) performed a wavelet packet-based feature extraction with a three-level decomposition of signals at 2.5 kHz along with the EuFNN classifier. The IEEE 13-bus system is considered for testing the method, which is a highly charged compact feeder with a rating of 4,053 kV A and a power factor of 0.85, and an extension of approximately 1.5 km from bus 650 to bus 680. Several line configurations, such as three-phase and single-phase lines, overhead, and underground sections, are considered. Different families of wavelet transform, namely, Haar, Symlet, Daubechies, Biorthogonal, and Coiflet, used to extract features from a one-cycle time window of current signals were chosen. The RMS and the entropy values calculated for Daubechie-8 give the best discrimination rate. Various WPT families, the MLP, learning vector quantization (LVQ), SVM, and EFuNN classifiers were compared, among which MLPNN gave the least accuracy, and all other classifiers gave an average of 97.14% accuracy. Nezamzadeh-Ejieh and Sadeghkhani (2020) performed the time-domain HIF detection algorithm by analyzing the substation current employing Kullback-divergence that measures the similarity between asymmetry and non-linearity of two consequent half cycles. Both IEEE 13-node and IEEE 34-node feeders are used to test the approach. The amplitude of the fault current of 15 A is approximately 3% of the normal feeder current. An intelligent electronic device samples the signals at 4.8 kHz and measures the current in each phase. The current vector measurement is formed by

$$M_j = \begin{bmatrix} i_j(t_0+T_s) & i_j(t_0+2T_s) & i_j(t_0+KT_s) \end{bmatrix}^T, \tag{2}$$

$$M_{ij} = \begin{bmatrix} |i_j(t_0+T_s)| & \dots & |i_j(t_0+(K/2)T_s)| \end{bmatrix}^T, \tag{3}$$

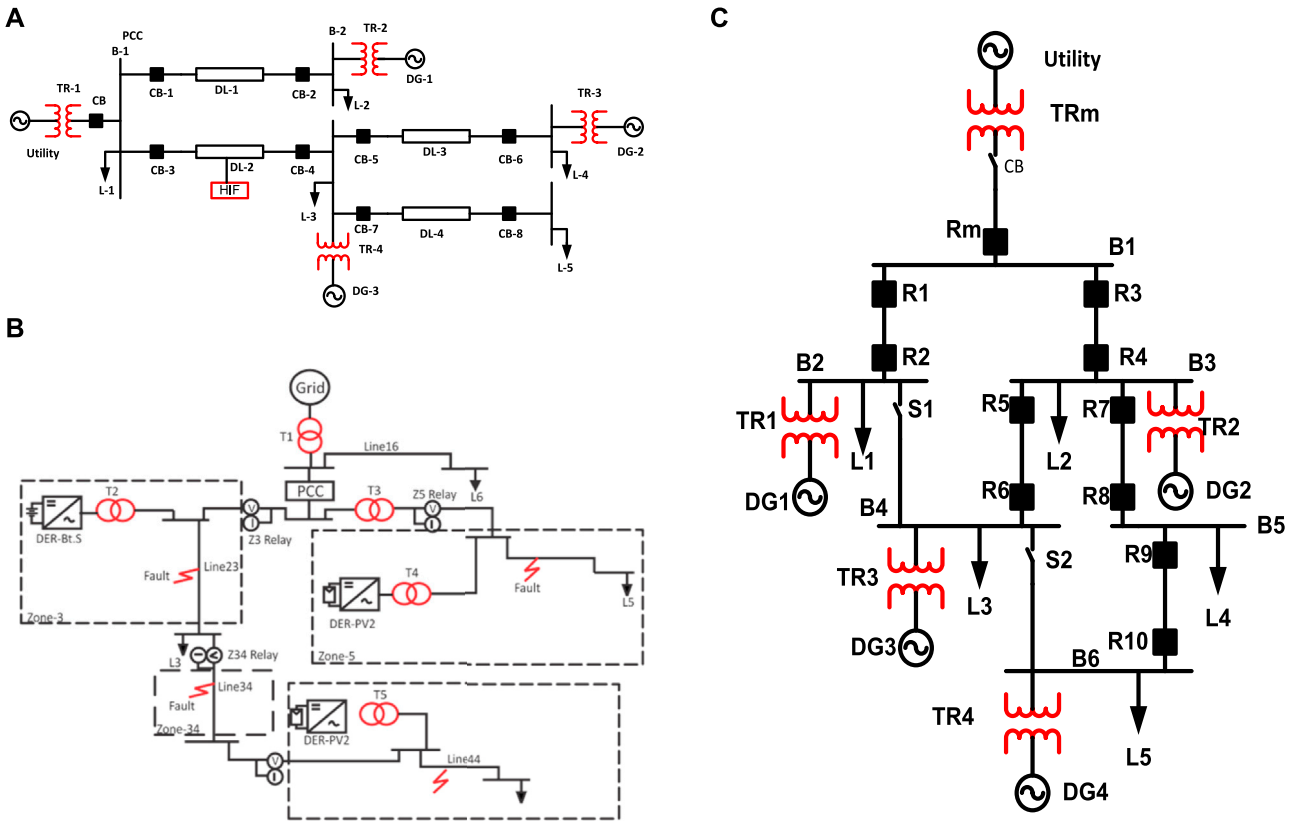

FIGURE 8
(A) Test microgrid system. **(B)** Representation of CERTS microgrid system structure. **(C)** Single-line representation of IEC microgrid.

$$M_{ij} = \left[\left|i_j\left(t_0 + (K/2)\,T_s\right)\right| \;\ldots\; \left|i_j\left(t_0 + K/T_s\right)\right|\right]^T, \tag{4}$$

$$D_{KL,j}\left(M_{1,j}\|M_{2,j}\right) = \sum_{r=1}^{N} M_{1,j}(r)\log\frac{M_{1,j}(r)}{M_{2,j}(r)}. \tag{5}$$

During normal operation, there is no change in the waveforms of two consecutive half-cycles $D_{KL} = 0$, and during a fault occurrence, there will be asymmetry and non-linearity in the half-cycles and $D_{KL} \neq 0$. During the HIF, the third harmonic current will be greater than the fifth harmonic current. The occurrence of an HIF is when $> \xi_{th}$, where ξ_{th} is the disturbance detection threshold. A small threshold will decrease the accuracy of the system and a high value will reduce the detection speed. The method effectively detects the presence of an HIF.

3.4.2 IEEE 34-node test system

Moravej et al. (2015) used an IEEE 34-node test feeder for testing, as given in Figure 7D, and simulated it in EMTP-RV software. There are four different conductors, in which the system is characterized by heavily and lightly loaded with a feeder voltage of 24.9 kV. Two-line regulators and one transformer (24.9/4.16 kV) are present in the feeder. There are single-phase and three-phase feeders and two shunt capacitors in the system. Dual-tree complex wavelet transforms is used for feature extraction and PNN for classifying the faulty and healthy conditions. In the method, various steps involved in HIF detection include disturbance detection, disturbance feature extraction, HIF detection, frequency tracking, over-current protection, and the main feeder break detection. In the first step, the fundamental frequency current of the three-phase current is calculated using the DFT algorithm. The post-disturbance and pre-disturbance data windows are saved in memory, and both are decomposed into five levels by DT-CWT. The detailed components of the post-disturbance data window are subtracted from those of the pre-disturbance, and after obtaining the detailed component of the disturbance signal, the proper feature is selected. The SD and normalized energy of the detailed coefficients of level 2–level 5 three-phase currents and residual current were selected as the features for the HIF detection algorithm. The algorithm is fast and detects the disturbance in 1.88 ms, giving an accuracy of 98.88%. Sekar and Mohanty (2017) proposed that MM extracts features, such as energy, mean, and SD, which train the DT (data mining based). The three-phase current signal is pre-processed by a dilation and erosion morphological filter. The data mining-based DT using software package "R" is used, as well as post-disturbance data window length of current signals at feeder processed through the MM filter and chosen data window. The IEEE 34-node test system with light loads is also used. The total number of cases considered is 300, of which 70% are used for training and 30% for testing. The accuracy is 98.83%, dependability is 98.88%, and security is 100%, with a detection time of 30 ms. The proposed method is also tested using the IEEE 13-node system, in

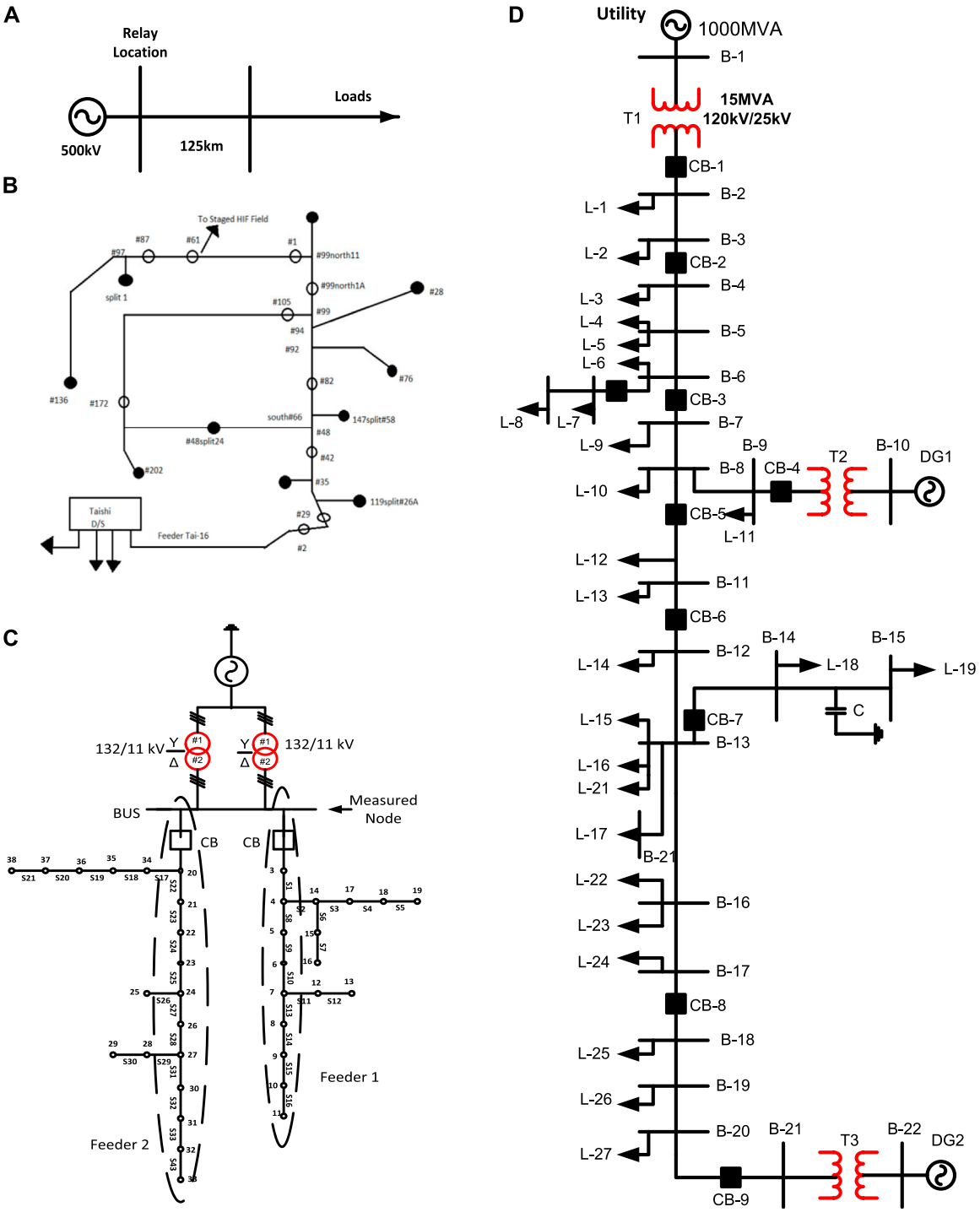

FIGURE 9
(A) Single-line representation of the JMARTY model transmission line test system. **(B)** Single-line representation of TAI-16 feeder distribution networks. **(C)** Single-line diagram of the 38-node test system. **(D)** Single-line representation of the benchmark system.

which the total cases considered are 300, of which 70% are used for training and 30% for testing. The accuracy is 98.83%, dependability is 98.88%, and security is 100%, with a detection time of 30 ms.

Fan and Yin (2019) used a convolutional neural network and transfer learning-based approach for HIF detection. The method is tested with 5,000 data sets, of which 2,500 are HIF data and 2,500 are non-HIF conditions in an IEEE 34-node feeder. From the data set, 80% was taken for training and 20% for testing. The sampling rate was 15 kHz, and there were 300 samples in the input data. Among the four layers of the CNN, each layer of the CNN model has convolution, rectified linear unit (ReLU), and max-pooling functions. The accuracy of the CNN obtained was 99.52%, and

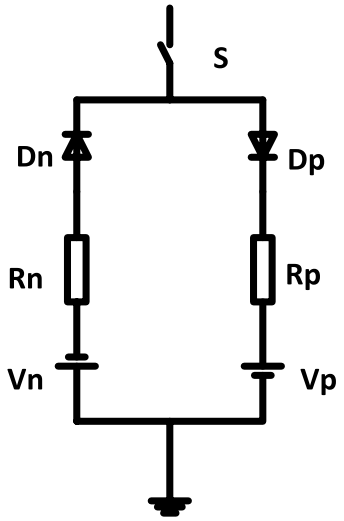

FIGURE 10
Emmanuel arc model of HIF. The Vn, Vp, Rn, and Rp values of wet sand are 4.5 V, 2.5 V, 400 ± 5 Ω, and 350 ± 5 Ω, respectively. For dry sod, the values are 4 V, 2 V, 300 ± 5 Ω, and Rp 250 ± 5 Ω. The wet grass Vn, Vp, Rn, and Rp values are 2.75 V, 1 V, 150 ± 5 Ω, and 125 ± 5 Ω, respectively. The Vn, Vp, Rn, and Rp values are 2.5 V, 0.75 V, 100 ± 5 Ω, and 75 ± 5 Ω, respectively, for reinforced concrete.

the computational cost was low compared with the traditional MLPNN (91.13%). Fewer data sets (<300) were in the IEEE 13-node system with 50% training and 50% testing data. The accuracy obtained for the CNN was 95.06% compared to CNNs, with 74.69%.

3.4.3 IEEE four-node test feeder

The test system used is the IEEE four-node system, as shown in Figure 7B. Three-phase load switching, capacitor switching, no-load transformer switching (energizing and de-energizing the transformer at various cycle times), harmonic loads (e.g., an unregulated four-pulse rectifier and induction motors), arc furnaces, and down-conductor and undowned conductor HIFs are discriminated using this method. The method of HIF detection (Sarlak and Shahrtash, 2008) uses PCA and LDA and is used along with SVM to detect the HIF, which gives 97.5% accuracy. PCA refers to the linear feature extraction method that computes *m* eigenvectors corresponding to *n*-dimensional patterns. PCA extracts uncorrelated features. Hence, it is more appropriate compared to other classification techniques. LDA measures the Fisher criterion that finds the *m* eigenvectors of the scatter matrix that discriminates HIFs from non-HIFs. The extracted features are sampled at the rate of 12.5 kHz. The feature set is divided into a training set of 66% and a testing set of 34%. The polynomial and radial bias function of SVM is used, in which the linear kernel function has the best classification accuracy.

3.4.4 IEEE-123 distribution feeder

An IEEE-123 distribution feeder as a test system is illustrated, characterized by unbalanced phases modeled with EMTP-RV software. Figure 7D displays the IEEE-123 distribution feeder. Some of the feeder buses are connected to smart meters in three-phase sections and not in single- and two-phase sections. Tonelli-Neto et al. (2017) found that the method uses WT along with ANN and fuzzy interference systems for HIF detection. Three-phase current signals are analyzed and sampled at a frequency of 15.36 kHz. An application of DWT, multi-resolution analysis extracts the features from the current signals using Daubechies mother wavelet with fourth-order filter (db4). An energy concept is applied to the features to increase efficiency and minimize the number of coefficients. The energy concept is used for the third-level detail coefficients because of the high number of coefficients created in MRA. Fuzzy ARTMAP neural networks and fuzzy interface systems are used for HIF classification. Each bus, where the signals are obtained, has a FIS responsible for identifying and qualifying the feeder operating condition in the detection based on FIS. The results combine a normal case, HIF phase a, HIF phase b, and HIF phase c. The detection method based on the fuzzy art neural network (FANN) is as follows: the vectors obtained are normalized for use as inputs to multiple neural networks. This normalization is performed by identifying the maximum current value of each analyzed vector. Comparing both FANN and FIS, the accuracy of FANN is 97.69%, and that of FIS is 99.25%.

3.5 Test microgrid system

The test microgrid system is used for HIF detection (Kar and Samantaray, 2017), as shown in Figure 8A. The base power of the test system is chosen as 10 MVA. The rated short-circuit of the utility is 1,000 MVA with f = 60 Hz, rated 120 kV. Distribution generations, DG1 and DG3, are rated as follows: synchronous generator rated at 9 MW and rated voltage of 2.4 kV, and DG2 is a wind farm consisting of three wind turbines (2 MW each), rated kV = 575 V. The transformer ratings used in this study are as follows: Transformer 1: 15 MVA, 120/25 kV. Transformers 2 and 4 are rated at 12, kV = 2.4 kV/25 kV, while Transformer 3 is rated at 2.5, kV = 575 V/25 kV. The distribution lines (DL) are DL1, DL2, DL3, and DL4: PI-Section, 20 km each. The total load is 20 MW, 10 MVAR, a sum of L1–L5. The MODWT is the feature extraction technique, and DT is the classifier used. The proposed method is tested in both grid-connected and islanded modes. The MODWT scaling filter and the wavelet filter related to the DWT filter are calculated, and the scaling coefficients of MODWT are obtained. The detailed approximation coefficient is obtained from the MODWT, and DT does accurate classification. The total cases are 1,493, of which 973 are HIF cases and 520 are faulty conditions. In the method proposed, 12 feature sets are considered, among which five were taken for classification. The training set (70%) and testing (30%) assess the performance. The software package "R" generates data mining for the DT. The detection accuracy, dependability, and security are 100% for the grid-connected mode, whereas for the islanded mode, the accuracy is 99.23%, security is 98.23%, and dependability is 100%.

Microgrid is considered while integrating distributed energy systems (Abdelgayed et al., 2017). The Consortium for Electric Reliability Technology Solutions (CERTS) was used for the case study of microgrids in this article. The microgrid system has two modes of operation: grid-connected and islanded mode of

TABLE 3 Performance evaluation of classifiers.

Criterion	Equation	Function
Accuracy (A)	$\frac{TP+TN}{TP+FP+FN+TN}\%$	Overall precision
Dependability (D)	$\frac{TP}{TP+FP}\%$	Faulty state detection precision
Security (S)	$\frac{TN}{FN+TN}\%$	Healthy state detection precision
Safety (S)	$\frac{TN}{FP+TN}\%$	Safety-related criterion
Sensibility (SN)	$\frac{TP}{FN+TP}\%$	Sensitive load-related criterion
Speed (v)	$\frac{Tone-cycle}{TDetection}\%$	Detection speed

Note: TP, true positive; TN, true negative; FN, false negative; FP, false positive; Tonecycle, time for one cycle; TDetection, time for detection.

operation. CERTS microgrid consists of a distribution system fed from three-phase distribution transformers rated at 13.8/0.48 kV, consisting of two solar photovoltaic sources and one battery energy storage source. Four loads are considered long in the distribution system. The method employs a semi-supervised machine learning strategy to handle labeled and unlabeled data. DWT extracts the hidden properties of voltage and current and applies them to a harmony search algorithm to find the HIF parameters. The DT and KNN classifiers are used to discriminate the HIF events. The overall accuracy of the DT is 100%, and that of the KNN is 95%.

The test system is a CERTS microgrid with two inverter-interfaced DG units and one synchronous generator-based DG unit (Gadanayak and Mallick, 2019). The representation CERT microgrid system is shown in Figure 8B. For HIF detection, the test system consists of five distribution lines and five relay units. MATLAB-SIMULINK is used to simulate the model, with a simulation sampling rate of 0.5 MHz. The MODWT approach for feature extraction and knot-based empirical mode decomposition is included in the methodology. The program recognized 855 cases of HIFs and 801 cases of non-HIFs. The average time to detect a fault was 0.12175 s. The test system used by Gashteroodkhani et al. (2020) was performed in a 25-kV IEC standard microgrid that gave high accuracy and robustness in noisy environments. The single-line representation of the IEC microgrid is represented in Figure 8C. A deep-belief neural network with TT-transform is employed where an intelligent relaying scheme-based real-time digital simulator is used, integrated with MATLAB. The process involves the measurement of three-phase currents at both ends and the feature extraction by Clark's transformation and TTT, which is sent to the DBNN. Six features are used for feature extraction, including energy, SD, and median absolute deviation. Microgrid models with grid-connected, islanded, radial, and mesh topologies are used to test the approach. With 3,600 fault situations and 3,125 no-fault cases, the sampling rate was set to 1.2 kHz. The proposed method gives 99.74% and 99.46% accuracy for a radial network with grid-connected and islanded modes, respectively, and 100% for mesh topology in both modes of operation.

3.6 JMARTY model test system

Eldin et al. (2007) considered the JMARTY model with Egyptian transmission line parameters, such as a transmission line length of 125 km and a resistive load of 600 MW, as shown in Figure 9A. DWT's feature extraction technique with classifier moving window pattern recognition is used in HIF detection in extra-high voltage transmission. The sampling rate is 250 samples/cycle at 50 Hz. In order to distinguish HIF from non-HIF events, the proposed technique uses high-frequency information from wavelet analysis db4. The effect of fault location, fault interception angle, fault type, switching of loads, switching of the HIF, and sudden load rejection is studied. The algorithm can be added to the existing digital relay microprocessor; it is fast, accurate, and simple.

Ibrahim et al. (2008) described two approaches: the first uses DWT analysis and the second analyses three-phase voltages using a high-frequency tap coupling capacitor voltage transformer. The chosen sampling rate is 20,000 Hz. A 100-m-long 345-kV double-end transmission line system is considered. The effect of fault location, fault type, fault interception angle, switching of loads, and switching of HIF are studied. The method is independent of load variations and unbalanced conditions. The algorithm is fast, accurate, and simple; it can be added to an existing digital relay microprocessor (Eldin et al., 2007).

3.7 TAI-16 feeder

In Yang et al.'s method (2006), the HIF was tested in a real-time Tai-16 feeder, Taishi substation near Mailiao, as shown in

Figure 9B. The fault was staged at pole #61 under grounded and ungrounded conditions, with dry and wet ground conditions. Data from the Shand-Ding substation and the She-Zi substation were considered to train the NN. The analog-to-digital recorder ADX-3000 was installed to monitor the neutral line current of the faulted feeder in the substation. A cross-linked polyethylene-covered conductor, a bare copper conductor, and ACSR conductors are used. A wavelet transform and pattern recognition-based feature extraction scheme is used and applied to backpropagation ANN for HIF detection. The detection of the HIF is carried out by introducing an intelligent HIF detector applied to a neutral line current, giving an 81% detection rate. A self-tuning algorithm based on the chi-square algorithm is applied to find the variations in neural current. A statistical confidence scheme is applied for neutral current estimation. For calculating the threshold of neutral current, a 95% confidence interval is applied.

3.8 Test system—38 nodes

A typical 11-kV distribution network in Malaysia is composed of 38 nodes serving 34-line sections, as shown in Figure 9C, displaying the single-line diagram of a 132/11-kV distribution network. The test unit has a frequency of 50 Hz, with a sampling frequency of 6.4 kHz, and delivers 128 samples/cycle. The feeder bus is simulated using the PSCAD program. Ali et al. (2014) proposed that DWT-based MRA is the feature extraction technique, and a matching approach technique is used for classification in the underground distribution system. The simulation tests of the three-phase voltage signal are obtained at a measurement point using the DWT-based multi-resolution technique. The voltage signal was decomposed into 128 samples and analyzed by Daubechies fourth order of DWT. The first level of the detailed coefficient, d1, detects the HIF by observing changes in the characteristics taken from three-phase voltage data. The sum of the first-level approximation coefficients obtained from the normal cycle, known as the approximation ratio, is divided by the sum of first-level approximation coefficients obtained from the normal cycle to classify the fault:

$$\text{Approximation Ratio} = \frac{\sum a(HIF)}{\sum a(normal)}. \quad (6)$$

The approximation ratio is considered for distinguishing SLGF, LLGF, LLLF, and LLF. If the ratio is less than 1 for one phase and greater for the other two phases, then an SLG fault has occurred. The three-phase ratios will be the same for LLLF. For locating the HIF, a matching technique based on the shortest distance is used. For each line section, the SD between the measured signal and the line section is computed. The summation of the detailed coefficients of voltage signals is done in three coordinate systems and represented in three-dimensional space. The SD of each section is calculated, and the average value is calculated. The average value is compared with the SD values of each section. Each section is then arranged in ascending order of its SD values, which list the possibility of a faulty section. The method successfully located the fault after four or five iterations.

3.9 Benchmark system

In Cui et al. (2017), the test system chosen is a benchmark system in a remote Canadian community with 25 kV 60 Hz, distribution feeders that serve an 11-MW load built by McGill Power Laboratory, as shown in Figure 9D. An L-G HIF at $t = 0.3$ s is implemented in a hybrid distribution system. The feeder's PCC (CB-1) will collect all the data where the HIF detector is located, two DGs at locations A and B, respectively. Three types of distribution systems are also possible to model: 1) the synchronous generator (SG) system is constructed by connecting the SG to location A without DG in location B; 2) the inverter-interfaced system is connected to location B with only type 4 wind turbines at location A and without DG; and 3) the hybrid DG system has an SG connected to location A and wind turbine generators at location B. The rated voltage is 4.17 kV for the SG, and 9 MVA is the power. Three wind turbine generators provide wind power, each rated at 575 V and 2.2 MVA. The proposed method was tested in hybrid systems, and inverter-based systems are grounded, as well as ungrounded conditions. HIF and non-HIF events of 1,944 cases each have been considered for testing and training. The method proposes an algorithm to rank the effective feature sets using a signal processing technique of DFT and Kalman filtering estimation. The effective feature set is derived from information gain or entropy. The information gain of each feature is calculated, and a calculation variable is obtained. Such calculated variables are compared and then ranked for further assessment in HIF detection. By measuring the currents and voltages at the point of the common coupling, 246 electrical features are obtained. Classifiers, such as Native Bayer's, SVM (Gaussian kernel), k-nearest neighbor (KNN), RF, and J48, are compared, among which RF and J48 proved to be the best with 99% accuracy for both.

3.10 Modeling of HIF

Researchers provide numerous HIF models because of stochastic behavior and complicated properties. In order to acquire a good representation of the HIF, it is necessary to develop a model that specifies the features and the harmonic content of the HIF. Because arcing, which has yet to be fully modeled, is involved in most HIF events, an HIF is a difficult example to model. HIFs are non-linear and asymmetric, according to some earlier studies, and random and dynamic arcing features should be used in modeling (Zamanan and Sykulski, 2014). The arc is a continuous luminous discharge of electricity in which many free electrons and ions in an insulating medium are converted into a conducting medium. The arc was first studied as a continuous luminous discharge of electricity through an insulating medium that becomes a conducting medium due to the presence of a large number of free electrons and ions. The arc was first researched about circuit breaker disruption capabilities, with arc models used to improve circuit breaker testing (Elkalashy, 2007). The Emanuel model replicates zero periods of arcing and asymmetry by connecting two DC sources anti-parallel with two diodes (see Figure 10). Variable resistors vary the fault resistance, and a voltage supply with random values mimics HIF unpredictability. Some of the other HIF models are, two-time varying series resistors with

different characteristics (Nam et al., 2001), Kizilcay's model (Zhang et al., 2016; Mishra and Panigrahi, 2019) and Matthews arc model (Gammon and Matthews, 2001).

4 Classifiers for identifying the healthy and faulty conductors

This section discusses classifiers, which distinguish between faulty and non-faulty conditions. Classifiers set a boundary between healthy and faulty conductors. In the classification process, two types of data are to be considered: training data consisting of information relating to known patterns and testing data, which are a collection of information relating to unknown patterns. Table 3 presents the performance evaluation of various classifiers with various criteria, such as accuracy, dependability, security, sensibility, speed, and safety.

The appropriate classifier is chosen depending on the application where it is being used. The various classification conditions are capacitor switching, load switching, noises (Christie et al., 1993), disturbances (Russell and Benner, 1995), and voltage spikes. Faulty conditions include L-L, L-G, L-L-L, LIF, HIF (Barnard and Pahwa, 1993), and non-linear load conditions (Sultan and Swift, 1992). A knowledge-based system (Sedighizadeh et al., 2010), microprocessor (Kwon et al., 1991), signature-based detection (Wester, 1998), mechanical detection (Balser et al., 1986), burst noise signals (Aucoin and Russell, 1987), and DSP were previously used in classification. Different classifiers, such as neural networks (Vyshnavi and Prasad, 2018), SVM (Mishra et al., 2016), fuzzy logic, ANN (Baqui et al., 2011), GA (Zamanan et al., 2007), PNN (Samantaray et al., 2008), ELM (Reddy et al., 2013), ANFIS (Abdel Aziz et al., 2011), and DT (Kar and Samantaray, 2017) are compared and discussed.

4.1 Neural networks

NN (Snider and Yuen, 1998) models are grouped according to their architecture (Sultan et al., 1992) (which gives the neural connection), processing (describes the production of output corresponding to weight and input), and training (explains the adaption of NN weight for every training vector). The architecture consists of the input, hidden, and output layers. The processed information of the NN is obtained at the output layer. NN architecture types are single-layer networks, such as an MLPNN (Sarlak and Shahrtash, 2011), a Hopfield network, and a Kohonen network (Ebron et al., 1990). ANN implementation is easy but is subject to the amount and quality of trained data. The ANN algorithm needs to be re-trained when there is a change in the data set, and the number of neurons and learning rate are found by the trial-and-error method.

An NN using a relay mechanism with HIF detection is described by Sharaf et al. (1993). The approach of a feed-forward network with backpropagation of one hidden layer and 15 neurons is used, which employs the discriminant vector of negative and zero sequence current and voltage in the substation. Twenty-two cases were taken for training and 10 cases for validation. They are noise-tolerant, require less detection time, and are economical. NN algorithm-based relaying scheme, implemented using NN hardware chips or software, promptly detects HIFs using Fourier analysis of lower-order harmonic vectors of measurements used as the input to the perceptron feed-forward network (Snider and Shan, 1998). The Emanual arc model is used as the HIF model. Logsigmoid hidden layers of three numbers with 10 neurons make the structure. As only lower-order harmonics are utilized for detection, the scheme is more feasible and flexible and has a high detection rate. The scheme is tested using simulation and real-time field measurements. A microprocessor-based pattern recognition technique is developed (Al-Dabbagh and Al-Dabbagh, 1999), which uses DFT to analyze signals. The scheme describes a sensitive Earth fault protection that is comparatively slow but gives better performance. The scheme is not tested with real-time data; only relaying current and voltage signals from the ATP simulation package are tested. Keyhani et al. (2001) used a subband decomposition method for current, which uses the energy of the subband to feed the input vector to the NN. The system is less noise-sensitive and can detect HIFs efficiently at high noise levels. The SNR chosen was 0–14 db. Emanuel and Gulachenski's HIF model is used for testing. A total of 800 cases were taken, and 16 neurons were used for fault analysis. Two NNs, namely, perceptron and FNN, are used; both give similar results with close to 100% accuracy. The scaling and translation characteristics of DWT are used to discriminate the transient and stable features of current signals (Yang et al., 2004). The extracted features of voltage and current signals and dissimilarity of wavelet component coefficients are calculated, which is used to train the NN and determine HIFs from the switching operations. The SD and mean are the features considered, with 20 neurons in the first hidden layer and 10 in the second hidden layer. A total of 600 events were taken, of which 500 are used for training and 100 for testing. The combination of the NN with DWT gives a good performance. Bansal and Pillai (2007) explained that FFT is the feature extraction technique used for 320 events taken. The magnitude of the third and fifth current harmonics is used for feature vector LVQ network classifiers for HIF detection. The output layer of LVQ contains two linear neurons. In comparison with the feed-forward network with backpropagation, LVQ gives a quicker response. LVQ gives the best results in random and selected subclasses if the subclass chosen is 10.

ANN and DWT are used for HIF detection (Vahidi et al., 2010). Distorted waveforms similar to fault current waveforms are generated, and DWT is used to denoise the signal and obtain signals with a high SNR. Sym8 wavelet function is used for detection, which gives 99% accuracy. The Levenberg–Marquardt algorithm is used for training the network, with 8-5-3-1 Baqui et al. (2011). The method is robust; it uses modified HIF models and discriminates between a wide range of signals, such as HIFs. The PNN model uses a probabilistic model, such as Bayesian classifiers and a supervised learning network, a type of feedforward network (FFN) that uses exponential activation functions. The PNN structure has four layers: the input layer, pattern layer (hidden layer), summation layer, and output layer. In the network used, the initial weights and the learning process are not required (Chen et al., 2016). Fan and Yin (2019) used the convolutional neural network that overcomes the disadvantages of conventional MLPNN; for example, the spatial structure of data is not considered, and large data sets are not required for training purposes. The four layers of CNN are convolution, rectified linear unit, and

max-pooling functions. Here, the classic HIF model with two anti-parallel DC sources, diodes, and variable resistors is used. Two separate conditions were studied using the proposed system: the first was tested with 5,000 data sets, of which 2,500 are HIF data sets and 2,500 are non-HIF conditions in an IEEE 34-node feeder. From the data set, 80% was taken for training and 20% for testing. The sampling rate was 15 kHz, and the input data contained 300 samples. The accuracy of the CNN obtained was 99.52% compared with the traditional MLPNN of 91.13%. The second case was performed with fewer data sets (<300) in the IEEE 13-node system with 50% training and 50% testing data. The accuracy obtained was 95.06% compared to conventional neural networks, with 74.69%. ELM is extracted from neural networks that improve feed-forward neural networks' efficiency. ELM is a single-layer neural network, which is hidden and does not need be tuned. In ELM, input weights and biases of hidden layers are selected randomly, and the output weights are chosen analytically (Mishra et al., 2017). FFT extracts the third and fifth harmonics current and voltage magnitudes and trains the ELM (Reddy et al., 2013). The number of events is 320, and 20 neurons with unipolar sigmoidal activation functions are used for training the algorithm. Here, ELM is used for fault classification and section identification. The scheme is faster with less human intervention and gives accurate classification and less training time compared to neural networks such as LVQ and MLP. DWT is the feature extraction technique that studies the cross-countryside HIF detection applied to the transmission and distribution systems (AsghariGovar et al., 2019). Three-phase current signals are extracted at both ends of the line for fault detection and identification. The Emanual arc model is used as the HIF model, and the IEEE 13-node system is tested. The hidden layer contains 20 nodes, with the number of inputs and outputs as one. Faulty conditions and other power system disturbances are classified by ELM. The novel protection algorithm is independent of interception angle, power swing, fault location, power system topology, and noise.

4.2 Genetic algorithm

A GA is an intelligent technology that detects faults (Kim et al., 1990). The behavior of the HIF is affected by many environmental parameters, and hence, a parameter-based generic technique method can be used. Detection of the HIF in a distribution system using a real coded genetic algorithm (RCGA) to analyze the tracking harmonics and current phase angles of the fault current signals was proposed by Zamanan et al. (2007). A fitness function is used by the GA that differentiates the performance between different strings. The scheme gives accurate results in differentiating harmonics and current angles of HIF. For GA, the simulation time is high, and as the processes are random, this cannot be used for fault location. GA cannot be used for online analysis because there is a possibility of inaccurate results.

Two methods for HIF detection have been compared (Sedighi et al., 2005b): the first method is the GA and Bayes classifier, where GA is used for feature vector reduction and Bayes for classification. The second method uses PCA and a NN for HIF identification. PCA and wavelet transform are used for feature extraction, for which GA gives the best results compared to the NN. The mother wavelet used is rbior3, with a sampling frequency of 24.67 kHz. It discriminates HIFs from non-HIFs, such as isolator leakage current, capacitor switching, and load switching. The tests were conducted 8.20 and 8.44 km from the source at different types of surfaces. The overall success rate of the Bayes classifier is 98.33%.

4.3 Support vector machine

SVM is a significant classifier commonly used in issues related to different power systems and environmental fields that find application in regression analysis, prediction, and classification. SVM is a non-linear kernel-based function that maps data from one space region to another (Veerasamy et al., 2018). Different types of kernel functions are the linear kernel, polynomial kernel, radial basis kernel, and sigmoid kernel. SVM provides a distinctive training algorithm to optimize the boundaries between different groups. Optimal parameter selection is highly important to obtain successful classification outcomes. The classifier of the support vector is mainly a binary linear classifier. Theoretically, SVM was derived from the principle of statistical learning. The linear classification algorithm for the SVM applies the training set to find the segregated hyperplane. The SVM algorithm calculates the number of support vectors for SVM (no training is required), which makes SVM a better algorithm for classification than ANNs (Gururajapathy et al., 2017). The elements of the training sets that characterize the dividing hyperplane are support vectors. Even for a large data set, SVM is quick in classification with fewer heuristics. Gashteroodkhani et al. (2019) proposed a method that uses TT transform and ST for feature extraction from the transient voltage signal measured at one end. The classification is conducted using SVM optimized by a particular swan optimization and is tested over the headline and underground cable. Bewley's lattice diagram identifies the fault location. The total number of cases was 2,376, of which 70% were used for training and 30% for testing the SVM. Compared with ST, the TT transform achieves 99.8% accuracy. Sahoo and Baran's method (2014) uses the DWT technique for feature extraction, which considers the SD and is tested in the radial distribution feeder at 138 kV. Maximum value and energy are decomposed into two parts. Mary's model for HIFs is used. Various classifiers, such as fuzzy, Bayes ANFIS, SVM (Kernel trick function is used), and MLPNN, are compared, among which ANFIS and SVM give the best results. A data-driven technique includes PCA, Fisher discriminant analysis, and binary and multi-class SVM for HIF detection. Compared with PCA, FDA can classify and locate HIFs successfully (Sarwar et al., 2020). PCA utilizes Hotelling's T^2 statistics for HIF discrimination. The IEEE 13-node system is used for testing. Diode-resistance source is the HIF model used, with opposite polarity. Vp = 1 kV and Vn = 0.5 kV with ±10%. Rp and Rn range from 1,000 to 1,500 Ω, with random variation. In the proposed method, multiclass-SVM gives the best results. MM is the feature extraction (Sarlak and Shahrtash, 2013) and was tested on the Palash feeder in the Southwestern Tehran distribution network. An HIF indicator is installed in various poles that detect HIFs at various locations. The dependability and security of the proposed system are best above the 20 db SNR. To evaluate the proposed method, a DST, DTT is used along with PNN, as well as DWT along with SVM. The proposed algorithm has 96.9% security and 97.2% dependability.

4.4 Adaptive neuro-fuzzy inference system

ANFIS includes the benefits of ANN and fuzzy logic principles in a single platform. ANFIS trains the fuzzy inference system to create fuzzy rules for IF-THEN and evaluate membership features for input and output variables. A NN trains the membership functions to minimize the error in fault classification. Tawafan et al. (2012) and Abdel Aziz et al. (2011) used the FFT for feature extraction, which was then tested in a radial 13.8-kV distribution feeder. Third harmonics, the magnitude of current, and phase of current are extracted, of which the first parameter is essential for HIF detection and the latter for HIF classification. It is noted that the HIF current is < 0.05 for NCs and >0.9 for HIF conditions. The main disadvantage is determining the global minimum using the membership function and enhancing feature extraction using the algorithm. The SD values drawn from the DWT are used to train fuzzy, Bayes, MLPNN, ANFIS, and SVM and compare the performances in Veerasamy et al. (2019). DWT with ANFIS and SVM classifiers discriminates between HIFs, SLGF, LLF, and DLGF, giving superior results. Apart from this, certain performance indices, such as absolute error, root mean square error, kappa statistic, success rate, and discrimination rate, were compared. In Veerasamy et al. (2018), DWT extracts SD features from a three-phase current and is used to train ANFIS. For fault analysis, a sampling rate of 20 kHz is considered. The mother wavelet used is Daubichies's wavelet (Db9). A radial distribution system is used for testing in MATLAB/SIMULINK. The fuzzy logic system discrimination rate is 66.6%, but ANFIS gives 100%. When discrimination rates of the fuzzy logic system and ANFIS are compared, ANFIS proves to be superior by 33.3%. The fundamental component (e.g., magnitude and phase) of current is used (Aziz et al., 2012; Abdel Aziz et al., 2012) for HIF detection, classification (LG, LL, LLG, LLLG, and HIF), and location. The fundamental component, such as third harmonics, plays an essential role in HIF detection and location. The ANFIS classifier unit gives correct output for faulty and non-faulty conditions. In fuzzy logic, the concept of possibility is used rather than the concept of probability. Jota and Jota (1999) explained the application of neo-fuzzy neurons trained to identify the SD responses where FFT is used for feature vector extraction. After the training, the neuron set becomes a decision core of the supervisory system. The method identifies the HIF in a real-time feeder, which works better for not very close fault instants. The correction index is 100% for very close faults and 81% for faults at a distance of less than 10 m. The field chosen is Caratinga in Brazil for data analysis. Silva et al. (1995) explained the HIF testing in both real-time feeders and simulation. The real-time feeder chosen was Caratinga in Brazil. The method is based on the traveling wave technique. Detection with fuzzy rules in normal and faulty cases was carried out, and faults within 10 m were identified. The SD of noise was identified to input the fuzzy. The method is focused on passive faults, which effectively work with harmonic frequencies. The feature extraction technique DWT (Silva et al., 2020) with neuro-fuzzy classifier is tested in the IEEE distribution test 13-bus feeder and the IEEE distribution test 34-bus feeder, which incorporates an evolving fuzzy neural network (EuFNN) that has an "adapt itself" ability and is excellent in terms of accuracy and robustness. Wavelet packet-based feature extraction is used with a neuro-fuzzy classifier. Different families of wavelet packet transform, namely, Haar, Symlet, Daubechies, Biorthogonal, and Coiflet, were used to extract features from a one-cycle time window of current signals. LVQ, MLP, SVM, and evolving fuzzy neural networks are compared with RMS and entropy values coefficients. Apart from other advantages, EuFNN gives a membership function for the possibility of fault occurrence. The method will not identify the fault location. DWT with a fuzzy interference system and Fuzzy ARTMAP neural network combination based on Dempster–Shafer evidence theory is tested in the IEEE-123 distribution feeder (Tonelli-Neto et al., 2017). The classification results show that the system is robust, efficient, and reliable. The Emanuel arc model is used for HIF modeling, where V_p ranges from 500 to 2,000 V and V_n from 2,000 to 2,500 V. Any new type of fault can be included in the classifier with ease. The method gives a classification efficiency of 97.69%. FFT extracts features from the signal, and fuzzy logic classifies HIF and non-HIF events (Suliman and Ghazal, 2019). The detection is performed by analyzing the third and fifth harmonics of magnitude and phase angle. The method is tested in three phase-4 wires of a 400-V radial distribution feeder in a downed conductor and wet sand. The third and fifth harmonics are extracted to train the classifier. The classifier is trained with real-time data from the practical test performed in the laboratory. By using a neuro-fuzzy interference system, tuning of the algorithm is performed.

4.5 Decision tree

DT represents the learned function in DT learning, which is a technique for approximating discrete-valued target functions. One of the possible values of this attribute corresponds to each branch that descends from the node. The DT-based method uses phase current (in RMS) and second, third, and fifth harmonic magnitudes to detect HIF (Samantaray, 2012). Shahrtash and Sarlak (2006) used pattern recognition with the DT algorithm, which has efficient training time and gives excellent results in even, odd, and between harmonics up to 400 Hz. Two cases are considered for HIFs: the first is when a broken conductor touches the ground and the other is when an energized conductor touches another object. The specified tree is constructed using the J48 algorithm in WEKA software. The classification factor is considered based on entropy that gives the variations in the data set. This study concludes that a 2-kHz sampling frequency and 30-cycle time interval using a small energy DT can give accurate results. EKF is used for feature extraction and ensemble DT (RF) for fault classification, compared with the DT algorithm (Samantaray, 2012). The method is tested in radial and mesh networks. The reliability and accuracy of RF is compared and is best in the two cycle window. The method is also tested in one- and three-cycle windows. For data with SNR 20, the reliability is more than 99%. The DT algorithm (Sheng and Rovnyak, 2004) can differentiate between the HIFs from normal switching, such as capacitor switching and transformer inrush currents. FFT is used for feature extraction and is tested in a radial distribution feeder. DT discriminates the extracted features for classification, which, compared with other pattern recognition

tools, gives better results. Current signals of each phase are sampled at 1,920 Hz, with a total number of cases of 5,700. The Emmanuel arc model is used, and the system is simulated in EMTP.

4.6 Miscellaneous HIF detection schemes

Several other HIF detection schemes, aside from these methods, play a crucial role in HIF detection. Using signal processing and pattern recognition techniques in the device relaying architecture with expert systems, Don Russell (1990) explained low current faults. Mamishev et al. (1996) suggested using fractal geometry to analyze the chaotic properties of high-impedance defects and RMS current values are used to classify the behavior of the temporal system, resulting in a relatively short time series usable for study. Sharaf et al. (1996) used a relay-based mechanism for HIF detection. The scheme utilizes the ripple frequencies and sub- and super-harmonics usually associated with the HIF phenomenon. Eldin et al. (2007) introduced two methods for detecting HIFs in extra-high-voltage transmission lines. Both approaches investigated the origins and dynamics of HIF-related arcing. The former employs DWT analysis, whereas the latter employs the coupling capacitor voltage transformer's high-frequency tap. The effects of fault location, interception angle, fault type, switch-off, and operations are analyzed. Both approaches are accurate and require less time.

5 Locating high impendence faults

HIF detection and identification are essential, and locating the fault accurately is the next step. Many methods are used for locating HIFs, such as the matching technique (Ali et al., 2014), intelligent algorithms (Chen et al., 2016), synchronized harmonic phasors (Farajollahi et al., 2017), phase shift measurement of a high-frequency magnetic field (Bahador et al., 2018), the advanced distortion detection technique (Bhandia et al., 2020), smart meters (Radhakrishnan, 2019), power line communication systems (Milioudis et al., 2012), and power line carriers (Chen et al., 2010), which will be elaborated in this section. A transient power direction-based method is used for locating HIFs in MV distribution systems, as proposed by Elkalashy et al. (2008). DWT extracts the features of the residual current and voltage of the measuring nodes. The product of DWT detailed coefficient d3 of residual current and voltage will give the polarity of the frequency band power (12.5–6.25 kHz). Wireless sensors placed at the measuring nodes will process the detailed coefficients of DWT in the distribution network. Daubechies wavelet 14 (db14) is effectively located at the fault. An unearthed 20-kV distribution system is simulated using ATP and HIFs because leaning trees are mimicked using a universal arc model to test the proposed method. Ali et al. (2014) used the matching technique and analyzed the three-phase voltage signals using DWT-based MRA. Approximately 128 samples are taken and analyzed using Daubechies' fourth order (Daub4). The fault location is identified by the smallest SD values. By iteration, the exact location can be found. A surge generator is used to pinpoint the exact location that injects a high-voltage DC pulse of 30 kV. The highest amplitude flash over with acoustic noise gives the exact location of a fault.

HIF detection by measurement of voltage imbalance in primary distribution feeder by smart energy meter was illustrated by Leite (2019). The proposed method is tested in a typical distribution feeder of 13.8 kV that gave accurate and robust results when tested in broken and unbroken conductors at the load or source side. The faulty section is identified by a parameter "K" factor when a situation of voltage unbalance threshold is crossed. The three-phase smart meters will calculate the voltage imbalance and locate the presence of the HIF. The voltage across the distribution feeder is measured by Thomas et al. (2016), as well as the voltage sequence components. Three HIF models were investigated (a high resistance model, a simpler two-diode model, and an arcing model), as well as several grounding options, such as a securely grounded network, a resistive grounded network, an ungrounded network, and a resonant grounded network. The method is tested in two identical feeders of 16 km in length and divided into four identical sections. The detection is based on the positive sequence voltage drop and the percentage of negative and zero sequences voltage drop. Chakraborty and Das (2019) found that the detection is based on the even harmonics present in the voltage waveform using smart meters called the even harmonic distortion index and evaluated in a PSCAD simulation and experimental setup. The communication interface of the smart meter will inform the detection of the HIF to the nearby substation. The two-diode model of the HIF is used, and the test system used is IEEE 13-node feeder. The performance of the proposed system is compared with the existing schemes based on MM, wavelet transform, and harmonics-based detection, in which the proposed method gives satisfactory results with an execution time of 3.98 ms. A two-terminal-based numerical algorithm for location estimation and arcing voltage calculation with synchronous phasors is proposed by Balser et al. (1986). Phasor measurement units are installed at either end of the transmission lines at a distance of 100 km. In the study, a 10-km fault distance along with an arcing voltage of 4.5 kV is calculated, and after 20 ms of fault inception, the synchronous phasors detect the location. ETP simulation is used for testing the algorithm. Ibrahim et al. (2010b) located the fault by computing the system offline zero and negative-sequence impedance as a function of fault location, which is dependent on the unsynchronized root mean square (RMS) value of the sending and receiving end zero-sequence currents for ground faults or the RMS value of the sending and receiving end negative-sequence currents for line faults. The method is independent of any HIF model, and the test system for evaluation chosen is a 345-kV double-end transmission-line system. The accuracy error does not exceed ±2% for accurate line parameters with different fault conditions, such as LG, LLG, LL, and LLLG. Radhakrishnan (2019) proposed installing smart meters for locating HIFs in the distribution system, including distribution systems, power electronic loads, and electric arc furnaces. Smart meters are introduced in each load point that measures the load current and second harmonic content of load voltage. The method is tested on the LV 906-bus European distribution network and IEEE 39-bus system using PSCAD simulation to evaluate the performance of the smart meters under various grid conditions. The method proposed gives satisfactory results in all the investigated conditions. As an HIF alarm is generated, test signals are fed into the power grid, and the location of the fault can be calculated using impulse responses

recorded by PLC devices (Milioudis et al., 2012). A frequency range of 3–95 kHz is used, and the method accurately locates the fault throughout the line. Lin et al. (2004) used a phasor measurement unit-based detection and locating system for permanent and arcing nature faults. PMUs installed on both terminal sides simultaneously monitor three-phase voltage and current phasors. The study proposes a communication link from the fault location. The measured phasors are communicated *via* communication channels to a central computer. However, only harmonic phasors are transmitted to the central computer after fault detection to reduce the burden of the communication channels. Santos et al. (2013) proposed the traveling wave method, which sends a high-frequency signal from one end of the terminal and is received at the other end. The amount of equipment required is high, and the method is expensive. A 90-bus feeder is used to test the proposed method.

6 Conclusion

This study reviewed most of the methods for feature extraction, classification, location, and test systems that have been produced over time, repeatedly, and the latest research developments used to detect HIFs in power distribution systems. Approximately 161 studies from the major referenced journals in the field of HIF detection have been discussed with primary importance on various test systems with different signal processing techniques and classification techniques. The feature extraction techniques using signal processing techniques include FFT, DWT, LWT, MODWT, LDA, PCA, MM, CWT, EKF, TT, DTWT, ST, and MODWPT. Different classifiers used to discriminate the HIF from non-HIF events, such as ANN, SVM, GA, ELM, PNN, FLC, ART, ANFIS, DT, RF, and CNN, are discussed. Various test systems, such as radial and mesh distribution networks, IEEE 4-, 13-, 34-, 39-, 123-node systems, Palash feeder, test microgrid, JMARTY, and Tai-16, are discussed in Section 3, with IEEE standards. Fault locating techniques are discussed, such as the traveling wave method, phasor measurement unit method, and the matching technique. This review also highlighted the basic principles, advantages, and disadvantages of frequently used works related to HIFs. We also highlight that the conventional HIF detection methods are simple, have easy measurement setups, and consume less computation time. Still, they are inaccurate when used in large power system networks. Overall, we suggest a combination of signal processing techniques along with an intelligent classifier for the HIF detection scheme as they improve system reliability and power quality in distribution systems.

Author contributions

Conceptualization was performed by RV along with the support of MS and NK. The first draft was written by RV with inputs from MS, SG, NK, ES, and SD. Supervision was carried out by MS and NK. All the authors were involved in revising the draft.

Conflict of interest

The authors declare that the research was conducted in the absence of any commercial or financial relationships that could be construed as a potential conflict of interest.

Publisher's note

All claims expressed in this article are solely those of the authors and do not necessarily represent those of their affiliated organizations or those of the publisher, the editors, and the reviewers. Any product that may be evaluated in this article, or claim that may be made by its manufacturer, is not guaranteed or endorsed by the publisher.

References

Abdel Aziz, M. S., Hassan, M. A. M., and El-Zahab, E. A. (2012). An artificial intelligence based approach for high impedance faults analysis in distribution networks. *Int. J. Syst. Dyn. Appl.* 1 (2), 44–59. doi:10.4018/ijsda.2012040104

Abdel Aziz, M. S., Moustafa Hassan, M. A., and Zahab, E. A. (2011). *Applications of ANFIS in high impedance faults detection and classification in distribution networks," SDEMPED 2011 - 8th IEEE Symp. Diagnostics Electr* Bologna, Italy: Mach. Power Electron. Drives, 612–619. doi:10.1109/DEMPED.2011.6063687

Abdelgayed, T. S., Morsi, W. G., and Sidhu, T. S. (2017). Fault detection and classification based on co-training of semisupervised machine learning. *IEEE Trans. Ind. Electron.* 65 (2), 1595–1605. doi:10.1109/TIE.2017.2726961

Akorede, M. F., and Katende, J. (2010). Wavelet transform based algorithm for high-impedance faults detection in distribution feeders. *Eur. J. Sci. Res.* 41 (2), 238–248.

Al-Dabbagh, M., and Al-Dabbagh, L. (1999). Neural networks based algorithm for detecting high impedance faults on power distribution lines. *Proc. Int. Jt. Conf. Neural Netw.* 5, 3386–3390. doi:10.1109/ijcnn.1999.836206

Ali, M. S., Abu Bakar, A. H., Mokhlis, H., Arof, H., and Azil Illias, H. (2014). High-impedance fault location using matching technique and wavelet transform for underground cable distribution network. *IEEJ Trans. Electr. Electron. Eng.* 9 (2), 176–182. doi:10.1002/tee.21953

Aljohani, A., and Habiballah, I. (2020). High-impedance fault diagnosis: A review. *Energies* 13 (23), 6447. doi:10.3390/en13236447

AsghariGovar, S., Pourghasem, P., and Seyedi, H. (2019). High impedance fault protection scheme for smart grids based on WPT and ELM considering evolving and cross-country faults. *Int. J. Electr. Power Energy Syst.* 107 (7), 412–421. doi:10.1016/j.ijepes.2018.12.019

Ashok, V., and Yadav, A. (2021). Fault diagnosis scheme for cross-country faults in dual-circuit line with emphasis on high-impedance fault syndrome. *IEEE Syst. J.* 15 (2), 2087–2097. doi:10.1109/JSYST.2020.2991770

Aucoin, B. M., and Russell, B. D. (1982). Distribution high impedance fault detection utilizing high frequency current components. *IEEE Trans. Power Appar. Syst.* (6), 1596–1606. PAS-101. doi:10.1109/TPAS.1982.317209

Aucoin, M., and Russell, B. D. (1987). Detection of distribution high impedance faults using burst noise signals near 60 hz. *IEEE Trans. Power Deliv.* 2 (2), 342–348. doi:10.1109/TPWRD.1987.4308114

Aziz, M. S. A., Hassan, M. A. M., and Zahab, E. A. (2012). High-impedance faults analysis in distribution networks using an adaptive neuro fuzzy inference system. *Electr. Power Components Syst.* 40 (11), 1300–1318. doi:10.1080/15325008.2012.689418

Bahador, N., Namdari, F., and Matinfar, H. R. (2018). Tree-related high impedance fault location using phase shift measurement of high frequency magnetic field. *Int. J. Electr. Power Energy Syst.* 100 (3), 531–539. doi:10.1016/j.ijepes.2018.03.008

Bakar, A. H. A., Ali, M. S., Tan, C., Mokhlis, H., Arof, H., and Illias, H. A. (2014). High impedance fault location in 11 kV underground distribution systems using wavelet

transforms. *Int. J. Electr. Power Energy Syst.* 55, 723–730. doi:10.1016/j.ijepes.2013.10.003

Balser, S. J., Clements, K. A., and Kallaur, E. (1982). *Detection of high impedance faults* Washington, DC, United States of America: Electr. Power Res. Institute, EPRI EL, 1–6.

Balser, S. J., Lawrence, D. J., and Clements, K. A. (1986). A microprocessor-based technique for detection of high impedance faults. *IEEE Power Eng. Rev.* 6 (7), 59–60. doi:10.1109/MPER.1986.5527876

Bansal, A., and Pillai, G. N. (2007). High Impedance Fault detection using LVQ neural networks. *Int. J. Electr. Comput. Energy Electron. Commun. Engg* 1 (4), 693–697.

Baqui, I., Zamora, I., Mazón, J., and Buigues, G. (2011). High impedance fault detection methodology using wavelet transform and artificial neural networks. *Electr. Power Syst. Res.* 81 (7), 1325–1333. doi:10.1016/j.epsr.2011.01.022

Barnard, J., and Pahwa, A. (1993). Determination of the impacts of high impedance faults on protection of power distribution systems using a probabilistic model. *Electr. Power Syst. Res.* 28 (1), 11–18. doi:10.1016/0378-7796(93)90074-O

Benner, C., Carswell, P., and Don Russell, B. (1989). Improved algorithm for detecting arcing faults using random fault behavior. *Electr. Power Syst. Res.* 17 (1), 49–56. doi:10.1016/0378-7796(89)90059-X

Bhandia, R., Chavez, J. D. J., Cvetkovic, M., and Palensky, P. (2020). High Impedance Fault detection using advanced distortion detection technique. *IEEE Trans. Power Deliv.* 35 (6), 1–2611. doi:10.1109/TPWRD.2020.2973829

Bhongade, S., and Golhani, S. (2016). HIF detection using wavelet transform, travelling wave and support vector machine. *Int. Conf. Electr. Power Energy Syst. ICEPES*, 151–156. doi:10.1109/ICEPES.2016.7915922

Bin Sulaiman, M., Tawafan, A. H., and Bin Ibrahim, Z. (2017). High Impedance Fault detection on power distribution feeder using subtractive clustering fuzzy system. *Int. Rev. Model. Simulations* 15 (5), `168–181.

Biswal, M., Mishra, M., Sood, V. K., Bansal, R. C., and Abdelaziz, A. Y. (2022). Savitzky-Golay Filter integrated matrix pencil method to identify high impedance fault in a renewable penetrated distribution system. *Electr. Power Syst. Res.* 210 (5), 108056. doi:10.1016/j.epsr.2022.108056

Calhoun, H., Bishop, M. T., Eichler, C. H., and Lee, R. E. (1982). Development and testing of an electro-mechanical relay to detect fallen distribution conductors. *IEEE Power Eng. Rev.* 2 (6), 50–51. doi:10.1109/MPER.1982.5521008

Carpenter, M., Hoad, R. F., Bruton, T. D., Das, R., Kunsman, S. A., and Peterson, J. M. (2005). Staged-fault testing for high impedance fault data collection. *2005 58th Annu. Conf. Prot. Relay Eng.* 2005, 9–17. doi:10.1109/CPRE.2005.1430417

Carr, J. (1981). Detection of high impedance faults on multi-grounded primary distribution systems. *IEEE Trans. Power Appar. Syst.* 100 (4), 2008–2016. doi:10.1109/TPAS.1981.316556

Chaitanya, B. K., Yadav, A., and Pazoki, M. (2020). An intelligent detection of high-impedance faults for distribution lines integrated with distributed generators. *IEEE Syst. J.* 14 (1), 870–879. doi:10.1109/JSYST.2019.2911529

Chakraborty, S., and Das, S. (2019). Application of smart meters in high Impedance Fault detection on distribution systems. *IEEE Trans. Smart Grid* 10 (3), 3465–3473. doi:10.1109/TSG.2018.2828414

Chen, J. C., Phung, B. T., Wu, H. W., Zhang, D. M., and Blackburn, T. (2014). Detection of high impedance faults using wavelet transform. *Australas. Univ. Power Eng. Conf. AUPEC 2014 - Proc.* (10), 1–6. doi:10.1109/AUPEC.2014.6966629

Chen, J. C., Phung, B. T., Zhang, D. M., Blackburn, T., and Ambikairajah, E. (2013). Study on high impedance fault arcing current characteristics. *Australas. Univ. Power Eng. Conf. AUPEC* 2013. doi:10.1109/aupec.2013.6725439

Chen, K., Huang, C., and He, J. (2016). fault detection, classification and location for transmission lines and distribution systems: A review on the methods. *High. Volt.* 1 (1), 25–33. doi:10.1049/hve.2016.0005

Chen, M. T., Chu, H. Y., Huang, C. L., and Wu, F. R. (1990). Performance evaluation of high impedance fault detection algorithms based on staged fault tests. *Electr. Power Syst. Res.* 18 (1), 75–82. doi:10.1016/0378-7796(90)90048-8

Chen, M. Y., Zhai, J. Q., Lang, Z. Q., Liao, J. C., and Fan, Z. Y. (2010). High impedance fault location in transmission line using nonlinear frequency analysis. *Lect. Notes Comput. Sci. Incl. Subser. Lect. Notes Artif. Intell. Lect. Notes Bioinforma.* 6328 (1), 104–111. doi:10.1007/978-3-642-15621-2_13

Christie, R. D., Zadehgol, H., and Habib, M. M. (1993). High Impedance Fault detection in low voltage networks. *IEEE Trans. Power Deliv.* 8 (4), 1829–1836. doi:10.1109/61.248291

Cui, Q., El-Arroudi, K., and Joos, G. (2017). An effective feature extraction method in pattern recognition based high impedance fault detection. *2017 19th Int. Conf. Intell. Syst. Appl. Power Syst. ISAP*, 2017. doi:10.1109/ISAP.2017.8071380

De Alvarenga Ferreira, G., and Mariano Lessa Assis, T. (2019). A novel high impedance arcing fault detection based on the discrete wavelet transform for smart distribution grids. *IEEE PES Conf. Innov. Smart Grid Technol. ISGT Lat. Am.*, 1–6. doi:10.1109/ISGT-LA.2019.8895264

Don Russell, B. (1990). Computer relaying and expert systems: New tools for detecting high impedance faults. *Electr. Power Syst. Res.* 20 (1), 31–37. doi:10.1016/0378-7796(90)90023-V

Ebron, S., Lubkeman, D. L., and White, M. (1990). A neural network approach to the detection of incipient faults on power distribution feeders. *IEEE Trans. Power Deliv.* 5 (2), 905–914. doi:10.1109/61.53101

Eldin, E. S. T., Ibrahim, D. K., Aboul-Zahab, E. M., and Saleh, S. M. (2007). "High impedance faults detection in EHV transmission lines using the wavelet transforms," in *2007 IEEE power eng. Soc. Gen. Meet. PES*. doi:10.1109/PES.2007.385458

Elkalashy, N. I., Lehtonen, M., Darwish, H. A., Izzularab, M. A., and Taalab, A. M. I. (2007). "DWT-based investigation of phase currents for detecting high impedance faults due to leaning trees in unearthed MV networks," in *2007 IEEE power eng. Soc. Gen. Meet. PES*, 1. –7. doi:10.1109/PES.2007.385652

Elkalashy, N. I., Lehtonen, M., Darwish, H. A., Taalab, A. M. I., and Izzularab, M. A. (2008). DWT-based detection and transient power direction-based location of high-impedance faults due to leaning trees in unearthed MV networks. *IEEE Trans. Power Deliv.* 23 (1), 94–101. doi:10.1109/TPWRD.2007.911168

Elkalashy, N. I., Lehtonen, M., Darwish, H. A., Taalab, A. M. I., and Izzularab, M. A. (2007). "Feature extraction of high impedance arcing faults in compensated MV networks. Part I: DWT-based analysis of phase quantities," in *IEEE PES PowerAfrica 2007 conf. Expo. PowerAfrica*, 16–20. doi:10.1109/PESAFR.2007.4498084

Elkalashy, N. I. (2007). *Modelling and detection of high impedance arcing fault in medium voltage networks*.

Emanuel, A. E., Cyganski, D., Orr, J. A., Shiller, S., and Gulachenski, E. M. (1990). High impedance fault arcing on sandy soil in 15kV distribution feeders: Contributions to the evaluation of the low frequency spectrum. *IEEE Trans. Power Deliv.* 5 (2), 676–686. doi:10.1109/61.53070

Fan, R., and Yin, T. (2019). *Convolutional neural network and transfer learning for high Impedance Fault detection*, 1–3. [Online]. Available at: http://arxiv.org/abs/1904.08863.

Farajollahi, M., Shahsavari, A., and Mohsenian-Rad, H. (2017). "Location identification of high impedance faults using synchronized harmonic phasors," in *2017 IEEE power energy soc. Innov. Smart grid technol. Conf. ISGT*, 2017. doi:10.1109/ISGT.2017.8086048

Faridnia, N., Samet, H., and Doostani Dezfuli, B. (2012 A new approach to high impedance fault detection based on correlation functions *IFIP Adv. Inf. Commun. Technol.*).381 (1). AICT, 453–462. doi:10.1007/978-3-642-33409-2_47

Gadanayak, D. A., and Mallick, R. K. (2019). Interharmonics based high impedance fault detection in distribution systems using maximum overlap wavelet packet transform and a modified empirical mode decomposition. *Int. J. Electr. Power Energy Syst.* 112 (5), 282–293. doi:10.1016/j.ijepes.2019.04.050

Gammon, T., and Matthews, J. (2001). Instantaneous arcing-fault models developed for building system analysis. *IEEE Trans. Ind. Appl.* 37 (1), 197–203. doi:10.1109/28.903147

Gashteroodkhani, O. A., Majidi, M., and Etezadi-Amoli, M. (2020). A combined deep belief network and time-time transform based intelligent protection Scheme for microgrids. *Electr. Power Syst. Res.* 182 (1), 106239. doi:10.1016/j.epsr.2020.106239

Gashteroodkhani, O. A., Majidi, M., and Etezadi-Amoli, M. (2021). Fire hazard mitigation in distribution systems through high impedance fault detection. *Electr. Power Syst. Res.* 192 (11), 106928. doi:10.1016/j.epsr.2020.106928

Gashteroodkhani, O. A., Majidi, M., Etezadi-Amoli, M., Nematollahi, A. F., and Vahidi, B. (2019). A hybrid SVM-TT transform-based method for fault location in hybrid transmission lines with underground cables. *Electr. Power Syst. Res.* 170 (1), 205–214. doi:10.1016/j.epsr.2019.01.023

Gautam, S., and Brahma, S. M. (2013). Detection of high impedance fault in power distribution systems using mathematical morphology. *IEEE Trans. Power Syst.* 28 (2), 1226–1234. doi:10.1109/TPWRS.2012.2215630

Ghaderi, A., Ginn, H. L., and Mohammadpour, H. A. (2017). High impedance fault detection: A review. *Electr. Power Syst. Res.* 143, 376–388. doi:10.1016/j.epsr.2016.10.021

Ghaderi, A., Mohammadpour, H. A., Ginn, H. L., and Shin, Y. J. (2015). High-impedance fault detection in the distribution network using the time-frequency-based algorithm. *IEEE Trans. Power Deliv.* 30 (3), 1260–1268. doi:10.1109/TPWRD.2014.2361207

Girgis, A. A., Chang, W., and Makram, E. B. (1990). Analysis of high-impedance fault generated signals using a kalman filtering approach. *IEEE Trans. Power Deliv.* 5 (4), 1714–1724. doi:10.1109/61.103666

Gururajapathy, S. S., Mokhlis, H., and Illias, H. A. (2017 fault location and detection techniques in power distribution systems with distributed generation: A review *Renew. Sustain. Energy Rev.*)., 74. March, 949–958. doi:10.1016/j.rser.2017.03.021

Huang, S. J., and Hsieh, C. T. (1999). High-impedance fault detection utilizing a Morlet wavelet transform approach. *IEEE Trans. Power Deliv.* 14 (4), 1401–1410. doi:10.1109/61.796234

Hubana, T., Saric, M., and Avdakovic, S. (2018). Approach for identification and classification of HIFs in medium voltage distribution networks. *IET Gener. Transm. Distrib.* 12 (5), 1145–1152. doi:10.1049/iet-gtd.2017.0883

Ibrahim, D. K., Eldin, E. S. T., Aboul-Zahab, E. M., and Saleh, S. M. (2008). High-impedance fault detection in EHV transmission lines. *2008 12th Int. Middle East Power Syst. Conf. MEPCON* 1 (1), 192–199. doi:10.1109/MEPCON.2008.4562363

Ibrahim, D. K., Eldin, E. S. T., El-Din Abou El-Zahab, E., and Saleh, S. M. (2010). Unsynchronized fault - location scheme for nonlinear hif in transmission lines. *IEEE Trans. Power Deliv.* 25 (2), 631–637. doi:10.1109/TPWRD.2009.2036182

Ibrahim, D. K., Tag Eldin, E. S., Aboul-Zahab, E. M., and Saleh, S. M. (2010). Real time evaluation of DWT-based high impedance fault detection in EHV transmission. *Electr. Power Syst. Res.* 80 (8), 907–914. doi:10.1016/j.epsr.2009.12.019

Jota, P. R. S., and Jota, F. G. (1999). Fuzzy detection of high impedance faults in radial distribution feeders. *Electr. Power Syst. Res.* 49 (3), 169–174. doi:10.1016/s0378-7796(98)00116-3

K Chaitanya, M. P. B., and Yadav, A. (2020). "High impedance fault detection Scheme for active distribution network using Empirical wavelet transform and support vector machine," in *IEEE explor. 15th int. Conf. Prot. Autom. Power syst* (IRAN: Shiraz Univ.), 30–31.

Kannan, A. N., and Rathinam, A. (2012). High impedance fault classification using wavelet transform and artificial neural network. *Proc. - 4th Int. Conf. Comput. Intell. Commun. Netw. CICN*, 831–837. doi:10.1109/CICN.2012.122

Kar, S., and Samantaray, S. R. (2017). High impedance fault detection in microgrid using maximal overlapping discrete wavelet transform and decision tree. *Int. Conf. Electr. Power Energy Syst. ICEPES*, 258–263. doi:10.1109/ICEPES.2016.7915940

Kavaskar, S., and Mohanty, N. K. (2019). Detection of high Impedance Fault in distribution networks. *Ain Shams Eng. J.* 10 (1), 5–13. doi:10.1016/j.asej.2018.04.006

Keyhani, R., Deriche, M., and Palmer, E. (2001). A high impedance fault detector using a neural network and subband decomposition. *6th Int. Symp. Signal Process. Its Appl. ISSPA 2001 - Proc. 6 Tutorials Commun. Image Process. Signal Anal.* 2, 458–461. doi:10.1109/ISSPA.2001.950179

Kim, C. J., Don Russell, B., and Watson, K. (1990). A parameter-based process for selecting high impedance fault detection techniques using decision making under incomplete knowledge. *IEEE Trans. Power Deliv.* 5 (3), 1314–1320. doi:10.1109/61.57972

Kistler, M., Kistler, M., and Utilities, P. P. L. E. (2019). *Practical experience with high-impedance fault detection in distribution systems practical experience with high-impedance fault detection in distribution systems*. [Online]. Available at: https://selinc.com/mktg/132137/?creative=350703817639&keyword=high impedance fault&matchtype=b&network=g&device=c&gclid=CjwKCAjwg4-EBhBwEiwAzYAlskrXp7M7oe_lGPdSEsFOWnpfE_JnaEV-4mKZTz82xCNGy4Bn2S0sbhoCkKcQAvD_BwE.

Kjølle, G. H., Gjerde, O., Hjartsjo, B. T., Engen, H., Haarla, L., Koivisto, L., et al. (2006). "Protection system faults - a comparative review of fault statistics," in *2006 9th int. Conf. Probabilistic methods appl. To power syst. PMAPS*, 1–7. doi:10.1109/PMAPS.2006.360319

Kwon, W. H., Lee, G. W., Park, Y., Yoon, M., and Yoo, M. (1991). High impedance fault detection utilizing incremental varianc. *IEEE Power Eng. Rev.* 11 (4), 58–59. doi:10.1109/MPER.1991.88839

Lai, T. M., Snider, L. A., Lo, E., and Sutanto, D. (2005). High-impedance fault detection using discrete wavelet transform and frequency range and RMS conversion. *IEEE Trans. Power Deliv.* 20 (1), 397–407. doi:10.1109/TPWRD.2004.837836

Langeroudi, A. T., and Abdelaziz, M. M. A. (2020). Preventative high impedance fault detection using distribution system state estimation. *Electr. Power Syst. Res.* 186 (4), 106394. doi:10.1016/j.epsr.2020.106394

Lazkano, A., Ruiz, J., Aramendi, E., and Leturiondo, L. A. (2004). Evaluation of a new proposal for an arcing fault detection method based on wavelet packet analysis. *Eur. Trans. Electr. Power* 14 (3), 161–174.

Lee, R. E., and Bishop, M. T. (1985). A comparison of measured high Impedance Fault data to digital computer modeling results. *IEEE Power Eng. Rev.* 5 (10), 35–36. doi:10.1109/MPER.1985.5528688

Leite, M. P. (2019). *A voltage-based approach for series high impedance using smart meters*.

Li, W. J., and Li, Y. C. (2005). Arc fault detection based on wavelet packet. *Int. Conf. Mach. Learn. Cybern. ICMLC* 2 (8), 1783–1788. doi:10.1109/icmlc.2005.1527234

Lima, É. M., Brito, N. S. D., and de Souza, B. A. (2019). High impedance fault detection based on Stockwell transform and third harmonic current phase angle. *Electr. Power Syst. Res.* 175 (6), 105931. doi:10.1016/j.epsr.2019.105931

Lima, É. M., Junqueira, C. M. dos S., Brito, N. S. D., de Souza, B. A., Coelho, R. de A., and de Medeiros, H. G. M. S. (2018). High impedance fault detection method based on the short-time Fourier transform. *IET Gener. Transm. Distrib.* 12 (11), 2577–2584. doi:10.1049/iet-gtd.2018.0093

Lin, Y. H., Liu, C. W., and Chen, C. S. (2004). A new PMU-based fault detection/location technique for transmission lines with consideration of arcing fault discrimination - Part I: Theory and algorithms. *IEEE Trans. Power Deliv.* 19 (4), 1587–1593. doi:10.1109/TPWRD.2004.832407

Louis, H. W. (2015). *Study of high Impedance Fault characteristics and detection methods*. Master thesis, 150 New South Wales, Sydney, Australia: Sch. Electr. Eng. Telecommun. Univ.

Mamishev, A. V., Russell, B., and Benner, C. (1996). Analysis of high impedance faults using fractal techniques. *IEEE Trans. Power Syst.* 11 (1), 435–440. doi:10.1109/59.486130

Michalik, M., Lukowicz, M., Rebizant, W., Lee, S. J., and Kang, S. H. (2007). Verification of the wavelet-based HIF detecting algorithm performance in solidly grounded MV networks. *IEEE Trans. Power Deliv.* 22 (4), 2057–2064. doi:10.1109/TPWRD.2007.905283

Michalik, M., Rebizant, W., Lukowicz, M. R., Lee, S. J., and Kang, S. H. (2006). High-impedance fault detection in distribution networks with use of wavelet-based algorithm. *IEEE Trans. Power Deliv.* 21 (4), 1793–1802. doi:10.1109/TPWRD.2006.874581

Milioudis, A. N., Member, S., Andreou, G. T., Labridis, D. P., and Member, S. (2012). Enhanced protection scheme for smart grids using power line communications techniques—Part II: Location of high Impedance Fault position. *Locat. High Impedance Fault Position* 3 (4), 1631–1640. doi:10.1109/tsg.2012.2208988

Mishra, M., and Panigrahi, R. R. (2019). Taxonomy of high impedance fault detection algorithm. *Meas. J. Int. Meas. Confed.* 148, 106955. doi:10.1016/j.measurement.2019.106955

Mishra, M., Routray, P., and kumar Rout, P. (2016). A universal high Impedance Fault detection technique for distribution system using S-transform and pattern recognition. *Technol. Econ. Smart Grids Sustain. Energy* 1 (9), 1. doi:10.1007/s40866-016-0011-4

Mishra, M., Sahani, M., and Rout, P. K. (2017). An islanding detection algorithm for distributed generation based on Hilbert–Huang transform and extreme learning machine. *Sustain. Energy, Grids Netw.* 9, 13–26. doi:10.1016/j.segan.2016.11.002

Moravej, Z., Mortazavi, S. H., and Shahrtash, S. M. (2015). DT-CWT based event feature extraction for high impedance faults detection in distribution system. *Int. Trans. Electr. Energy Syst.* 25 (12), 3288–3303. doi:10.1002/etep.2035

Naik, V. K., and Yadav, A. (2018). "High impedance fault detection and classification on IEEE-15 bus radial distribution system by using fuzzy inference system," in *2018 2nd int. Conf. Power, energy environ. Towar. Smart technol*, 1–6.

Nam, S. R., Park, J. K., Kang, Y. C., and Kim, T. H. (2001). A modeling method of a high impedance fault in a distribution system using two series time-varying resistances in EMTP. *Proc. IEEE Power Eng. Soc. Transm. Distrib. Conf.* 2 (5), 1175–1180. doi:10.1109/pess.2001.970231

Narasimhulu, N., Kumar, D. V. A., and Kumar, M. V. (2020). LWT based ANN with ant lion optimizer for detection and classification of high impedance faults in distribution system. *J. Electr. Eng. Technol.* 15 (4), 1631–1650. doi:10.1007/s42835-020-00456-z

Nezamzadeh-Ejieh, S., and Sadeghkhani, I. (2020). HIF detection in distribution networks based on Kullback-Leibler divergence. *IET Gener. Transm. Distrib.* 14 (1), 29–36. doi:10.1049/iet-gtd.2019.0001

Nikoofekr, I., Sarlak, M., and Shahrtash, S. M. (2013). Detection and classification of high impedance faults in power distribution networks using ART neural networks. *2013 21st Iran. Conf. Electr. Eng. ICEE*, 1–6. doi:10.1109/IranianCEE.2013.6599760

Panigrahi, R. R., Mishra, M., Rajan, A., and Mohapatra, S. (2018). High Impedance Fault detection based on mathematical morphology for radial distribution network. *2018 Int. Conf. Appl. Electromagn. Signal Process. Commun. AESPC* 2018. doi:10.1109/AESPC44649.2018.9033309

Prasad, C. D., Biswal, M., Mishra, M., Guerrero, J. M., and Malik, O. P. (2022). Optimal threshold-based high impedance arc fault detection approach for renewable penetrated distribution system. *IEEE Syst. J.*, 1–11. doi:10.1109/JSYST.2022.3202809

Radhakrishnan, A. (2019). *Location of high impedance faults using smart meters in distribution systems with DGs, power electronic loads and Electric Arc furnaces*. IEEE Milan PowerTech, 1–6.

Reddy, S. H., Garg, R., and Pillai, G. N. (2013). High Impedance Fault classification and section identification using extreme learning machines (ELM). *Ripublication. Com.* 3 (7), 839–846.

Roberts, J., Altuve, H. J., and Hou, D. (2001). Review of ground fault protection methods for grounded, ungrounded, and compensated distribution systems. *27th Annu. West. Prot. Relay Conf.* 40.

Routray, P., Mishra, M., and Rout, P. K. (2016). High Impedance Fault detection in radial distribution system using S-Transform and neural network. *2015 IEEE Power, Commun. Inf. Technol. Conf. PCITC 2015 - Proc.*, 545–551. doi:10.1109/PCITC.2015.7438225

Russell, B. D., and Benner, C. L. (1995). Arcing Fault detection for distribution feeders: Security assessment in long term field trials. *IEEE Trans. Power Deliv.* 10 (2), 676–683. doi:10.1109/61.400864

Russell, B. D., Chinchali, R. P., and Kim, C. J. (1988). Behaviour of low frequency spectra during arcing fault and switching events. *IEEE Trans. Power Deliv.* 3 (4), 1485–1492. doi:10.1109/61.193947

Sahoo, S., and Baran, M. E. (2014). A method to detect high impedance faults in distribution feeders. *Proc. IEEE Power Eng. Soc. Transm. Distrib. Conf.*, 1–6. doi:10.1109/tdc.2014.6863531

Samantaray, P. K. D. S. R., Gouvea, M., Lacerda, A., Alves, F., and Leite, D. (2009). High impedance fault detection in power distribution systems using wavelet transform and evolving neural network. *Electr. Power Syst. Res.* 154 (2), 474–483. doi:10.1016/j.epsr.2017.08.039

Samantaray, S. R., Dash, P. K., and Upadhyay, S. K. (2009). Adaptive Kalman filter and neural network based high impedance fault detection in power distribution networks. *Int. J. Electr. Power Energy Syst.* 31 (4), 167–172. doi:10.1016/j.ijepes.2009.01.001

Samantaray, S. R. (2012). Ensemble decision trees for high impedance fault detection in power distribution network. *Int. J. Electr. Power Energy Syst.* 43 (1), 1048–1055. doi:10.1016/j.ijepes.2012.06.006

Samantaray, S. R., Panigrahi, B. K., and Dash, P. K. (2008). High impedance fault detection in power distribution networks using time-frequency transform and probabilistic neural network. *IET Gener. Transm. Distrib.* 2 (2), 261–270. doi:10.1049/iet-gtd:20070319

Santos, W. C., Lopes, F. V., Brito, N. S. D., and Souza, B. A. (2017). High-impedance fault identification on distribution networks. *IEEE Trans. Power Deliv.* 32 (1), 23–32. doi:10.1109/TPWRD.2016.2548942

Santos, W. C., V Lopes, F., Brito, N. S. D., Souza, B. A., Fernandes., J. D., and Neves, W. L. A. (2013). High Impedance Fault detection and location based on electromagnetic transient analysis. *Int. Conf. Power Syst. Transients*. [Online]. Available at: http://www.ipstconf.org/papers/Proc_IPST2013/13IPST135.pdf.

Sarlak, M., and Shahrtash, S. M. (2008). "High impedance fault detection in distribution networks using support vector machines based on wavelet transform," in *2008 IEEE electr. Power energy conf. - energy innov*, 1–6. doi:10.1109/EPC.2008.4763380

Sarlak, M., and Shahrtash, S. M. (2011). High impedance fault detection using combination of multi-layer perceptron neural networks based on multi-resolution morphological gradient features of current waveform. *IET Gener. Transm. Distrib.* 5 (5), 588–595. doi:10.1049/iet-gtd.2010.0702

Sarlak, M., and Shahrtash, S. M. (2013). High-impedance faulted branch identification using magnetic-field signature analysis. *IEEE Trans. Power Deliv.* 28 (1), 67–74. doi:10.1109/TPWRD.2012.2222056

Sarwagya, K., De, S., and Nayak, P. K. (2018). High-impedance fault detection in electrical power distribution systems using moving sum approach. *IET Sci. Meas. Technol.* 12 (1), 1–8. doi:10.1049/iet-smt.2017.0231

Sarwar, M., Mehmood, F., Abid, M., Khan, A. Q., Gul, S. T., and Khan, A. S. (2020). High impedance fault detection and isolation in power distribution networks using support vector machines. *J. King Saud. Univ. - Eng. Sci.* 32 (8), 524–535. doi:10.1016/j.jksues.2019.07.001

Scott, J. A. (1994). *Impulse response analysis of a real feeder*. Ieee Explor., 276–283.

Sedighi, A. R., Haghifam, M. R., Malik, O. P., and Ghassemian, M. H. (2005). High impedance fault detection based on wavelet transform and statistical pattern recognition. *IEEE Trans. Power Deliv.* 20 (4), 2414–2421. doi:10.1109/TPWRD.2005.852367

Sedighi, A. R., Haghifam, M. R., and Malik, O. P. (2005). Soft computing applications in high impedance fault detection in distribution systems. *Electr. Power Syst. Res.* 76 (1–3), 136–144. doi:10.1016/j.epsr.2005.05.004

Sedighizadeh, M., Rezazadeh, A., and Elkalashy, N. I. (2010). Approaches in high impedance fault detection a Chronological review. *Adv. Electr. Comput. Eng.* 10 (3), 114–128. doi:10.4316/aece.2010.03019

Sekar, K., and Mohanty, N. K. (2020). A fuzzy rule base approach for High Impedance Fault detection in distribution system using Morphology Gradient filter. *J. King Saud. Univ. - Eng. Sci.* 32 (3), 177–185. doi:10.1016/j.jksues.2018.12.001

Sekar, K., and Mohanty, N. K. (2017). Combined mathematical morphology and data mining based high Impedance Fault detection. *Energy Procedia* 117, 417–423. doi:10.1016/j.egypro.2017.05.161

Sekar, K., and Mohanty, N. K. (2018). Data mining-based high impedance fault detection using mathematical morphology. *Comput. Electr. Eng.* 69 (5), 129–141. doi:10.1016/j.compeleceng.2018.05.010

SEL (2007). *Arc sense technology (AST) detect more faults than ever before.*

Shahrtash, S. M., and Sarlak, M. (2006). High impedance fault detection using harmonics energy decision tree algorithm. *Int. Conf. Power Syst. Technol. POWERCON2006* 00, 1–5. doi:10.1109/ICPST.2006.321441

Sharaf, A. M., El-Sharkawy, R. M., Al-Fatih, R., and Al-Ketbi, M. (1996). High impedance fault detection on radial distribution and utilization systems. *Can. Conf. Electr. Comput. Eng.* 2, 1012–1013. doi:10.1109/ccece.1996.548326

Sharaf, A. M., Snider, L. A., and Debnath, K. (1993). A neural network based relaying scheme for distribution system high impedance fault detection. *ANNES 1993 - 1st New Zeal. Int. Two-Stream Conf. Artif. Neural Netw. Expert Syst.*, 321–324. doi:10.1109/ANNES.1993.323013

Sheng, Y., and Rovnyak, S. M. (2004). Decision tree-based methodology for high impedance fault detection. *IEEE Trans. Power Deliv.* 19 (2), 533–536. doi:10.1109/TPWRD.2003.820418

Silva, P. R., Santos, A., and Jota, F. G. (1995). Intelligent system for automatic detection of high impedance faults in electrical distribution systems. *Midwest Symp. Circuits Syst.* 1, 453–456. doi:10.1109/mwscas.1995.504474

Silva, S., Costa, P., Santana, M., and Leite, D. (2020). Evolving neuro-fuzzy network for real-time high impedance fault detection and classification. *Neural comput. Appl.* 32 (12), 7597–7610. doi:10.1007/s00521-018-3789-2

Snider, L. A., and Shan, Y. Y. (1998). Artificial neural networks based relay algorithm for distribution system high impedance fault detection. *IEE Conf. Publ.* 46 (450), 100–106. doi:10.1049/cp:19971812

Snider, L. A., and Yuen, Y. S. (1998). The artificial neural-networks-based relay algorithm for the detection of stochastic high impedance faults. *Neurocomputing* 23 (1–3), 243–254. doi:10.1016/S0925-2312(98)00068-X

Soheili, A., Sadeh, J., and Bakhshi, R. (2018). Modified FFT based high impedance fault detection technique considering distribution non-linear loads: Simulation and experimental data analysis. *Int. J. Electr. Power Energy Syst.* 94, 124–140. doi:10.1016/j.ijepes.2017.06.035

Suliman, M. Y., and Ghazal, M. T. (2019). Detection of high impedance Fault in distribution network using fuzzy logic control. *2nd Int. Conf. Electr. Commun. Comput. Power Control Eng. ICECCPCE*, 103–108. doi:10.1109/ICECCPCE46549.2019.203756

Sultan, A. F., Swift, G. W., and Fedirchuk, D. J. (1994). Detecting arcing downed-wires using fault current flicker and half-cycle asymmetry. *IEEE Trans. Power Deliv.* 9 (1), 461–470. doi:10.1109/61.277718

Sultan, A. F., Swift, G. W., and Fedirchuk, D. J. (1992). Detection of high impedance arcing faults using a multi-layer perceptron. *IEEE Trans. Power Deliv.* 7 (4), 1871–1877. doi:10.1109/61.156989

Sultan, A. F., and Swift, G. W. (1992). *Security testing of high impedance fault detectors*, 191–197. doi:10.1109/wescan.1991.160545

Tag Eldin, E. S., Khalil Ibrahim, D., Aboul-Zahab, E. M., and Saleh, S. M. (2009). High impedance fault detection in EHV series compensated lines using the wavelet transform. *IEEE/PES Power Syst. Conf. Expo. PSCE*, 2009. doi:10.1109/PSCE.2009.4840082

Tawafan, A., Bin Sulaiman, M., and Bin Ibrahim, Z. (2012). Adaptive neural subtractive clustering fuzzy inference system for the detection of high Impedance Fault on distribution power system. *IAES Int. J. Artif. Intell.* 1 (2). doi:10.11591/ij-ai.v1i2.425

Tengdin, J., Westfall, R., and Stephan, K. (1996). *High Impedance Fault detection technology* Los Angeles, CA, United States of America: Rep. PSRC Work. Gr., 1–4. [Online]. Available at: http://grouper.ieee.org/groups/td/dist/documents/highz.pdf.

Theron, J. C. J., Pal, A., and Varghese, A. (2018). Tutorial on high impedance fault detection. *71st Annu. Conf. Prot. Relay Eng. CPRE* 2018, 1–23. doi:10.1109/CPRE.2018.8349833

Thomas, M. S., Bhaskar, N., and Prakash, A. (2016). Voltage based detection method for high Impedance Fault in a distribution system. *J. Inst. Eng. Ser. B* 97 (3), 413–423. doi:10.1007/s40031-015-0203-7

Tonelli-Neto, M. S., Decanini, J. G. M. S., Lotufo, A. D. P., and Minussi, C. R. (2017). Fuzzy based methodologies comparison for high-impedance fault diagnosis in radial distribution feeders. *IET Gener. Transm. Distrib.* 11 (6), 1557–1565. doi:10.1049/iet-gtd.2016.1409

Vahidi, B., Ghaffarzadeh, N., Hosseinian, S. H., and Ahadi, S. M. (2010). An approach to detection of high Impedance Fault using discrete wavelet transform and artificial neural networks. *Simulation* 86 (4), 203–215. doi:10.1177/0037549709340823

Veerasamy, V., Abdul Wahab, N. I., Ramachandran, R., Mansoor, M., Thirumeni, M., and Othman, M. L. (2018). High impedance fault detection in medium voltage distribution network using discrete wavelet transform and adaptive neuro-fuzzy inference system. *Energies* 11, 3330. doi:10.3390/en11123330

Veerasamy, V., Abdul Wahab, N. I., Ramachandran, R., Thirumeni, M., Subramanian, C., Othman, M. L., et al. (2019). High-impedance fault detection in medium-voltage distribution network using computational intelligence-based classifiers. *Neural comput. Appl.* 31 (12), 9127–9143. doi:10.1007/s00521-019-04445-w

Vyshnavi, G., and Prasad, A. (2018). Detection and location of high impedance faults in distribution systems: A review. *Int. J. Adv. Sci. Technol.* 119, 53–66. doi:10.14257/ijast.2018.119.05

Wali, M. K., Hussain, A. N., and Hani, W. F. (2018). High impedance fault detection based on power spectrum technique. *Proc. 2017 Int. Conf. Eng. Technol. ICET 2017* 2018, 1–6. doi:10.1109/ICEngTechnol.2017.8308169

Wang, B., Geng, J., and Dong, X. (2018). High-impedance fault detection based on nonlinear voltage-current characteristic profile identification. *IEEE Trans. Smart Grid* 9 (4), 3783–3791. doi:10.1109/TSG.2016.2642988

Wang, X., Gao, J., Wei, X., Song, G., Wu, L., Liu, J., et al. (2019). High impedance fault detection method based on variational mode decomposition and teager-kaiser energy operators for distribution network. *IEEE Trans. Smart Grid* 10 (6), 6041–6054. doi:10.1109/TSG.2019.2895634

Wester, C. G. (1998). High impedance fault detection on distribution systems. *Pap. - Rural. Electr. Power Conf.* doi:10.11591/ijaas.v8.i2.pp95-102

Xie, S., Wang, X., Qu, C., Wang, X., and Guo, J. (2013). DT-CWT based event feature extraction for high impedance faults detection in distribution system. *Int. Trans. Electr. energy Syst.* 20, 1–6. doi:10.1002/etep

Xie, S., Wang, X., Qu, C., Wang, X., and Guo, J. (2013). High impedance fault detection in distribution feeders using extended kalman filter and support vector machine. *Int. Trans. Electr. energy Syst.* 20, 1–6. doi:10.1002/etep

Yang, M. T., Gu, J. C., Guan, J. L., and Cheng, C. Y. (2006). Evaluation of algorithms for high impedance faults identification based on staged fault tests. *2006 IEEE Power Eng. Soc. Gen. Meet. PES*, 1–8. doi:10.1109/pes.2006.1709122

Yang, M. T., Gu, J. C., Jeng, C. Y., and Kao, W. S. (2004). Detection high impedance fault in distribution feeder using wavelet transform and artificial neural networks. *Int. Conf. Power Syst. Technol. POWERCON* 1 (11), 652–657. doi:10.1109/icpst.2004.1460075

Yeh, H. G., Sim, S., and Bravo, R. J. (2019). Wavelet and denoising techniques for real-time HIF detection in 12-kV distribution circuits. *IEEE Syst. J.* 13 (4), 4365–4373. doi:10.1109/JSYST.2019.2942093

Yeh, H. G., Tran, D. H., and Yinger, R. (2014). High impedance fault detection using orthogonal transforms. *2014 IEEE Green Energy Syst. Conf. IGESC*, 67–72. doi:10.1109/IGESC.2014.7018642

Zamanan, N., Sykulski, J., and Al-Othman, A. K. (2007). Arcing high impedance fault detection using real coded genetic algorithm. *Proc. 3rd IASTED Asian Conf. Power Energy Syst. AsiaPES* 2007, 35–39.

Zamanan, N., and Sykulski, J. (2014). The evolution of high impedance fault modeling. *Proc. Int. Conf. Harmon. Qual. Power, ICHQP*, 77–81. doi:10.1109/ICHQP.2014.6842852

Zhang, W., Jing, Y., and Xiao, X. (2016). Model-based general arcing fault detection in medium-voltage distribution lines. *IEEE Trans. Power Deliv.* 31 (5), 2231–2241. doi:10.1109/TPWRD.2016.2518738

Nomenclature

ANFIS Adaptive neuro-fuzzy inference system
AEKF Adaptive extended Kalman filter
ANN Artificial neural network
CWT Continuous wavelet transform
CNN Convolution neural network
CERTS Consortium for Electric Reliability Technology Solutions
DLGF Double-line-to-ground fault
DWT Discrete wavelet transform
DTWT Dual-tree complex wavelet transform
DG Distributed generators
DT Decision tree
ELM Extreme learning machines
EKF Extended Kalman filter
FFT Fast Fourier transform
FFN Feedforward network
FLC Fuzzy logic control
FANN Fuzzy art neural network
GA Genetic algorithm
HT Hilbert Transform
HIF High-impedance fault
HIL Hardware-in-loop
ILC Insulator leakage current
IMF Intrinsic mode functions
KNN k-Nearest neighbor
LLF Line-to-line fault
LDA Linear discriminant analysis
LWT Lifting wavelet transform
LVQ Learning vector quantization
MODWT Maximum overlap discrete wavelet transform
MMF Mathematical morphology filters
MG Morphology gradient
MLPNN Multi-layer perceptron neural network
MWT Morlet wavelet transform
PNN Probabilistic neural network
PCA Principal component analysis
PTDS Power transmission and distribution system
PCC Point of common coupling
RTDS Real-time digital simulator
RF Random forest
RCGA Real coded genetic algorithm
ReLU Rectified linear unit
SLGF Single-line-to-ground fault
ST S transform
SVM Support vector machine
SNR Signal-to-noise ratio
SD Standard deviation
STFT Short-time Fourier transform
SG Synchronous generator
TFA Time-frequency analysis
TSK Takagi–Sugeno–Kang
TZSCs Transient zero sequence currents
LLLGF Triple-line-to-ground fault
TTT Time–time transform
VCCP Voltage–current characteristic profiles
WCC Wavelet correlation coefficient
WHTs Walsh–Hadamard transforms

Frontiers in
Energy Research

Advances and innovation in sustainable, reliable and affordable energy

Explores sustainable and environmental developments in energy. It focuses on technological advances supporting Sustainable Development Goal 7: access to affordable, reliable, sustainable and modern energy for all.

Discover the latest Research Topics

See more →

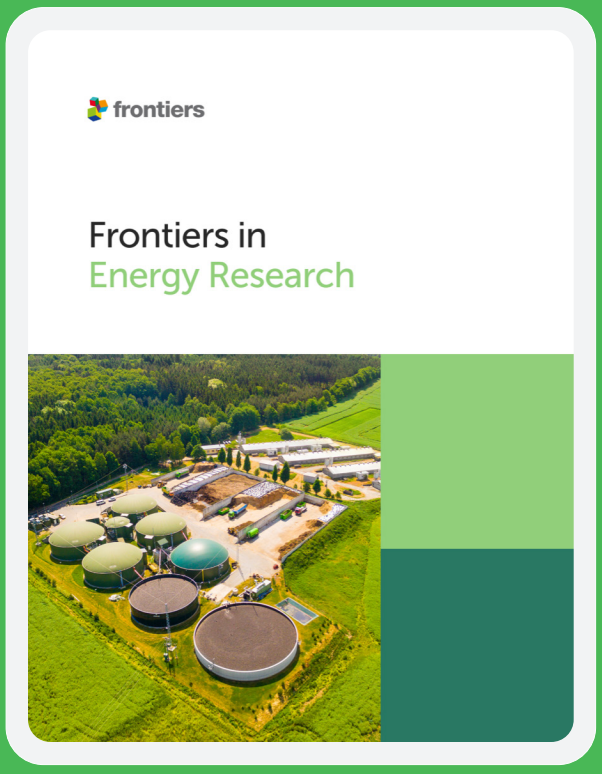

Frontiers

Avenue du Tribunal-Fédéral 34
1005 Lausanne, Switzerland
frontiersin.org

Contact us

+41 (0)21 510 17 00
frontiersin.org/about/contact